

LUND UNIVERSITY

Luminosity determination and simulation of the LUCID detector at the ATLAS experiment

Groth-Jensen, Jacob; ATLAS Collaboration

2010

Link to publication

Citation for published version (APA):
Groth-Jensen, J., & ATLAS Collaboration (2010). *Luminosity determination and simulation of the LUCID detector at the ATLAS experiment*. [Doctoral Thesis (monograph), Particle and nuclear physics]. Lund University , Department of physics.

Total number of authors:
2

General rights
Unless other specific re-use rights are stated the following general rights apply:
Copyright and moral rights for the publications made accessible in the public portal are retained by the authors and/or other copyright owners and it is a condition of accessing publications that users recognise and abide by the legal requirements associated with these rights.
• Users may download and print one copy of any publication from the public portal for the purpose of private study or research.
• You may not further distribute the material or use it for any profit-making activity or commercial gain
• You may freely distribute the URL identifying the publication in the public portal

Read more about Creative commons licenses: https://creativecommons.org/licenses/

Take down policy
If you believe that this document breaches copyright please contact us providing details, and we will remove access to the work immediately and investigate your claim.

LUND UNIVERSITY

PO Box 117
221 00 Lund
+46 46-222 00 00

ISBN 978-91-7473-060-9
LUNFD6/(NFFL-7231)2010

Luminosity determination and simulation of the LUCID detector at the ATLAS experiment

Thesis submitted for the degree of
Doctor of Philosophy

by

Jacob Groth-Jensen



LUNDS
UNIVERSITET

DEPARTMENT OF PHYSICS
LUND, 2010

Organization **LUND UNIVERSITY** Department of Physics Lund University Box 118 SE-221 00 Lund SWEDEN	**Document name** **DOCTORAL DISSERTATION** **Date of issue** November, 2010 **CODEN** LUNFD6/(NFFL-7231)2010
Author(s) Jacob Groth-Jensen	**Sponsoring organization**

Title and subtitle
Luminosity determination and simulation of the LUCID detector at the ATLAS experiment

Abstract
The aim of this thesis is to describe how the luminosity can be measured in the ATLAS experiment at the Large Hadron Collider. Luminosity is a fundamental quantity that is used in most physics studies at the LHC. For example in order to measure cross sections.
Firstly, the detector description of LUCID which has been implemented in the global ATLAS software framework is described and validated. Secondly, algorithms to determine the luminosity are derived and the simulation of LUCID is used to test the precision of these. Thirdly, the feasibility of using Z^0 production as a alternative way to measure the luminosity or to calibrate LUCID is studied. The performance of LUCID is addressed by comparing results from the early 2010 data-taking period with predictions from the simulations. Several techniques to calculate the efficiency of LUCID are described and the results for each method is presented. Several classes of luminosity algorithms studied and applied to the signals from the LUCID detector. The first class has been designed to be used online and to extract the luminosity using two different counting methods, namely event and hit counting. An empirical model is introduced as an attempt to parametrize the non-linear effect by polynomial fits to the event and hit rate. A final attempt to minimize the non-linear effects was presented by introducing a new method that uses the full hit multiplicity distribution to determine the luminosity offline. A method to measure the absolute luminosity using the production of Z^0 boson is outlined . Each step of the procedure to select $Z \to \mu^+\mu^-$ events has been studied in detail using Monte Carlo simulations of the various background and signal samples. The selection procedure is applied to a data sample recorded by the ATLAS detector over a period of 5 month and the resulting integrated luminosity is determined from the number of reconstructed $Z \to \mu^+\mu^-$ events.

Key words:
LHC, ATLAS, LUCID, Performance study, Luminosity determination, Gauge boson production

Classification system and/or index terms (if any)

Supplementary bibliographical information:		**Language** English
ISSN and key title:		**ISBN** 978-91-7473-060-9
Recipient's notes	**Number of pages** 216	**Price**
	Security classification	

Distribution by (name and address)
Jacob Groth-Jensen, Department of Physics
Box 118, SE-221 00 Lund, SWEDEN

I, the undersigned, being the copyright owner of the above-mentioned dissertation, hereby grant to all reference sources permission to publish and disseminate the abstract of the above-mentioned dissertation.

Signature Jacob Groth-Jensen **Date** 2010-11-03

To my family

Contents

Preface **1**

I Theory **7**

1 The Standard Model of Particle Physics **8**

1.1 Inputs to the Standard Model 9

1.1.1 Fundamental Particles 9

1.1.2 Mathematical Framework 11

1.2 Quantum electrodynamics 11

1.3 Quantum chromodynamics 12

1.4 Electroweak Theory 13

1.4.1 Chiral fermions 14

1.4.2 $SU(2)_L \times U(1)_Y$ gauge invariant Langrangian 14

1.4.3 Higgs mechanism and the W and Z mass 16

II The ATLAS experiment at the Large Hadron Collider **21**

2 The Large Hadron Collider **22**

2.1 Design considerations 22

2.2 The LHC accelerator system 23

2.2.1 The injection chain 25

2.2.2 Beam structure 25

2.3 LHC Experiments 25

2.4 LHC trivia 27

3 The ATLAS detector **28**

3.1 Detector overview . . . 29
3.2 Magnet Systems . . . 33
3.3 Inner detector . . . 34
3.3.1 The pixel detector . . . 34
3.3.2 The semiconductor tracker . . . 34
3.3.3 The transition radiation tracker . . . 35
3.3.4 Pile-up at high luminosity . . . 36
3.4 Calorimeters . . . 37
3.4.1 The Electromagnetic Calorimeter . . . 38
3.4.2 The Hadronic Calorimeter . . . 39
3.5 Muon Spectrometer . . . 40
3.5.1 Precision tracking chambers . . . 41
3.5.2 Trigger chambers . . . 42
3.6 Beam Monitors . . . 42
3.6.1 Beam Condition Monitor . . . 42
3.6.2 Minimum Bias Trigger Scintillators . . . 43
3.7 Forward Detectors . . . 44
3.7.1 LUCID . . . 44
3.7.2 ZDC . . . 45
3.7.3 ALFA . . . 46
3.8 Trigger and Data Acquisition systems . . . 46
3.8.1 Level 1 . . . 47
3.8.2 High Level Trigger: Level 2 and Event Filter . . . 48
3.8.3 Data Acquisition system . . . 48

4 Principles of Luminosity Determination 49
4.1 Introduction to luminosity . . . 49
4.1.1 The Need for a Precise Luminosity Determination . . . 50
4.2 Luminosity determination at the LHC . . . 50
4.3 Absolute Luminosity Measurement . . . 52
4.3.1 LHC Machine Parameters - Van der Meer scans . . . 52
4.3.2 Resonance counting . . . 53
4.3.3 Coulomb scattering amplitude . . . 54
4.4 Relative Luminosity Measurement . . . 55
4.5 Summary . . . 56

III The LUCID Detector **59**

5 Detector description **60**

5.1 Goal of the detector . . . 60
5.2 Design and working principle . . . 61
5.2.1 Detector design . . . 62
5.2.2 Detection principle and background suppression . . . 63
5.3 Electronics and readout system . . . 66
5.3.1 The LUMAT card . . . 67
5.3.2 Calibration . . . 67

6 Simulation of LUCID **69**

6.1 Detector desciption . . . 70
6.1.1 Cerenkov light emission . . . 71
6.1.2 Light propagation and detection . . . 73
6.2 Response to a single particle . . . 75
6.2.1 Signal from on-axis particles . . . 75
6.2.2 Signal from off-axis particles . . . 77
6.3 Response to *pp* collisions . . . 78
6.3.1 Event generators . . . 79
6.3.2 Track propagation inside ATLAS . . . 80
6.3.3 On the origin of secondary particles . . . 81
6.3.4 On the photo-electron spectrum and the definition of a hit . . . 84
6.3.5 Particle kinematics . . . 85
6.4 Simulation of the front-end electronics (Digitization) . . . 90
6.4.1 General digitization procedure for LUCID . . . 90
6.4.2 Step 1 - Unpacking of the simulated hits. . . . 90
6.4.3 Step 2 - Simulation of the detector response . . . 91
6.4.4 Step 3 - Production of detector response digits. . . . 94
6.4.5 Step - 4 Level 1 trigger simulation. . . . 94
6.4.6 Step 5 - Conversion to byte stream format . . . 95
6.5 Systematic uncertainies . . . 95
6.5.1 The simulation step . . . 96
6.5.2 Digitization step . . . 97
6.6 Conclusion . . . 98

7 Performance of LUCID in the early 2010 data-taking period 100
7.1 Data Samples and Event Selection . . . 100
7.1.1 Real data . . . 100
7.1.2 Monte Carlo simulation . . . 100
7.2 Data formats . . . 101
7.3 Charge distributions . . . 102
7.4 Hit multiplicity distributions . . . 106
7.4.1 Hit probability for different tubes . . . 106
7.4.2 Hit multiplicity and asymmetry . . . 108
7.4.3 Hit multiplicity vs. pseudo-rapidity . . . 112
7.5 Efficiency determination . . . 114
7.5.1 Online trigger selection . . . 114
7.5.2 Efficiency determination from Monte Carlo events . . . 115
7.5.3 Data driven efficiency determination . . . 115
7.5.4 Efficiency and systematic uncertainty . . . 117
7.6 Background determination and final results . . . 120
7.7 Conclusion . . . 122

IV Luminosity Determination 125

8 Performance Study of Luminosity Algorithms in ATLAS 126
8.1 Introduction . . . 126
8.1.1 Data samples . . . 128
8.2 Simulation of high luminosity events . . . 129
8.3 Counting methods . . . 129
8.4 Online Algorithms : The combinatorial model . . . 132
8.4.1 Probability functions . . . 133
8.4.2 Event counting : single side mode ("OR" mode) . . . 134
8.4.3 Event counting : coincidence mode ("AND" mode) . . . 136
8.4.4 Hit counting : single side mode ("OR" mode) . . . 138
8.4.5 Hit counting : coincidence mode ("AND" mode) . . . 141
8.5 Online Algorithms : Polynomial parameterization method . . . 144
8.6 Offline Algorithms . . . 147
8.6.1 Description of the proposed method . . . 147

8.6.2 Application of the method . . . 150
8.7 Systematic Uncertainties . . . 154
8.7.1 Detector related uncertainties . . . 156
8.7.2 Event composition . . . 156
8.7.3 Bunch to bunch variation in μ_{true} . . . 157
8.7.4 Applying an external trigger . . . 158
8.7.5 Trigger conditions . . . 158
8.7.6 Background . . . 159
8.7.7 Evaluation of the total systematics . . . 159
8.8 Summary and conclusion . . . 160

9 Luminosity determination using the LUCID detector at $\sqrt{s} = 7$ TeV 164
9.1 The Data sample . . . 164
9.2 Event rates . . . 165
9.2.1 Bunch Patterns and Luminosity Backgrounds . . . 165
9.3 Calibration scenario . . . 167
9.3.1 Absolute calibration using Van der Meer scans . . . 167
9.3.2 Absolute calibration using Monte Carlo results . . . 167
9.4 Results . . . 168

V Luminosity measurements at ATLAS using single gauge boson production 173

10 Theoretical context 174
10.1 Introduction . . . 174
10.2 Accuracy of the predicted cross-section . . . 175
10.2.1 Event generation . . . 176
10.2.2 Uncertainties due to Initial and Final State Radiation . . . 177
10.2.3 Uncertainties due to Higher Order Corrections . . . 179
10.2.4 Scale dependence . . . 180
10.2.5 Uncertainties due to the parton density function . . . 180
10.3 Conclusions . . . 182

11 Single Gauge Boson Production at the LHC 183
11.1 Data and Monte Carlo samples . . . 183

11.2 Event selection 183
11.2.1 Kinematics of selected sample 186
11.2.2 Efficiency determination 186
11.3 Background processes 189
11.3.1 Electroweak processes 190
11.3.2 QCD processes 190
11.3.3 Background estimate 191
11.4 Optimization of the selection procedure 192
11.5 Signal extraction and absolute luminosity calculation 194
11.5.1 Systematic Uncertainties 194
11.5.2 Results 195
11.6 Summary and conclusion 197

12 Summary and outlook **199**

VI Appendix **203**

A Simulation of LUCID - Systematic uncertainties **204**

B Performance Study of Luminosity Algorithms in ATLAS **208**

C $Z \to \mu^+\mu^-$ analysis : Optimization of the selection cuts **209**

Bibliography **210**

Preface

The main goal of high-energy physics is to identify the fundamental constituents of matter and to understand their mutual interactions. The persistent search for these elementary particles has over the last 30 years lead to some of the most remarkable discoveries in modern science. The constant strive to push the frontiers in particle physics further and further has resulted in the construction of increasingly powerful accelerators throughout the last couple of decades. By constantly increasing the collisions energy and the interaction rate of these accelerators is has been possible to steadily uncover pieces of a puzzle that describes the fundamental forces and building blocks of nature.

The standard model is a mathematical framework that joins together three out of the four fundamental forces (the electromagnetic, the weak and the strong) in nature. The standard model has ever since its formulation been extraordinary successful in describing and predicting basically all observed phenomenon within the realm of particle physics.

The Large Hadron Collider (LHC) started operation in November 2009 by providing proton-protons collisions at a center-of-mass energy of 900 GeV. The collision energy was later increased to 7 TeV in the beginning of 2010 setting a new world record. The largest experiment at the LHC is ATLAS (A Toroidal LHC ApparatuS) which is a general purpose experiment optimized towards the discovery of the Higgs boson. Apart from the Higgs searches in the various decay channels, ATLAS will also focus on a wider scientific program that stretches from precision measurement of standard model parameters to the discovery of new physics signatures beyond the standard model. Common for all of these topics is that there is a need to not only maximize the collision energy but also the interaction rate. In the case of Higgs searches and searches beyond the standard model, the production cross section is expected to be very small and thus a high interaction rate is needed. Not only is it important to achieve a high interaction rate but it is also important to obtain a precise measurement of the luminosity which quantifies the interaction rate. A precise measurement of the luminosity at hadron colliders is of the uttermost importance since it provides a prediction of the expected event rate of processes with a known cross section. Furthermore a precise measurement of the luminosity is needed to set limits on new processes under study. Once the existence of a new process is settled the luminosity is needed to provide a measurement of the production cross section. In many cases, the measurement of the luminosity will provide the dominating uncertainty on the final cross section measurement. It is therefore crucial to be able to measure the luminosity with high accuracy. Apart from physics studies, continuous measurements of the luminosity will also assist in the monitoring of the accelerator performance and help optimize the performance of the LHC.

Outline of the thesis

The focus of this thesis and the work behind it can be divided into three topics:

1. The development and study of a Monte Carlo based model to describe the LUCID detector in ATLAS (part III of the thesis).

2. The performance of LUCID as an ATLAS luminosity monitor (part IV of the thesis).

3. A study to estimate the possibility of using the production of Z bosons as an alternative to measure the luminosity (part V of the thesis).

The first two topics are to a large extent connected in the sense that in order to study the performance of the LUCID detector as a luminosity monitor it is crucial to have a realistic Monte Carlo simulation of the detector. It is therefore important, not only to develop a realistic simulation of the detector but also to track down areas where the simulation might fail to describe the real data. In order to do so, the Monte Carlo description must first be exposed to a series of self-consistency check both in stand-alone mode and as a part of the full ATLAS detector simulation framework. This is both to validate the final design in terms of expected performance and perhaps most importantly to identify possible sources of systematic uncertainty from the simulation. Especially the latter is important to study, since any uncertainties being introduces by the Monte Carlo description of the detector will propagate directly into the luminosity measurements and affect the ability to provide a precise result. After the self-consistency check, the results from the detector simulation must be compared to the response of the detector to real data. Only then will it be possible to estimate how realistic the detector simulation really is. Another source of systematic uncertainty, which will affect the precision of the luminosity measurement comes from the methods and algorithms, which are used to calculate the luminosity.

In summary, the main aim of the thesis is:

To develop methods to measure the luminosity at ATLAS and to study the precision of these methods. Emphasis in this study is put on methods using the LUCID detector but also on the possibility to use Z boson production for luminosity measurements.

The aim is reflected in the general layout of the thesis. Chapter 1 gives a brief introduction to the standard model with the intention to provide the reader with the basic concept to understand the production of gauge bosons which will be used later in the thesis. A detailed description of the LHC and the ATLAS experiment is given chapter 2 and 3. Emphasis is put on the description of the muon spectrometer and the forward detectors since these are used later in the thesis. The concepts of luminosity determination is given in chapter 4 which also explains the difference between relative and absolute luminosity determination. Chapter 5 gives a detailed description of the LUCID detector. Both the general layout of the detector and the readout electronics are addressed in this chapter. Chapter 6 describes the Monte Carlo model of LUCID as it has been implemented in the general ATLAS software framework. The chapter presents results from a simulation study which has been carried out to validate the description of the detector. At the end of the chapter the various sources of

systematic uncertainty from the detector description are identified and the various contributions are estimated. The performance of the LUCID detector is addressed in chapter 7 where results from the early 2010 data-taking period are compared to results from simulations. The detection efficiency and the average hit multiplicity will also be addressed in this chapter since they are needed later for the luminosity determination. Chapter 8 first introduces the concepts of luminosity algorithms and later derives a set of online and offline algorithms. The performance and precision of the different algorithms are tested using Monte Carlo simulations. The precision of the luminosity measurements is further addressed at the end of the chapter where the sources of systematic uncertainty from the algorithms are addressed. The algorithms are in chapter 9 used to determine the luminosity for a selected list of runs taken in 2010. Two different types of calibration are used to obtain the final results. Chapter 10 and 11 presents a feasibility study carried out to investigate the possibility of using Z^0 production as a way to measure the absolute luminosity. Chapter 10 addressed the theoretical sources of systematic uncertainties from the predictions of the Z^0 production cross section. Chapter 11 presents an event selection procedure designed to select $Z \to \mu^+\mu^-$ event. The performance of the selection procedure is tested using Monte Carlo simulations and later applied to a real data set recorded by the ATLAS detector. The results from this method are compared to the results obtained by LUCID at the end of the chapter.

The author's contribution

Unless otherwise stated, the results presented in this thesis are obtained based on studies done by the author. However, it goes without saying that even though I would like to, I cannot take credit for the formulation of the standard model or the design and construction of the ATLAS experiment.
Every PhD student in ATLAS is asked to carry out a technical tasks in parallel to their thesis work. I was lucky enough to be able to partially merge the two. My technical task consisted in designing and implementing a Monte Carlo description of the LUCID detector in the global ATLAS software framework, ATHENA. This work consisted of designing a realistic description of the detector and through a series of tests described in the thesis to validate the implementation. As part of a small team of developers my main task has been to revise and greatly improve a simple stand-alone simulation of the LUCID detector. This also included a complete redesign of the simulation of the beam pipe in ATLAS which is important for LUCID. Furthermore I was the main responsible for designing and implementing a simulation of the readout electronics in LUCID. This also included implementing a trigger simulation and a simulation of the reconstruction process for LUCID. Beside the work on simulation I have also been heavily involved in the development and study of data-driven method to determine the detection efficiency of LUCID. The successful use of these methods combined with the complete implementation of the simulation for LUCID resulted in LUCID being selected in early May 2010 as the preferred detector to provide the official luminosity measurement for ATLAS.
The successful implementation of LUCID in the ATLAS software framework has been used by myself and others to derive and study algorithms designed to determine the luminosity. This includes various online algorithms and the introduction of a novel offline approach.
Furthermore I have also carried out one of the studies in ATLAS using real data to measure

the absolute luminosity from the production of Z^0 bosons at $\sqrt{s} = 7$ TeV. This has been done in parallel with the large effort in ATLAS to determine the $W^{\pm}$ and Z^0 cross sections at 7 TeV with first data.

Papers and analysis that I have contributed to are summarized in the following list:

Publications in scientific journals

1. ATLAS Collaboration, *Luminosity determination at 7 TeV using the ATLAS detector at the LHC*, ATL-COM-LUM-2010-029, to be submitted to EPJC
2. ATLAS Collaboration, *The ATLAS Experiment at the CERN Large Hadron Collider chapters plots*, JINST 3 S08003 (2008)
3. ATLAS Collaboration, *The ATLAS Simulation Infrastructure*, accepted by EPJC (submitted 20 May 2010)
4. ATLAS Collaboration, *Performance of the ATLAS Detector using First Collision Data*, JHEP 1009:056,2010 (28 May 2010)
5. ATLAS Collaboration, *Measurement of the $W \to l\nu$ and $Z/\gamma^* \to ll$ production cross sections in proton-proton collisions at $\sqrt{s} = 7$ TeV with the ATLAS detector*, submitted to JHEP (11 Oct. 2010)

Internally refereed ATLAS notes

1. J. Groth-Jensen et al., *Luminosity determination during the 2009 run using the LUCID detector* , ATL-COM-LUM-2010-014
2. J. Groth-Jensen et al., *Simulation of luminosity monitoring with LUCID in ATLAS* , ATL-INT-LUM-2010-005

Contribution to conferences on these topics

1. J. Groth-Jensen, *LUCID in ATLAS* , DIFF2010 - Diffractive and electromagnetic processes at the LHC , ATL-LUM-SLIDE-2009-377
2. ATLAS Collaboration, *Luminosity Determination Using the ATLAS Detector* , ATLAS-CONF-2010-060, 20 July 2010, Submitted to the 35th Int. Conf. on High Energy Physics, Paris, France.
3. ATLAS Collaboration, *Performance of the Minimum Bias Trigger in p-p Collisions at $\sqrt{s} = 900$ GeV* , ATLAS-CONF-2010-025, 23 April 2010, Submitted to the 35th Int. Conf. on High Energy Physics, Paris, France.
4. ATLAS Collaboration, *Performance of the Minimum Bias Trigger in p-p Collisions at $\sqrt{s} = 7$ TeV* , ATLAS-CONF-2010-068, 19 July 2010, Submitted to the 35th Int. Conf. on High Energy Physics, Paris, France.

5. ATLAS Collaboration, *Measurement of the $W \to l\nu$ production cross-section and observation of $Z \to ll$ production in proton-proton collisions at $\sqrt{s} = 7$ TeV with the ATLAS detector* , ATLAS-CONF-2010-051, 21 July 2010, Submitted to the 35th Int. Conf. on High Energy Physics, Paris, France.

6. ATLAS Collaboration, *Measurement of the $Z \to ll$ production cross section in proton-proton collisions at $\sqrt{s} = 7$ TeV with the ATLAS detector* , ATLAS-CONF-2010-076, 23 July 2010, Submitted to the 35th Int. Conf. on High Energy Physics, Paris, France.

Acknowledgments

The work presented here is the result of four years of the study at the division of High Energy Physics at Lund University. My employment has partly been financed by the European Commission through the Marie Curie Early stage training program and partly by the Swedish research council and the Kurt and Alice Wallenberg foundation.
It is needless to say that this thesis could not have become a reality without the help from a lot of people.
First and foremost I would like to express my sincere gratitude to my supervisor Vincent Hedberg for his persistency and support during the last couple of years. The willingness to always help out and the insightfulness to do so, has lead to a lot of fruitful discussions which I have gained a lot from.
I would also like to express my warmest thanks to Marco Bruschi for generously sharing his ideas and technical knowledge of the LUCID detector with me. I also own a big thanks to Antonello Sbrizzi, my colleague and other half of the LUCID Monte Carlo team. The ATHENA framework is not always the easiest thing to work with but it helps to have someone to share the workload with. I this connection I would also like to express my thanks to Vakho Tsulaia for his friendly guidance through the early stages of LUCID detector. Thanks also go to Thomas Kittelmann for helping with the incorporation of LUCID in the VP1 visualization framework and other software related issues.
In general I would like to extent my thanks to the LUCID collaboration for being so welcoming for providing a warm work-atmosphere. Thanks to Benedetto Giacobbe and Carla Sbarra for always providing quick and useful feedback on issues related to early data analysis with LUCID. A special thanks to John Chapman who have shown great patience and willingness to help with the implementation of the LUCID digitization. Also a warm thanks to William Bell for assisting with everything from software advice to helping out with trigger related issues. A warm thanks to all my colleagues at Lund University and a special thanks to Bozena Wlosinska for dealing with all the bureaucracy related to being stationed abroad. This can not have been that easy all the times. In the same connection I would like to thank Torsten Åkesson for being so understanding towards my wish to remain stationed at CERN throughout a large part of my PhD. Also thanks to Oxana Smirnova for proof-reading of the thesis.

My warmest thanks to my family for their everlasting optimism and good spirit. Also a special thanks to Lisbet Groth-Jensen for providing the artwork for the thesis. Last but not least I would like to thank my wonderful girlfriend for her love and support. I could not have done this without you!

Part I
Theory

Chapter 1

The Standard Model of Particle Physics

The notion that all matter consists of fundamental and indivisible building blocks can be traced back to ancient Greece in the 6th century BC. These ideas where studies by the philosophers Epicurus, Democritus and Leucippus [1] who lay the ground to the doctrine of atomism. They postulated that everything is composed of *atoms* which are physical entities in empty space. By the nature of the doctrine these early ideas were founded in abstract, philosophical reasoning rather than experimentation and empirical observation. In the early 19th century, John Dalton an English chemist, could through his work on stoichiometry conclude that a single and unique type of particle would give raise to the the elements of nature [2]. It was believed that this particle was fundamental and indivisible and was therefore named atom after the Greek word for indivisible. Towards the the turn of the century the discovery of the electron, and subsequently the discovery of the atomic nucleus convinced physicists that atoms were not the fundamental particles of nature but in fact, composed of even smaller particles. Throughout the 20th century several experiments were caried out in the areas of nuclear and quantum physics, culminating in the discovery of nuclear fusion [3] and nuclear fission [4] in 1939. In the same spirit various scattering experiments were used during the 1950s and 1960 to uncover a larger variety of different particles. These were referred to as the *particle zoo*. The lack of any apparent system to explain the relationships between the hundreds of known strongly interacting particles (*hadrons*) lead to a confusing situation in the late 1960s. However during the 1970s a large effort went into formulating a model in which the large number of particles could be explained as combinations of a (relatively) small number of fundamental particles. This model came afterwards to be known as the *Standard Model* and is the cornerstone of modern particles physics.

In modern particle physics the main focus is the study of elementary particles[1]. An elementary particle or a fundamental particle is a particle without substructure which means that it is not made up from smaller particles. As such the elementary particles must be the fundamental building block of nature out of which all other particles are formed. In the

[1]Strictly speaking, the term particle is a misnomer because the dynamics of particle physics are governed by quantum mechanics. As such, they exhibit wave-particle duality, displaying particle-like behavior under certain experimental conditions and wave-like behavior in others.

Standard Model, the quarks, leptons, and gauge bosons are elementary particles [5].
The basic tennet of the standard model is that all matter is composed of elemetrary spin$-\frac{1}{2}$ *fermion* constituents, namely the *quarks* and *leptons*. Quarks, unlike the leptons with integral charge, carry fractional charge ($\frac{2}{3}e$ and $-\frac{1}{3}e$) . These constituents can interact by exchange of various spin-1 *bosons* which in the Standard Model are the mediators or carriers of the different types of interactions. *Electromagnetic* interactions account for the formation of atoms and molecules by providing the binding force between the nucleus and the electron. Another fundamental interaction is the *Strong* interaction or the strong nuclear force. The Strong interaction is often considered as the most complicated of the interactions in the standard model because of the way it varies with distance. On a smaller scale the residual force of the strong interaction (strong nuclear force) is responsible for the formation of protons and other hadrons by binding quarks together. On a larger scale the strong interaction is responsible for binding the protons and neutrons together to form the nucleus of an atom. The third interaction of the Standard Model is the *Weak* interaction. The weak force is responsible for a wide range of nuclear phenomena e.g the slow process of radioactive $\beta-$decay of the nuclei. In addition to the electromagnetic, strong and weak interaction between quarks and leptons, there is a fourth force of nature - *gravity*. However, in comparison with the other three forces, gravity is so weak that it can safely be ignored at the scales relevant for experimental particle physics. Also no attempt has yet been successful in merging General Relativity, the theory of gravity, with the standard model.

1.1 Inputs to the Standard Model

As mentioned above, the basic assumption of the Standard Model is that the fundamental constituents of matter are the quarks and leptons. However, the Standard Model do not explain the number of quarks and leptons or explain such properties as their mass. They are as such taken at this level to be truly fundamental in nature and are thereby considered as *inputs* to the Standard Model. As it turns out this is not an unreasonable assumption. There are so far no experimental evidence that quarks and leptons have an internal structure in terms of form factors or excited states.

1.1.1 Fundamental Particles

The fermionic part of the Standard Model consists of twelve fermions categorized into three generations. Each fermion belongs to a generation according to its mass and charge. Particles from the first generation are the lightest and do not decay; hence all ordinary (baryonic) matter is made of such particles. Second and third generation charged particles decay with very short half lives and are observed only in very high-energy environments. Neutrinos on the other hand are stable but only interact weakly. Table 1.1 summarizes some properties of the Standard Model fermions.

Leptons There are six flavors of leptons in the Standard Model along with their antiparticles. Starting from the first generation, the members of the lepton families are: The electron e and electron neutrino ν_e, the muon μ and the muon neutrino ν_μ, the tau τ and tau neutrino ν_τ. The first lepton to be identified was the electron which was discovered by J.J. Thomson

Generation	Leptons		Quarks	
1	e	ν_e	u	d
	(0.511 MeV)		($\sim$ 2 MeV)	($\sim$ 2 MeV)
2	μ	ν_μ	c	s
	(106 MeV)		(1205 MeV)	(95 MeV)
3	τ	ν_τ	t	b
	(1777 MeV)		(172$\times 10^3$ MeV)	(4500 MeV)
Electromagnetic charge	-1	0	$\frac{2}{3}$	$-\frac{1}{3}$
Strong interactions	no	no	yes	yes
Weak interactions	yes	yes	yes	yes

Table 1.1: *The basic fermions of the Standard Model included approximate observed masses [6]. Antiparticles such as e^+, $\bar{u}$ etc have charges of opposite sign. The neutrinos ν_e , ν_μ and ν_τ are per construction massless in the Standard Model but future experiment might provide unambigious evidence for neutrino masses. Eletromagnetic charges are given as multiples of the proton charge e.*

in 1897. After nearly 40 years the muon was then discovered by Carl D. Anderson in 1936. It was originally believed that the muon was a meson on account of its relatively large mass. It later became clear that the muon had to be a lepton similar to the electron due to its lack of sensitivity to the strong force. The *tauon* or the τ was discovered by Martin Lewis Perl and his colleagues in a series of experiments from 1974 to 1977 at the Stanford Linear Accelerator Center (SLAC). The neutrinos was first postulated by Wolgang Pauli in order to establish energy and momentum conservation in beta decay where an atomic nuclus decays into a proton, an electron and a neutrino. All flavors of neutrinos were subsequently discovered by various experiments [7] [8].

Quarks The history of the quark model dates back to the beginning of the sixties when Gell-Mann [9] and Zweig [10] proposed that the spectrum of the strongly interacting particles could be accounted for by introducing some elementary constituents called *quarks*[2]. In the quark model mesons were considered to be quark antiquark bound states and likewise baryons as bound states of three quarks. The integer charge of the (then) known hadrons were explained by assuming that the quarks could exist in three different flavors, up(u), down(d) and strange(s) with fractional charge (see tab. 1.1). According to Fermi-Dirac statistics, the existence of particles composed of three quarks has to be precluded, since three identical fermions with their spins aligned cannot exist in a symmetric s-wave ground state. This led to the idea that quarks carry an additional quantum number called *color*, a conjecture supported by experimental observations. The color charge of a quark has three possible values: red(r), green(g) and blue(b). Leptons do not carry color, and hence they do not participate in strong interactions. The implication of the color charge of quarks are discussed in greater detail in section 1.3.

[2]Gell-Mann found inspiration to the word quarks, from a passage in *Finnegan's Wake* by James Joyce: "Three quarks for Muster Mark".

1.1.2 Mathematical Framework

Symmetries have always played an important role in the development of physics. Not only have they provided a useful tool when deriving solutions to a specific problem but additionally the Noether theorem [11] establishes that symmetries implies conservation laws. A special class of internal symmetries, called *gauge*-symmetries, arise when a mathematical description of a quantum field posses unphysical degrees of freedom. More specifically, gauge symmetries occur when the physical system described by a certain langrangian is invariant under a local phase transformation. In the light of Noether theorem a natural question to ask would be: upon imposing invariance of a physical system to a certain group of symmetries, would it be possible to predict the form of the interactions between the particles in the physical system? Or phrased in another way - do symmetries also imply dynamics? This is in fact what happened in the case of *Quantum ElectroDynamics* (QED) in which electromagnetic interactions between charged particles can be attributed to a gauge field - the photon - which follow directly from the principles of invariance under local gauge transformations of the $U(1)$ group. This principle can likewise be generalized to other types of interactions. The non-Abelian[3] groups $SU(3)_C$ and $SU(2)_I \times U(1)_Y$ represent respectively *Quantum Chromo-Dynamics.* (QCD), the theory that describes the strong force, and *electroweak theory*, which unifies the Electromagnetic and Weak forces. The complete symmetry group of the Standard Model is thus:

$$SU(3)_C \times SU(2)_I \times U(1)_Y \tag{1.1}$$

where the subscripts C, I and Y refer to the conserved charges of each group: the color charge, weak isospin and weak hypercharge.

Since the Standard Model is a quantum field theory it utilises a Lagrangian operator to completely describe the particles and the interactions between them. In the following sections the gauge field theories describing the Elecromagnetic, Strong and Weak forces and the resulting Lagrangians will be described in more detail. For a more complete discussion see, for example [12] [13] [14] and [15].

1.2 Quantum electrodynamics

Historically, Quantum electrodynamics was the first of the modern quantum field theories. It is the most theoretically and experimentally well studied of the Standard Model sectors and provides as such a good introduction to the Standard Model as well as to the notion that symmetries can imply dynamics.
The structure of the QED Langrangian is obtained by requiring that the system remains unchanged after a space time dependent phase transformation. The starting point to illustrate this is the free Dirac Lagrangian for a free fermion field ψ with mass m:

$$\mathcal{L}_\psi = \bar{\psi}(i\partial\!\!\!/ - m)\psi \tag{1.2}$$

which is not invariant under the local gauge transformation,

$$\psi \to \psi' = e^{-i\alpha(x)}\psi \tag{1.3}$$

[3] a *non-abelian* group is a group, in which the elements do not commute.

since

$$\mathcal{L}_\psi \rightarrow \mathcal{L}'_\psi = \mathcal{L}_\psi + \bar{\psi}\gamma_\mu\psi(\partial^\mu\alpha) \tag{1.4}$$

However if a *gauge* field is introduced trough a minimal coupling in terms of a covariant derivative

$$(D_\mu) \equiv \partial_\mu - ieA_\mu \quad \text{requiring that} \quad A_\mu \rightarrow A'_\mu = A_\mu + \frac{1}{e}\partial^\mu\alpha \tag{1.5}$$

the Langrangian from eq 1.2 now transforms as:

$$\mathcal{L}_\psi \rightarrow \mathcal{L}'_\psi = \mathcal{L}_\psi - e\bar{\psi}\gamma_\mu\psi A^\mu \tag{1.6}$$

canceling the extra term in eq. 1.4 thus leaving $\mathcal{L}_\psi$ invariant under $U(1)$ gauge transformations. From eq. 1.6 it is seen that the coupling between ψ (e.g electrons) and the gauge field A_μ arises naturally when it is required that the kinetic terms of the free fermion Lagrangian are invariant under local gauge transformations - illustrating the point that symmetries do in fact imply dynamics. Apart from the fermionic part, the QED Langrangian also includes a pure gauge term due to the fact that gauge fields are truly propagating fields:

$$\mathcal{L}_A = -\frac{1}{4}F_{\mu\nu}F^{\mu\nu} \quad \text{where} \quad F_{\mu\nu} \equiv \partial_\mu A_\nu - \partial_\nu A_\mu \tag{1.7}$$

This Lagrangian together with 1.6 describes Quantum electrodynamics

$$\mathcal{L}_{QED} = -\frac{1}{4}F_{\mu\nu}F^{\mu\nu} + \bar{\psi}(i\not{D} - m)\psi \tag{1.8}$$

1.3 Quantum chromodynamics

Quantum chromodynamics, the modern description of the strong interactions, contains quarks as its basic degrees of freedom instead of electrons as is the case for QED. As mentioned above, quarks carry color charge and can as such be seen as a physical manifestation of $SU(3)_C$. Hence, quarks of the same flavor are fundamental representations of $SU(3)_C$, i.e. a triplet $q = (q_r, q_g, q_b)$, where r, g, b denote the color quantum numbers of the quarks. Apart from the quarks, QCD also contains an additional set of particles. These are the force carriers and unlike QED where the force is mediated by a single boson, QCD has eight force carrying bosons called *gluons*. Since the gluons also belong to $SU(3)_C$ which is non-Abelian, gluons can couple to the quarks as well as to each other.
Just as for QED, the functional form of the QCD Lagrangian is derived by requiring that the interacting system of quarks and gluons must be invariant under the gauge group of the theory, namely $SU(3)_C$:

$$\mathcal{L}_{QCD} = -\frac{1}{4}F^a_{\mu\nu}F^{\mu\nu}_a + \sum_q \bar{\psi}^q_j(i\not{D}_{jk} - m^q\delta_{jk})\psi^q_k \tag{1.9}$$

where,

$$F^a_{\mu\nu} = \partial_\mu A^a_\nu - \partial_\nu A^a_\mu + 2\sqrt{\pi\alpha_s}f_{abc}A^b_\mu A^c_\nu \tag{1.10}$$

$$(D_\mu)_{ij} = \delta_{ij}\partial_\mu - i\sqrt{\pi\alpha_s}\lambda^a_{ij}A^a_\mu \tag{1.11}$$

Here α_s represents the strength of the strong interaction, f_{abc} are the structure constants of the $SU(3)$ symmetry group. The subscripts a, b, c take values from 1 to 8. λ_{ij}^a are the generators of the $SU(3)$ group and ψ_i^q are 4-component Dirac spinors describing quarks of color i and flavor q. A_μ^a are the eight gauge bosonic gluon fields.
One of the great triumphs of QCD is the discovery that the strong coupling constant depends on the separation between the interacting particles. This dependence makes the strong interaction constant a *running coupling constant*. At relatively large distances or low energy, the coupling constant is large. As a result no free quarks have ever been observed, a fact which is known as *quark confinement*. At short distances, on the other hand, the coupling is small and the theory is said to be asymptotically free. It should be noted that also the electroweak coupling is running, but its dependence on the scale is reversed. This difference is the non-abelian nature of QCD, which gives rise to the last term in eq. 1.10. It is this third term which distinguishes QCD from QED, leading to triplet and quadratic gluon self-coupling and ultimately to asymptotic freedom.

Asymptotic freedom In QED the charge of the electron appears smaller at large distances due to screening of its electric charge by vacuum polarization. In QCD the same thing happens, only here the explanation is not so simple and the consequences dramatically different. In contrast to QED where the electrons only carry electrical charge, in QCD the virtual quark pairs also carry color charge which makes the inclusion of gluons into the picture unavoidable. Since each gluon carries both a color and an anti-color charge the net effect is to polarize the vacuum by means of virtual gluon pairs. However, because of the nature of the gluon this does not lead to a screening of the field but rather to augment it and affect its color - a so-called anti-screening effect. This effect diminishes as one gets closer to the quark and as a result the effective charge and thereby also α_s decreases with decreasing distance. Asymptotic freedom can be derived by calculating the beta-function that describes the variation of the theory's coupling constant under the renormalization group. To the lowest order in α_s the variation at a certain momentum scale Q is given by

$$\frac{\partial \alpha_s(Q^2)}{\partial \ln(Q^2)} \equiv \beta(\alpha_s(Q^2)) \simeq -\frac{1}{12\pi}(33 - 2n_f)\alpha_s^2(Q^2) \tag{1.12}$$

where n_f are the number of quark flavours. Since there are 6 quark flavours within QCD it can be seen that α_s will decrease with increasing Q^2. In fact QCD will exhibit asymptotic freedom as long as $n_f < 17$.

1.4 Electroweak Theory

All through the history of modern particle physics there have been several attempts to construct a gauge theory for the electroweak interaction. One of the first attempts was proposed by Swinger [16] in 1957 with a model based on the group $O(3)$ with a triplet of gauge fields (V^0, V^+, V^-). Here the neutral gauge field V^0 was associated with the photon and the two charged fields with the weak gauge bosons. This model laid the foundation for the later formulation and incorporation of the $V - A$ structure in a gauge theory for the Weak interactions by Buldman [17] [18] in 1958. His model, based on the weak isospin group $SU(2)$, also required the existence of three vector bosons. However as opposed to Swingers model

the neutral gauge boson was now associated with a massive vector boson and not the photon. A hypothesis which meant that weak interactions could be propagated not only by charged gauge bosons but also by a neutral gauge boson. The so-called *neutral current* was later discovered in a CERN neutrino experiment [19] in 1973.
In 1961 Glashow [20] noted that it was needed to go beyond $SU(2)$ to successfully unify the electromagnetic and weak interactions. In order to account for both the weak isospin and the leptonic hypercharge, he suggested the gauge group $SU(2)_I \times U(1)_Y$. A theory based on this group now requires the presence of four gauge bosons: a charged triplet (W^1, W^2, W^3) associated to the generators of $SU(2)$ and a neutral boson (B) related to $U(1)$. In this model, and in a similar model proposed by Salam and Ward [21], the physical gauge bosons of the theory ($W^{\pm}$ and Z^0/γ) now appear as linear combinations of the $W^{1,2,3}$ and B fields. These theories have, however, one major drawback. Since they do not account for the mass terms of the W and Z bosons these had to be put in "by hand". Such terms would explicitly break the gauge invariance and in turn also ruins the prospect of making the theory renormalizable. To preserve gauge invariance and give mass to the weak bosons Weinberg [22] and Salam [23] employed the idea of spontaneous symmetry breaking and the Higgs mechanism. The Glashow-Weinberg-Salam model has had immense success during the past decades and is now referred to as the *Standard Model of electroweak interactions*.

1.4.1 Chiral fermions

From experiments studying nuclear beta decay it has been observed that charged weak interactions are only possible between fermions with left-handed helicity. In terms of $SU(2)$ representations this means that left-handed fermions are placed in weak iso-doublets , while the right-handed part are placed in weak iso-singlets. Hence, the structure of the first generation[4] Standard Model fermions with respect to the weak force is given by:

$$\text{Leptons} \quad : l \equiv \begin{pmatrix} \nu_e \\ e \end{pmatrix}_L \quad e_R \tag{1.13}$$

$$\text{Quarks} \quad : q \equiv \begin{pmatrix} u \\ d \end{pmatrix}_L \quad u_R, \quad d_R \tag{1.14}$$

In fact the subscript of $SU(2)$ in eq 1.1 is sometimes replaced by a L to indicate that only left-handed fermions participate in charged weak interactions. Another delimiting factor in the structure of the weak interaction is the assignment of conserved quantum numbers. Just as in QCD where the gluons couple to quarks by color charge, in electroweak theory the gauge bosons couple to fermions by means of hypercharge and weak isospin. As a result the assignment of quantum number like weak isospin T_{W3} and weak hypecharge Y (see table 1.2) play an important role in categorizing the structure of the electroweak interactions.

1.4.2 $SU(2)_L \times U(1)_Y$ gauge invariant Langrangian

The Glashow-Weinberg-Salam Lagrangian divides naturally into three additive parts, namely the gauge (G), fermion (F) and Higgs part (H):

$$\mathcal{L}_{GWS} = \mathcal{L}_G + \mathcal{L}_F + \mathcal{L}_H \tag{1.15}$$

[4] A similar structure is true for the two other generations.

Leptons	T_{W3}	Y	Quarks	T_{W3}	Y
ν_e	$1/2$	-1	u_L	$1/2$	$1/3$
e_L	$-1/2$	-1	d_L	$-1/2$	$1/3$
e_R	0	-2	u_R	0	$4/3$
			d_R	0	$-2/3$

Table 1.2: *$SU(2)_L \times U(1)_Y$ assingment of quantum numbers . A further constraint among these number are that $Y = 2(Q - T_{W3})$, where Q refers to the electric charge of the specific fermion.*

The gauge fields which couple to the weak hypercharge and isospin are respectively B_μ and $\overrightarrow{W}_\mu = (W^1_\mu, W^2_\mu, W^3_\mu)$. The contribution from these fields to the gauge part of the Langranian is:

$$\mathcal{L}_G = -\frac{1}{4}F^i_{\mu\nu}F^{\mu\nu}_i - \frac{1}{4}B_{\mu\nu}B^{\mu\nu} \tag{1.16}$$

where $F^i_{\mu\nu}$ $(i = 1, 2, 3)$ is the $SU(2)$ field strength:

$$F^i_{\mu\nu} = \partial_\mu W^i_\nu - \partial_\nu W^i_\mu - g_2\epsilon^{ijk}W^j_\mu W^k_\nu \tag{1.17}$$

and $B_{\mu\nu}$ is the $U(1)$ field strength:

$$B_{\mu\nu} = \partial_\mu B_\nu - \partial_\nu B_\mu \tag{1.18}$$

The fermionic sector of the Langrangian is constructed by including fermions with both right and left handed chiralities. Summing over all the contributions from weak iso-doublets ψ_L and weak iso-singlets ψ_R , $\mathcal{L}_F$ can be obtained as:

$$\mathcal{L}_F = \sum_{\psi_L} \bar{\psi_L} i \not{D} \psi_L + \sum_{\psi_R} \bar{\psi_R} i \not{D} \psi_R \tag{1.19}$$

Since only left-handed fermions couple to iso-spin, the expression for the covariant derivative will differ when acting on ψ_L and ψ_R. The covariant derivative for the $SU(2)_L$ doublet is given by:

$$D_\mu \psi_L = \left(\boldsymbol{I}(\partial_\mu + i\frac{g_1}{2}YB_\mu) + ig_2\frac{\boldsymbol{\tau}}{2} \cdot \overrightarrow{W}_\mu \right)\psi_L \tag{1.20}$$

where g_2 is the $SU(2)$ gauge coupling constant and the 2×2 matrices $\boldsymbol{I}$, $\boldsymbol{\tau}$ are the unit matrix and Pauli matrices respectively. The corresponding expression for the covariant derivative when acting on the iso-single ψ_R is in principle the same as eq. 1.20. Since right-handed chiral fermions do not couple to isospin the last term will be missing and the covariant derivative is given by:

$$D_\mu \psi_R = (\partial_\mu + i\frac{g_1}{2}YB_\mu)\psi_R \tag{1.21}$$

As a remark it should be noted that eq. 1.21 serves to define the $U(1)$ coupling constant g_1 whereas g_2 was defined already in 1.17.
The system defined by $\mathcal{L}_G$ and $\mathcal{L}_F$ is consistent with a gauge theory of the weak isospin and weak hypercharge. However this can not be the full story since due to the requirement of local gauge invariance, the fields must be massless which inflicts the theory not to be physically viable. A solution to this problem is to retain the gauge symmetry of the full Lagrangian but

let the masses be generated by a breaking of the vacuum state symmetry. This phenomenon is known as *Spontaneous Symmetry Breaking* and will be discussed further in Sect. 1.4.3. To facilitate this type of symmetry breaking an additional sector must be added to $\mathcal{L}_G$ and $\mathcal{L}_F$ to complete the full Glashow-Weinberg-Salam model. This is done by adding a complex doublet of so-called Higgs fields to the theory:

$$\Phi = \begin{pmatrix} \phi^+ \\ \phi^0 \end{pmatrix} \tag{1.22}$$

with hypercharge $Y = +1$, zero spin and electrical charge assignments as indicated. As a result two new contributions to the full Lagrangian arises. One which contains the Higgs to gauge field coupling $\mathcal{L}_{HG}$ and one which contains the Higgs to fermions coupling $\mathcal{L}_{HF}$. The former contribution can be written as:

$$\mathcal{L}_{HG} = (D^\mu \Phi)^* D_\mu \Phi - V(\Phi) \tag{1.23}$$

where

$$D_\mu \Phi = \left(\boldsymbol{I}(\partial_\mu + i\frac{g_1}{2} Y B_\mu) + i g_2 \frac{\boldsymbol{\tau}}{2} \cdot \vec{W}_\mu \right) \Phi \tag{1.24}$$

and V denotes the self-interaction of the Higgs fields:

$$V(\Phi) = -\mu^2 \Phi^\dagger \Phi + \lambda (\Phi^\dagger \Phi)^2 \tag{1.25}$$

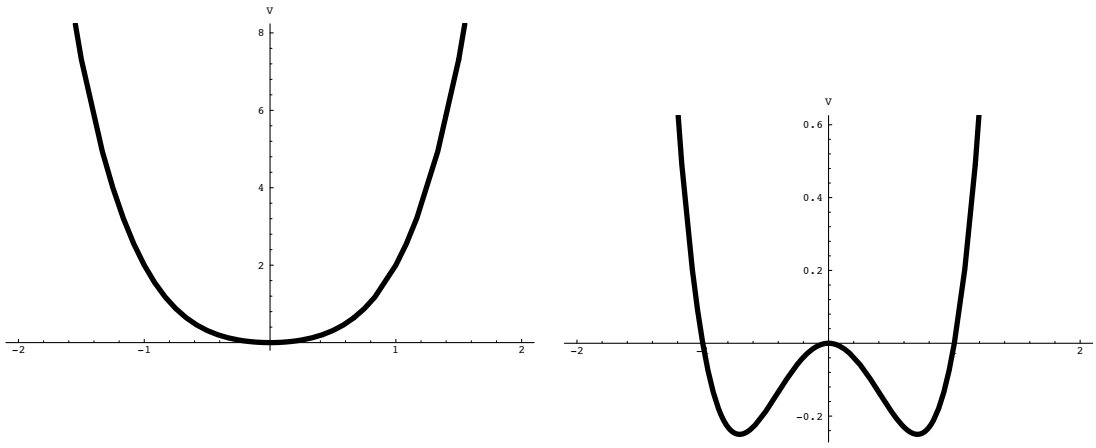
The parameter μ and λ are positive but otherwise arbitrary.
Just as the Higgs potential, the part of the Lagrangian that contains the Higgs to fermion coupling $\mathcal{L}_{HF}$ lie outside of the guiding principle of gauge invariance, since neither of them includes any gauge fields. In fact, due to the absence of constraints from the gauge principle, all of the parameters in V and $\mathcal{L}_{HF}$ are arbitrary. The Standard Model on its own does not contain any hints to the numerical value of these parameters and they will have to be determined by experiments.
Denoting left-handed quarks and leptons doublets as q_L and l_L , $\mathcal{L}_{HF}$ can be written as:

$$\mathcal{L}_{HF} = -f_u \bar{q}_L \widetilde{\Phi} u_R - f_d \bar{q}_L \widetilde{\Phi} d_R - f_d \bar{l}_L \widetilde{\Phi} e_R + \cdots + h.c \tag{1.26}$$

where $\widetilde{\Phi} = i\tau_2 \Phi^*$ is the charged conjugated Φ and f_u , f_d ... denotes the coupling constants. The Yukawa coupling between the Higgs field and a particular fermion in eq. 1.26 gives rise to the experimentally observed phenomenon of *quark mixing*, a phenomenon in which a quark from one generation changes flavor into a quark from another generation as seen from eq. 1.26. This is accounted for in the Standard Model by letting weak eigenstates be different from the mass eigenstates.

1.4.3 Higgs mechanism and the W and Z mass

As hinted in the previous section, the mass generation for fermions and gauge bosons proceeds by the means of *Spontaneous Symmetry Breaking*. In this type of symmetry breaking the Lagrangian of the system is invariant under a given transformation but the vacuum state is not. This will lead to an assignment of a non-zero vacuum expectation value to the fields of the theory which in turn can be interpreted as a non-zero mass. A first example of



(a) (b)

Figure 1.1: *Scalar potential (eq. 1.25) for $\mu^2 < 0$ (a) and for $\mu^2 > 0$ (b).*

spontaneous symmetry breaking is given by the Goldstone mechanism [24] which states that if a global symmetry of a system is spontaneously broken then the theory contains one massless scalar for each broken generator of the original symmetry group. In the electroweak theory a spontaneous symmetry breaking is facilitated by the Higgs potential in eq. 1.25. Here the original symmetry group is broken in the following way:

$$SU(2)_L \times U(1)_Y \to U(1)_{em} \tag{1.27}$$

This means that after the spontaneous symmetry breaking, the sub-group $U(1)_{em}$ remains a symmetry of the vacuum state, ensuring that the electric charge is conserved.
To show that the Higgs potential $V(\Phi)$ is responsible for a symmetry breaking of this nature we start by minimizing V:

$$\Phi(-\mu^2 + 2\lambda\Phi^\dagger\Phi) = 0 \tag{1.28}$$

Since λ should be positive to guarantee that the energy of the system remains bounded, the minimum depends on the sign of μ. For $\mu^2 < 0$ the system has only one vacuum state at $\langle\Phi\rangle_0 = 0$ (see fig. 1.1(a)). However for $\mu^2 > 0$ the equation has two solutions and therefore two vacuum states (see fig. 1.1(b)):

$$\langle\Phi^\dagger\Phi\rangle_0 = \pm\frac{v^2}{2} \quad \text{where} \quad v \equiv \sqrt{\frac{\mu^2}{\lambda}} \tag{1.29}$$

In this context only the latter and non-trivial solution is interesting since it is the only solution which has the capability of generating mass. Here this is done by choosing a specific sign in eq. 1.29 and reformulating the Higgs Lagrangian around this vacuum configuration. This will lead to the vacuum states loosing their original $SU(2)_L \times U(1)_Y$ symmetry which is spontaneously broken down to $U(1)_{em}$. In the following only the positive solution in eq. 1.29 is taken into account and the new vacuum configuration is thereby given as:

$$\langle\Phi\rangle_0 = \begin{pmatrix} 0 \\ v/\sqrt{2} \end{pmatrix} \tag{1.30}$$

The fermion and gauge boson masses can now be determined by reformulating the Higgs Lagrangian $\mathcal{L}_H = \mathcal{L}_{HF} + \mathcal{L}_{HG}$ in terms of $\langle\Phi\rangle_0$ in eq. 1.30:

$$\mathcal{L}_{mass} = - \frac{v}{\sqrt{2}}(f_u\bar{u}u + f_d\bar{d}d + f_e\bar{e}e + \cdots) + \left(\frac{vg_2}{2}\right)^2 W_\mu^+ W_-^\mu \tag{1.31}$$

$$+ \frac{v^2}{8}\begin{pmatrix} W_\mu^3 & B_\mu \end{pmatrix}\begin{pmatrix} g_2^2 & -g_1g_2 \\ -g_1g_2 & g_1^2 \end{pmatrix}\begin{pmatrix} W_3^\mu \\ B^\mu \end{pmatrix} \tag{1.32}$$

where the charged fields $W_\mu^\pm$ are defined as:

$$W_\mu^\pm = \sqrt{\frac{1}{2}}(W_\mu^1 \mp iW_\mu^2) \tag{1.33}$$

and correspond to the gauge bosons $W^\pm$. The fermions masses can be read off directly from the first term in eq. 1.31 as:

$$m_i = \frac{v}{\sqrt{2}}f_i \quad (i = u, d, e, \cdots) \tag{1.34}$$

Just as for the coupling constants f_i, the energy scale v cannot be predicted by the Standard Model and must be extracted from experiments. This means that even though the model can accommodate fermions of any mass, it does not predict the actual values. On the other hand, once the fermions masses have been measured they can be used to constrain Higgs-fermion couplings. The mass of the charged boson W can also be read off directly from the second term in eq. 1.31 as:

$$M_W = \frac{v}{2}g_2 \tag{1.35}$$

For the masses of the neutral gauge bosons γ/Z^0 the situation is a bit more complicated. Since the mass matrix in the last term of eq. 1.31 is not diagonal in the basis of the W^3, B states, the mass term for physical bosons γ and Z^0 will be a linear combination of those:

$$Z_\mu = \cos\theta_W W_\mu^3 - \sin\theta_W B_\mu \tag{1.36}$$

$$A_\mu = \sin\theta_W W_\mu^3 - \cos\theta_W B_\mu \tag{1.37}$$

where the θ_W is the Weinberg mixing angle defined as:

$$\tan\theta_W = \frac{g_1}{g_2} \tag{1.38}$$

By diagonalizing the neutral gauge boson mass matrix in the basis defined by eq. 1.36 the masses are found to be:

$$M_\gamma = 0, \qquad M_Z = \frac{v}{2}\sqrt{g_1^2 + g_2^2} = \frac{M_W}{\cos\theta_W} \tag{1.39}$$

Taking into account low-energy phenomenology and experiments it is possible to extract a numerical value for the energy scale v at which the spontaneous symmetry breaking occurs[6].

$$v = \left(\sqrt{2}G_F\right)^{1/2} \simeq 246 \text{ GeV} \tag{1.40}$$

Once the numerical value of v is found it is possible to make predictions for other masses within the Standard Model since these are proportional to v:

$$M_W^2 = \frac{\pi\alpha}{\sin^2\theta_W} v^2 \simeq \left(\frac{37.2}{\sin^2\theta_W}\ GeV\right)^2 \sim (80\ \text{GeV})^2 \tag{1.41}$$

$$M_Z^2 \simeq \left(\frac{37.2}{\sin^2\theta_W \cos^2\theta_W}\ GeV\right)^2 \sim (90\ \text{GeV})^2 \tag{1.42}$$

assuming the experimental value of $\sin^2\theta_W \sim 0.22$ [6].

Part II
The ATLAS experiment at the Large Hadron Collider

The measurements outlined in this thesis will be made using the ATLAS detector. ATLAS will utilize the proton-proton collisions generated by the Large Hadron Collider (LHC) to address the most fundamental questions of physics, hopefully allowing progress in understanding the deepest laws of nature. The following chapter provides an overview of the LHC and the ATLAS experiment.

Chapter 2

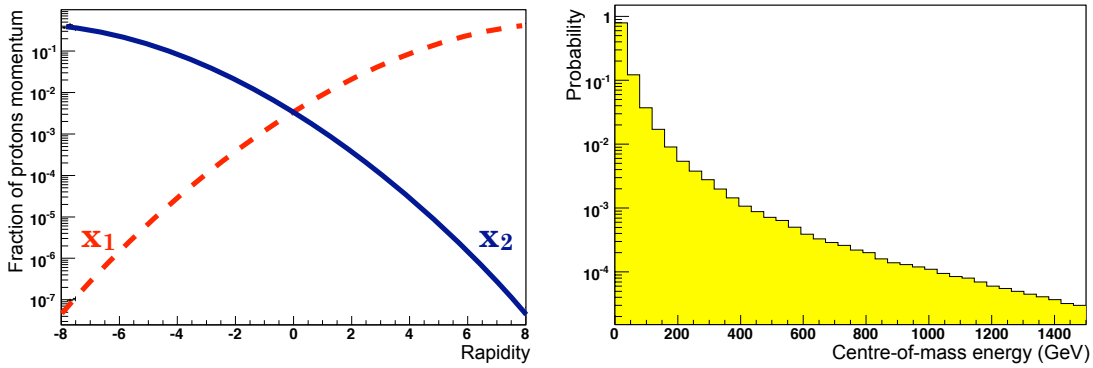
The Large Hadron Collider

The Large Hadron Collider (LHC) [25] is a two-ring, superconducting accelerator and collider installed in the tunnel previously occupied by its predecessor LEP [26]. The LHC is located at the French-Swiss border near Geneva at the research facility CERN [27] and is the largest accelerator system in the world. The next section is dedicated to describing the design and performance of the LHC.

2.1 Design considerations

Many considerations need to be taken into account when designing a complex system like the LHC. A considerable amount of environmental constraints come into play when building a project at such magnitude as the LHC. The aim of the physics programs and the time scale of the experiments are, however, the most important issues since they will determine the required performance of the accelerator. From the point of view of the experiments at LHC, only a few key parameters needs to be optimized. One such parameter is the total energy available in the centre of mass frame of the two colliding particles. This parameter, commonly referred to as the centre of mass energy ($\sqrt{s}$), is important since it sets the upper energy scale at which new physics can be probed. At hadron colliders this scale is set mainly by geometrical and magnetic constraints and the reason for this is that the magnetic field strength required to force particle beams around the collider increases linearly with the beam energy. In the case of the LHC the geometrical constraint was set by the circumference of the pre-existing LEP tunnel which essentially means that upper bound of $\sqrt{s}$ is entirely determined by the magnetic field sustainable in the LHC dipole magnets. The highest operational magnetic field in the LHC superconducting magnets is 8.65 T which results in a maximal achiveable center-of-mass energy of 14 TeV.
If the proton was a an elementary particle, then the energy available for creating new particles would be $\sqrt{s} = 14$ TeV. However, this is not true since at hadron colliders the primary hard scattering occurs between two partons[1] in the hadrons and not between the hadrons themselves. The energy available for the creation of new particles is therefore not $\sqrt{s}$ but the centre of mass energy of the primary partonic interaction, $\sqrt{\hat{s}} = x_1 x_2 \sqrt{s}$, where x_1 and x_2 are the fractional momenta carried by the two interacting partons. For proton-proton

[1] The word *parton* will be used in the following to refer to quarks and gluons as a whole.



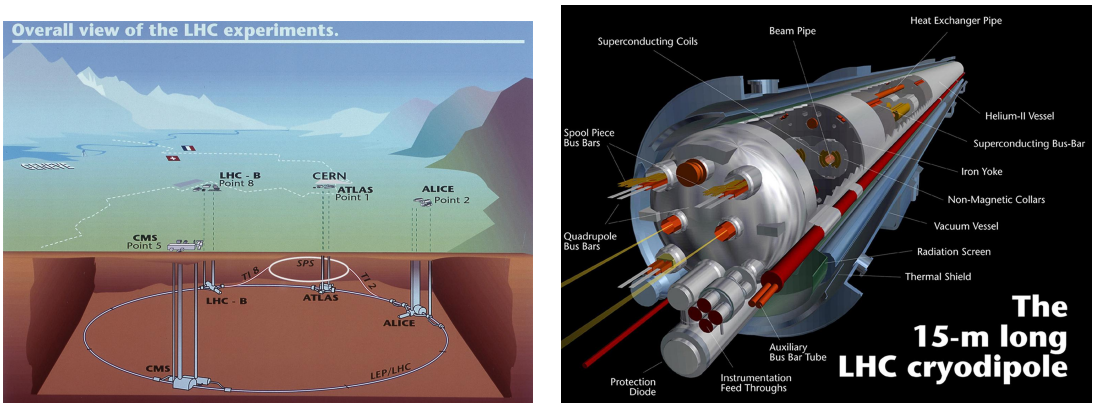
(a) (b)

Figure 2.1: *[28] (a) Average fractional momenta carried by the two interacting partons, x_1 and x_2, in proton- proton collisions at the LHC as a function of the rapidity of the hard interacting sub-system.(b) Probability distribution for the centre of mass energy of the primary partonic interaction in proton-proton collisions at the LHC.*

collisons at $\sqrt{s} = 14$ TeV, the average values of x_1 and x_2 as a function of the rapidity of the hard interacting sub-system are shown in fig.2.1(a). This type of information is provided by analyzing the parton density functions (PDF) and is useful since it provides valuable insight into the anatomy of the hard interaction. With this information it is for example possible to predict the most probable value of $\sqrt{\hat{s}}$ for proton-proton collisions at LHC (see figure 2.1(b)). The large spread in $\sqrt{\hat{s}}$ makes hadron colliders the perfect facilities for the discovery of new physics involving particles of unknown mass, since it is possible to probe many energy regions at the same time. This is in contrast to lepton colliders where the accelerator is tuned to a specific center-of-mass energy, making the search for some physics more time consuming.
An interesting feature displayed by figure 2.1(b) is that even though the center-of-mass energy is high, the available energy for production of new particles in the hard interaction is likely to be low in most interactions. In order to optimize the discovery potential for high mass new physics at LHC, the accelerator must provide a high rate of collisions. This rate is related to another parameter of great significance, namely the luminosity which will be mentioned briefly below and discussed in greater detail in chapter 4.

2.2 The LHC accelerator system

Hadron colliders like the Tevatron [29] are using beams of protons and anti-protons circulating in opposite directions in a common beam-pipe. The requirement of a very high luminosity at the LHC excludes the use of oppositely charged beams which implies the use of two proton beams in separate vacuum chambers. Hence, LHC is designed as a proton-proton collider with separate magnetic fields and vacuum chambers and with common sections only at the insertion regions where the experiments are located.
The basic layout of the LHC follows the LEP tunnel geometry which is depicted in fig. 2.2(a). The LHC has eight arcs and eight straight sections. Each straight section is approximately 545 m long and can serve as an experimental or utility insertion. The arcs, however, are made up



(a) (b)

Figure 2.2: *(a) Location of the LHC accelerator system [30] (b) Cross- section view of one of the LHC dipole magnets [30].*

of dipoles magnets designed to bend and keep the proton beams in orbit. As mentioned above each dipole magnet has to produce a field of 8.65 T at a current of 11.85 kA to constrain the 7 TeV protons. These requirements are met by constructing the coil of each dipole magnet out of a superconducting Niobium-Titanium alloy. To preserve the superconductive properties of the alloy, each magnet is placed in a cryostat and cooled with superfluid helium at 1.9K. A cross section view of one of the dipole magnets is shown in fig. 2.2(b). Each of the main dipole magnets is 14.3 m in length with an overall cold mass of 23.8 tonnes. In total the LHC consists of 1232 dipole magnets and 392 quadrupole magnet to focus the beam, giving the LHC a total circumference of almost 27 km to match the circumference of the LEP tunnel.

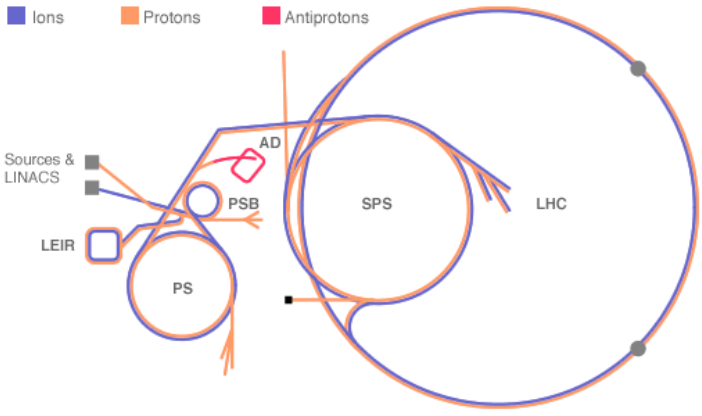


Figure 2.3: *The LHC injector chain. Before the protons enter the LHC they are pre-accerated in the following accelerators: (i)Linac, (ii)PSB (Booster), (iii)PS, (iv)SPS and finally (v)LHC.*

2.2.1 The injection chain

At LHC a 400 MHz Radio Frequency (RF) system operating at 16 MV is used to accelerate the proton beams. LHC on its own does not have the capability of accelerating particles all the way from rest energy to the full potential, when the protons reach a relativistic γ-factor of almost 7500. A series of pre-accelerators is therefore used to take the protons through several steps of shaping and acceleration before they are fed to the LHC (see figure 2.3). This system is collectively called the *injection chain* and consists of the following accelerators:

(*i*): **LINAC2** [31]. The first step of the LHC injection chain is the LINAC2 at which the Duoplasmatron provides a proton source for further acceleration. At the LINAC2, protons are accelerated up to an energy of 50 MeV and then delivered to the *Proton Synchrotron Booster* (PSB) via a 80 m long beam transport line.

(*ii*): **PSB** [32] is a circular accelerator comprised of 4 superimposed rings with a radius of 25m. In the PSB, protons injected from LINAC2 are accelerated to 1.4 GeV and injected to the PS - *the Proton Synchrotron*.

(*iii*): **PS** [33]. With a circumference of 628 m, the PS is capable of accelerating protons to an energy of 25 GeV. With the introduction of the SPS - *the Super Proton Synchrotron* the role of the PS changed to supply particles for the new machines.

(*iv*): **SPS** [34]. The SPS is the last step of the injector chain before the protons are passed onto LHC. Using a total of 1317 magnets the SPS is capable of accelerating protons from 25 GeV to the LHC injection energy at 450 GeV.

2.2.2 Beam structure

Particles are accelerated in the LHC by the use of a RF system deployed in specially designed RF cavities. A time-dependent electrical field is applied in such a way that particles sitting at a position of positive field gradient will receive an acceleration while particles sitting at a place of negative field gradient will be decelerated and thereby move towards the bottom of the field potential. In this way, a continuous beam of protons being injected into the LHC will naturally be grouped together in so-called *bunches*. The number of bunches and the possible locations of these, are fully defined by the settings of the RF system. At the LHC there are 3564 possible locations for the bunches but only a certain number of them will be filled [35]. During the initial physics operation and machine commissioning, a large bunch spacing is desirable. For this purpose only a single colliding bunch was used during the initial 2010 data taking period. In the preceding months, an increasing number of bunches were made to collide in order to increase the luminosity. As a consequence of the increased number of colliding bunches combined with higher intensity beams, the instantaneous luminosity was increased by a factor of 10^4 from LHC startup to August 2010.

2.3 LHC Experiments

Six different detectors, or experiments, have been constructed to study the collisions at LHC. The counter circulating beams will collide at four interaction points around the LHC ring

		Running scenarios	
	Unit	900 GeV	7 TeV
Bunch area (2σ)	[eV]	1.0	2.5
Bunch length (4σ)	[ns]	1.71	1.06
Number of particles per bunch		1.15×10^{11}	
Number of bunches		1-36(*)	
Revolution frequency	[kHz]	11.24	
RF frequency	[MHz]	400.8	
Energy gain/turn (20 min. ramp)	[eV]	485	485
Transverse normalized emmitance	[μm rad]	3.5	3.75
Betatron function	[m]	18	0.55
Crossing angle factor F			0.836

Table 2.1: *LHC beam parameters [25]. (*) A total of 36 was used by August 2010.*

at which the four major experiments (ATLAS, CMS, LHCb and ALICE) are situated. The other two experiments (LHCf and TOTEM) are smaller and situated close to already existing interaction points. The different experiments are briefly summarized below.

- **ALICE (A Large Ion Collider Experiment)** [36]. A detector which, as the name indicates, is dedicated to the study of heavy ion collisions. This field includes the study of quark-gluon plasma, a state of matter believed to be present shortly after the big bang. ALICE uses the fact that LHC will also be able to accelerate heavy ions (Pb nuclei) in addition to protons, at a center-of-mass energy of 2.76 TeV per nucleon for a total collision energy of 1150 TeV.

- **ATLAS (A Toroidal LHC ApparatuS)** A large general purpose detector discussed in detail in chapter 3.

- **CMS (Compact Muon Solenoid)** [37]. CMS is like ATLAS, a general purpose detector. The physics program at CMS ranges from Higgs searches to seaches of extra dimensions and super symmetry. The main structural difference between ATLAS and CMS is the layout of the muon magnet system. In CMS, the detector is build around a single solenoid magnet, whereas the magnetic field in ATLAS is generated by both a solenoid as well as a three toroidal magnets.

- **LHCb (Large Hadron Collider beauty)** [38]. A specialized detector which focuses on the problem of the imbalance of matter vs. anti-matter in the Universe. At LHCb this study is carried out by looking for B-mesons produced in the forward direction.

- **LHCf (Large Hadron Collider forward)** [39]. A smaller experiment to be installed close to the ATLAS interaction point. It is intended study the calorimeter response to high-energy particles created at the LHC. The calorimeter will later be used in cosmic ray studies.

- **TOTEM (TOTal Elastic and diffractive cross section Measurement)** [40]. TOTEM will be installed close to the CMS interaction point. The main goal of TOTEM

is to study particles produced in the very forward direction that are usually not accessible to the general purpose detectors such as ATLAS and CMS. In the context of this thesis TOTEM is relevant since it will from start-up hopefully measure total cross section.

2.4 LHC trivia

- On 10 September 2008, the proton beams were successfully circulated in the main ring of the LHC for the first time.
- On 19 September 2008, the operations were halted due to a serious fault between two superconducting bending magnets. Repairing the resulting damage and installing additional safety features took over a year.
- On 20 November 2009 the proton beams were successfully circulated again.
- On 23 November 2009, the first proton-proton collisions were recorded, at the injection energy of 450 GeV per particle.
- On 18 December 2009 the LHC was shut down after its initial commissioning run, which achieved proton collision energies of 2.36 TeV, with multiple bunches of protons circulating for several hours and data from over one million proton-proton collisions.
- The LHC resumed operations in February 2010, but it will operate at only half of the design collision energy. In 2012 it will be shut down for the repairs necessary to bring it to its full design energy, and then it will start up again in 2013.

Chapter 3

The ATLAS detector

The design of the ATLAS detector [41, 28, 42] is obviously to a large extent dictated by the physics programs to be conducted at the experiment. The high interaction rate, radiation dose and particle multiplicity at the LHC, combined with the requirements for precision measurements sets new standards for the detector performance demands, which has to be met by the particle physics experiment.
The general purpose nature of ATLAS means that it can provide a wide range of physics studies spanning from precision measurements of standard model parameters to the uncovering of phenomenon due to new physics. The search for the Standard Model Higgs boson has especially been used as a benchmark to establish the desired performance of the different ATLAS subsystems. The main production and decay channels of the Higgs boson is expected to depend on the mass. At low masses ($M_h < 2M_Z$) the most favorable decay will be purely photonic giving the Higgs boson a natural width of only a few MeV. In this case the instrumental resolution of the electromagnetic calorimeters will put a limit on the observed width. For Higgs boson masses above 130 GeV, the favored decay channel is expected to be via electroweak gauge boson pairs and their subsequent decay into high p_T leptons. In this scenario ATLAS will have to provide precise tracking and particle identification.
Viewed in this context, these benchmark physics goals can be turned into a set of general requirements for the ATLAS experiment.

- A large acceptance in pseudorapidity $\eta = -\ln\tan(\theta/2)$ and azimuthal angle ϕ
- Precise tracking and reconstruction efficiency of charged tracks in the part of the detector close to the interaction point. Important for precise vertex determination and tagging of b and τ-jets.
- Precise reconstruction of electromagnetic and hadronic showers. Important for particle identification and jet identification.
- Identification of muons and a high momentum resolution over a wide range in momenta. Important for the charge determination of high p_T muons.
- Accurate rejection of background on the trigger level. Important to most physics studies.

The following section will be dedicated to the description of how these requirements are met at ATLAS by employing a wide range of different detector techniques in several subsystems.

Firstly it will be described how the physics requirements in terms of particle identification and tracking will be met by an interplay of different detector techniques. Secondly, the separate subdetector systems will be described in greater detail. Special emphasis will be put on the forward detectors as they will play an important role in this thesis. The overall ATLAS detector layout is shown in figure 3.1.

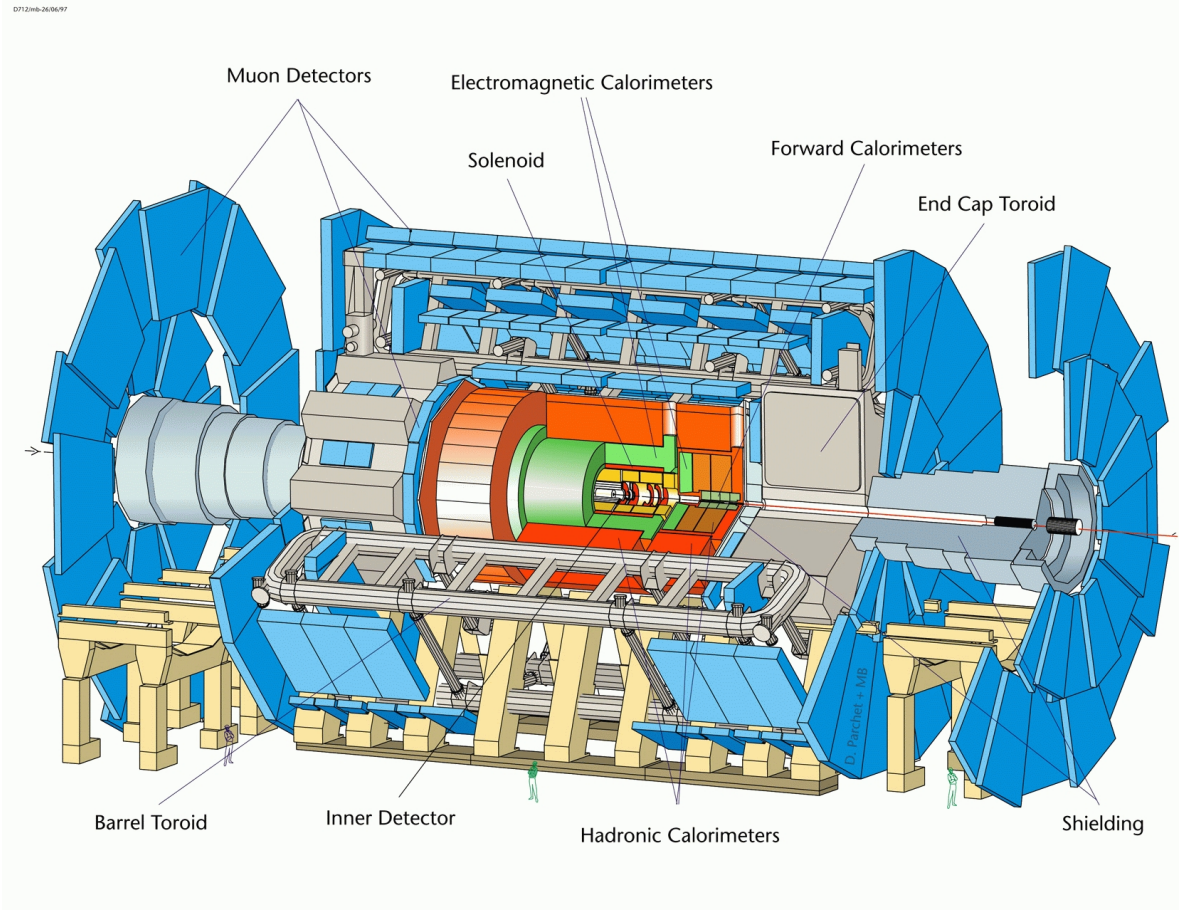


Figure 3.1: *Schematic view of the ATLAS detector. The dimensions of the detector are 25 m in height and 44 m in length. The overall weight of the detector is approximately 7000 tonnes [30]. The coordinate system used at ATLAS has the origin in the collision point and the z-axis parallel with the beam direction. The the positive y-axis is defined as pointing upwards and the positive x-axis as pointing from the interaction point to the center of the LHC ring.*

3.1 Detector overview

At design luminosity as much as 1000 particles will emerge from the collision point every 25ns. In order to cope with such large track density and still preserve a high momentum and vertex resolution, detectors close to the interaction point must have a fine granularity. In ATLAS pixel and silicon microstrip (SCT) trackers are used in conjunction with the straw tubes of the Transition Radiation Tracker (TRT) to match these requirements.

Tracking The tracking close to the interaction region is handled by the inner detector (ID). The ID combines high-resolution detectors at inner radii with continuous tracking elements at outer radii, all contained in a solenoidal magnet with a central field of 2T. The layout of the Inner Detector (ID) is illustrated in figure 3.2(a) and detailed in section 3.3.

In the region closest to the interaction region the highest granularity is obtained by using a detector based on silicon pixels technology. The pixel detector is designed to provide precise and unambiguous measurements of charged tracks emerging from the interaction point (IP) to aid the reconstruction of the impact parameter[1] for short lived particles. In order to do so, the pixel detector is constructed from three separate layers of pixel chips each segmented in R, ϕ and z. In the barrel region the three layers are arranged in concentric cylinders around the beam axis while in the end-cap regions they are arranged as disks perpendicular to the beam axis. This ensures a large acceptance of the detector and in addition that each particle from the IP traverses at least three layers of the pixel detector, leaving at least three space points for the tracking system.

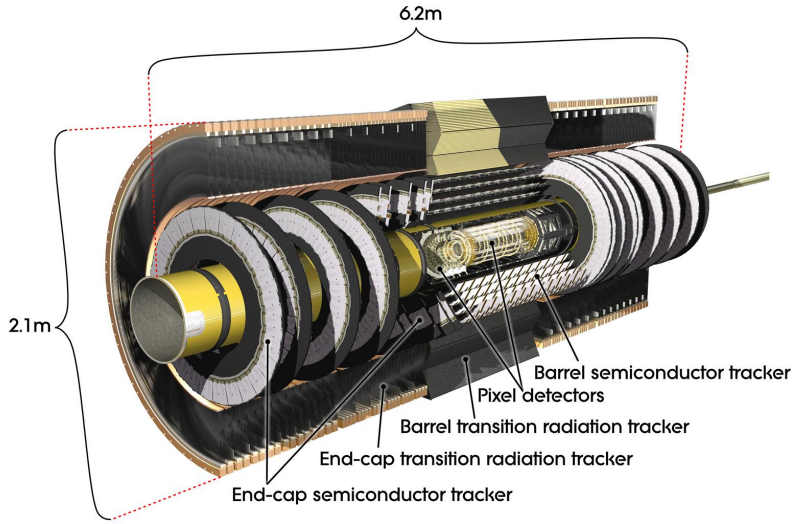
Moving away from the IP, the next detector after the pixel detector is the SemiConductor Tracker (SCT). From a tracking perspective, the job of the SCT is very similar to the pixel detector, namely to provide measurements of charged tracks coming from the IP in terms of space points. In this way the information from the SCT can be added to the already existing pixel information and used to improve the tracking. From a hardware point of view the SCT consists of four layers of silicon microstrip detectors likewise segmented in R, ϕ, z. Just as for the pixel detector, the layers of the SCT are in the barrel region arranged in concentric cylinders around the beam axis while in the end-cap regions they are arranged as disks perpendicular to the beam axis(see figure 3.2(a)).

The last part of the inner detector is the Transition Radiation tracker (TRT). The TRT is a straw detector, which allows for multiple measurements of the same track even in scenarios where the track density is high. In this way a better tracking performance can be obtained by combining the measurements of the precision tracker at small radii with the TRT information at larger radii. For instance due to the relative long path of a particle in the TRT, the precision of the momentum measurements can be greatly improved by adding the straw hit information from the TRT to the measurements from the pixel and SCT, despite the fact that resolution is worse. Apart from tracking, the TRT utilizes transition radiation from a radiator between the straws to detect and identify electrons.

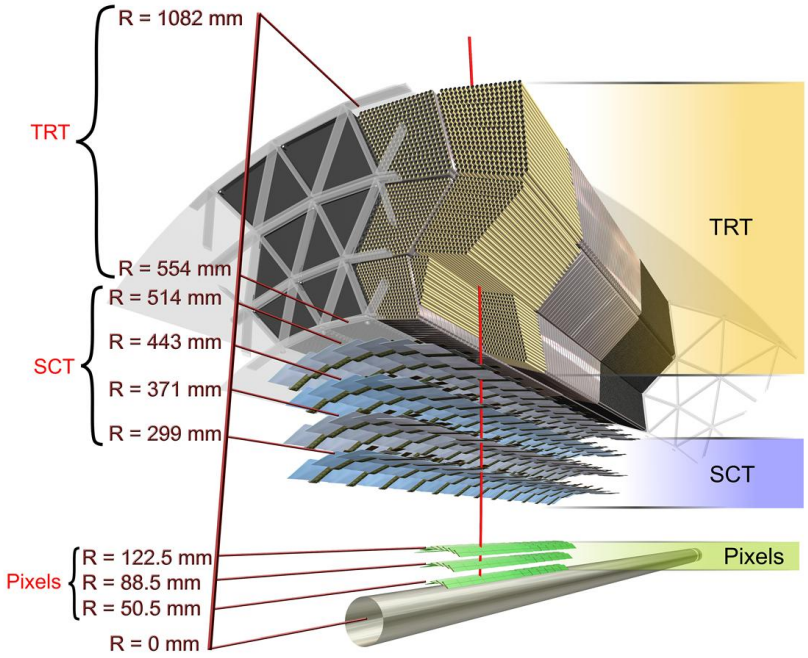
Figure 3.2(b) gives a schematic summary of the detector elements a particle originating from the IP sees. Typically, three pixel layers and four strip layers are crossed by each track, giving a total of seven space points. Additionally, a large number of tracking points (typically 36 per track) is provided by the straw tube tracker (TRT). Apart from the tracking provided by the inner detector, tracking of muons is carried out by a dedicated muon system as discussed in section 3.5.

Calorimetry To fully establish the properties and identification of all particles produced in a high energy collision, information available from the tracking systems such as momentum and charge is not sufficient. Additional information such as the energy needs to be measured and added to the preexisting tracking information to fully establish their properties. The type of detectors, capable of measuring both energy and position is called *Calorimeters*. As opposed to tracking detectors in which the particle is in principle left unaffected, the calorime-

[1] The transverse distance between the trajectory of the decay product of unstable particle and the IP.



(a)



(b)

Figure 3.2: *(a) Schematic outline of the inner detector [30] (b) Drawing showing the sensors and structural elements traversed by a charged track of p_T = 10 GeV in the barrel inner detector (η = 0.3). The track traverses successively the beryllium beam-pipe, the three cylindrical silicon-pixel layers , the four cylindrical double layers of barrel silicon-microstrip sensors (SCT) and the barrel transition-radiation tracker modules [30].*

ters are destructive in nature. This means that in order to measure the initial energy of a particle it has to be fully absorbed in the detector and will therefore not be available for further measurements. The absorption of particles with the intent to measure their energy is usually done by letting the particle pass thought dense material creating a cascade of secondary particles and stopping them. The initial energy of the particle, that give rise to the shower of secondary particles is then assumed to be proportional to the number of particles in the shower. Apart from energy measurements, the calorimeters can also provide particle identification relying on the fact that different particles give rise to different shower shapes. Usually the calorimeter system consists of the two types of calorimeters, namely the electromagnetic (EM) and the hadronic part since it is necessary to treat electromagnetic interacting particles such as electrons and photons differently from strongly interacting particles. In ATLAS, the EM calorimeter is based on a technique which uses liquid argon (LAr) as active medium while the hadronic calorimeter uses both the liquid argon technique and a traditional sampling calorimeter technique (see figure 3.3). The EM calorimeter is a lead-LAr detector with accordion-shaped kapton electrodes and lead absorber plates. Placed directly outside the EM calorimeter is the hadronic tile calorimeter, a sampling calorimeter using steel absorbers and scintillating tiles as the active material. The LAr hadronic end-cap calorimeter is situated behind the end-cap parts of the EM calorimeter. In the forward direction the Forward Calorimeter (FCal) is integrated into the end-cap cryostats, as this provides clear benefits in terms of uniformity of the calorimetric coverage as well as reduced radiation background levels in the muon spectrometer. The FCal will be discussed in greater detail in section 3.7. The general performance goal in terms of tracking and calorimetry is summarized in table 3.1

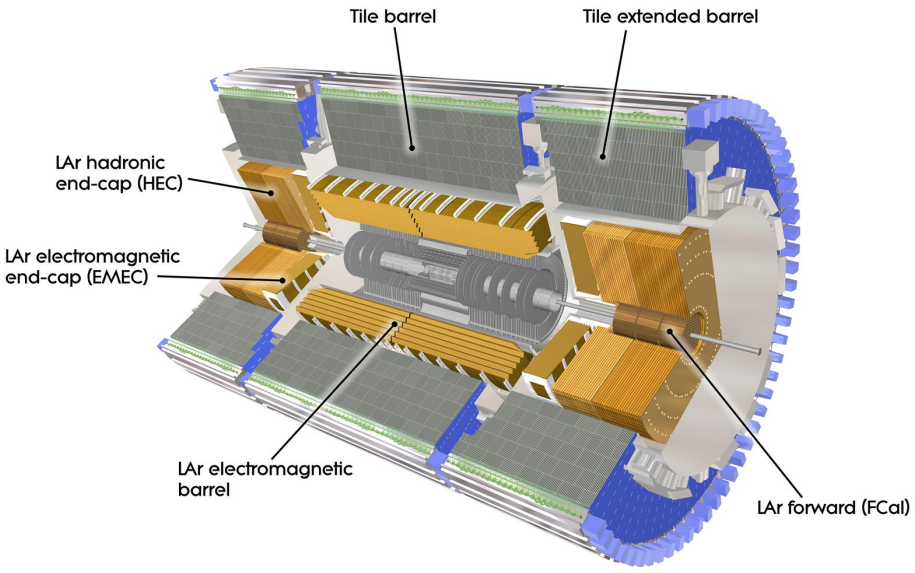


Figure 3.3: *Cut-away view of the ATLAS calorimeter system [30].*

Detector component	η coverage		Required resolution
	Measurement	Trigger	
Tracking	$\pm$ 2.5		$\sigma_{p_T}/p_T = 0.05\% p_T \bigoplus 1\%$
EM calorimetry	$\pm$ 3.2	$\pm$2.5	$\sigma_E/E = 10\%/\sqrt{E} \bigoplus 0.7\%$
Hadron calorimetry:			
Barrel and end-cap	$\pm$ 3.2	$\pm$3.2	$\sigma_E/E = 50\%/\sqrt{E} \bigoplus 3\%$
Forward region	$3.1 < \lvert\eta\rvert < 4.9$	$3.1 < \lvert\eta\rvert < 4.9$	$\sigma_E/E = 100\%/\sqrt{E} \bigoplus 10\%$
Muon spectrometer	$\pm$ 2.7	$\pm$ 2.4	$\sigma_{p_T}/p_T = 10\%$ at $p_T = 1$ TeV

Table 3.1: *General performance goals of the ATLAS detector [41]. The units for E and p_T are in GeV.*

3.2 Magnet Systems

The magnet system used at ATLAS is unique in many ways. It has be designed to provide the optimal conditions for particle identification and momentum measurement for each detector system separately. As such the magnet system consists not only of a single magnet but of four independent magnet systems, namely the *Central Solenoid* [43] and three separate *Toroid* systems [44]. The combined magnet system is indicated at figure 3.1.

Central Solenoid The Central Solenoid is situated around the inner detector and is designed to provide a magnetic field of 2T in the inner tracker. This field strength was chosen in order to maintain good tracking for low p_T particles. With a larger field strength in the central solenoid, low p_T particles will simply curl up before reaching the inner detector layers[2]. Another design consideration of the central solenoid was to minimize the amount of material before the electromagnetic calorimeter. To achieve these goals the central solenoid is constructed from single-layer coil that consists of a high-strength Al-stabilised Nb/Ti conductor. The axial length of the solenoid is 5.8 m and the inner and outer diameters are 2.46 m and 2.56 m respectively, resulting in a total thickness of 0.66 radiation lengths.

Barrel and end-cap toroids The toroid system is split into three parts with a barrel part installed outside the hadronic tile calorimeter and two end-cap parts installed outside the liquid argon hadronic calorimeter. The parts can be operated independently and are designed to produce an average toroidal magnetic field of approximately 0.5 T and 1 T for the muon detectors in the central and end-cap regions, respectively (the peak field is 4T). The barrel system consists of eight identical racetrack-shaped coils encased in individual stainless-steels cryostats (see figure 3.1). Each coil measures 25.5 m $\times$ 5.4 m and is made from an Al-stabilised Nb/Ti/Cu superconducting alloy. When all the eight modules are combined they produce the bending power for tracks in the central region of $|\eta| < 1$. For tracks in the region of $1.4 < |\eta| < 2.7$ the bending power is instead provided by the end-cap toroids. The end-cap part is very similar to the barrel part in layout and choice of material. Only the dimensions are different and the fact that all end-cap modules are encased in a single cryostat. In the end-cap region each module measures 4 m $\times$ 4.5 m.

[2] 16 MeV for the first layers and 335 MeV for the final layer for particles emitted at $\eta = 0$.

The combination of the slim solenoid system and the open design of the toroid system is optimized to provide continuos bending of charged particles all the way from the IP to the end of the muon system while keeping the amount of multiple scattering in the muon system at a minimum and thereby maintaining a good momentum resolution for muons. This is in line with one of the ATLAS design goals, namely to optimize the detector for a discovery of the Higgs particle in the fully muonic channel ($H \rightarrow ZZ^* \rightarrow 4\mu$).

3.3 Inner detector

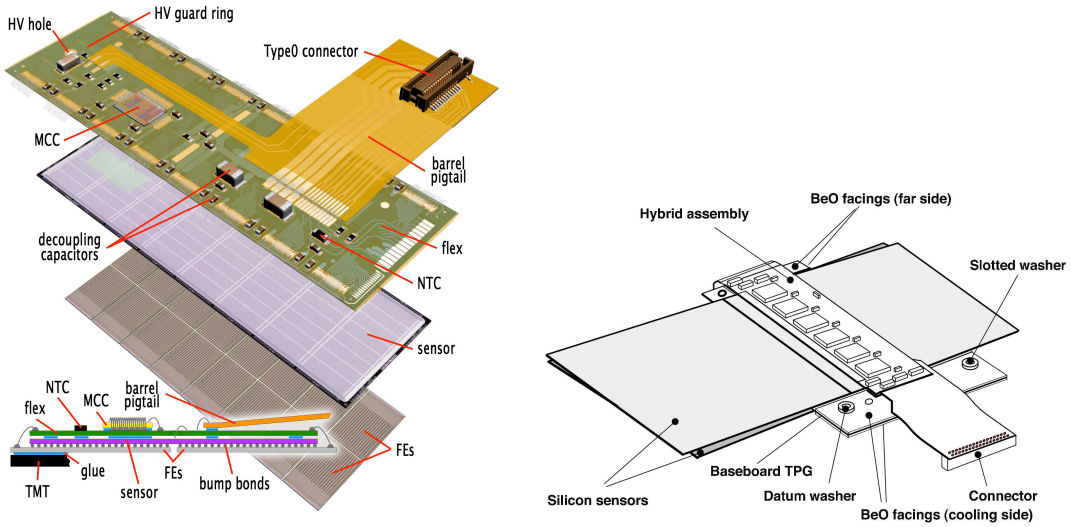
As mentioned above, the Inner Detector (ID) is designed to provide hermetic and robust pattern recognition, excellent momentum resolution and both primary and secondary vertex measurements [45][46] for charged tracks above a given p_T threshold and within the pseudo-rapidity range $|\eta| < 2.5$. It also provides electron identification over $|\eta| < 2.0$ at a wide range of energies.
The ID consists of three independent but complementary sub-detectors which will be described in detail in the following sections. Since the layout of the subdetectors has already been discussed the following section will focus on the active elements of each detector.

3.3.1 The pixel detector

The resolution of gaseous tracking detectors are intrinsically limited due to diffusion [47]. Limits of the order of 100 μm for drift distances $\sim$ 1 cm are put on the spacial resolution due to localization of the drifting ionization [48]. For the study of heavy quarks in ATLAS it is a requirement of the vertex detector to have a spacial resolution better than the characteristic length scale of the heavy quark decay. Since the typical decay length in heavy quark decays is of the order of $c\tau$ = 100 - 400 μm the vertex detector in ATLAS needs to employ a detector technique which matches this requirement.
A spatial resolution of 12 μm in $R - \phi$ and 100 μm in z is obtained [49] in the ATLAS vertex detector by using a finely segmented silicon pixel sensors. Here the nominal pixel size is 50 μm in the ϕ direction and 400 μm in z (barrel region, along the beam axis) or r (end-cap region). Every pixel sensor is fabricated in the same way by implanting high negative (n+) and positive (p+) dose regions on each side of a wafer and thus creating a asymmetric depletion region which extends over the whole sensor bulk volume. Here, one is able to collect and detect charge carriers generated as electron-hole pairs in the active volume. This specific design of the sensor pixels was chosen since it guarantees single pixel isolation, minimizes leakage current and makes the active elements tolerant to radiation damage.
As a whole the pixel detector is made from 1744 tile-like modules each containing 47232 pixel sensors arranged in 144 columns and 328 rows resulting in over 80 million read-out channels. To ensure maximal coverage, the sensor modules are mounted in staves along the z-axis and tilted by 1 degree to create a small overlap between the modules in the ϕ-direction [41].

3.3.2 The semiconductor tracker

The SCT sensors rely on many of the same ideas and much of the same semiconductor technology as is used in the pixel detector. Where the pixel detector uses high granularity



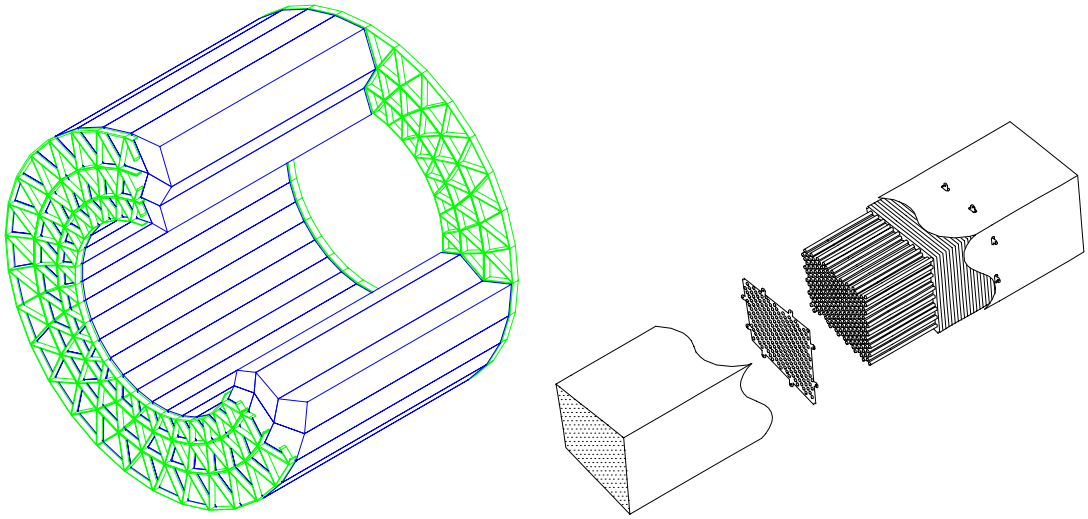
(a) (b)

Figure 3.4: *(a) The elements of a pixel barrel module [49] (b) 3D view of the ATLAS SCT barrel module [50].*

silicon pixel sensors, the SCT uses silicon micro-strip sensors. In this type of detector the active sensor or the sensitive area is composed of p+ diode strips implanted onto a n-type silicon base. As such the resolution of a micro-strip detector is bound to have a much better resolution in the direction perpendicular to the strip direction. However, this can be rectified by mounting two micro-strip layers back-to-back in a stereo-angle and thereby providing two dimensional tracking information. In the SCT, a strip pitch of 80 μm with two 6 cm-long sensors daisy-chained was chosen for the rectangular barrel sensors and radial strips of constant azimuth with mean pitch of $\sim$ 80 μm were chosen for the trapezoidal end-cap sensors. One side of the detectors have readout strips aligned along the z axis; on the other side the strips are rotated by 40 mrad to improve the resolution in the z-direction. The intrinsic accuracies per module in the barrel are 17 μm $(R-\phi)$ and 580 μm (z) and in the disks they are 17 μm $(R-\phi)$ and 580 μm (R). The total number of readout channels in the SCT is approximately 6.3 million.

3.3.3 The transition radiation tracker

The last subsystem in the inner detector is, as opposed to the pixel and the SCT detector, not based on a semiconducting technology but on a more conventional technology using gaseous drifts tubes. Polyaimide drift (straw) tubes of 4 mm diameter are the basic TRT detector elements [51]. Each straw is filled with a gas mixture of 70% Xe, 27% CO_2 and 3% O_2 at slight overpressure and the signal is read out by a 31 μm gold-plated tungsten anode wire suspended in the center of the straw. The Xe component is used in this context to absorb photons from transition radiation. To ensure good electrical and mechanical properties each straw is coated on the inside with a 25 μm thick layer of kapton film and an additional layer of Aluminum film. The straws in the barrel region are arranged in such a way that they form



(a) (b)

Figure 3.5: *(a) Layout of the barrel TRT showing the three layers of barrel modules (b) Exploded view of a 1.5 m long barrel module showing the straws. Both figures are from [28].*

a uniform array parallel to the beam axis, with an average spacing of about 6.6 mm between centers radially and tangentially. In total the straws are assembled in 96 modules of three different types (see figure 3.5(a) and 3.5(b)) for the barrel region whereas the end-cap straws are arranged in 14 wheels and point radially away from the beam axis. This layout of the drift tubes was chosen in order to maximize the number of hits along a given track and to open up for the possibility to perform particle identification by means of transition radiation. In the TRT the transition radiation is produced by layers of 15 μm thick polypropylene radiator foils located in the space between the straw layers. Transition radiation arises when an ultra-relativistic charged particle traverses the boundary between materials of different dielectric constants. This effect is proportional to the γ-factor of the traversing particle and can provide particle identification capabilities from the amount of transition radiation produced by a given particle.

3.3.4 Pile-up at high luminosity

The total inelastic cross section for pp interactions at LHC energies is expected to be 80 mb [52]. This means that at a design luminosity of 10^{34} cm^{-2}s^{-1} with a bunch spacing of 25 ns, the mean number of minimum bias events which will be seen by the Inner Detector can be as much as 25 on average. This implies that when an interesting event is selected by the trigger, there will be 24 single minimum bias events superimposed - so called *pile-up*[3] events.
As mentioned before, the bunch structure of the LHC is such that a train of many successive filled bunches will be followed by a number of empty bunches. For the inner detector this means that an interesting event will usually follow and be followed by pile-up events. Consequently the inner detector must be equipped with read-out electronics capable of separating

[3]The concept of pile-up and luminosity will be discussed in further detail in chapter 4.

the signal from an interesting bunch crossing from the signals of the prior and the following bunch crossing. In the case of the pixel detector and the SCT, the fast response of the silicon technology combined with fast readout electronics makes it possible to associate interesting signals to the correct beam-crossing and there is little contamination by fast particles from out-of-time events. However for the TRT the maximal drift time is 40 ns which is significantly more than the 25 ns bunch spacing. As a result a timing gate is applied in order to be efficient to in-time hits.

3.4 Calorimeters

All calorimeters used in ATLAS are of the sampling type. The basic model for sampling calorimeters is that the shower from a particle develops in a high Z material and is sampled in low Z material such as scintillator plastic or liquid argon. The total energy of the particle is then taken to be proportional to the energy which has been actively sampled. Since the energies of particles produced in pp collisions at ATLAS come in a wide range it is necessary to construct the calorimeters in such a way that even the most energetic particles get stopped fully. Figure 3.6 shows the amount of material in units of radiation length that each part of the calorimeters is designed to have in order to meet these requirements. This kind of information

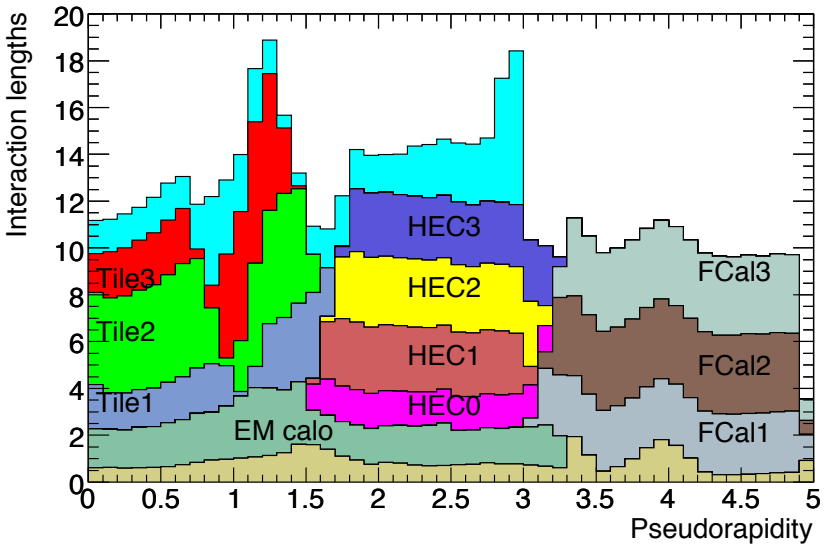


Figure 3.6: *Cumulative amount of material, in units of interaction length, as a function of $|\eta|$. The contribution from the different parts of EM and hadronic calorimeters are indicated by the name of specific module [41]. Also shown for completeness is the total amount of material in front of the first active layer of the muon spectrometer (up to $|\eta| < 3.0$).*

is also very useful for the operation of detectors in the very forward direction. For example, a high η primary particle from the IP might traverse only parts of the calorimeter and instead of getting stopped it will produced a shower of secondary particles and thereby produce a large contribution to the signal of such detectors as LUCID or the MBTS. Such effects will be discussed in greater detail in the following chapters.

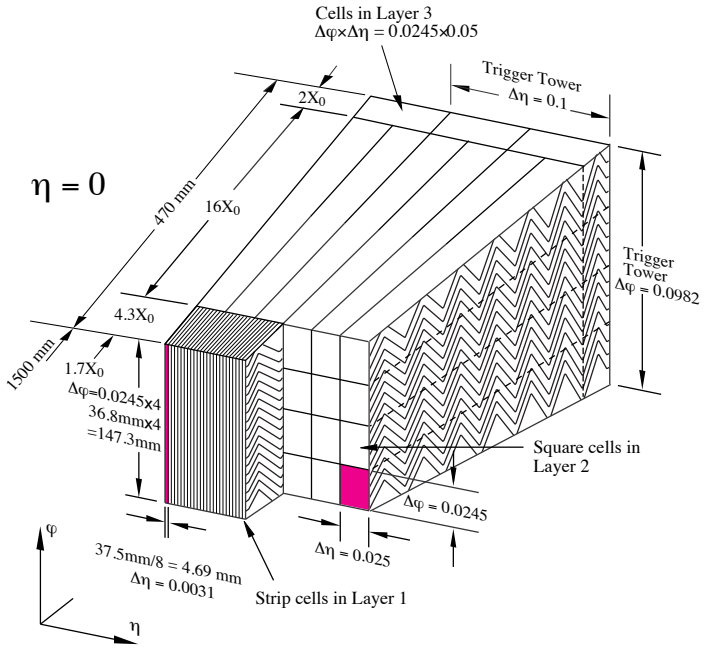


Figure 3.7: *Sketch of a LAr EM barrel module where the different layers are clearly visible The granularity in $|\eta|$ and ϕ of the cells of each of the three samplings are also shown [53].*

3.4.1 The Electromagnetic Calorimeter

The EM calorimeter [53] surrounds the inner detector and is designed to identify and measure the energy of electrons and photons. It is divided into a barrel part, situated within $|\eta| < 1.475$, and two endcaps found within $1.375 < |\eta| < 3.2$. Its granularity is especially fine in the region closest to the inner detector, making it possible to distinguish between partially overlapping showers. Both the barrel and the end-cap modules are divided into three parts, the so-called *samplings*. The first sampling is situated closest to the IP and has the finest granularity which allows for precise cell clustering. The second sampling is in terms of radiation lengths the deepest and thus the electrons and photons will deposit most of their energy in this layer. The last sampling is designed to recover high energetic showers from particles which passes the second sampling. Since hadronic showers are likely to extend beyond the EM calorimeter all together, the last sampling will allow for discrimination between electromagnetic showers and hadronic showers. The three sampling layers are indicated in figure 3.7 which shows a module of the EM LAr barrel.
Figure 3.7 also shows the readout segmentation of the detector in units of η and ϕ. To obtain this level of segmentation a total of 1024 1.8 mm thick lead absorber sheets are folded in an accordion shape and stacked in ϕ leaving a gap of 3.6 mm between two successive sheets. The lead gives the shower development with its short radiation length and the secondary electrons create ionisation in the narrow gaps of liquid argon. The signal is read out from each gap by a 300 μm copper plated kapton sheet which is folded to match the accordion shape of the lead absorbers. In order to achieve a readout segmentation in η and z appropriate divisions are etched in the copper sheets. A readout segmentation in ϕ is likewise obtained by collecting signals from four double gaps into the same readout which give a radial segmentation of $2\pi/256$. The general performance of the EM calorimeter is summarized in table 3.1.

3.4.2 The Hadronic Calorimeter

The hadronic calorimeters in ATLAS consists of three parts: the Tile Calorimeter (TileCal), the liquid-argon Hadronic End-cap Calorimeter (HEC) and the liquid-argon Forward Calorimeter (FCal).

The tile calorimeter is placed directly outside the EM calorimeter envelope (see figure 3.3) where the level of radiation is relatively low. Unlike the LAr calorimeter the tile calorimeter does not have an end cap region but is divided into a barrel which covers the region $|\eta| < 1.0$, and two extended barrels in the range $0.8 < |\eta| < 1.7$. The tile calorimeter [54] is a sampling calorimeter using steel as the passive absorber and scintillating tiles as the active medium. As such, the tile calorimeter is a very conventional choice when it comes to hadronic calorimeters in high energy collider experiments. However, one unique feature sets the tile calorimeter apart from other sampling calorimeters used in the past. Namely the orientation of the scintillating tiles relative to the direction of the particles from the interaction point. In this detector, as shown in figure 3.8, the tiles are made to point radially out from the beam line making the particles emerging from the IP traverse the tiles in the longitudinal direction. The advantage with such a design is that a finer readout segmentation in the z direction for high p_T particles can be achieved giving a better shower shape determination and E_T^{miss} resolution. Each tile is 3 mm thick and is read out by a pair of wavelength shifting (WLS) fibers attached to the tile on two sides and subsequently coupled to the photomultiplier. The readout is furthermore segmented in to a three-dimensional cell structure, creating a projective geometry for triggering and energy reconstruction. The $\Delta\eta \times \Delta\phi$ granularity equals to 0.1×0.1 in the first two samplings and 0.2×0.1 in the outermost sampling.

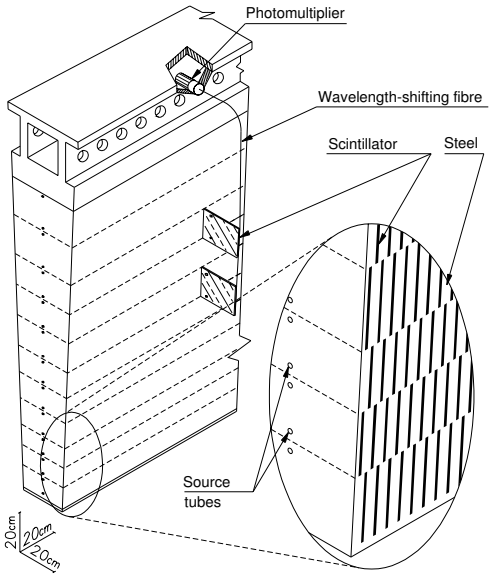


Figure 3.8: *The principle of the Tile Calorimeter design [54] The fibers transports the (shifted) light from the scintillating tiles to the photomultiplier.*

At higher η, the radiation level will be higher and thus the hadronic calorimeter (HEC) in the region behind the EM end-caps is based on the more radiation resistant liquid argon technology. Copper is used as an absorber material. Since the HEC is similar in design to the EM LAr calorimeters it will not be discussed further here[4]. The final component of the hadronic calorimeter system is the Forward Calorimeter which is located in the region $3.1 < |\eta| < 4.9$ where the particle flux is very high and it must therefore be designed to cope with this. FCal is discussed further in section 3.7. The overall performance is summarized in table 3.1

[4]For details see [53].

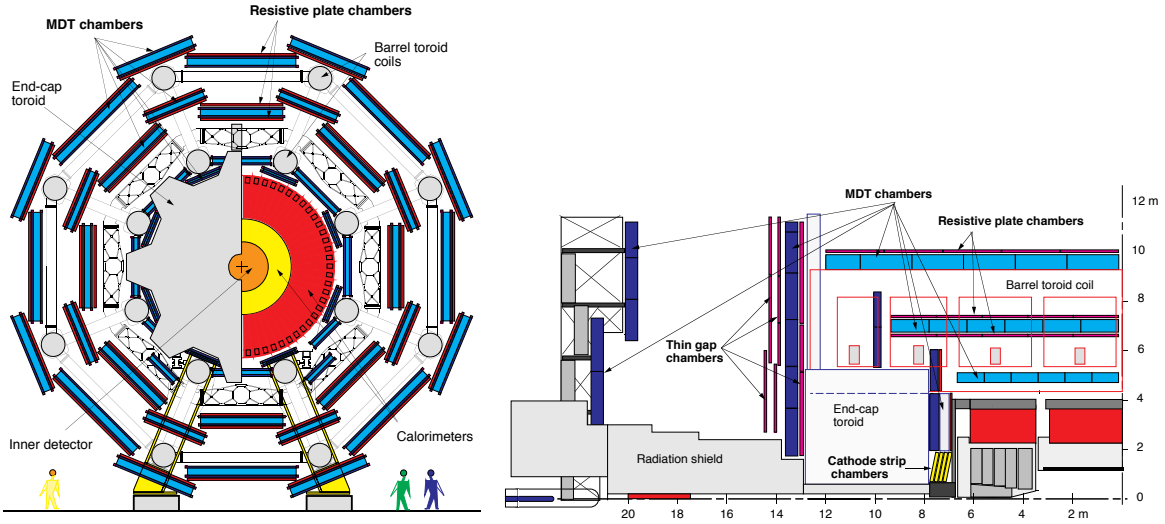


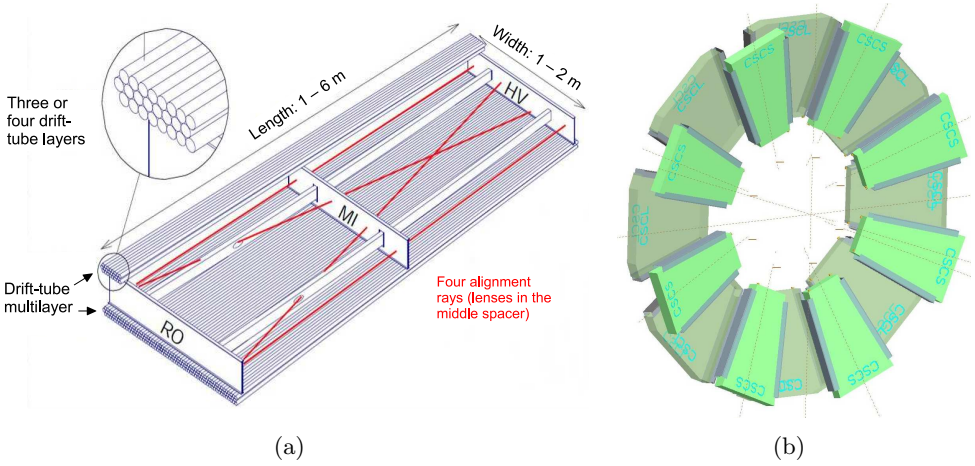
Figure 3.9: *End and side view of the muon spectrometer. (See also figure 3.1).*

3.5 Muon Spectrometer

The muon spectrometer [55] is by far the largest tracking system at ATLAS, extending from a radius of 4.25 m around the calorimeters out to the full radius of the detector (11 m) and thus defining the outer perimeter of the ATLAS detector. The main design goal of the muon system is to detect muons exiting the barrel and end-cap calorimeters and to measure their momentum in the range $|\eta| < 2.7$. The main requirement of the muon spectrometer as a tracking system is to be able to resolve a sagitta along the z-axis with a precision of less than 50 μm. This requirement is set forth by the wish to perform a stand-alone p_T measurement of a 1 TeV muon with a resolution better than 10 %. To meet these requirements the muon system uses two types of precision tracking chambers, namely the Monitored Drift Tube chambers (MDT's) at low $|\eta|$ and the Cathode-Strip Chambers (CSC) at high $|\eta|$.
The layout of the precision-tracking chambers is such that is reflects the ϕ-symmetry of the toroids. In the barrel region three concentric cylindrical layers of MDT chambers are placed before, after and inside the toroid field at radii of approximately 5 m, 7.5 m, and 10 m (see figure 3.9). In the end-caps there are three layers of MDT's, one before the end cap toroid and two after. The first layer is 8 tubes deep, the other layers are 6 tubes deep. The CSC's are situated at low radius before the toroid. Apart from the tracking an additional design criteria of the muon system is the capability to trigger on muon tracks. For this purpose, dedicated fast trigger chambers have been installed in between the precision chambers in both the barrel and the end-cap region. In the barrel region ($|\eta| < 1.05$), Resistive Plate Chambers (RPC) were selected for this purpose while in the end-cap ($1.05 < |\eta| < 2.4$) Thin Gap Chambers (TGC) were chosen. Table 3.2 summarizes the performance goals of each of the four sub-systems of the muon spectrometer.

		Chamber resolution (RMS) in			Nmber of	
Type	**Function**	z/R	ϕ	time	chambers	channels
MDT	tracking	35 μm (z)	-	-	1088 (1150)	339k (354k)
CSC	tracking	40 μm (R)	5 mm	7 ns	32	30.7k
RPC	trigger	10 μm (z)	10 mm	1.5 ns	544 (606)	359k (373k)
TGC	trigger	2-6 μm (R)	3-7 mm	4 ns	3588	318k

Table 3.2: *Parameters of the four sub-systems of the muon detector [41].*



(a) (b)

Figure 3.10: *(a) Mechanical structure of a MDT chamber. (b) Layout of a CSC end-cap with eight small and eight large chambers. Both figures are from [41].*

3.5.1 Precision tracking chambers

The sensitive element of the MDTs is an Ar/CO_2 filled drift tube operated at a pressure of 3 bar. Each tube has a radius of 30 mm and is read out by a central tungsten-rhenium wire with a diameter of 50 μm. The shapes and dimensions of the drift tubes were in general chosen to optimize solid angle coverage. In the barrel region, all drift tubes are of the same length(3.7m [56]) and mounted along the ϕ-direction in such a way that centre points of the tubes are tangential to circles around the beam axis. In the end-cap region the tubes are likewise mounted along the ϕ-direction only here the length is adjusted according to the distance from the beam axis. One drawback of having drift tubes with such a relative large radius is long drift times manifesting itself in long readout pulse trains. Taking the radius and the choice of gas into consideration it can be shown that electrons resulting from ionizing tracks can have a drift time as large as 700 ns [41], which is about 50% longer than for linear gases such as Ar/CH_4.
To obtain high spatial resolution the MDTs are mounted in modules of 2×4 and 2×3 as shown in figure 3.10(a). In this way an overall spatial resolution of 30 μm can be achieved.
The sensitive element of the CSC's is a multi-wire proportional chambers with the wires oriented in the radial direction. Each chamber is composed of several layers where each layer is made from an 18.75 mm thick sheet of polyurethane foam sandwiched between two 0.82 mm

thick copper-clad laminates in which a 17 μm thick copper cladding forms the cathodes. Both cathodes are segmented, one with the strips perpendicular to the wires (providing the precision coordinate) and the other parallel to the wires providing the transverse coordinate. The position of the track is obtained by interpolation between the charges induced on neighbouring cathode strips. The anode wires have a diameter of 30 μm and are made of gold-plated tungsten with 3% rhenium , however the anode signal is not read out. The CSC's chambers are arranged in two disks of eight chambers each, as shown in figure 3.10(b).

3.5.2 Trigger chambers

The trigger chambers of the muon system provide fast information on muon tracks traversing the detector, allowing the L1 trigger logic to recognize their multiplicity and approximate energy range.
The RPC is a gaseous parallel electrode-plate (i.e. no wire) detector. Two resistive plates, made of phenolic-melaminic plastic laminate, are kept parallel to each other at a distance of 2 mm by insulating spacers. The electric field between the plates of about 4.9 kV/mm allows avalanches to form towards the anode, along the ionizing tracks. The signal is read out via a capacitive coupling to metallic strips, which are mounted on the outer faces of the resistive plates.
Thin Gap Chambers (TGC's) are used in the end-cap region. They operate on the same principle as multi-wire proportional chambers, and they provide good time resolution and high rate capability. TGC's are multi-wire proportional chambers with a wire-to-cathode distance of 1.4mm being smaller than the wire-to-wire distance of 1.8 mm, as shown in figure 3.9. With a highly quenching gas mixture of CO_2 and $n - C_5H_{12}$ (n-pentane), this cell geometry allows for an operation in a quasi-saturated mode, i.e. with a gas gain of 3×10^5.
The trigger system and other details of the muon system relevant for this thesis will be discussed further in chapter 11.

3.6 Beam Monitors

A possible scenario at LHC arises when several proton bunches hit the collimators designed to protect the detectors. In such situations the high instantaneous dose might cause serious detector damage to especially the inner detector. The ATLAS Beam Condition Monitor (BCM) is designed to detect such incidents and trigger an abort before they cause damage.

3.6.1 Beam Condition Monitor

The BCM [57] detector consists of two stations (forward and backward) each with four modules placed close to the beam pipe within the inner detector. The stations are located symmetrically around the interaction point, positioning the modules at $z = \pm 184$ cm and $r = 55$ mm (a pseudo-rapidity of about 4.2). Each module includes two diamond sensors read out in parallel. When a charged particle traverses one of the diamond sensors, the crystals get ionized and a MIP signal[5] is generated. The signal is read out by fast electronics placed close

[5]Minimum ionizing particle.

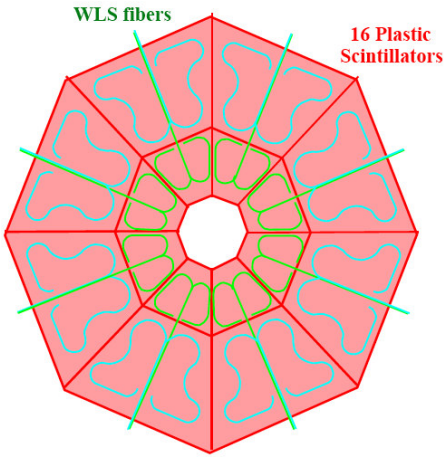


Figure 3.11: *schematic view of the MBTS disk configuration.*

to the actual sensors. The reason for placing the readout electronic so close to the beam pipe is dictated by the requirement to have electronics with a time resolution of a few ns. With the position of the detector stations and time resolution of the electronics, the BCM is capable of measuring time-of-flight and pulse height of a traversing particles in order to distinguish events resulting from lost beam particles from those normally occurring in proton-proton interaction. The BCM also provides a measurement of bunch-by-bunch luminosities in ATLAS by counting in-time and out-of-time collisions.

3.6.2 Minimum Bias Trigger Scintillators

Apart from monitoring capabilities of the BCM a further need exists for a simple system which is able to tell, with high efficiency, whether or not a collision took place during a bunch crossing. In most situations this can be handled by the inner detector which will monitor the amount of minimum bias activity during a bunch crossing by counting the number of space points in the pixel and SCT layers. However, as a measure of precaution, certain parts of the inner detector are only enabled when the beam conditions are suitable for it. For this reason ATLAS has been equipped with scintillation counters in order to provide an interaction trigger even when the beam conditions are not optimal.
The Minimum Bias Trigger scintillators (MBTS) [58, 41] consist of 32 scintillating tiles, 2 cm thick, organized into 2 disks, one on each side of the interaction point of ATLAS. A schematic sketch of one disk is shown in figure 3.11. Each disk is segmented in eight units in ϕ and two units in η resulting in a total of 16 independent counters per side. The radial dimensions of the inner and outer rings are (153, 426) mm and (246, 890) mm respectively and with a position at $z = \pm 3560$ mm this results in a η coverage of $[2.82, 3.84]$. The scintillators are installed on the front face of the end-cap calorimeter cryostats and shares readout electronics with the tile calorimeter. The light emitted in each counter by a traversing charged particle is collected by wavelength-shifting optical fibers and guided to a photomultiplier tube. After being shaped and amplified by TileCal electronics, the signal from the photomultiplier tubes are passed through a leading edge discriminator and then further on to the central ATLAS trigger system. The MBTS plays a central role in the determination of luminosity at ATLAS

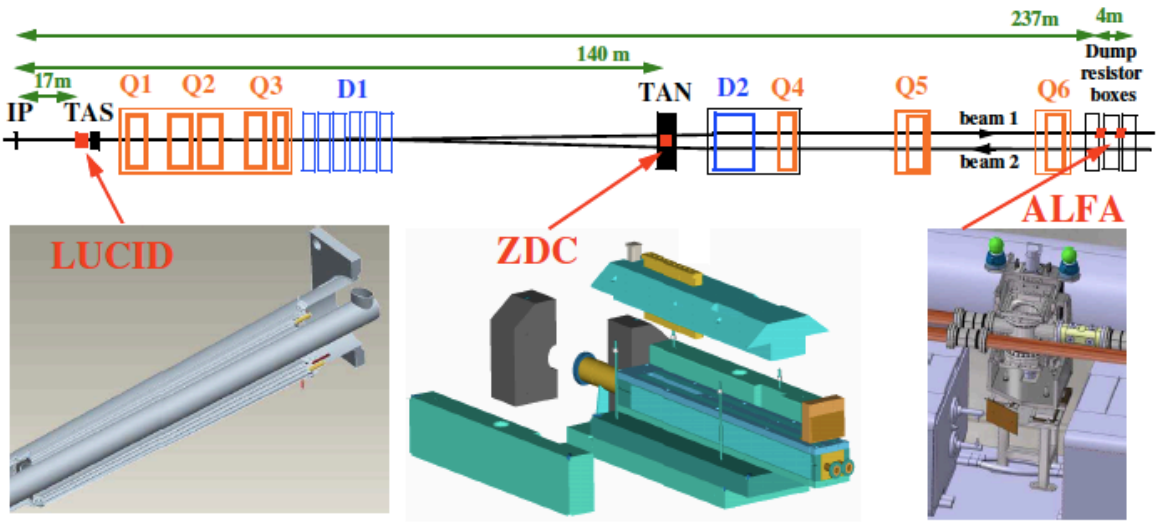


Figure 3.12: *Overview of the forward detectors [59]. The location of each detector downstream to the interaction point are indicated on the picture.*

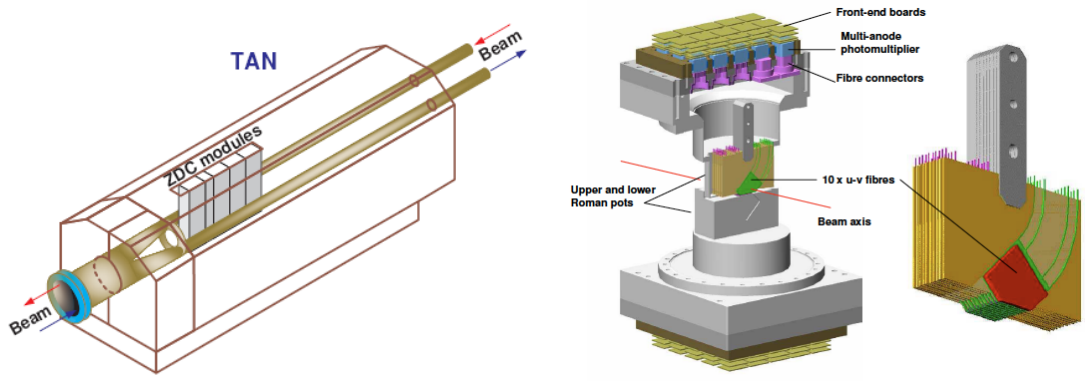
and thus will be discussed further in the following chapters.

3.7 Forward Detectors

In addition to the main ATLAS detector systems, a set of three detectors are placed along the beam line and will provide coverage in the very forward region. Ordered according to their distance from the interaction point as shown in figure 3.12 , the first system is a Cerenkov detector called LUCID (LUminosity measurement using Cerenkov Integrating Detector). LUCID is the ATLAS detector dedicated to monitoring of the LHC luminosity, and is designed to have a sufficient time resolution in order to identify individual bunch crossings. The second system is the Zero-Degree Calorimeter (ZDC) located at the point where the two vacuum pipes of the LHC are merged into one. The ZDC is dedicated to the study of forward neutrons in heavy ion collisions. The third and last of the forward detectors is ALFA (Absolute Luminosity For ATLAS) located at a distance of almost 240 m from the IP. Apart from providing a measurement of the absolute luminosity ALFA is also intended to be used for tagging of forward protons for diffractive physics studies.

3.7.1 LUCID

LUCID consists of two rings of Cerenkov tubes filled with C_4F_{10} mounted on each side of the interaction point at a distance of 17 m. Given the location and the physics scope of the detector, the design of LUCID is optimized to be radiation hard and to provide fast and reliable information about the luminosity in ATLAS. A complete description of the detector is given in Chapter III.



(a) (b)

Figure 3.13: *(a) One arm of the ZDC. (b) Schematic layout of the ALFA detector in the Roman pot.*

3.7.2 ZDC

An important quantity in heavy ion collisions is the centrality of the interaction. This quantity is strongly correlated to the number of neutrons produced in the very forward direction - the so called *spectator* neutrons. For this purpose ATLAS has been equipped with calorimeters to detect neutrons with $|\eta| > 8.3$. The ZDC [60] consists of four modules on each side of the interaction point. Each module is embedded in the TAN (Target Absorber Neutral) which is located at ± 140m from the IP, at the place where the straight-section of the beam-pipe is divided back into two independent beam-pipes (see 3.13(a)). Out of the 4 modules in each arm one is a electromagnetic module while the remaining three are hadronic modules. Each module is a sampling type calorimeter which consist of 11 tungsten plates mounted perpendicular to the beam direction. Two slightly larger steel plates have been installed in addition, on the front and back of the modules to assist in the initiation of particle showers. The active parts of the module is made of 96 quartz rods with a diameter of 1 mm. The rods are arranged such that all 11 tungsten plates are penetrated by each rod in the direction parallel to the beam, an forming 8×12 matrix. In order to read out the Cerenkov light created by shower products, all rods are bent 90° vertically and are viewed from above by multi-anode phototubes (MAPMTs) (see fig-

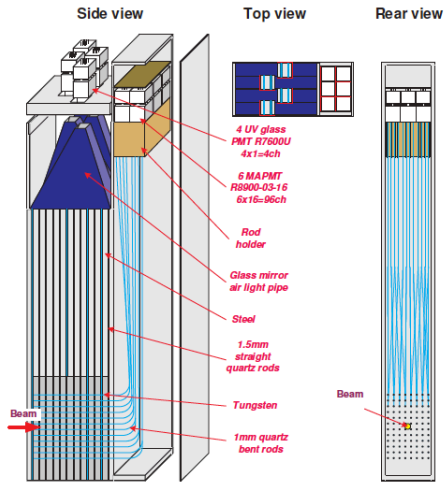


Figure 3.14: *Electromagnetic ZDC module. Beam impinges on tungsten plates at bottom of module, and showers [60].*

ure 3.14). In addition to the quartz rods, 1.5 mm quartz strips are mounted vertically between the tungsten plates and read out by photomultiplier tubes from above via air light guides. The purpose of the quartz strip is to improve the energy measurement done by the quartz rods.
The hadronic modules are similar to the EM modules with the only difference being the granularity of the readout. While in the EM modules each rod is mapped to a single pixel in the multi-anode photomultiplier, the hadronic modules map groups of four rods into conventional photomultipliers.

3.7.3 ALFA

The aim of the ALFA detector [61] is to determine the absolute luminosity by measuring elastic scattering at small angles. The amplitude of such processes is related by the optical theorem to the total cross section and thereby also to the absolute luminosity. The extremely small scattering angles (3 μrad) needed to make these measurements are smaller than the nominal beam divergence. This means that ALFA will only be able to perform measurements of the luminosity in situations where the beams have been prepared to meet certain conditions. Because of the small scattering angles needed to perform such a measurement, the beam emittance is has to be reduced.
In order to measure scattering angles of 3 μrad the detectors also have to be placed far away from the interaction point and as close as possible to the beam. In ATLAS this has been achieved by using a Roman-pot technique which allows the active detector volume to be moved close to the beam (see figure 3.13(b)). Positions as close as 1 mm to the beam can be obtained with the ATLAS Roman pot system making it possible for ALFA to detect particles at the required scattering angles. The Roman pots will be located $\pm$240 m away from the interaction point, and on each side there will be two Roman-pot stations separated by four metres. The sensitive area of the ALFA detector is made from scintillating-fibres stacked in ten double-sided modules. Each module has 64 square fibres with a width of 0.5 mm arranged in stereo geometry on both sides. The light from a traversing particle is read out on a module per module basis by multi-anode photomultipliers with a number of channels with match the number of fibers in each module.
During the 2010 data taking period only one side of the detector has been installed. The installation of the remaining parts of the detector will take place during the christmas shutdown of 2010.

3.8 Trigger and Data Acquisition systems

At LHC, the production cross section of interesting physics signatures such as Higgs production is not only expected to be rather low, but is also expected to be at least seven orders of magnitude lower than the cross section of minimum bias QCD events. This has two consequences: Firstly, the instantaneous luminosity at the LHC needs to be very high which is achieved by a short bunch separation (25 ns) and multiple interactions (~ 25) at each bunch crossing. Secondly, it is essential to be able to filter out the minimum bias events with a rejection factor of at least 10^7 while keeping $O(1)$ efficiency in the selection of interesting physics.

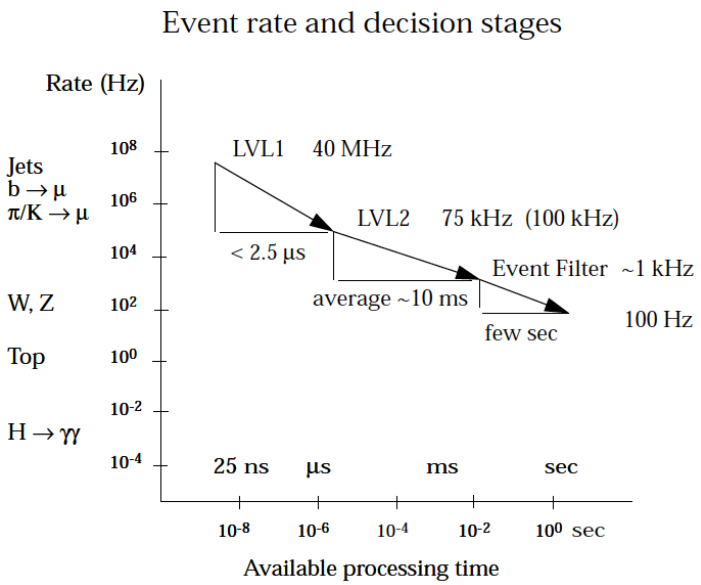


Figure 3.15: *The three levels of the ATLAS trigger and their event rates and processing times [28].*

At ATLAS this is achieved by employing a trigger system which is divided into three levels of event selection: Level-1 (LVL1), Level-2 (LVL2), and the Event Filter (EF). Each trigger level refines the decisions made at the previous level and, where necessary, applies additional selection criteria. The three levels of the trigger and corresponding processing times are shown in figure 3.15

3.8.1 Level 1

The main task for the LVL1 trigger is to select the bunch crossings which might contain interesting events. However with a brunch crossing rate of 25 ns this is a very challenging task which will become increasingly difficult as the luminosity increase. To overcome these difficulties the LVL1 trigger is based on a fast identification and processing of so-called *Regions-of-Interests* (RoI's). The RoI's are essentially geographical coordinates in η and ϕ , for which the LVL1 selection process has identified an interesting signature. The LVL1 trigger defines RoI's based on a selection of reduced-granularity information from a subset of detectors. For example, information from the Resistive Plate Chambers (RPC) and Thin-Gap Chambers (TGC) are used to identify high-p_T muons. In the same way, jets and τ-leptons are identified by the LVL1 trigger by using information from all calorimeter sub-systems.
The maximum LVL1 accept rate which the detector readout systems can handle is 75 kHz and the LVL1 decision must reach the front-end electronics within 2.5 μ s after the bunch-crossing with which it is associated. The overall decision of whether or not to accept an event at LVL1 is made by the Central Trigger Processor (CTP). The CTP bases its decision on all the available information within the RoI's which is matched to a set of trigger menus which can be programmed with up to 256 distinct items, each item being a combination of requirements on the input data. The trigger decision, together with the 40.08 MHz clock and other signals, is distributed to the detector front-end and readout systems via the Timing, Trigger and Control (TTC) system, using an optical-broadcast network

3.8.2 High Level Trigger: Level 2 and Event Filter

The starting points for the HLT are the RoI's provided by the LVL1 trigger. The HLT uses these areas and the full detector information to provide a trigger decision in a series of steps. Every step is meant to refine the information from the previous step by acquiring additional data from increasingly more detectors. The list of steps to be taken by the HLT for each physical signature is called a *trigger chain*. An important step of the HLT is called feature extraction. Here dedicated algorithms request detector data from within the RoI and attempt to identify features, e.g. a track or a calorimeter cluster. For all interesting signatures a second algorithm determines whether the identified feature meets a criteria (such as a shower shape, track-cluster match or E^T threshold) necessary to continue. In this manner every event can be rejected at any step of the HLT if no signatures remain viable at the following step. The full data set associated with the RoI is transferred only for those events which fulfill the complete LVL2 trigger selection criteria.
The LVL2 menus are designed to reduce the trigger rate to approximately 3.5 kHz, with an event processing time of about 40 ms, averaged over all events. The final stage of the event selection is carried out by the *event filter*, which reduces the event rate to roughly 200 Hz. The event filter uses offline analysis procedures on fully-built events to further select events down to a rate which can be recorded for subsequent offline analysis.

3.8.3 Data Acquisition system

The Data Acquisition system (DAQ) system handles the distribution of data between the different levels of the trigger system and ultimately to mass storage for the events that passed the full trigger selection. The different steps of the DAQ system are indicated on the right side of the block diagram in figure 3.15. Apart from the dataflow component the DAQ also provides Online software component. The Online Software system controls the overall experiment: it provides run control, configuration of the HLT and DAQ system and manages the mass storage. This component constitutes the interface point between the DAQ system and the Detector Control System DCS.

Chapter 4

Principles of Luminosity Determination

4.1 Introduction to luminosity

Inspired by the terminology used in astronomy, the word *luminosity* in experimental particle physics refers to the number of particles per unit area per unit time. Assuming that the intensity of the two beams are the same then the interaction rate is proportional to the luminosity. With other words, the event rate $R_X(t)$ for a given process X and the instantaneous luminosity, $L(t)$, are directly proportional to one another. The factor of proportionality that relates these two quantities is the cross section for the given process, σ_X:

$$R_X(t) = \sigma_X \cdot \mathcal{L}(t) \tag{4.1}$$

It is important to note that the luminosity by definition is independent of the process. Two completely independent physical processes should yield the same result when used to monitor the luminosity. This is an advantage, both in terms of systematic uncertainties but also in terms of a greater flexibility in the way that the luminosity can be measured.

For cross sections measurements at a collider experiment, the quantity of greatest significance is usually the number of selected events passing the final analysis cuts during a given running period $N_X^{observed}$. In this connection the integrated luminosity (L) which is the instantaneous luminosity integrated over the running period (T) is more commonly used:

$$N_X^{observed} = \sigma_X \cdot \varepsilon \cdot L = \sigma_X \cdot \varepsilon \cdot \int_0^T \mathcal{L}(t)dt \tag{4.2}$$

where ε is a general efficiency term combining the detector and trigger efficiency as well as the acceptance. Instantaneous luminosity is expressed in units of $cm^{-2}s^{-1}$, whereas integrated luminosity is expressed in units of cm^{-2}. The integrated luminosity is often given in units of *barn (b)* where one *barn* is equivalent to $10^{-24}cm^2$.

4.1.1 The Need for a Precise Luminosity Determination

The various physics analysis at ATLAS puts emphasis on the different aspects of the luminosity programs. Clearly, for cross section measurements, the requirement is to have as precise as possible a measurement of the integrated luminosity, since it is used to convert an observed number of events to a cross section. At the same time a precise measurement of the bunch by bunch luminosity may be needed to correct some physics measurement for the effects of pile-up. Even in a discovery analysis, which do not aim at measuring cross section, it is usually necessary to know the luminosity in order to normalize the background calculations.

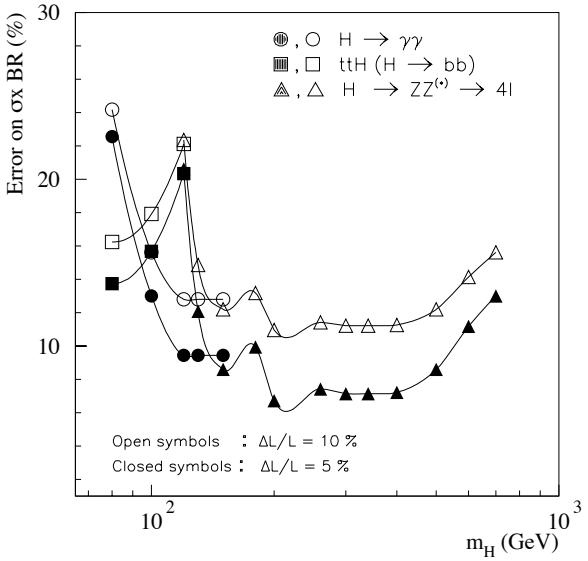


Figure 4.1: *Relative precision on the measurement of the Higgs-boson cross section ($\sigma \times BR$) for various channels, as a function of m_H, for various channels, assuming an integrated luminosity of 300 fb^{-1} [42]. The luminosity is assumed to be known to 10% (open symbols) or to 5% (black symbols).*

In terms of physics goals the main focus of ATLAS and CMS will be the search for the Higgs boson and signs of new physics. Depending on the decay channels, these processes are expected to have cross sections as low as a few tens of a femto-barn at LHC energies. As a result both ATLAS and CMS will require high running luminosities and accordingly the LHC has a design luminosity of $10^{34} cm^{-2} s^{-1}$, which corresponds to a factor of 100 increase on the luminosity obtained at the previous energy frontier accelerator - the Tevatron at Fermilab. Figure 4.1 shows how the expected uncertainty on the Higgs boson production cross section at LHC depends on the uncertainty of the luminosity measurement and the decay channel [42]. For instance for a Higgs mass of 140 GeV the expected uncertainty on the cross sections in the leptonic channel is expected to be 10 % for an uncertainty of 5% in the luminosity measurement. In fact in the mass region where the Higgs boson is expected to be discovered, the main source of systematic uncertainty on cross section measurements is given by the luminosity which sets a lower limit on the precision of the measurement.
At the end of the 2010 *pp*-run it is already the accuracy of the luminosity measurements that determines the accuracy of the cross sections measurement of W and Z bosons at 7 TeV.

4.2 Luminosity determination at the LHC

The luminosity $\mathcal{L}$ and also can be expressed in terms of beam parameters [62]:

$$\mathcal{L} = n_b f_r I_1 I_2 \int \rho_1(x,y)\rho_2(x,y)dxdy \tag{4.3}$$

where n_b is the number of colliding bunches, f_r is the machine revolution frequency, $I_{1(2)}$ is the number of particles per bunch in beam 1(2) and $\rho_{1(2)}(x, y)$ is the particle density in the transverse plane of beam 1 (2) at the interaction point. Assuming that there is no correlation between x and y, the particle densities can be factorized such that:

$$\mathcal{L} = n_b f_r I_1 I_2 \Omega_x(\rho_1, \rho_2)\Omega_y(\rho_1, \rho_2) \tag{4.4}$$

where

$$\Omega_x(\rho_1, \rho_2) = \int \rho_1(x)\rho_2(x)dx \tag{4.5}$$

is the beam overlap integral in the x direction (with an analogous definition for the overlap integral in the y direction).
Equation 4.5 can be rewritten [63] in terms of the parameters which are directly accessible from LHC:

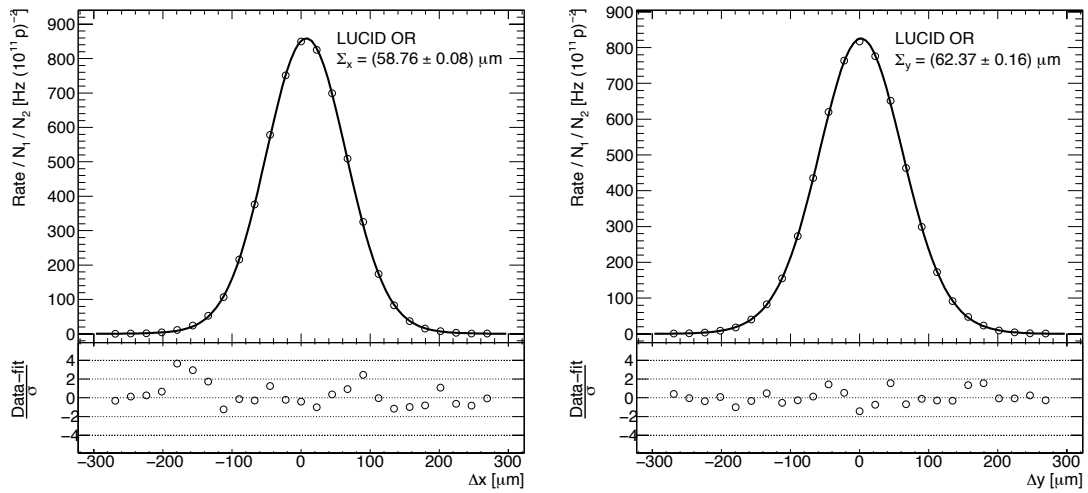
$$\mathcal{L} = F\frac{N_1 N_1 n_b f_r \gamma}{4\pi\beta^*\varepsilon} \tag{4.6}$$

where N_1 and N_2 are the number of particles in the bunches, γ is the relativistic factor for the colliding particles (i.e. E_p/m_p for the colliding protons at the LHC), ε is the emittance which describes the extent occupied by the particles of the beam both in space and phase space. The beta functions β^* describes the focusing properties of the magnetic lattice and F is a factor that takes into account the angle at which the beams cross each other. The design values of these factors at the LHC are given in table 2.1.
Of particular interest is the product $n_b \times f_r$ since it defines a fundamental time step of the LHC, namely the frequency at which two bunches cross at the IP of the various experiments. Any luminosity monitor which is meant to measure the luminosity for the individual bunch crossings must have a time resolution better than $n_b^{MAX} \times f_r \approx 30$ MHz to work at design luminosity. Another important time interval used in luminosity determination at ATLAS is the *Luminosity Block*.

Luminosity Block

"A luminosity block (LB) is a time interval, for which the integrated, dead-time- and prescale-corrected luminosity can be determined" [64]. From a practical point of view the length of a luminosity block should be long enough so that the data acquired in that period is sufficent for the luminosity determination. One requirement could be that the statistical error on the measured quantity should be smaller than systematic error. But in general the length of the luminosity block should be chosen in such a way that the instantaneous luminosity remains roughly constant during the course of the LB. It is known that the instantaneous luminosity of the LHC decreases exponentially with a time constant of $\mathcal{O}(6.28h)$ [25]. Under nominal conditions, this would mean that the luminosity would drop by 1 % over a time span of 10 minutes. Thus the size of the an LB in ATLAS should be at the order of minutes not to compromise the assumption of constant instantaneous luminosity within a LB. Under this assumption the delivered luminosity over the course of a luminosity block which spans n_{turns} beam turns, can be written as:

$$L_{LB}^{delivered} = 25 \text{ ns} \cdot \sum_{k=1}^{n_{turns}} \sum_{i=1}^{3563} \mathcal{L}_{(BCID=i)} \tag{4.7}$$



(a) (b)

Figure 4.2: *Results of a luminosity scan in the horizontal (a) and vertical plane (b) using the LUCID detector [65] [66]. The plots show the specific rate per* $10^{22}(protons/bunch)^2$ *as a function of beam separation. A Double Gaussian fit with a common mean is superimposed, together with the resulting values for* Σ_x *and* Σ_y *as defined in equation 4.9.*

where $\mathcal{L}_{(BCID=i)}$ is the instantaneous luminosity of the bunch with $BCID = i$. A detailed discussion of the luminosity determination and the effect of the detector and trigger is presented in [64].

4.3 Absolute Luminosity Measurement

In general a distinction is made between luminosity measurements and luminosity monitoring. Measurements via the methods described above give an absolute determination of the luminosity. Other methods may, however, be used to monitor the luminosity and can be calibrated using the absolute methods - for this reason luminosity monitor are often said to provide a relative measurement of the luminosity . Such relative luminosity measurements provide a convenient way to follow the luminosity evolution during a accelerator fill and also between different fills. The methods and concepts behind both absolute and relative luminosity determination will be discussed in the following sections.

4.3.1 LHC Machine Parameters - Van der Meer scans

To determine the luminosity by means of equation 4.8 is difficult since a good measurement of the lateral beam sizes is needed. One way to obtain reliable measurement of the beam sizes at the IP is to measure the beam profile in some place away from the IP and then extrapolate to the IP. The drawback of this method is that a good knowledge of the β^* function is needed for the extrapolation. Since the uncertainty of the β^* function can be as high as 10%, this sets a upper limit in the precisions at which the absolute luminosity can be determined using

this method. This uncertainty could possibly be reduced if the beam divergence at the IP can be measured.
Another way to measure the beams widths at the IP was originally proposed by Van der Meer in 1968 [67]. In this method the beam sizes can be determined by moving the two beams across each other and simultaneously monitor the relative change in counting rate. If the beam scans are performed in both the vertical and horizontal plane, the overlap integral in equation 4.5 (for example in the x direction) can be calculated as:

$$\Omega_x(\rho_1, \rho_2) = \frac{R_x(0)}{\int R_x(x)dx} \tag{4.8}$$

where $R_x(x)$ is the rate measured by a luminosity monitor detector during a horizontal beam scan when the beam separation is x. One can define Σ_x by the equation:

$$\Sigma_x = \frac{1}{\sqrt{2\pi}} \frac{\int R_x(x)dx}{R_x(0)} \tag{4.9}$$

In the case that $R_x(x)$ is a Gaussian, Σ_x coincides with the standard deviation of the rate distribution. By using the previous two equations, equation 4.4 can be rewritten as:

$$\mathcal{L} = \frac{n_b f_r I_1 I_2}{2\pi \Sigma_x \Sigma_y} \tag{4.10}$$

which is a general formula to extract luminosity from machine parameters by performing a beam separation scan. Equation 4.10 is in principle very general and does not dependent upon the actual shape of the experimental rate distribution during the separation scans. The assumption is made that there is no correlation between the particle density distributions in x and y. Figure 4.2 shows the counting rate versus a separation for the Van Meers Scan performed during the data taking period of 2010 [65]. A double Gaussian fit has been performed to extract $\Sigma_{x,y}$ of the distributions.
The main source of systematics to the luminosity determined from beam parameters is the uncertainty in the measurements of the beam currents. Other errors come from the relative centering of the two beams and systematic uncertainties related to the change of the beam emmitance during the scans. The total systematic uncertainty is estimated in [66] to be 11 % for the early LHC running.

4.3.2 Resonance counting

As suggested by equation 4.1 and 4.2, the absolute luminosity ($\mathcal{L}$) can be extracted from the measurement of a rate (R) of a theoretically well-understood process. After correcting for acceptance A, efficiency ε , and backgrounds B, a measurement of R can be directly translated into a luminosity measurement:

$$\mathcal{L} = \frac{R - B}{A \cdot \varepsilon \cdot \sigma} \tag{4.11}$$

Here the cross section of the process (σ) should be calculable to the required precision from theory or available from experiments. A limiting factor in terms of precision is that every aspect of the quantities in equation 4.11 must be well known. Due to the complicated nature of the partonic initial state at hadron collider, the list of processes which meets this requirement

is short. Besides having a dominant influence on the cross section, the theoretical knowledge of the production mechanism will also have an indirect impact on A and ε though the inherit uncertainty on the kinematical distributions. One of the main sources of systematic uncertainty in the cross section is the knowledge of the parton distribution functions (PDF) in the proton and of the partonic cross section. One type of processes where the theoretical uncertainties are relatively well constrained is the electroweak production of W and Z bosons. The cleanness of the leptonic decay channels combined with the well understood nature of the production mechanism make the potential sources of systematics in the luminosity measurement small. It is estimated that with current knowledge of PDF uncertainties and detector related effects, absolute luminosity can be determined from leptonic decays of W/Z bosons to about 14%. A study of the absolute luminosity determination using the production of Z^0 bosons will be presented in part V of this thesis.

4.3.3 Coulomb scattering amplitude

It is possible to obtain a measurement of the absolute luminosity via elastic scattering. In this method the total cross section and luminosity is deduced from a measurement of the differential elastic cross section $d\sigma_{el}/dt$ at small angles.
For elastic scattering, the amplitude can be written as a superposition of the Coulomb (f_c) and strong (f_s) amplitudes. The former dominates at small values of the momentum transfer $-t = (p\theta)^2$, where p is the beam momentum and θ the forward scattering angle. A simplified expression of the differential elastic cross section is [63]:

$$\lim_{t\to 0} \frac{d\sigma_{el}}{dt} = \frac{1}{L}\frac{dN_{el}}{dt}\Big|_{t=0} = \pi|f_c + f_s|^2 \simeq \pi\Big|\frac{2\alpha_{em}}{-t} + \frac{\sigma_{tot}}{4\pi}(\rho + i)e^{Bt/2}\Big|^2 \tag{4.12}$$

where α_{em} is the electromagnetic fine-structure constant, ρ is the ratio between the real and the imaginary parts of the forward elastic scattering amplitude and B is the nuclear slope for pp scattering. If the differential distribution dN_{el}/dt is measured over a large enough range, the unknown parameters σ_{tot}, ρ, B and L can be determined from a fit to the data.
Traditionally this type of measurements are carried out in the region of t where the strong amplitude is equal to the electromagnetic. Under nominal running conditions at the LHC this region is at $|t| = 0.00065\ GeV^2$ which corresponds to a scattering angle of 3.5 μrad. Due to the small scattering angle any measurement of the Coulomb amplitude requires detectors sitting a few millimeters from the actual beam. A set of Roman pot detectors called ALFA (previously discussed in section 3.7.3) will be installed in ATLAS to do luminosity measurements of this type. This measurement will only be made at low luminosity ($L = 10^{27} cm^{-2} s^{-1}$). The simulation of the ALFA detector with the proposed beam optics indicates that luminosity can be measured with a precision of 3% [61].

4.4 Relative Luminosity Measurement

The main task of any luminosity monitor at ATLAS is to provide a fast and reliable way to monitor any change in luminosity and beam conditions during the course of a run. A luminosity monitor must furthermore be able to precisely extrapolate a measurement of the absolute luminosity to any other running condition. Since the calibration point for a specific monitor might lie several orders of magnitude away from nominal LHC running conditions, it is crucial for a good luminosity monitor to maintain stability over many orders of magnitude in $\mathcal{L}$. A list of ATLAS luminosity monitors with their main features is reported in table 4.1.

	Pseudo-rapidity range	Luminosity range $[cm^{-2}s^{-1}]$	time resolution
LUCID*	$\|\eta\| \in [5.6, 5.9]$	$10^{27} \rightarrow 10^{34}$	BX
MBTS	$\|\eta\| \in [1.9, 3.8]$	$10^{27} \rightarrow 10^{33}$	
BCM	$\|\eta\| \in [3.9, 4.1]$	$10^{27} \rightarrow 10^{34}$	BX
LAr Calorimeter	$\|\eta\| < 5.0$	$10^{27} \rightarrow 10^{34}$	
Tile Calorimeter	$\|\eta\| < 1.7$	$10^{27} \rightarrow 10^{34}$	

Table 4.1: *Luminosity monitors of the ATLAS experiment. The $*$ denotes that LUCID has since the early 2010 data taking period been the preferred luminosity detector for ATLAS.*

The ideal luminosity monitor would be linear over the entire dynamical range of the LHC ($\mathcal{L} = 10^{27} cm^{-2}s^{-1} \rightarrow 10^{34} cm^{-2}s^{-1}$). The assumption of linearity for a given luminosity monitor can be tested with Monte Carlo simulations. Dedicated algorithms may be derived, based on these tests, to correct the raw detector response for non-linear effects. The derivation and performance study of such algorithms is presented in chapter 8.

Calibration procedure

The procedure to calibrate a relative luminosity monitor using an absolute measurement can be carried out in several different ways, but the ideas behind it, is to a large extent the same. The basic idea is to simultaneously measure the absolute luminosity and the rate of inelastic interactions R_{inel} by the relative monitor. In this way the rate from the relative monitor will be mapped directly to a value of the absolute luminosity and the conversion factor between the two luminosities is the calibration constant k_{cal}:

$$\underbrace{\mathcal{L}}_{\text{by absolute measurement}} = \frac{1}{\sigma_{inel}} \cdot \underbrace{R_{inel}}_{\text{by relative measurement}} = k_{cal} \cdot R_{inel} \tag{4.13}$$

where σ_{inel} is the total inelastic cross section. Taking the efficiency (ε_{inel}) and acceptance (A_{inel}) of the detector to the inelastic interactions into account, the expression above changes to:

$$\mathcal{L} = \frac{R_{LUCID}}{A_{inel} \cdot \varepsilon_{inel} \cdot \sigma_{inel}} \tag{4.14}$$

In principle all of the absolute methods mentioned in section 4.3 can be used in combination with one of the luminosity monitors in table 4.1. Not all combinations might be equally good

but the combination of the LUCID and ALFA detectors is expected to provide an accurate luminosity measurement. In this calibration scenario, LUCID will measure the rate of inelastic interactions and from the absolute luminosity determined by ALFA, LUCID will be calibrated so that a rate measured by LUCID corresponds to an absolute luminosity. With other words the product $A_{inel} \cdot \varepsilon_{inel} \cdot \sigma_{inel} = k_{cal}^{-1}$ will be calculated from a combined run with ALFA and LUCID. In this way LUCID can be used to measure luminosity without any knowledge of the inelastic cross section or the acceptance and efficiency of LUCID.
An alternative method to the one presented above is to use Monte Carlo simulations to determine the product $A_{inel} \cdot \varepsilon_{inel} \cdot \sigma_{inel}$ in equation 4.14. However, the uncertainty in the cross section is, at least at the start of LHC, expected to be large and so a calibration of the method using only simulations will not give a very precise result. To reduce the model dependent part of the uncertainties, the combined efficiency and acceptance can be measured by real data if an unbiased minimum bias trigger is available. The two latter methods are important since they provide the only means of calibration of the luminosity monitors in the absence of an absolute calibration. This was in fact the case in the early 2010 data taking period where all luminosity monitors were calibrated using Monte Carlo simulations. Result from this period will be presented in section 7.5 for the LUCID detector.

4.5 Summary

During the initial period of LHC operation, the absolute calibration procedure for LUCID will use calculations based on LHC machine parameters, initially determining luminosity to a precision of $\sim 10\%$. A more precise method of calibration will be obtained with the ALFA detector once it becomes operational. Here elastic Coulomb scattering is used to measure the absolute luminosity and thereby provide a calibration for LUCID with an uncertainty better than 5%. Alternative methods of calibration include monitoring rates of physical processes with a well-know cross section such as W/Z production [68].

Part III
The LUCID Detector

In ATLAS the luminosity is measured by several detectors. Among these is LUCID [59] (LUminosity measurement using Cerenkov Integrating Detector) which is the only detector dedicated primarily to monitoring the luminosity online. In Section 5.1 the goals of LUCID are presented. A detailed description of the design and layout of the detector will be given in section 5.2 and the chapter will be concluded with a discussion of the readout system in section 5.3.

Chapter 5

Detector description

5.1 Goal of the detector

The luminosity is traditionally monitored at hadron colliders using dedicated scintillation counters placed in the forward direction. The working principle of such detectors is to determine the luminosity from rate of empty bunch crossing. The use of these kind of detectors is limited to situations where the luminosity and the level of radiation is expected to be low. At the LHC design luminosity, most bunch-crossings will result in multiple pp interactions, so additional techniques have to be employed. The luminosity at ATLAS is therefore not only monitored by counting the fraction of empty or filled bunches but also by measuring the number of pp-interactions per bunch crossing - the so-called μ value. The luminosity per bunch crossing ($\mathcal{L}_{BX}$) can be found if μ and the cross section is know since $\mu = \sigma \times \mathcal{L}_{BX}$ (equation 4.1). The proportionality factor is now called the bunch crossing luminosity which essentially is the luminosity integrated over the time of a single bunch crossing[1].
The most frequent process to occur, in pp-collisions at high energies, is inelastic scattering resulting in a large particle multiplicity in the forward direction. This means that any luminosity monitor at ATLAS has to be based on a radiation hard design with a fast response in order to be able to monitor the luminosity also for individual bunch crossings. LUCID [59] meets these requirements with a design based on the principle that the number of interactions in a bunch-crossing μ is proportional to the number of particles detected in the detector. LUCID is therefore able to monitor the luminosity $\mathcal{L}_{BX}$ by measuring μ.

The main requirements to LUCID as a luminosity monitor are:

- Good acceptance for detecting pp collisions;
- Pointing capability in order to suppress signals from background events;
- High enough time resolution to separate tracks coming from different bunch-crossings;
- Radiation hard readout electronics.

[1] methods how to determine μ will be discussed in greater detail in chapter 8.

LUCID is based on a preexisting design developed by the CDF collaboration [69]. The main detector elements are gaseous Cerenkov tubes installed in the forward direction on each side of the interaction point. A gaseous Cerenkov radiator fulfill the above requirements since it is radiation hard and the Cerenkov light is emitted promptly when a charged particle passes the radiator. The main challenge, however, in using this type of detector at the LHC is the much higher radiation and background levels as will be addressed in the next section.
One consequence of this design is the inability to provide an absolute luminosity measurement and LUCID is therefore primarily a relative luminosity monitor. This means that LUCID has to obtain an absolute calibration in order to measure the full LHC luminosity. Potentially, LUCID could also be used for diffractive studies, for example as a rapidity-gap veto or as a tag for a diffractive signal [70].

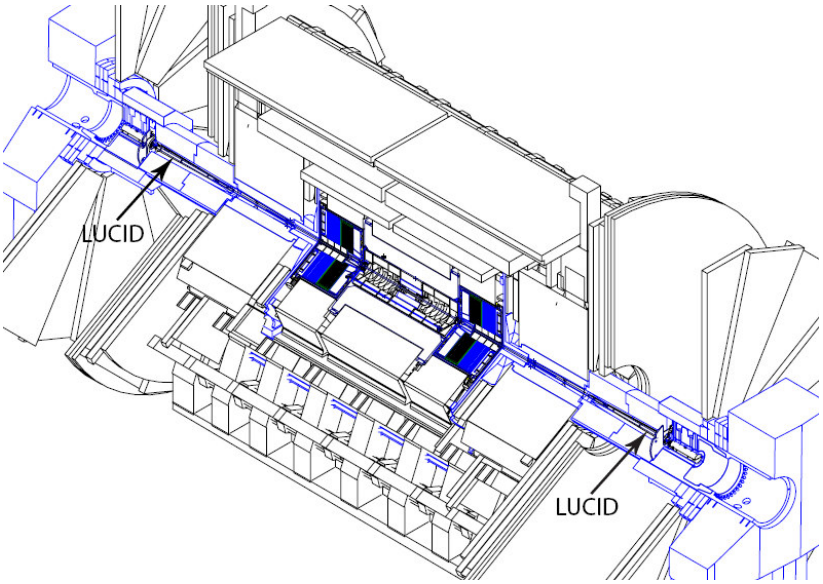
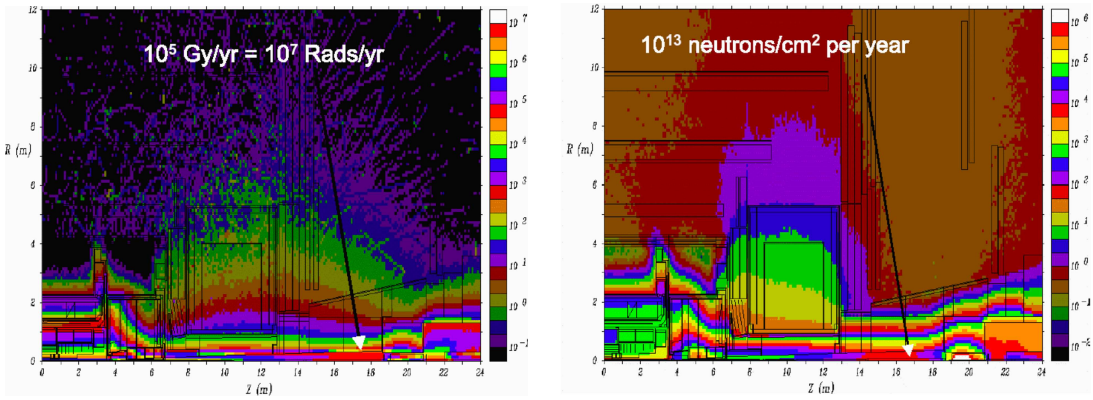


Figure 5.1: *Location of LUCID in ATLAS.*

5.2 Design and working principle

The LUCID detector consists of two modules installed in each end-cap region of ATLAS, 16.7m from the interaction point. Each module is installed in the available space between the beam pipe and the forward shielding giving LUCID a pseudo-rapidity coverage of $|\eta| \in [5.4, 5, 9]$. A schematic representation of the location of the two LUCID modules is given in figure 5.1. In that region the radiation hardness of the detector and its readout is an important issue. At design luminosity the total dose per year seen by LUCID will be at the order of 7 Mrad per year (see figure 5.2). For this reason it has been decided to split the operation of the LUCID project up into two phases, each with its own dedicated detector design. In the initial phase with a maximum instantaneous luminosity at the order of $10^{33} cm^{-2} s^{-1}$, LUCID will be operated in Phase I. Later a more radiation hard detector will have to be designed and installed.



(a) (b)

Figure 5.2: *Simulation of the radiation levels in a full Atlas quadrant [71]. (a) Ionizing radiation (b) The neutron flux ($E_n > 100keV$). The approximate dose in the region of LUCID is indicated in the plots.*

5.2.1 Detector design

Each of the two LUCID modules consists of 20 mechanically polished aluminum tubes arranged around the beam pipe. The tubes are 1.495 m long with an inner radius of 7 mm and a thickness of 1 mm. Sixteen of the twenty tubes are mounted in two rings with eight tubes in each at a radial distance of 96.3 mm and 114.7 mm from the beam pipe. In order to suppress background (see section 5.2.2) the tubes are pointing towards the interaction point giving the tubes in the two rings an angle with respect to the beam of $\theta_{ring1} \approx 0.33°$ and $\theta_{ring2} \approx 0.39°$. The remaining 4 tubes are placed in between the two rings and are likewise made to point towards the interaction point. The full set of 20 tubes is placed in a light-weight aluminum gas vessel which ensures that the tubes are filled with C_4F_{10} at a constant pressure of 1.1 bar. A schematic side view of a LUCID module with its tubes is given in figure 5.3.

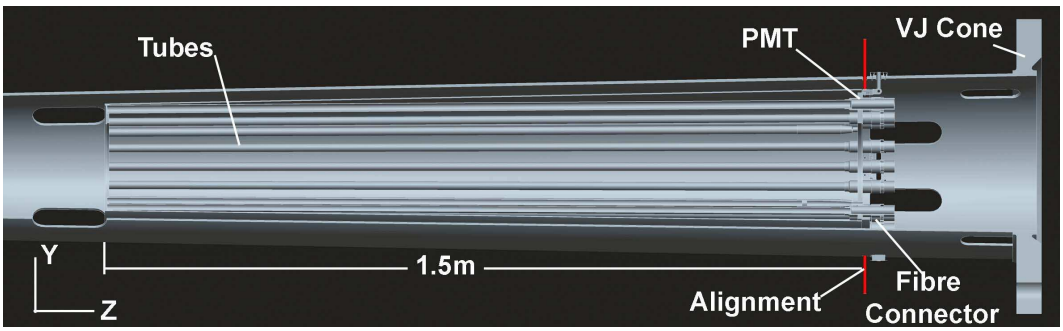


Figure 5.3: *Schematic side view of a LUCID module.*

The reason why C_4F_{10} was chosen as a radiator is that it provides one of the highest indexes of refraction ($n = 1.00137$) available for a commercially produced non-flammable gas. The high index of refraction results in large momentum thresholds for charged particles to produce Cerenkov light. The thresholds for electrons and pions are 9.3 MeV and 2.7 GeV respectively

making the choice of C_4F_{10} gas as a radiator an additional feature to the suppression of soft background. C_4F_{10} also has a good transparency for photons in the UV region. Since this is the region where most of the light is emitted, only small losses of Cerenkov photons in the gas itself is expected.

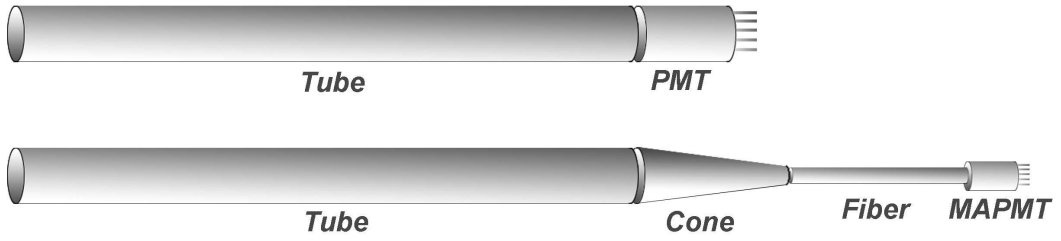


Figure 5.4: *A sketch of the two types of readout techniques used at LUCID. (top) A Cerenkov tube read out by a PMT. (bottom) A Cerenkov tube read out by a combination of a light cone, optical fibers and a MAPMT.*

The light produced in the Cerenkov tubes is read out by two different techniques. For the sixteen tubes placed in the two rings the Cerenkov light is read out by Photo-Multiplier Tubes (PMT) mounted directly on the aluminum tubes themselves. In order not to loose parts of the light signal, the PMTs have a diameter which matches exactly the diameter of the tubes (14 mm). The thickness (1.2 mm) of the quartz window in front of the PMT is furthermore optimized to provide a uniform detection efficiency[2]. The four remaining tubes are read out with MultiAnode Photo-Multiplier Tubes (MAPMT) via optical fiber bundles. This type of read-out is meant to serve as a testbench for the Phase II design where the increase in radiation doses makes the use of a direct coupling of photomultipliers to Cerenkov tubes unfeasable. A sketch of the two types of readout techniques used at LUCID is given in figure 5.4. A cut-away view of a LUCID module with the PMTs mounted is shown in figure 5.3 and the main design parameters are given in table 5.1.

5.2.2 Detection principle and background suppression

As mentioned above, LUCID detects charged particles by means of the light emitted in Cerenkov tubes. Cerenkov light is emitted when a charged particle traverses a material with a velocity v larger than the speed of light in the medium c/n [72]. With the given choice of radiator gas in LUCID, Cerenkov light is emitted from a charged particle above the momentum threshold, in a cone with an average angle $\sim 3°$ with respect to the particle trajectory (see figure 5.6). The Cerenkov light travels down the tube with multiple reflections of the inner tube surface. Taking the tube dimensions (see table 5.1) into account, it can be shown that a Cerenkov photon on the average makes about 3 reflections before being collected by the PMT. The Cerenkov light is emitted continuously over the full length of the particle trajectory in the radiator. This means that it is possible to provide a background suppression by pointing the Cerenkov tubes at the interaction point. Prompt particles coming from the IP (primaries) will traverse the full length of the counter and generate a large signal in the PMT. Particles originating from secondary interactions of prompt particles in the detector material and beam

[2]Details regarding the conversion of Cerenkov light into electronic signals will be given in chapter 6 where the simulation of LUCID is addressed.

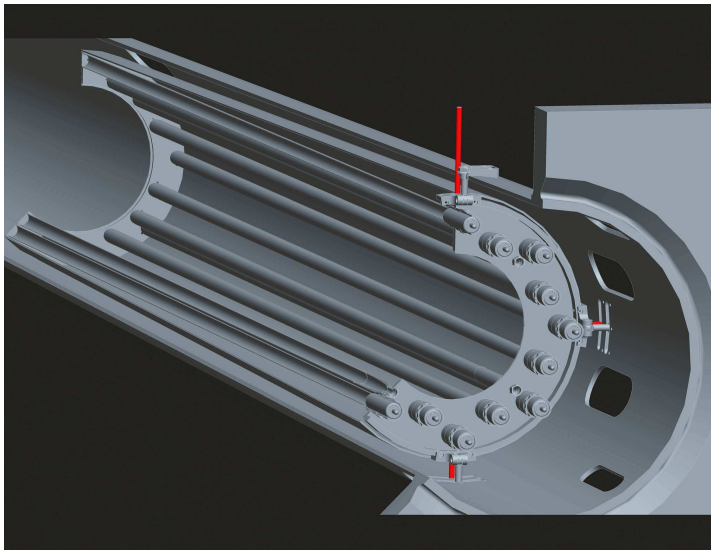


Figure 5.5: *Cut-away view of LUCID, viewed from the downstream end (Looking at the direction of IP).*

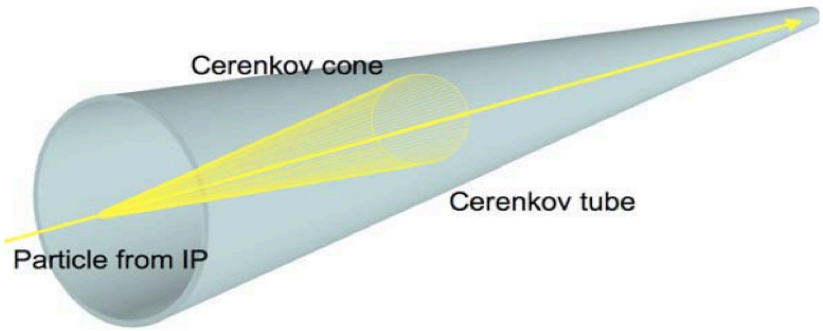


Figure 5.6: *Schematic view of a charged particle entering a Cerenkov tube and emitting light.*

Gas vessel		
	Distance from the IP [mm]	16715.5
	Module length [mm]	1532
	Module inner radius [mm]	85
	Module outer radius [mm]	125.15 (min), 147 (max)
	Module bulkhead thickness [mm]	3.2
	Radiator Gas	C_4F_{10}
	Working pressure	1.1 bar
Cerenkov tubes		
	Tube length [mm]	1495
	Tube radius [mm]	7.0
	Tube thickness [mm]	1.0
	Radial distance Tube-Beam [mm]	96.3 (ring1) 114.7 (ring2)
	PMT window thickness [mm]	1.2
	PMT radius [mm]	7.0
Cooling system		
	Cooling system radius [mm]	78
	Cooling system thickness [mm]	2

Table 5.1: *Major Design Parameters of LUCID.*

pipe (secondaries) are often softer and will traverse the counters at larger angles and with shorter path lengths (see figure 5.7). In addition, the light from these particles will also suffer from a larger number of reflections.

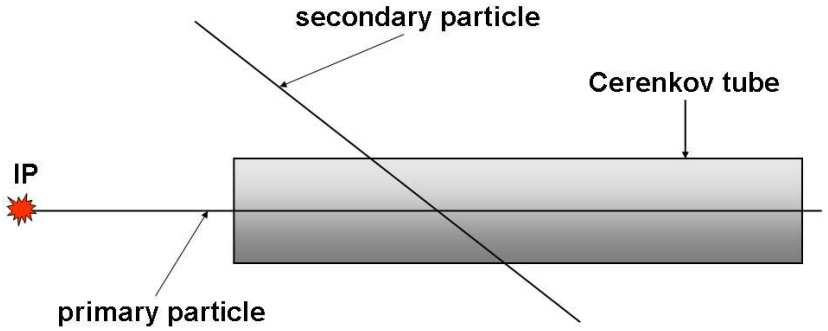


Figure 5.7: *Comparison between the path travelled by a primary and a secondary particle.*

The signals from these secondaries are therefore usually significantly smaller than those from the primaries and can be discriminated against by using suitable amplitude thresholds in the electronics and in the offline data analysis. This is not possible with scintillation counters where it would be impossible to distinguish the signal from primary particles originating at the IP and a secondary particle produced in the material between the IP and LUCID. As a consequence all background events, including background from the beam, will be treated as *pp*-collisions and will result in a wrong estimate of the luminosity.
Another advantage that Cerenkov detectors have over scintillation counters is the lack of a

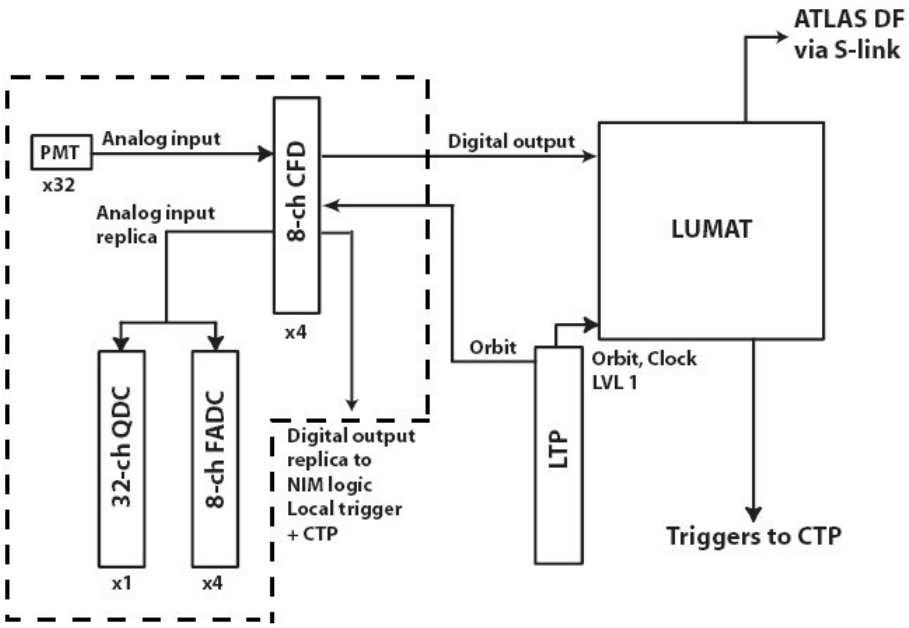


Figure 5.8: *Schematic diagram of the LUCID readout system [73]. The dashed line shows the components which are relevant to the local stream of data.*

Landau tail. This means that it is in principle easier to determine the number of particles which have entered a Cerenkov tube by using pulse-height measurements (particle-counting mode). The probability that several particles enter the same tube is, however, quite low for the LUCID design phase I, typically a few percent at a luminosity of $10^{33} cm^{-2} s^{-1}$ and even smaller at lower luminosities. As will be shown in chapter 8, a measurement consisting in counting only the number of tubes with a signal above a preset threshold (hit-counting mode) provides a measurement for online monitoring with an acceptable systematic error.

5.3 Electronics and readout system

At the photocathode of each PMT all Cerenkovs photons are converted into *photo-electrons (p.e)* with a probability given by the quantum efficiency of the PMT. The relative weak signal from the photo-electrons is then amplified by using a series of secondary emission electrodes or *dynodes* to produce a measurable current at the anode of the PMT [47]. The current is integrated over time and send to a Front End (FE) board placed 10 meters away from the detector. Here the signals are amplified and passed on to a Constant-Fraction Discriminator (CFD), which registers a hit each time the PMT signal is above a pre-set threshold. At this stage the signals are duplicated with one copy being sent to a Charge to Digital Converter (QDC) for measurements of the amplitude, while another copy is sent to a Flash-ADC (FADC) for both amplitude and timing measurement. The logical OR of all the CFD signals provides a trigger which allow the event to be written into a local data stream. This means that if a single CFD has a signal above threshold then the full information from all the QDC and FADC units are flushed into a local data stream and later stored to disc. Figure 5.8 shows a layout of the LUCID readout system. The local stream of data is independent of the global

ATLAS data stream and is mostly meant for fast data quality monitoring. As will be shown later in the thesis, the information from the local data stream can also be used for an offline determination of the luminosity (see section 8.6). In addition to the local stream of data, the outputs from the CFDs are also propagated to the global ATLAS data stream in terms of hit patterns. The link between the local LUCID readout electronics and the global ATLAS TDAQ system is called the LUMAT (LUMinosity Algorithm and Trigger) card.

5.3.1 The LUMAT card

As the name indicates, the LUMAT card has two main functions: to provide the ATLAS trigger system with relevant information and to calculate the online luminosity.
Since the LUMAT card is synchronized with the ATLAS clock, it is able to send information to the CTP every bunch crossing. The type of information sent to the CTP is the hit pattern telling the CTP exactly which tubes where hit within the current bunch-crossing. The CTP sends back the LVL1 trigger decision based on this information together with similar signals from other subdetectors. If the event is accepted LUMAT sends the hit pattern to the main ATLAS data flow. The LUMAT card also holds the possibility to implement luminosity algorithms directly in the firmware making it possible to determine the luminosity per bunch. The LUMAT card can implement up to four independent luminosity algorithms for all bunch crossings. Each algorithm calculates the luminosity by using a set of 3564 scalers, one for each bunch in the beam. A given scaler is reset by the start of each run and incremented when the specific algorithm registers a hit in the corresponding bunch crossing based on the hit patterns sent to the LUMAT card by the CFDs. Since the the four algorithms are implemented directly on the LUMAT card the results are unaffected by the busy conditions and dead-times of the TDAQ[3]. The data formats and streams used by LUCID is further discussed in section 7.2.

5.3.2 Calibration

The PMT signal charge is as mentioned in section 5.3 measured in units of QDC counts. A QDC count is in principle an arbitrary unit that is proportional to the charge. In order to establish the exact relation between QDC counts and photo-electrons, the detector must be calibrated. The process of calibration is divided in two separate steps. The first step is to find the noise level of each PMT - the socalled pedestal measurement.
The pedestal is found by letting the detector collect data in a period where there is no beam in that LHC. In this way it is possible to sample the charge distribution with no light in the Cerenkov tubes. The width of the pedestal is expected to be small but a sizable contribution from dark current processes widens the distribution considerably as can be seen from figure 5.9(a).
The second step of the calibration procedure is to measure the number of QDC counts from a single photo-electron [74] . For this purpose each Cerenkov tube has been equipped with a LED capable of shining monochromatic light from the front end of the tube in the direction of the PMT. The number of photo-electrons produced when a the LED light hits the PMT will be Poissonian distributed and is adjusted to have a mean of 1 photo-electron. This means that after the contribution from the pedestal, the largest contribution to the QDC spectra

[3] a "busy condition" can occur when an event is triggered and the gate is closed. Dead time in this context refers to a 2 ms hold in the TDAQ due a ATLAS wide reset every 5 sec.

will be from the production of a single photo-electron as can be seen from figure 5.9(b). From 5.9(c) it can be seen that also contributions from a higher number of photo-electrons are non-negligible . The calibration constant is obtained by fitting the single photon spectrum to extract the difference in QDC counts between the mean of the pedestal and the single photo-electron peak. Figure From 5.9(d) shows such a fit in a situation where the calibration constant is roughly 15 QDC counts per photoelectron.

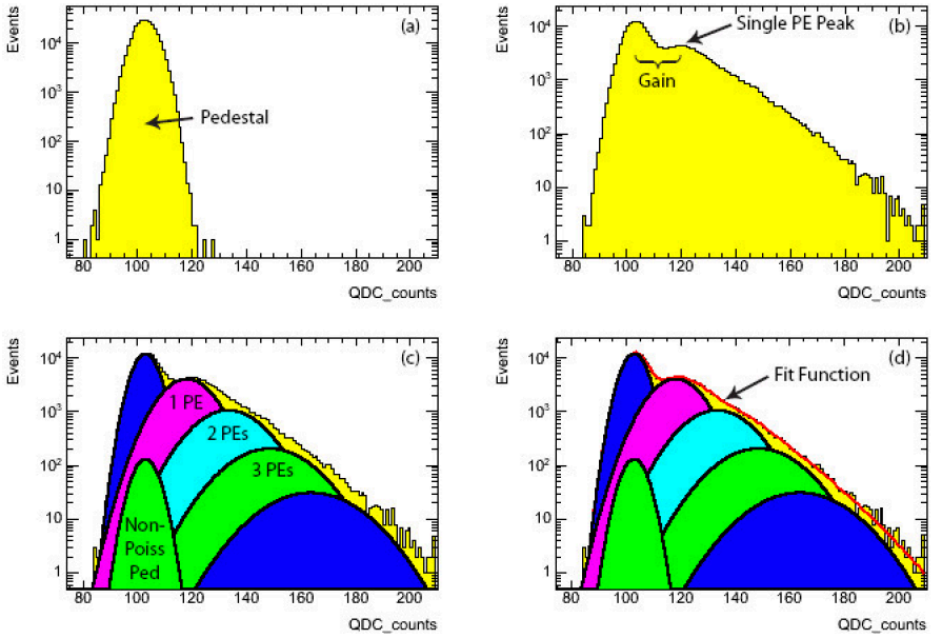


Figure 5.9: *(a) A pedestal distribution. (b) A single photoelectron spectrum . (c) A multiple photoelectron spectrum. (d) A multiple photoelectron spectrum with the calibration fit function superimposed [73].*

Chapter 6

Simulation of LUCID

One of the major challenges in designing and analyzing data from an experiment like ATLAS is to relate the observed quantities to the underlying physics. Due to the complexity of this process it will inevitably be necessary to rely on realistic and trustworthy Monte Carlo simulation. Not only to simulate the physical final states but also to simulate the often complicated detector response allowing for a detailed comparisons with data.
The simulation of events proceeds in several steps: For physics studies the first step is the phenomenological simulation of the hard physics processes which occur in the interactions and the resulting semi-/stable particles emerging from the interaction point. This step of the simulation chain is often referred to as the *generator step* and is usually not specific to any given experiment. It will be driven by certain assumptions regarding the parameters of both established particles and new physics and should be based on the latest theoretical models. The nature of this step in the simulation dictates that the level of realism in the output is limited by the level of theoretical understanding of a given process. At hadron colliders this means that the uncertainties of QCD will unavoidably be present in this step of the simulation in terms of uncertainties in the knowledge of parton density functions and in the process of hadronization.
The second step in the simulation chain is to simulate the passage of the generated particles through the different detector elements and the in resulting response. To do so, a precise geometrical description has been implemented for each detector in ATLAS. Such a description includes a description of both the active material of the detectors as well as the passive parts such as support structure and shielding. For interactions with active material - i.e. some sub-detector volume, the position, time and energy deposit is recorded as a "simulation hit" (simhit). In the case of LUCID, the active material is defined as the PMT window which will be discussed in greater detail below. Apart from propagating tracks through the detector, the detector simulation also takes care of decaying any long lived particles on the way. For the propagation, detailed magnetic field- and detector geometry maps are utilized, so that the direction of each particle in a given step is calculated based on the initial particle momentum and the local fields (electrical or magnetic). Depending on the material and particle, the cross section for all possible interactions with the material is calculated, and based on random draws, it is decided whether or not some given interaction takes place in the given step. In ATLAS the simulation step is handled by dedicated software tool such as the GeoModel [75] for the detector description and GEANT4 [76] for particle propagation.

The final step of the simulation chain is the *digitization step* where the simulated signals are transformed into a realistic digitized output as it would appear coming directly from the front-end electronics. This part of the simulation is specific to the given subdetector and need to take into account all the different aspects of signal processing. This means that the digitization step usually involves both simulation of physical effects such as electron multiplication in the PMT dynode chain as well as signal shaping and noise sources. The digitalized data are then converted to Raw Data Object (RDO) format before they are passed to the reconstruction process, where the responses of different detector parts are combined to determine the track of the particles, identify particles, calculate their 4-momentum, etc.
The following sections describe the simulation of LUCID step by step, starting with section 6.1 which illustrates the detector description as it is implemented in ATLAS software framework. Sections 6.2 and 6.3 will be dedicated to a study of the detector response of LUCID while the simulation of front-end electronics is delegated to section 6.4. Specific electronic issues such as simulation of the amplification chain and noise generation are also addressed in this section. The performance of LUCID in the 2010 data taking period will be discussed in chapter 7.
The analysis performed in the following sections is to a certain extent based on the ideas presented in [77].

6.1 Detector desciption

The general layout of LUCID in the simulation is in many ways the same as in the real detector. All the major parts of the detector such as the vessel, radiator, tubes, optical surfaces, PMTs and cooling system are included in the simulation. However smaller elements such as bolts and cabling are not included in the detector description. This has been done are as compromise to minimize the required human and computer resources while still providing a realistic detector description.

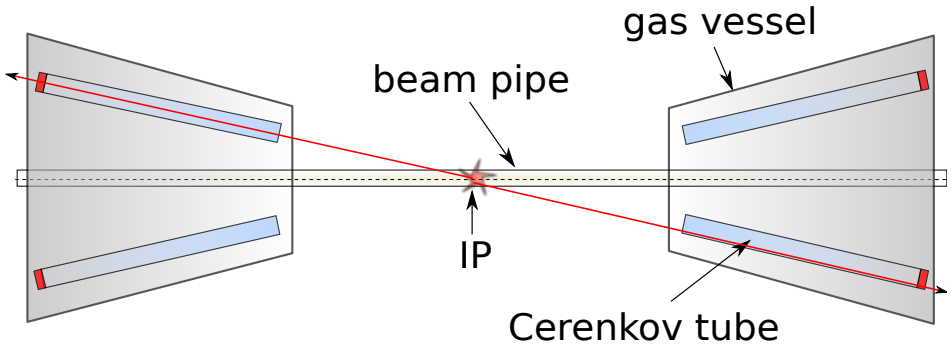


Figure 6.1: *A schematic drawing of the two LUCID modules illustrating the pointing geometry of the Cerenkov tubes. (Not to scale). The two red lines are meant to show two primary particles being created in the IP and afterwards traversing the full length of a Cerenkov tube.*

Since the design of LUCID has already been discussed in section 5.2 only issues in which detector description differs from the actual design will be addressed here. Figure 6.1 shows a very simplified sketch of the LUCID detector description including the two modules and a few Cerenkov tubes. Figure 6.2 illustrates the baseline design of a single Cerenkov tube as

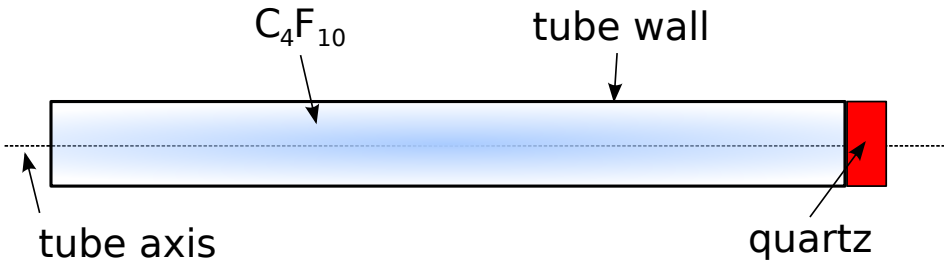


Figure 6.2: *Geometrical description of the Cerenkov tube (Not to scale).*

it is implemented in the detector description. The PMT is simulated with a thin quartz disc matching the transversal dimension of the tube. The photo-cathode and the chain of dynodes inside the PMT are not included in this step of the simulation but will be added later when the simulation of the front-end electronics is discussed.
A photon crossing the surface of the window is detected with a probability corresponding to the quantum efficiency provided by PMT manufacturer Hamamatsu. The simulation of the PMT quartz window is crucial since it acts as a source of Cerenkov light, in addition to the main gas radiator. All relevant parameters used to describe the detector geometry are listed in Table 5.1.

6.1.1 Cerenkov light emission

Cerenkov radiation is electromagnetic radiation emitted when a charged particle passes through an electrically polarizable medium at a speed greater than the speed of light in that medium [72]. Electrons in the atoms of the medium will be displaced, and the atoms become polarized by the passing EM field of the charged particle. Photons are emitted as the electrons of the medium restore themselves to equilibrium after the disruption has passed. In normal circumstances, these photons destructively interfere with each other and no radiation is detected. However, when a disruption which travels faster than light is propagating through the medium, the photons constructively interfere and intensify the observed radiation. For a particle to travel faster than the speed of light in a given medium its velocity must be above a threshold given by:

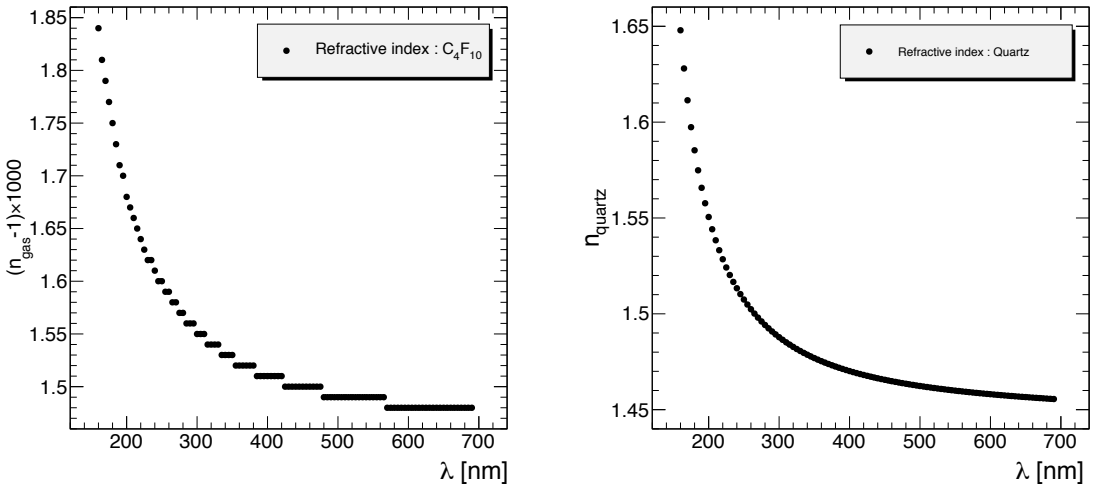
$$v > v_{th} = \frac{c}{n} \rightarrow \beta = \frac{v}{c} > \frac{1}{n} \tag{6.1}$$

where n is the refractive index of the medium which in this case is called a *radiator*. In particle physics it is often more convenient to consider the energy of a particle than the velocity. In this case the threshold in velocity can be reformulated as a threshold in energy:

$$E_{th} = \gamma m_0 c^2 = \frac{m_0 c^2}{\sqrt{1 - \left(\frac{v}{c}\right)^2}} > \frac{m_0 c^2}{\sqrt{1 - \left(\frac{1}{n}\right)^2}} \tag{6.2}$$

where m_0 is the rest mass of the charged particle. In C_4F_{10} and (quartz) this translates into a energy threshold of 9.3 MeV (0.7 MeV) for electrons and 2.7 GeV (190 MeV) for pions. For charged particles above the energy threshold, Cerenkov light will then be emitted in an angle which is given by the refractive index of the radiator:

$$\cos\theta_C = \frac{1}{n\beta} \tag{6.3}$$



(a) (b)

Figure 6.3: *The refraction index of C_4F_{10} (a) and quartz (b) as a function of the wavelength of the emitted Cerenkov light.*

The emission angle is a key quantity in the design of LUCID, since a certain choice of radiator will put certain constrains on the quality and layout of the Cerenkov tubes. For instance a combination of a radiator with a high refractive index and Cerenkov tubes in a material with low reflective power is less favorable. In such a situation θ_C will be large and the emitted Cerenkov photons will in general tend to be reflected on the tube walls many times before being detected by the PMT. If also the reflective power of the tube surface is low then photons are more likely to get absorbed and as a consequence the light yield from a primary particle is severely reduced. Since it is very difficult to make and maintain a material with reflective power close to 100 %, a radiator with low refractive index can be chosen instead. This would mean less reflection of the light on the tube wall and consequently less reduction of the light and thereby larger signal in the PMT. The reflectivity of the Cerenkov tube will be discussed further in the next section (Section 6.1.2).
The refractive index of a gas is a function of the emitted photon energy E [eV], the pressure P [bar] and the temperature T [kelvin] of the gas [78]. In the case of C_4F_{10} n is given by:

$$n_{C_4F_{10}}(E) = \sqrt{\frac{2\delta+1}{1-\delta}} \quad \text{where} \quad \delta = \delta(E,P,T) = \frac{KP}{T\Big(1-\Big(\frac{E}{E_0}\Big)^2\Big)} \tag{6.4}$$

where the constants take the values $E_0 = 17$ and $K = 0.25938$. For solids such as quartz, the refractive index can be calculated with a three term Sellmeier equation considering quartz as an optical glass:

$$n^2_{quartz}(E) = 1 + \sum_{i=1}^{3} \frac{B_i}{C_i^2 - E^2} \tag{6.5}$$

with $B_1 = 46.41, C_1 = 10.666, B_2 = 228.71, C_2 = 18.125, C_3 = 0.014$ and $B_3 = 0.125$. The values of $n_{C_4F_{10}}$ and n_{quartz} which are used in the simulation are shown in figure 6.3 as a

function of the photon wavelength.
Once the refractive index for both C_4F_{10} and quartz is known as a function of the Cerenkov light wavelength it is possible to calculate how many photons are emitted on average by a primary particle traversing LUCID. The average number of photons emitted per unit of radiator length (L) in the wavelength range $[\lambda_1, \lambda_2]$ is approximately given by the following formula [72] in the case where $L >> \lambda$:

$$\frac{dN}{dx[nm]} = 2\pi\alpha \sin^2\theta_C \int_{\lambda_2}^{\lambda_1} \frac{d\lambda}{\lambda^2} = 2\pi\alpha\Big[1 - \Big(\frac{1}{n\beta}\Big)^2\Big] \int_{\lambda_2}^{\lambda_1} \frac{d\lambda}{\lambda^2} \tag{6.6}$$

For a constant refractive index of 1.00149 for C_4F_{10} and 1.47 for quartz, a relativistic particle ($\beta \approx 1$) traversing the full length of a LUCID Cerenkov tube along its axis will emit in the order of 990 photons in the gas and 140 in the quartz (see table 6.1). These numbers are obtained assuming that photons are emitted in a wavelength range between 160 to 700 nm and that the pressure and temperature of the gas in the tube is $P = 1.1$ bar and $T = 293°$.

	$\langle n \rangle$	θ_C [°]	$E_{th}(e)$ $[MeV]$	$E_{th}(\pi^{\pm})$ $[MeV]$	L $[nm]$	N_{ph}
C_4F_{10}	1.00149	3.1	9.3	2700	1495	990
Quartz	1.47	46.8	0.7	190	1.2	140

Table 6.1: *Main simulation parameters used to model Cerenkov photon emission inside LUCID.*

Estimations like the one above are important since they are used along with test-beam data to optimize the electronic threshold needed to define a hit in the detector. However, just estimating the average number of Cerenkov photons produced by a charged particle is not enough. Further issues like the reflectivity of the inner tube surface and the quantum efficiency of the PMT are important in order to get a realistic simulation of the signal's size and shape.

6.1.2 Light propagation and detection

The Cerenkov photons generated in the tubes by a traversing particle have a typical emission angle of $\sim 3°$. Since the diameter of the tubes is small compared to the length, each photon will have a certain probability to hit the tube walls before reaching the PMT. When a Cerenkov photon meets the tube walls it will have a certain probability to be reflected instead of being absorbed. This probability is called the *reflectivity* and is given in figure 6.4(a) for the tubes in LUCID. A typical aluminum surface reflectivity curve as a function of the photon wavelength can be found in [47]. This curve has been rescaled to match a bench measurement performed with red light lasers.

Depending on the position and the angle of the incoming particle, multiple reflections might occur before photons are detected as illustrated in figure 6.5. The average number of light reflections inside the tube is 2.8.
Apart from the absorption on the tube walls, Cerenkov photons can also be absorbed in the C_4F_{10} gas itself. The absorption of photons in the gas is likewise wavelength dependent an has also been implemented in the detector description. In the implementation it has been assumed that the absorption length of photons in C_4F_{10} is similar to that of Isobutane [78] (see figure 6.4(b)). Here the gas absorption length is around 5.5 m in the wavelength from 650 to

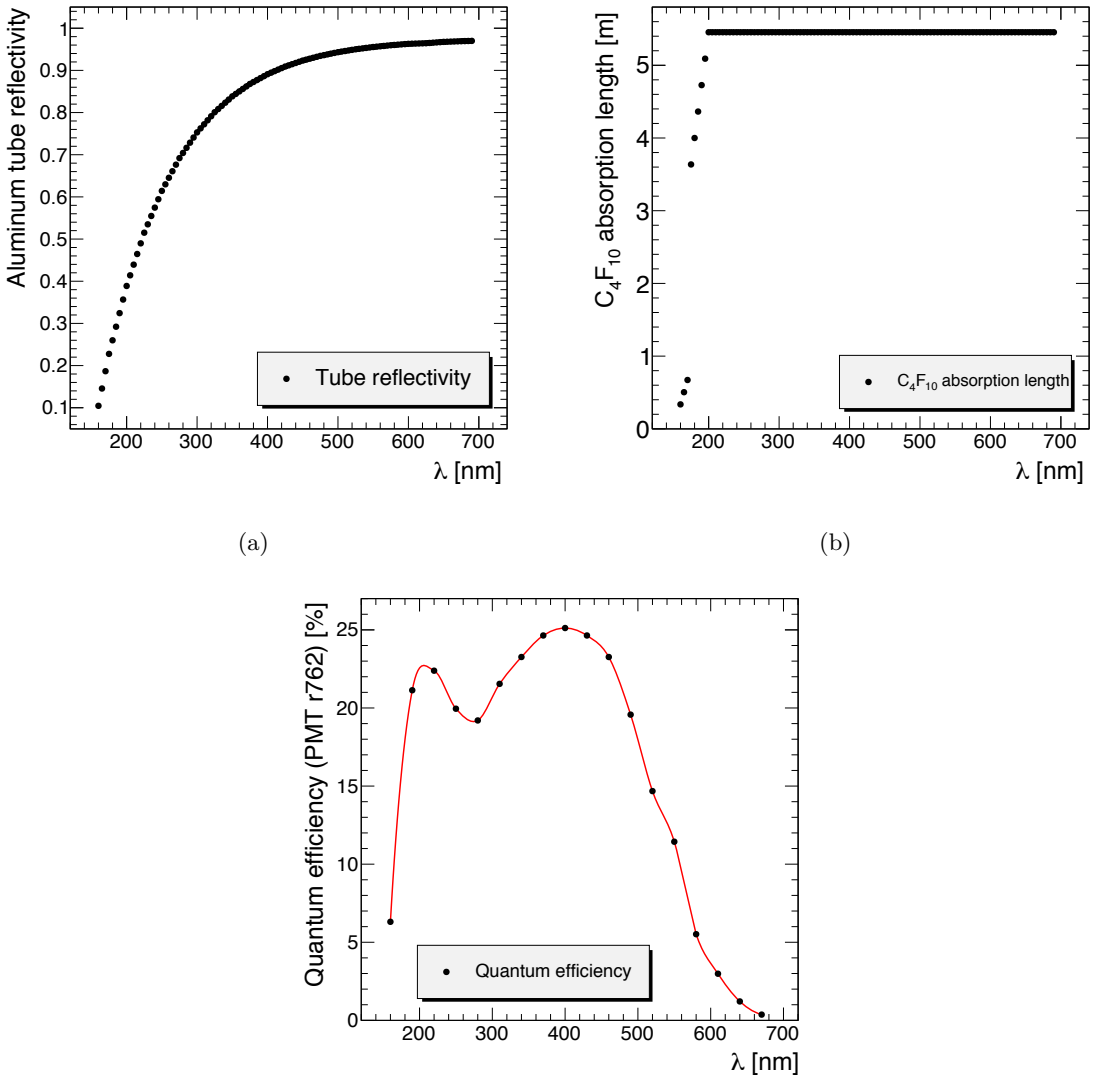


Figure 6.4: *Aluminum tube reflectivity (a) , absorption length of photons in C_4F_{10} and the PMT quantum efficiency (c) as a function of photon wavelength.*

200 nm and drops to 1 mm at $\lambda = 150$ nm. Photons which are not absorbed by the gas, reach the end of the tube and are converted by the PMTs into photo-electrons. The conversion efficiency, also called the quantum efficiency, is provided by the manufacturer Hamamatsu and displayed in figure 6.4(c). The quantum efficiency also includes the effect of absorption in the quartz.
Other effects such as dependence of the reflectivity on photon polarization has not yet been implemented.

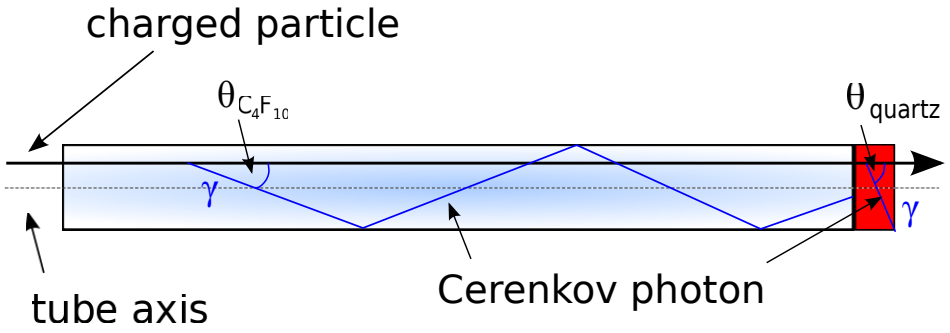


Figure 6.5: *Illustration of light propagation inside a Cerenkov tube.*

6.2 Response to a single particle

A number of tests has been carried out in the process of validating the different aspects of the simulation. These test are designed to address specific features of the simulation such as the pointing geometry of the Cerenkov tube, reflectivity of the tubes, pulse height spectrum and the PMT quantum efficiency. Due to the nature of the features being investigated, the premises of the tests are kept simple in order to isolate the property under investigation. Since the geometry of LUCID is designed in such way that a particle originating from the IP (a primary particle) produces more light than a particle coming from any other direction (a secondary particle) the baseline setup for the first few tests is a series of 180 GeV charged pions originating at the IP that are aimed directly at the LUCID detector. It will in this way be possible to simulate the response of LUCID to single particles from the IP traveling either along the tube axis (on-axis) or at a random direction (off-axis). Figure 6.6 shows a cut-away visualization of the detector description as it is implemented in the simulation/GeoModel. Superimposed on the figure in red is an eta-cone giving the direction of a primary particle creating at the IP and traversing one LUCID module. To keep the output of the tests in this section as clear as possible, the only detector volume which has been included in the simulation is LUCID as depicted in figure 6.6. The volume is defined in such a way that it contains only LUCID and does not clash with the neighboring ATLAS detector subsystems once included in the simulation.

6.2.1 Signal from on-axis particles

When a charged particle enters a tube and travels along its axis, it emits Cerenkov photons both in the gas and in the PMT quartz window.

Wavelength distribution: Figure 6.7(a) shows the wavelength distribution of the photons generated in the C_4F_{10} gas at the different steps until detection in the PMT. The black line gives the wavelength distribution of photons as they are generated in the gas. The spectrum exhibits the expected $1/\lambda^2$ dependence characteristic for Cerenkov light emission.
Once the photons are generated in the gas they traverse the gas and are reflected by the aluminum tube walls until they reach the quartz window. As a result, the original wavelength distribution is folded with both the curve for the tube reflectivity (figure 6.4(a)) and the curve for the C_4F_{10} absorption length (figure 6.4(b)) to obtain the wavelength spectrum of

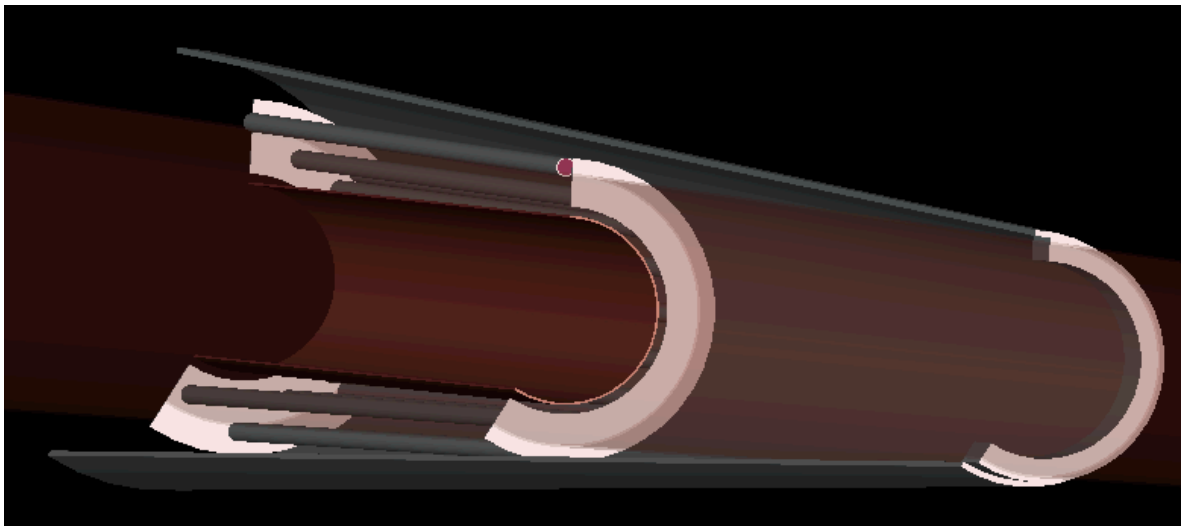
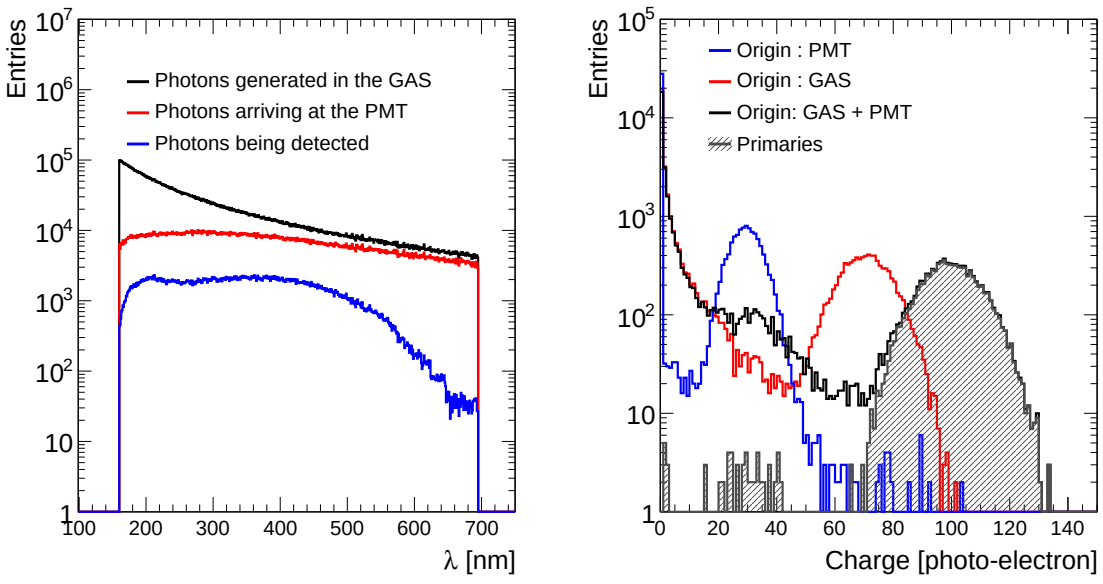


Figure 6.6: *Visualization of the LUCID detector description using the the VP1 tool [79].*



(a) (b)

Figure 6.7: *(a) Wavelength distribution of Cerenkov photons generated in LUCID (black line). The wavelength distribution of the fraction of photons reaching the PMT (red line) and finally detected (blue line) are superimposed. (b) Distribution of photo-electrons detected by LUCID. The two plots are generated using a data set of 10000 events of single charged pions coming from the IP with $E = 180$ GeV, $\theta = 0.39°$ and $\phi = 0$ (on-axis).*

the Cerenkov photons which reach the PMT (red line) . The strong suppression at low λ is due to the steep fall of both the tube reflectivity and gas absorption length for rising photon energy i.e. for ultraviolet light.

The final step in the simulation of Cerenkov light detection is the conversion of photons which have reached the PMT to photo-electrons. This is done by folding the wavelength distribution for photons which have reached the PMT with the quantum efficiency (figure 6.4(c)). The resulting spectrum is given in figure 6.7(a) by the blue line. A clearly visible effect of applying the quantum efficiency is a suppression of the final wavelength distribution above 600 nm.

Photo-electron distribution: Of the photons detected by the PMT a certain fraction will be generated in the gas and another fraction will be generated in the PMT window. Figure 6.7(b) shows the number of photo-electrons read-out by the PMTs when 180 GeV charged pions travel along a tube axis (the signals from all 30 tubes are displayed). The red (blue) line shows the number of photo-electrons from Cerenkov photons generated in the gas (quartz window) and detected by the PMT. The black line shows the sum of the two contribution and thereby represents the full expected signal from a primary particle. By fitting each contribution with a Gaussian (not shown in the figure) it can be shown that the contribution from the gas (quartz window) alone is 71 (29) photo-electrons and the total signal is around 100 photo-electrons. The value of the width for the different contributions is due to two effects: the Poissonian fluctuations of the Cerenkov emission and the binomial fluctuations of the photo-electron production inside the PMT. It can in fact be shown that because of the latter effect the ratio between the width of the signal and the amplitude (σ_A/A) remains constant (see section 6.4 for details).
The tails in the lower part of the spectra are due to secondaries created when the primary pion hits detector material like the beam pipe support or the gas vessel. Such secondaries are usually created at an angle to the tube axis and thereby deflected away from the original direction of the primary. Because of the angle and consequently the shorter path length, these secondaries will only induce a small signal in the tube they traverse[1]. The fact that the lower tails are due to secondaries is confirmed when the contribution from the primary pions is isolated (the grey hatched histogram in figure 6.7(b)). It is seen that the lower tail disappears in this case.

6.2.2 Signal from off-axis particles

In a slightly more realistic situation, primaries will not cross the Cerenkov tube parallel to their axis, but with a small angle. Such a situation can be simulated by repeating the test from the last section with the modification that now the pions are generated in a full 2π range in ϕ and within the LUCID coverage in η ($|\eta| \in [5.4, 6.1]$). Since the diameter of the tube is small compared to the distance between LUCID and the interaction point, the angle between the trajectory of an off-axis primary particle entering the tube and the tube axis is very small. However compared to the on-axis scenario in the previous section, primaries can now create secondaries in other parts of the detector material as well as in the tube walls. The tube wall is thin ($\sim 1mm$) but for a primary particle traversing a detector module off-axis, the effective material thickness of the tubes can be as high as 1.5 m. The higher material thickness leads to a higher probability of creating secondaries as illustrated in figure 6.8. Due to the increased number of secondaries in this scenario it is expected that the resulting photo-electron spectrum will have a larger contribution to the lower tails than in the on-axis

[1] See section 6.3.5 for a more detailed study of how secondaries affect the signal.

scenario. The resulting photo-electron spectrum is shown in figure 6.9. It can be seen from the plot that the peak position of the different contributions remains the same but the level of background from secondaries is significantly larger now. It is noteworthy here to mention that the peak at 30 photo-electrons for the total spectrum (PMT+ GAS) is larger in this scenario. This is due to the fact that such a contribution can be created by secondaries only. Another noteworthy feature is that the contribution from the primaries is essentially unchanged. The reason for this is that the LUCID tubes are so "far" from the IP (about 17 m) that off-axis primary particles are almost parallel to the tube axis, therefore the path inside the radiator of off-axis and on-axis primaries are similar.

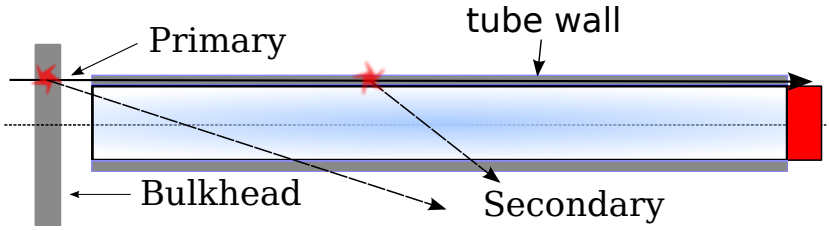


Figure 6.8: *Sketch of a primary particle interacting with the detector material and thereby creating secondaries.*

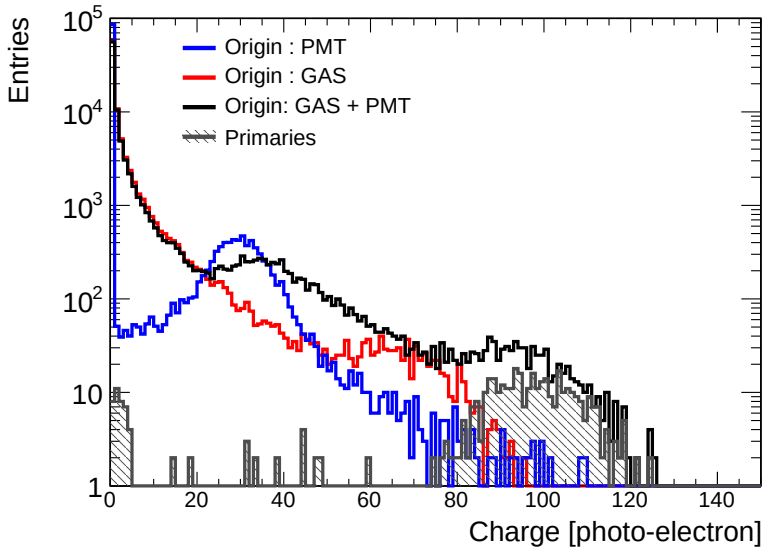


Figure 6.9: *Distribution of photo-electrons detected by LUCID from 10000 events of single charged pions coming from the IP with $E = 180$ GeV and a random direction* $(5.4 < \eta < 6.1, 0 < \phi < 2\pi)$.

6.3 Response to pp collisions

It was shown in the previous sections that the response of LUCID to a single particle that is going along the tube axis is relatively clean and background free. The contributions in terms of photo-electrons from different parts of the detector are visible as distinct peaks on top of

a small background from secondaries. It was also shown that the level of background from secondaries increases dramatically if the single particles are shot at the LUCID modules at an angle to the tube axis. In the following section it will be investigated how the shape of the photo-electron distribution changes when the single particle scenario is replaced with *pp* collisions. The emphasis will be put on studying quantities which characterizes the particles giving a signal in LUCID. Since the collected charge distribution is expected to be dominated by signals from secondaries it is also important to study what sets the signal from secondaries apart from the primaries. This is done to help optimize the electronics threshold that defines a hit in LUCID and to estimate the effect of such a threshold on the background level. In order to do so each relevant quantity is plotted both for the full range of particles giving a signal in LUCID and also for those giving a signal above the threshold.

6.3.1 Event generators

An event generator program can be used to generate high-energy-physics 'events', i.e. sets of outgoing particles produced in the interactions between two incoming particles. The objective is to provide as accurate as possible a representation of event properties in a wide range of reactions, within the Standard Model. For inelastic minimum bias collisions the two most widely used event generators are PYTHIA [52] and PHOJET [80]. The differences between the two generators are discussed in the references and in [81, 82].
In these models the total *pp* cross section can be expressed as a sum of the components,

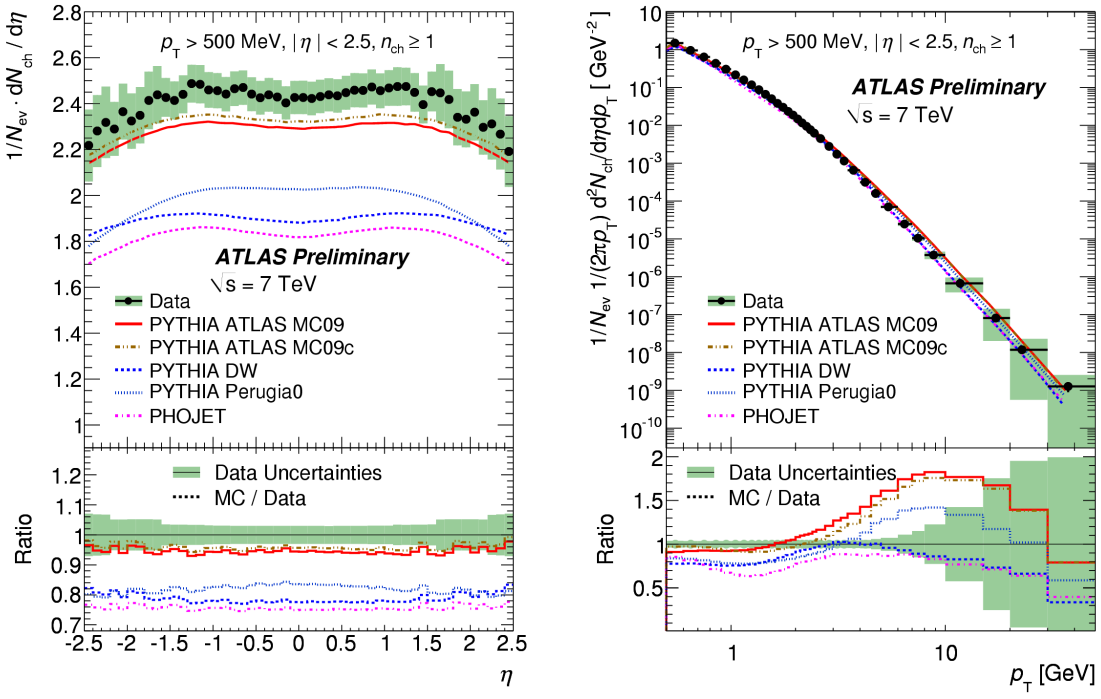
$$\sigma_{TOT} = \sigma_{ELAS} + \sigma_{SD} + \sigma_{DD} + \sigma_{ND} \tag{6.7}$$

where these cross sections are elastic (σ_{elas}), single diffractive (σ_{sd}), double diffractive (σ_{dd}) and non-diffractive (σ_{nd}). In this study, the small central diffractive component of the cross section is ignored. Predictions for the inelastic cross sections at 7 TeV are given in table 6.2 for both PYTHIA and PHOJET. It should be noted here that there are at present no concrete reason to chose one generator over the other. In fact, different generators are often used in parallel to study the impact of different physics models.

Type of *pp* collision	**σ[mb] in PYTHIA**	**σ[mb] in PHOJET**
Non-diffractive (ND)	48.5	61.6
Single-diffractive (SD)	13.7	10.7
Double-diffractive (DD)	9.3	3.9
Total inelastic	71.5	76.2

Table 6.2: *Cross section of the different inelastic processes (single-, double- and non-diffractive) predicted by PYTHIA and PHOJET.*

To illustrate the difference between the predictions of the different generators figure 6.10 shows the the charged-particle multiplicities produced in inelastic processes predicted by PYTHIA and PHOJET compared to 7 TeV collision data. Although the predictions of the total cross section of PYTHIA and PHOJET are close, the two generators predict a different particle multiplicity and a different sharing of event types. However, when extrapolated to the pseudo-rapidity coverage of LUCID ($|\eta| \in [5.4, 5.9]$) the difference in predictions is less pronounced.



(a) (b)

Figure 6.10: *Charged-particle multiplicities for events with $n_{ch} \geq 1$ within the kinematic range $p_T > 500$ MeV and $|\eta| < 2.5$ at $\sqrt{s} = 7TeV$ [81] [82]. The panels show the charged particle multiplicity as a function of the pseudo-rapidity (a) and transverse momentum (b). The points represent the data and the curves the predictions from different Monte Carlo models. The vertical bars represent the statistical uncertainties, while the shaded areas show statistical and systematic uncertainties added in quadrature. The values of the ratio histograms refer to the bin centroids.*

The main difference between the two generators is the treatment of event topologies for various physical processes. This is important to study since some event types and topologies will have a larger impact than others on the signal in LUCID. For instance, all elastic collisions can be ignored altogether since the scattering angle of the proton is so small that any interaction outside the beam pipe happens further downstream than the position of LUCID. The systematics related to the choice of generator is discussed in chapter 7.

The study presented in the following section is done with a sample of about 10000 events of single *pp* interactions generated with PYTHIA 6.4 at 7 TeV center of mass energy in the full pseudo-rapidity range.

6.3.2 Track propagation inside ATLAS

After the generation step all outgoing particles are fed to a GEANT4 simulation of the full ATLAS detector. In order to make the simulation as realistic as possible it is imperative that all detector modules are included in the simulation. This is especially important for the

simulation of signal formation in LUCID since the signal here is dominated by secondaries created in the forward part of the ATLAS detector. This is the case since LUCID is located so close to the beam pipe inside the forward muon shielding. In fact, primary particles produced by inelastic *pp* collisions interact with the material of the experiment producing secondary particles that may reach LUCID from any direction. For this reason the geometrical description of the beam pipe and the forward shielding has been revisited in connection with the implementation of the LUCID detector description [83].

6.3.3 On the origin of secondary particles

Since a large part of the signal in LUCID is created by particles from secondary interactions, it is useful to know the spacial origin of such particles. This is partly important in the process of validating the pointing geometry of the Cerenkov tubes but also to investigate the electronic threshold needed to define when a particle is detected or not. The latter is studied by comparing the collected charge distribution from secondaries originating from different parts of the ATLAS detector to the charge distribution from primaries. Also here it will be possible to see which part of the ATLAS detector, including LUCID itself, will contribute the most to the amount of secondaries. Figure 6.11 shows a two dimensional map of where in the

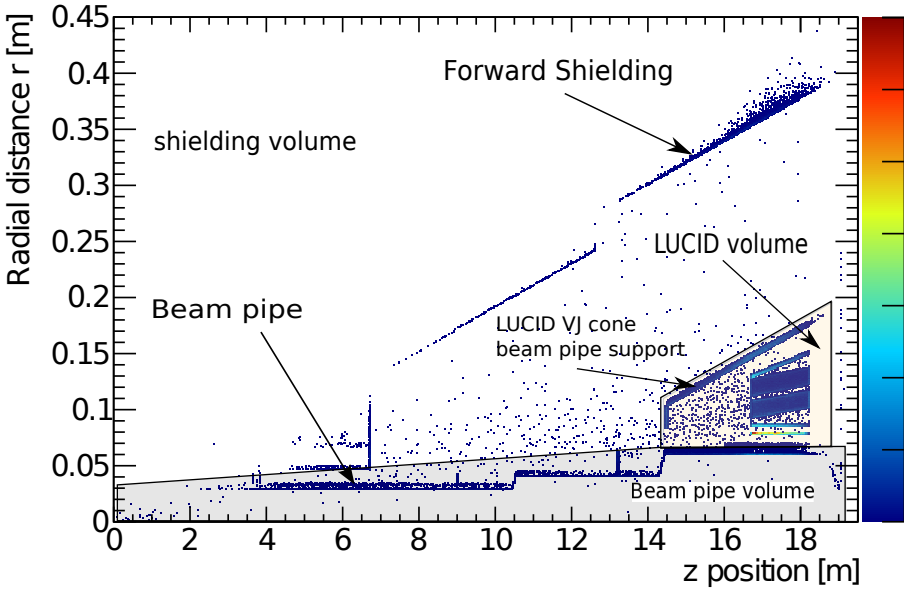
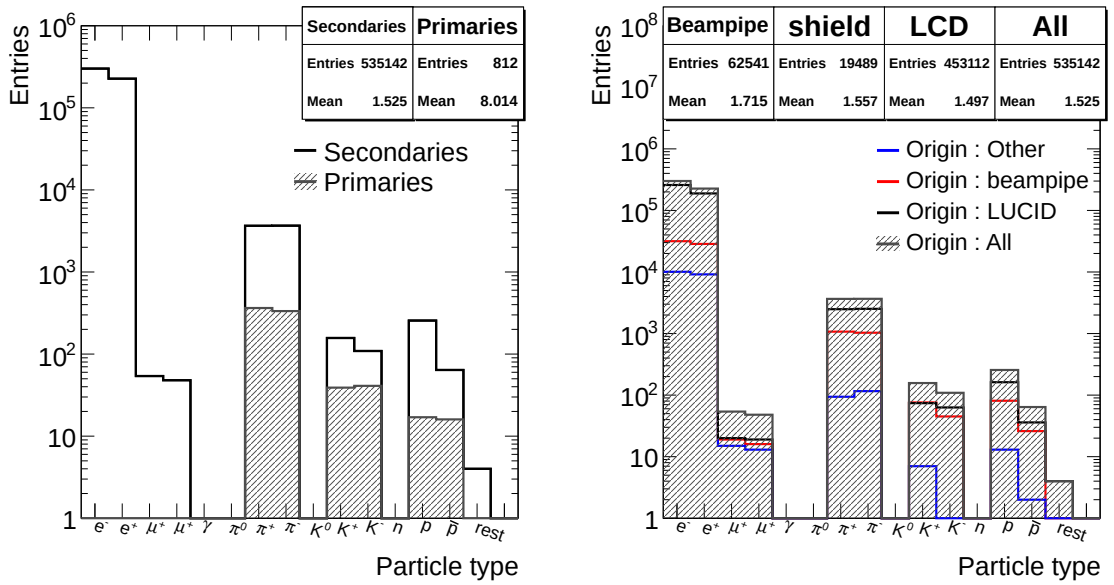


Figure 6.11: *A $r - z$ topology of the origins of secondaries which give a signal in LUCID. Only the positive side of the detector is shown here but the situation is symmetrical around $z = 0$.*

ATLAS detector the secondaries are created. Three regions are defined which individually corresponds to a separate category of secondaries: the beam pipe region , the LUCID modules and the *other* parts of the ATLAS detector such as the forward muon shielding. To filter out soft particles, only secondaries which give a signal in LUCID are included in the plot. In this context a signal is defined as a charged secondary emitting at least one photon in at least one



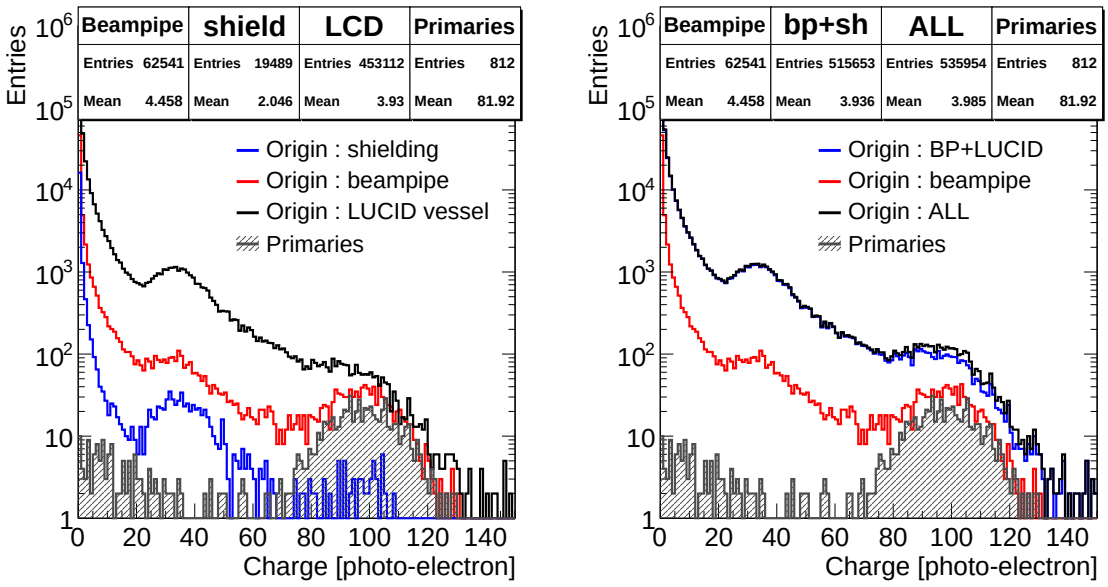
(a) (b)

Figure 6.12: *(a) Distribution of primary (grey hatched histogram) and secondary (solid line) particles. (b) Distribution of secondary particles from different parts of the ATLAS detector.*

Cerenkov tube[2]. Unless otherwise stated, only this type of particles is taken into account in what follows.

It can be seen from the plot that many secondaries are created in the LUCID modules themselves. These particles are most likely coming from secondaries interacting with the detector material in the walls of the Cerenkov tubes and thus creating a shower of particles which then gives a signal. Another part of the ATLAS detector which contributes significantly to the secondaries is the beam pipe. Primaries emerging from the IP with a direction towards a LUCID module will in general traverse the beam pipe about 7 m downstream to the IP. The relative small incident angle at which these particles hits the beam pipe, results in an non-negligible effective thickness of the beam pipe as seen by the primaries. At an incident angle of 0.39° the otherwise 1 mm thick beam pipe has an effective thickness of ∼15 cm. This means that not only will the primary particles have a larger change of producing secondary interactions in the beam pipe, but so will the secondaries themselves. For instance semi soft secondaries produced in the flanges of the beam pipe will have a probability to start a shower in the beam pipe and the LUCID volume and thus contributing to the lower tail in the photo-electron distribution. To illustrate the difference in number of secondaries versus primaries figure 6.12(a) shows the number of primaries and secondaries which gives a signal in LUCID divided into particle type. The first interesting feature here is that the fraction of primaries is less than 0.2%. This is supported by the fact that most secondary particles reaching the LUCID volume are electrons from electromagnetic showers. Also photons from prompt $\pi^0 \to \gamma\gamma$ decays will contribution to this category of secondaries.

[2]Secondaries which give a signal in two or more tubes still counts as a single entry on a particle level but as multiple entry when it comes to photons.



(a) (b)

Figure 6.13: *(a) Photo-electrons spectrum from pp collisions at 7 TeV separated into contribution from different categories of secondaries and (b) the sum of the individual contributions.*

Figure 6.12(b) displays how the secondaries can be divided up into particle type and origin. The majority of the secondaries are electrons and positrons from electromagnetic showers within the LUCID volume. Apart from the lepton secondaries, a substantial fraction of the remaining secondaries are pions from hadronic interactions in the beam pipe and the LUCID volume.

Figure 6.13 shows the photo-electron distributions from different categories of secondaries. The photo-electron distribution from the primaries have been superimposed on both plots. Despite the fact that the secondaries originate from many different parts of the ATLAS detector, the overall photo-electron spectra still exhibits peaks at the same position as the spectra from on-axis pions (see figure 6.7(b)). This demonstrates an important observation from the simulation, namely that the position of the various peaks of the photo-electron spectrum does not depend on the origin of the particles giving rise to the signal, but solely on the details of the detector description. The relative contribution of the peaks might depend on the origin of particles, but the absolute position will not. This is important since it help in deciding the value of the electronics threshold that is used to minimize the background from soft secondaries while keeping the contribution from primaries intact. Both figure 6.13(a) and figure 6.13(b) confirms this by showing that all the three categories of secondaries and the sum of them exhibits clear peaks at 29 photo-electrons due to Cerenkov radiation in the PMT window and at 100 photo-electrons due to radiation in the C_4F_{10} gas and the PMT window. It is also seen in the two plots, that the majority of the signal is created by secondaries from the LUCID volume itself. This contribution has a pronounced peak at 30 photo-electrons from secondaries with a large angle to the beam pipe which only traverse the PMT window.

The large angle to the beam pipe is also reflected in the less pronounced peak at 100 photo-electrons stemming from the fact that this type of secondaries is less likely to traverse the full length of the Cerenkov tubes and hit the PMT window. The category of secondaries which originates from the beam pipe tends to show the opposite behavior since they are produced with a smaller angle to the beam pipe and therefore have a higher probability of traversing the full length of the Cerenkov tubes and thus give a larger signal. The smallest contribution to the photo-electron spectrum comes from the category of secondaries which originate in the forward shielding. These are, like the secondaries created in the LUCID volume, also produced with a large angle to the beam pipe and as a result only give a contribution at the low end of the photo-electron spectrum.

6.3.4 On the photo-electron spectrum and the definition of a hit

The response of LUCID to inelastic *pp* collisions in terms of collected charge is shown in figure 6.14.

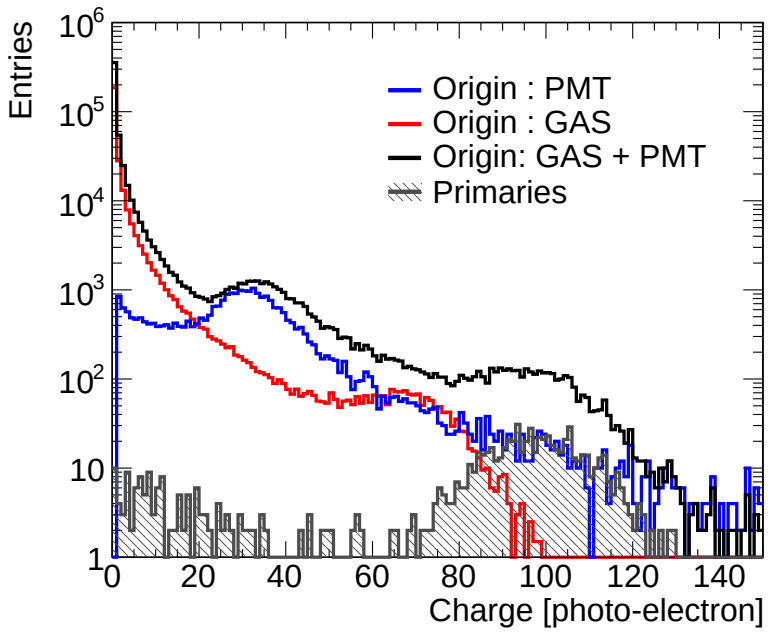


Figure 6.14: *Origin of Cerenkov light.*

The photo-electron distribution peaks at the same positions as observed when shooting single particles at LUCID (71 in the gas, 29 in the quartz and 100 in total). The normalization is done so the different contributions corresponds to the same number of *pp* interactions. It will in this way be easier to study the threshold which defines wether a particle is detected or not. Since such an electronics threshold is set in the CFD for each Cerenkov tube, it will not be possible to distinguish the combined signal from two or more particles from the signal of a single particle as long as the total signal is above the threshold. For this reason, the situation in which a tube registers a signal above threshold is called a *tube hit* or just a *hit*. The precise implication of the fact that LUCID only is capable of counting hits and not detected particles

will be addressed later when the performance of LUCID as a luminosity monitor is discussed. Most of the secondaries give rise to a signal below 15 photo-electrons. This means that a cut-off threshold of 15 photo-electrons keeps the entire signal from primary particles, while suppressing a large fraction of the secondaries. It can be seen from figure 6.13 that with a cut at 15 p.e (or a cut at any value) there will be more secondary particles than primary particles that produce a hit in LUCID. This is not a problem in the luminosity analysis since the average number of secondaries is proportional to the number of primaries which in turn is proportional to the luminosity. The detector is to some extent working as a calorimeter and it should be noted that secondaries are not really a background in the luminosity analysis. Further reasoning for this specific choice of threshold value is postponed to section 6.4 where the simulation of the front-end electronics is discussed. For now, the only need for a threshold is to have a way of defining whether or not a particle is detected. This proves useful in the validation of the LUCID simulation since it is now possible to compare the kinematics of detected and not-detected particles.

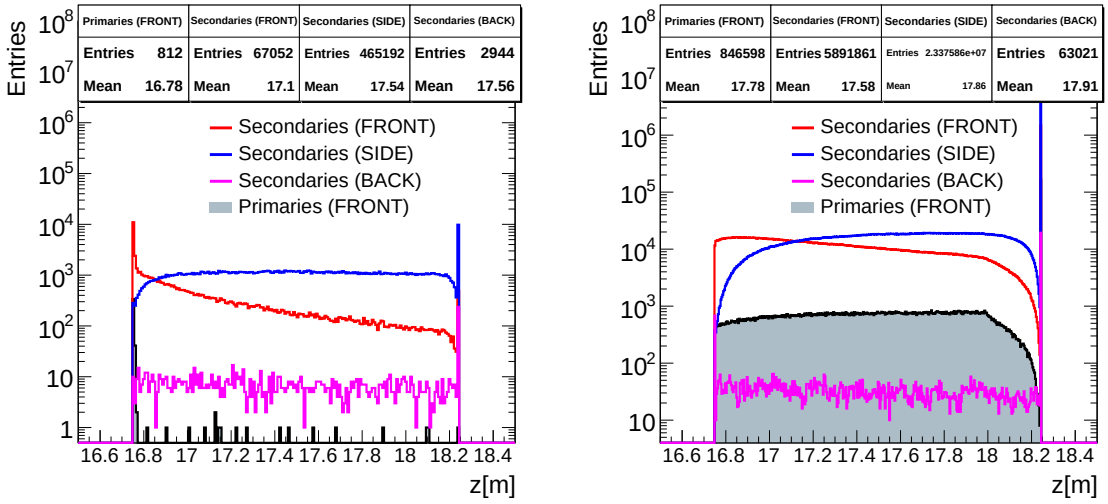
6.3.5 Particle kinematics

The total number of photo-electrons produced by a charged particle crossing a LUCID tube is proportional to the path length inside the Cerenkov radiators (gas and quartz). Particles coming from the interaction point and hitting the LUCID volume from the front are expected to travel a longer path inside the tubes and to give a larger signal of photo-electrons.

Definition of the particle direction In order to study the correlation between the original direction of the particles and the size of the signal inside LUCID, a direction is associated to each particle. The coordinate of the impact point (x, y, z) and the momentum (p_x, p_y, p_z) of primary and secondary particles are used to define a direction for each particle. In this context the impact point of a particle is defined as the spacial point at which the first Cerenkov photon is produced. Three classes of particles are defined:

- **Back:** If $z \times p_z < 0$, the particle is defined as coming from the 'back'.
- **Side:** If the particle is not 'back' and if $|z| > 16601$ mm (the distance of the LUCID frontfrom the IP), the particle is defined as coming from the 'side'.
- **Front:** The remaining particles are defined as coming from the 'front'.

The z coordinate of the impact point for the different classes of particles is shown in figure 6.15(a). Of the particles hitting LUCID only 0.15% are primaries. Most of the particles hitting the LUCID volume are particles coming from the side (86.78%). Once the requirement is made that only detected particles (i.e track which gives a signal above the threshold of 15 p.e) are considered then the relative contribution from primaries grows by a factor of more than 10 to 1.83% while the amount of secondaries from the side is diminished by a factor of 10. This proves that introducing a cut-off threshold does in fact remove more soft secondaries than primaries. The same type of conclusion can be drawn from figure 6.15(b) where the number of Cerenkov photons created in the tubes is shown as function of the distance from the IP. By comparing the impact point of the primaries in figure 6.15(a) to the emission point of the



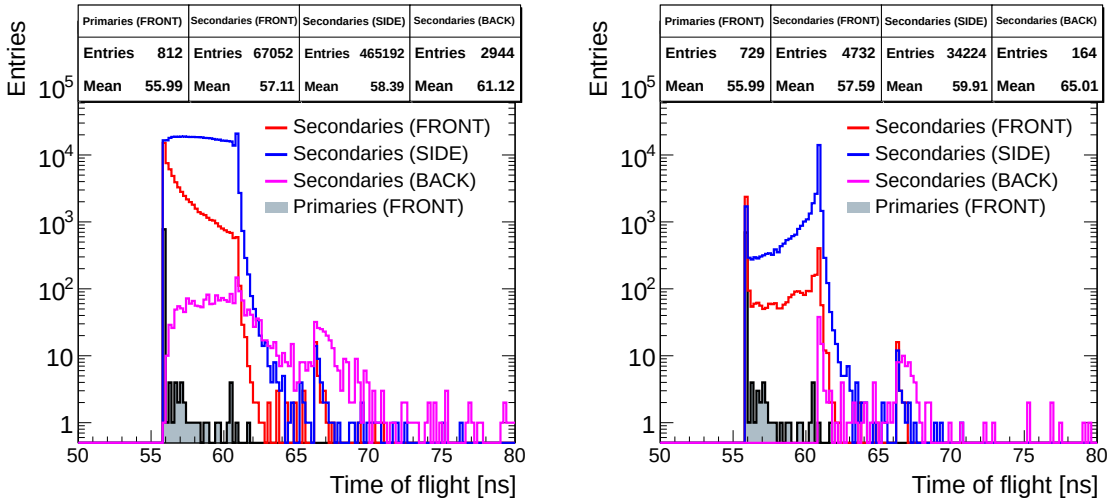
(a) (b)

Figure 6.15: *Distance from the IP (along the beam axis) (a) of the impact point on the LUCID volume and (b) of the creation point of Cerenkov photons in the tubes. The results are shown for three classes of secondary particles ('front', 'side' and 'back') and for primary particles.*

Cerenkov light from primaries in 6.15(b) it can be seen that while the impact point is limited to the front of the detector, the Cerenkov photons are emitted throughout the full length of the detector. This means that a primary particle in general emits more light than a secondary and therefore suffers less from a threshold cut. The ratio of primaries to secondaires is 0.15% in figure 6.15(a) while the ratio of Cerenkov photons created from secondaries to primaries 2.81% in figure 6.15(b). Hence the average primary emits around 18 times more light than the average secondary.

Time of flight

When a particle is produced at the IP it travels throughout the ATLAS detector approximately at the speed of light. At this speed it takes about 56 ns for a particle to cover the distance from the IP to the front of LUCID. However this is only true if the particle travels in a straight line which is not the case for most secondaries. It is therefore expected that the time of flight is longer for secondaries than for primaries due to the longer travel path of the combined trajectory. The time of flight to the LUCID volume for all particles and those which are detected are shown in figure 6.16.
From figure 6.16(a) it can be seen that the contribution from primary particles are sharply peaked at 56 ns with a small tail towards higher value of arrival time. The contributions from secondaries are however, spread out over a larger range, indicating that secondaries in general travel a longer path before reaching LUCID. Secondaries parallel to the beam axis will hit the LUCID module from the side over the full length of the detector giving rise to a flat distribution in arrival time from 56 ns at the front of LUCID to 61 ns at the position of the PMTs. By comparing the individual contributions in figure 6.16(a) and 6.16(b) it is seen



(a) (b)

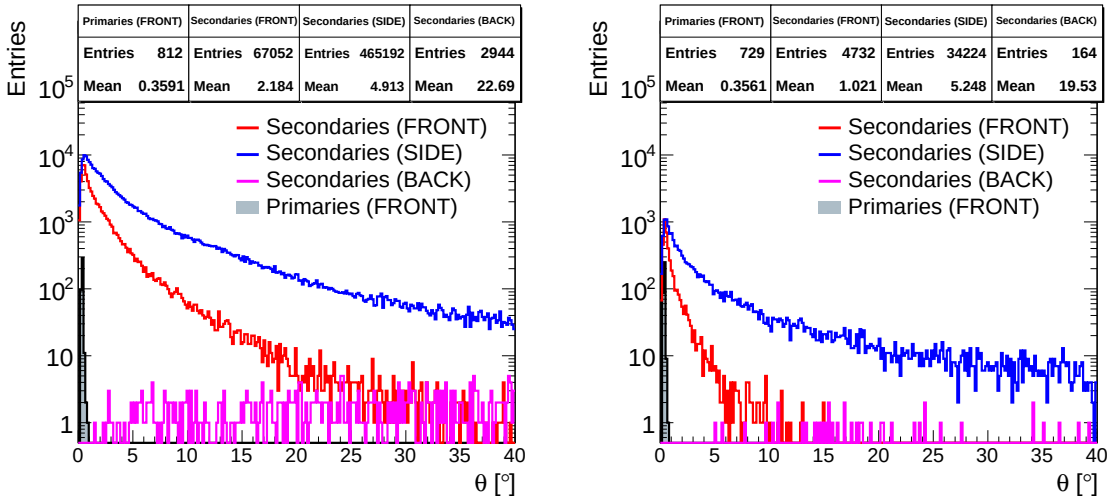
Figure 6.16: *Time of arrival at the LUCID volume of all particles (a) and of those which are detected with a 15 p.e. threshold (b).*

that imposing a cut-off threshold suppresses the low end part of the spectrum[3] making the distribution for the secondaries peak at the position of the PMT window at 61 ns. This is in line with the observation in section 6.3.4 that a large part of secondaries only emit light in the PMT window. This is partly due to the larger angle with respect to the beam pipe but also because of the lower Cerenkov threshold of the PMT quartz window (see table 6.1).

Angle to the beam

It was shown in the previous section that primary and secondary particles arrive at the LUCID volume at different times. It was postulated that this difference and spread in arrival time is due to the fact that secondary particles, being the product of scattering of primary particles through different materials, are expected to travel along different directions with respect to primaries. The angle between the beam axis and the trajectory of primary and secondary particles is shown in figure 6.17(a) for all particles and in figure 6.17(b) for those which are detected.
As in the case of the time-of-flight distributions, the contribution from the primary particles does not change significantly between particles which give a signal compared to those which get detected. Both distributions have a mean of 0.36° which is consistent with the inclination of the Cerenkov tubes to the beam axis. The same inclination is also the reason why detected secondaries with an angle above 2° are strongly suppressed. In fact the contribution of secondary particles coming from the back is almost entirely removed when a threshold cut is imposed.

[3]Apart from the peak at 56 ns.



(a) (b)

Figure 6.17: *Angle to the beam of particles giving a signal of at least one photon in LUCID (a) and particles detected by producing more than 15 photo-electrons (b).*

Energy

Charged particles will only give a signal in LUCID if their energy is above the Cerenkov threshold for either the C_4F_{10} gas or the quartz PMT window (see table 6.1). As a result, the contribution from the softest part of the energy spectrum is already removed from the set of particles giving a signal in LUCID. The energy distributions of particles giving a signal in LUCID are shown in the left column of figure 6.18 for different particle types. From 6.18(a) it can be seen that the mean energy of a primary particle is around 130 times larger than the mean energy of secondary particle. It is expected that secondaries are softer than primaries but it is also expected that secondary electrons and positions will contribute mostly to the low energetic part of the spectrum. An expectation which is confirmed by figure 6.18(d) and (e) where it is seen that secondary pions are significantly more energetic than their leptonic counterpart.
The requirement of being detected by LUCID further suppresses soft particles. By comparing 6.18(c) and (d) it can be seen that the mean energy of an electron giving a signal in LUCID is 0.29 GeV while the mean energy for the subset which gets detected is 0.80 GeV - a relative increase of 177 %. As for electrons and positrons, the requirement of being detected also suppresses the soft part of the energy spectrum for pions. The mean energy of a detected 'front' ('side') secondary pion is 23.75 GeV (9.64 GeV) which is a relative increase of 57 % (28%) compared to the situation where it is only required that the secondary pion gives a signal in LUCID. Most secondary particles from the 'back' have an energy smaller than the Cerenkov threshold and can be neglected together with the small contribution from primary electrons.

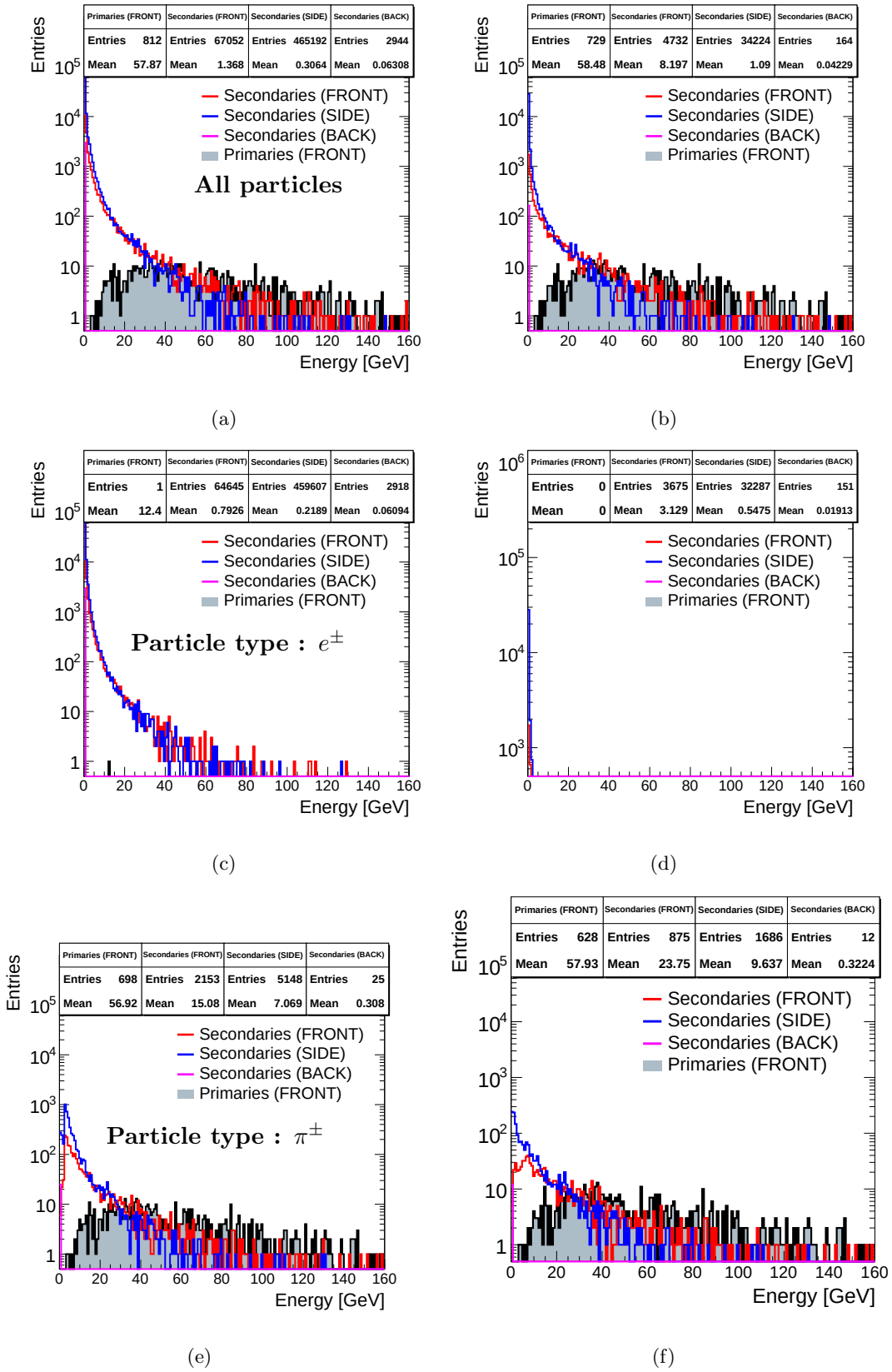


Figure 6.18: *Energy distributions for particles of at least one photon in LUCID (a)(c)(e) and particles detected by LUCID (b)(d)(f).*

6.4 Simulation of the front-end electronics (Digitization)

The ATLAS digitization software is part of the overall ATLAS software chain used to produce Monte Carlo events. The digitization process runs after the GEANT4 simulation and is constructed in such a way that full sets of simulated hits are first read in on an event per event basis. Since simulated hits essentially are energy deposits[4] in a specific part of the sub-detector, namely the *sensitive volumes*, the digitization procedure is constrained to the particle information seen by that volume. In other words, the digitization can only use kinematical information from particles traversing the sensitive volumes and is blind to what happens in the remaining parts of the sub-detector. The digitization software then converts the energy deposits into detector responses, "digits", typically voltages or times.
In the case of LUCID the sensitive detector is defined as the PMT window. The task of the digitization software is to generate digits for each tube based on the information available from the GEANT4 simulation.

6.4.1 General digitization procedure for LUCID

The digitization scheme for LUCID can be divided into five steps which are carried out in the following order for each simulated event:

1. Unpacking of the simulated hits to a format which can be used in the digitization;
2. Simulation of the photo-multiplier response and the response of the amplification chain;
3. Formation of so-called detector response *digits*;
4. Level 1-trigger simulation;
5. Conversion of digits to byte stream format.

Out of the five steps above only the second and the fourth are of real relevance to this thesis, but for the sake of completeness the other step will be discussed briefly as well.

6.4.2 Step 1 - Unpacking of the simulated hits.

Even though the simulation provides a wide range of information about particles which traverses the sensitive detector, only a fraction of that information is used in the actual digitization process. In fact only the number of photo-eletrons generated by Cerenkov photons traversing the sensitive detector, is used to simulate the PMT response. The total number of photo-electrons is obtained on a tube-by-tube basis by simply counting the number of simulated hits, since each GEANT4 hit by construction represents a photo-electron. The remaining information is used for debugging purposes and studies like the one presented in the previous section.

[4] A GEANT4 simulated hit can in principle contain any kind of information about the particle that goes though the detector.

6.4.3 Step 2 - Simulation of the detector response

Photo-multiplier response

The number of incident photons is a Poisson distributed variable, and the photo-electric conversion of photons to photo-electrons can be considered to be a binary process. The distribution of photo-electrons is thus given by

$$P_\lambda(n) = \frac{\lambda^n e^{-\lambda}}{n!} \tag{6.8}$$

where $P_\lambda(n)$ is the probability that n photo-electrons will be collected given that the average number of photo-electrons λ. After being collected, each photo-electron is amplified by the PMT. The resulting charge follows a Gaussian distribution $G(\lambda, n)$ with a mean value of λ. The total output charge from the photomultiplier is therefore obtained as a convolution of the n-photoelectron distributions (Gaussian) weighted by its occurrence probability (Poisson):

$$P(\lambda) = \sum_{n=0}^{\infty} G(\lambda, n) \cdot \frac{\lambda^n e^{-\lambda}}{n!} \tag{6.9}$$

where $P(\lambda)$ is the probability that the output charge from the PMT is λ.
The above expression fails, however, to take into account any particularities of the PMT amplification chain, such as a deviation from Gaussian behavior. The following section explains the ideas behind a more detailed simulation of the PMT amplification procedure in terms of a more precise description of the PMT dynode chain.

Dynode chain simulation Starting with the assumption that the PMT has an N stage dynode system and that one electron hitting the i'th dynode will create an average g_i of secondary electrons, it can be shown that [84]

$$\sigma_1^2 = Q_1^2\Big(\Big(\frac{\delta_1}{g_1}\Big)^2 + \frac{1}{g_1}\Big(\frac{\delta_2}{g_2}\Big)^2 + \cdots + \frac{1}{g_1 g_2 \cdots g_{N-1}}\Big(\frac{\delta_N}{g_N}\Big)^2\Big) \tag{6.10}$$

where Q_1 is the mean anode charge initiated by one electron captured by the first dynode, σ_1^2 is its variance and δ_i is the standard deviation of the number of secondary electrons created from the i'th dynode by one electron. Assuming that the fluctuations of the created secondary electrons are Poissonian distributed and that the gain is equally divided by the dynodes (i.e. $g_1 = g_2 = ... = g_N = g$), equation 6.10 can be rewritten as:

$$\frac{\sigma_1^2}{Q_1^2} = \frac{1}{g} + \frac{1}{g^2} + \cdots + \frac{1}{g^N} = \frac{1}{g-1} \tag{6.11}$$

The above formula is valid for one electron captured by the first dynode. In the case where photo-electrons are produced at the PMT photocathode as well, it can be shown that [85]

$$\begin{cases} \dfrac{\sigma_A^2}{A^2} = \dfrac{1}{N_{pe}} F \\ F = \dfrac{g}{g-1} \end{cases} \tag{6.12}$$

where A is the PMT signal amplitude, σ_A^2 its variance and the factor F measures the deviation of the variance from a pure Poissonian behavior. Equations 6.11 and 6.12 do not take into account other effects such as inhomogeneities of various kind (at the dynode surfaces, collection inefficiency, etc.). All these effects tend to broaden the width of the PMT spectra. Nevertheless these two equations can be used as a valid first approximation to analyze and interpret the PMT spectra.
One direct consequence of equation 6.12 is that the ratio:

$$\frac{\sigma_A^2}{A} = \frac{A}{N_{pe}} \frac{g}{g-1} = k_{cal} F \tag{6.13}$$

is a constant which value depends on the average dynode gain and on the calibration constant k_{cal} of the reading instrument (in the LUCID case is a charge to digital converter (QDC) or a flash analog to digital converter ($FADC$). Another important consequence of Equation 6.13 is that

$$\sigma_A^2 = k_{cal}^2 F N_{pe} \tag{6.14}$$

which allows one to estimate the deviation from the pure Poissonian behavior of the amplitude peak variance. Note that in the case of $g \gg 1$ then $F \to 1$ and the signal peak shape approaches a pure Poissonian behavior. With the voltage divider mounted on the R762 PMT's, the overall gain of about 10^6 is equally shared among 10 dynodes. As a consequence, in the LUCID readout case $g \simeq 4$ and therefore $F \simeq 1.33$ [5]. However, this value of F assumes a constant quantum efficiency as a function of the wavelength, which was shown not to be the case in section 6.1.2. A non-constant quantum efficiency will have the tendency to widen out the signal in the PMT and thereby give a larger value of F. Figure 6.19(a) shows the photo-electron distribution from on-axis pions in a simulation scenario where the quantum efficiency is fixed to a constant value of 20% and the dynode chain simulation has not been carried out. In this situation the F parameter assumes a value of 1.083 which is compatible with Poissonian behavior within three standard deviations. If the same type of simulation scenario is repeated with a non-constant quantum efficiency the value of F increases, signaling the departure from pure Poissonian behavior of the PMT signal formation. This can be seen from figure 6.19(b) where the value of F no longer is compatible with 1. If now the PMT dynode chain simulation is added to the simple simulation scenario with the parameters given in table 6.3, the value of F is expected to increase further.

G_{PMT}	G_{AMP}	Q_{noise}	Q_1	σ_0	$\frac{Q_1}{\sigma_0}$
1.25×10^6	7.5	6.5	15	4	3.75

Table 6.3: *Reference values of the relevant quantities in the MC simulation that describes the 2010 data taking configuration. The units of Q_{noise}, Q_1 and σ_0 are QDC counts.*

The resulting spectrum in figure 6.19(c) confirms the obtained with a F value of 1.488 which is higher than the value expected from the calculations above with a constant quantum efficiency. The deviation of F from the value of 1.33 that is expected from the calculation, can be explained by a non-constant quantum efficiency of the PMT.

[5] It has to be noticed here that, due to the very low dependence of g on the overall PMT gain, $G_{PMT} = g^N$, for all practical purposes ($(0.5 < G_{PMT} < 2) \times 10^6$) and we can assume $F = 1.335$ for the PMTs installed in LUCID.

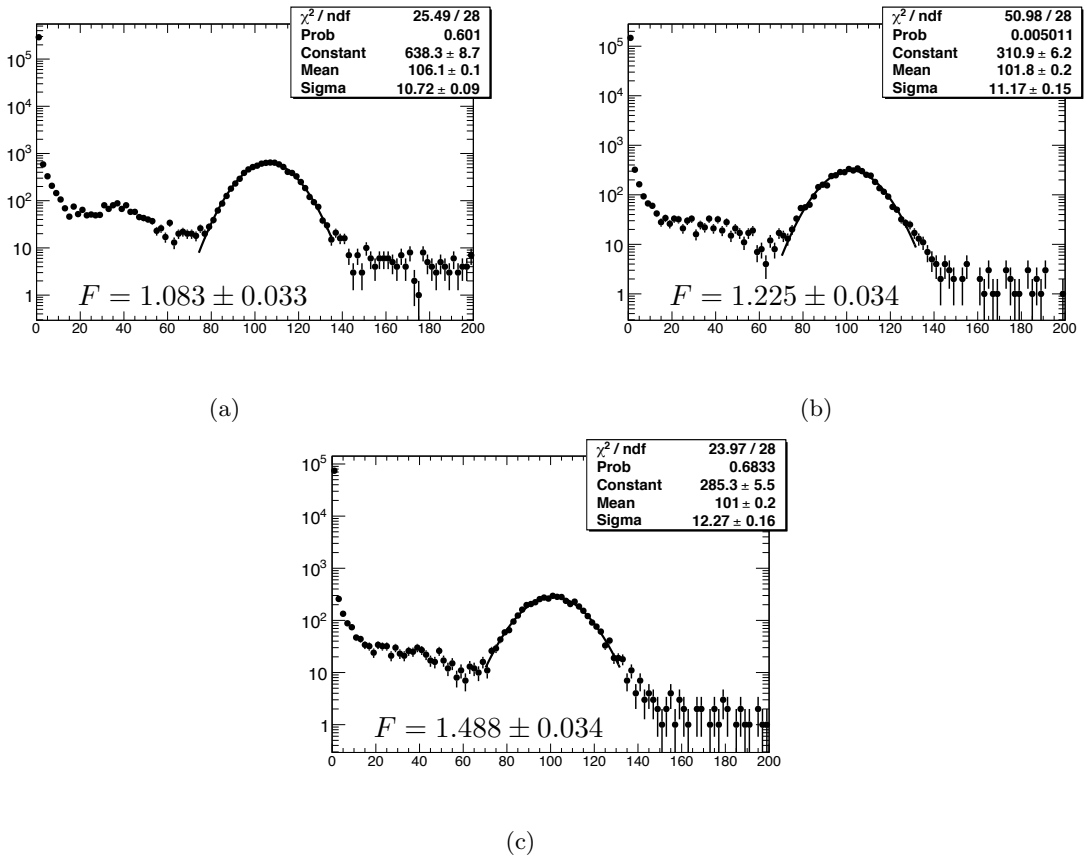


Figure 6.19: *A simulation study of the PMT signal shape under different conditions of the readout electronic. The baseline for the study is a total of 10000 events in which 180 GeV on-axis pions are shot at a LUCID tube. The difference in the three simulation scenarios is that a constant quantum efficiency is assumed in (a), a non-constant quantum efficiency is assumed in (b) and a combination of a non-constant quantum efficiency and the full dynode chain simulation is used in (c). Each signal peak is fitted with a gaussian and the results are superimposed on the plots.*

Saturation of the readout electronics

In addition to the effect from the PMT dynode chain, another feature needs to be taken into account to create a realistic simulation of the readout electronics. During a test-bench setup in which signals of a known magnitude was injected into the electronics immediately after the PMTs, it was shown that electronics used in the readout process has a finite range of linearity. When the signals from a PMT becomes too large, the output begins to saturate. This can potentially present a problem if the saturation begins in the same range as the signal from on-axis particles. In such a situation the shape of the signal peak will be distorted.
The first step towards finding the optimal working point for the detector is thus to determine the linearity range of the amplification chain. This is done by measuring the output signal when a signal with a known amplitude is injected into the system. The input signal is then gradually increased and the measurement repeated until the output is known for every input, yielding a transfer function like the one in figure 6.20. Since the transfer function is unique

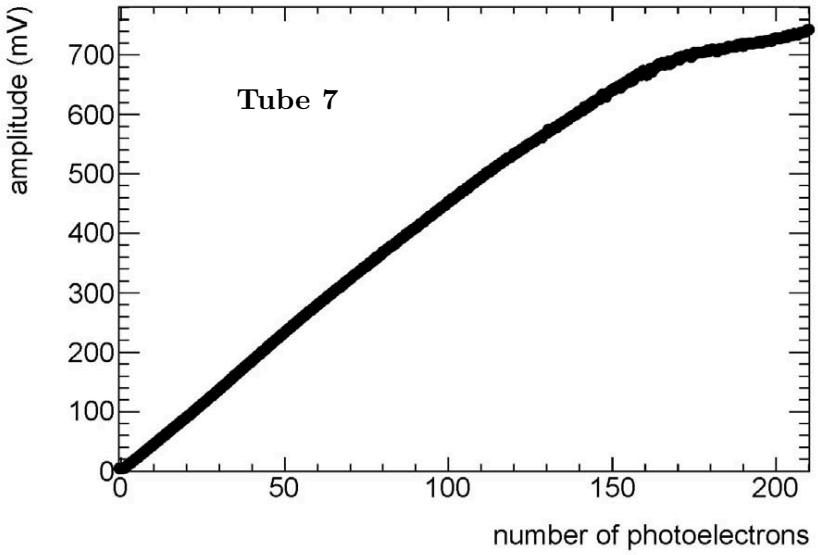


Figure 6.20: *The relationship between the amplitude recorded by the Flash analog-to-digital converter (FADC) and the charge measured by the QDC. The charge has been converted to the number of photo electrons produced in the photomultiplier. It can be seen that the FADC saturates when the number of photo-electrons exceeds a value of about 150.*

for each PMT, any implementation of the saturation effect in the simulation of LUCID, has to be carried out on a tube by tube basis. This has been done according to the test-bench results and constitutes along with the simulation of the PMT dynode chain, the simulation of the LUCID front-end electronics.

6.4.4 Step 3 - Production of detector response digits.

After simulating the response from the front-end electronics, the QDC count for each tube is stored in the form of a Raw Data object (RDO) which will be the input to the reconstruction step together with the results from the level 1 trigger simulation.

6.4.5 Step - 4 Level 1 trigger simulation.

The layout of the level 1 trigger simulation for LUCID is in principle identical to the real one. This means that with the current hardware configuration, LUCID provides two trigger bits as input to the Central Trigger Processor (CTP). These trigger-bits are denoted LUCID_A and LUCID_C, where at least one PMT above the electronics threshold is required in either the A or C side respectively. These bits are combined into the level 1 trigger items given in table 6.4. Out of the four trigger items listed in the table, only the two last ones are composite items in the sense that two or more bits are combined to form the specific item. Inspired by the bit logic required to form the items these are often referred to as the AND/coincidence and the OR/single-side trigger items.
The main part of the level 1 trigger simulation for LUCID is a dedicated algorithm which determines which trigger bits to be filled based on the available QDC information from the

Trigger Item	Required Logic	Required nr. of hits
L1_LUCID_A	LUCID_A	$N^A_{hits} > 1$
L1_LUCID_C	LUCID_C	$N^C_{hits} > 1$
L1_LUCID_A_C	(LUCID_A & LUCID_C)	$N^A_{hits} > 1$ & $N^C_{hits} > 1$
L1_LUCID	(LUCID_A OR LUCID_C)	$N^A_{hits} > 1$ OR $N^C_{hits} > 1$

Table 6.4: *LUCID LVL1 trigger items and the threshold logic required to form the items.*

front-end electronics. The result is then packed into two LucidCTP objects which are send to the CTP simulation. The CTP simulation then reads the two LucidCTP objects and performs the trigger logic to form the trigger items listed in table 6.4. The input (PIT) and output (TBP, TAP, TAV) information from the CTP simulation is recorded in a CTP_RDO object which is likewise passed onto the reconstruction.

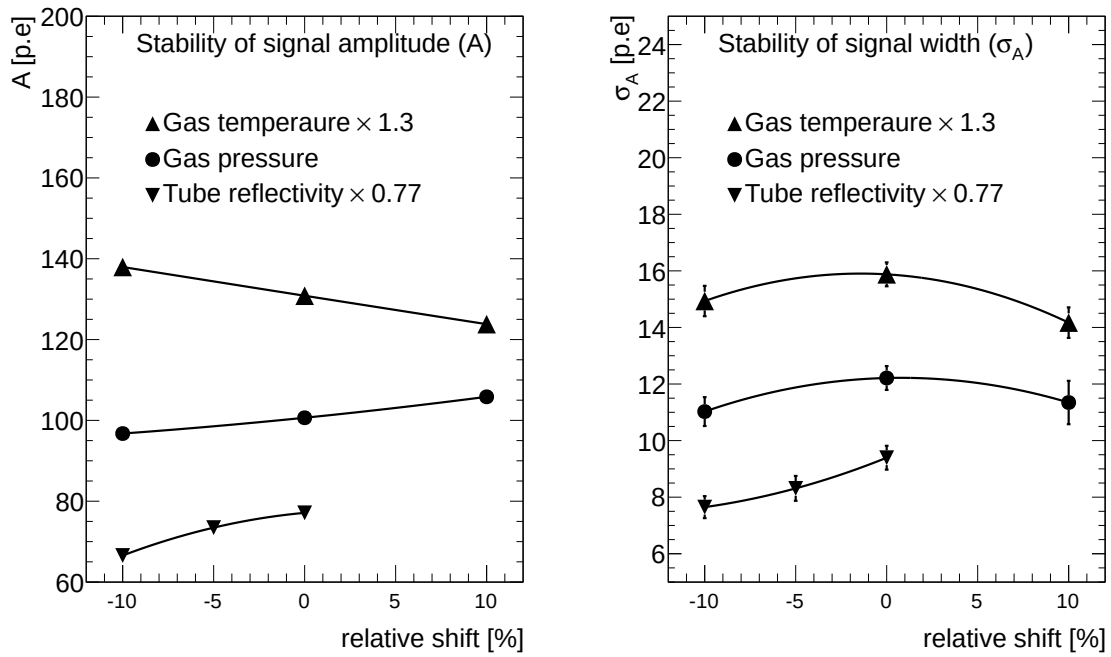
6.4.6 Step 5 - Conversion to byte stream format

The final step in the simulation of the front-end electronics is a conversion of the signal information into a binary format called *bytestream* format. The bytestream format for LUCID consists of 2 data words which contain the hit information tube-by-tube for side A and C seperately. The layout of the bytestream is the same for simulated data and for real data. This is done to mimic the output from the real detector as closely as possible by letting the same reconstruction algorithm run on both types of data in the same manner.

6.5 Systematic uncertainies

The main experimental systematic errors in the luminosity measurement arise from two sources: the detector itself and its calibration. In this section emphasis will be put on the first category, which includes contributions from: the gas pressure and temperature stability, tube reflectivity, PMT gain stability and noise level. A study of these types of systematic uncertainties is important since variations of these quantities will affect the signal amplitude and shape and thereby potentially change the efficiency. For instance, an unexpected change in the gas pressure may lead to a shift in the signal amplitude and thus a potential change in efficiency of the detector. Since the efficiency is used as a calibration constant when the luminosity is determined, any unforeseen variation in efficiency will lead to a wrong determination of the luminosity. In the following section it will be investigated how variations in the simulation parameters will affect the signal stability and shape. The immediate impact of such variations on the luminosity determination will be readdressed in chapter 8.

The category of systematic uncertainties mentioned above, can even be divided further into sources related to the detector itself (*the simulation step*) and to sources from the readout electronics (*the digitization step*).



(a) (b)

Figure 6.21: *Stability of the signal amplitude (a) and signal width (b) as a function of variation in the simulation parameters. To improve the clarity of the plots, the results for the variation in gas temperature and tube reflectivity have been rescaled. See table A.1 in the appendix for precise values.*

6.5.1 The simulation step

Gas pressure

Theoretically, the number of Cerenkov photons produced in the detector is proportional to the pressure of the radiator gas (see eq. 6.4 and 6.6). However, at a higher pressure, the emission angle of Cerenkov photons is also larger (see eq. 6.4 and 6.3).The Cerenkov angle is 3° at 1 bar of C_4F_{10}, while it is 5° at 2 bar. A larger angle means that the photons experience more reflections in the tube and thus more light is lost. This in turn means that the signal amplitude as a function of gas pressure will have a turning point in which the signal amplitude starts to decrease with increasing gas pressure[6].
The absolute pressure in LUCID is set to 1.1 bar i.e., 0.1 bar over atmospheric pressure, and it is monitored to a precision of $\sim \pm 10$ mbar. A simulation study was performed by adjusting the working pressure to (1.10 ± 0.01) bar and afterwards interpolating the results down to the monitored precision. From the filled circles in figure 6.21 it can be seen that the signal amplitude does indeed increase as the gas pressure is increased. A pressure variation which matches the precision of the pressure gauge, results in a relative change of the signal amplitude of $\pm 0.5\%$ and a relative change in the signal width of $\pm 1\%$.

[6]The contribution to the signal from the quartz window remains unaffected by any change in gas pressure.

Gas temperature

The signal amplitude is in addition expected to be inverse proportional to the gas temperature. With LUCID operating at room temperature (20°), a worst case temperature variation of 19°C to 21°C is assumed, which corresponds to ±5%. In the same manner as above, a simulation study was performed by adjusting the working temperature by 10% and afterwards interpolating the results down to the maximal expected temperature variance of 5 °C. From the triangles in figure 6.21 it can be seen that the signal amplitude does indeed decrease as the gas temperature is increased. A induced temperature variation which matches the maximal expected temperature variation, results in a relative change in the signal amplitude of ±3% and a relative change in the signal width of ±5%.

Tube reflectivity

Another possible source of systematics is the level at which the tubes are polished. The tube polish is important to know since it is directly related to the tube reflectivity and thereby the percentage of Cerenkov photons absorbed on the tube wall. Despite the importance of this quantity the precision to which it is known is relatively low, resulting in a large systematic uncertainty. In the simulation the tube polish is assumed to be perfect meaning that the tube reflectivity is taken to be the one showed in figure 6.4(a). To study the effect of not having a perfect tube reflectivity, variations of 5% and 10% have been introduced and the result on the signal amplitude and width are shown in figure 6.21. The maximal deviation is here assumed to be 5% leading to a relative change in signal amplitude of ±5% and a relative change in the signal width of ±10%.

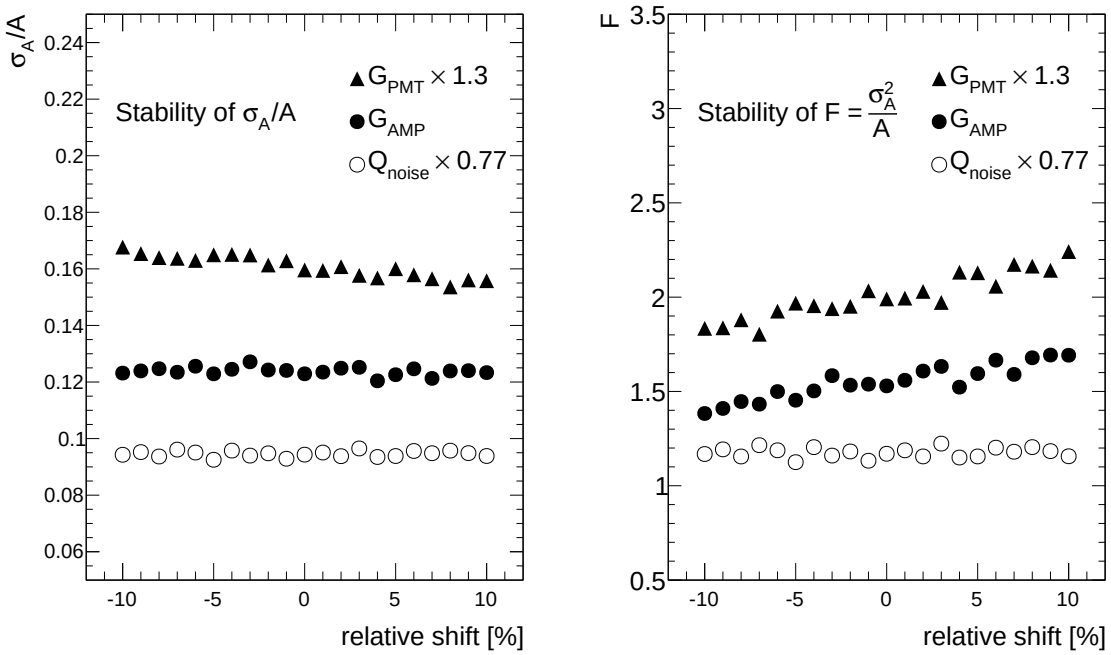
6.5.2 Digitization step

PMT gain (G_{PMT}) and amplification factor (G_{AMP})

The amplitude of the signal which is produced by the PMT is directly proportional to the gain and amplification factor of the PMT. This means that an increase of 5% in either the gain or the amplification factor results in a 5% increase of the readout charge. Fortunately the PMT in itself is designed in such a way that the ratio σ_A/A should remain constant and thereby provide a large degree of stability. Figure 6.22(a) shows that the simulation reproduces this feature when the gain and amplification factor is varied in the range of ±10%. The same feature is not expected in the case of the $F = \sigma_A^2/A$ factor (see figure 6.22(b)) on the account of the extra factor of σ_A in the nominator which is proportional to G_{PMT} and G_{AMP}.
Both G_{PMT} and G_{AMP} can be monitored by the LED calibration system to an accuracy of ±5%. By correlating the stability information given in figure 6.22(a) and 6.22(b) it can be shown that for a variation of ±5% in $G_{PMT}(G_{AMP})$ the shift in signal amplitude (A) and width (σ_A) is ±2.1%(±0.1%) and ±3.9%(±4.2%) respectively.

PMT noise factor (Q_{noise})

The operational lifespan of a PMT is to a large extent determined by the collective dose the PMT is subjected to. One of the effects of radiation damage is an increased level of dark



(a) (b)

Figure 6.22: *Stability of σ_A/A and F as a function of variations in G_{PMT} , G_{AMP} and Q_{noise}. The values of the data points of the two graphs are given in table A.2 of appendix A. It should be noted that stability studies presented here are carried out on a larger data sample than the one used in section 6.4.3 which is reflected in the smaller statistical errors on the data points.*

current leading to an increased noise level of the PMT. The effect of an increased PMT noise level is to widen the signal peaks and thereby decease the significance of the signal with respect to the background. At normal operation, the noise level is not expected to fluctuate with more than 5%. From figure 6.22 is can be seen that fluctuation in the noise level of 5% lead to shift in the signal size and shape of less than 1%.

6.6 Conclusion

A detailed description of the LUCID detector has been implemented in the ATLAS software framework. This description incorporates all major effects needed to obtain a realistic description of light production and propagation in a detector based on the detection of Cerenkov light. This includes a truthful description of the tube reflectivity and a realistic adaptation of the quantum efficiency of the PMT. The detector description has been validated through a series of test aimed at identifying the response of the detector in different situations.
By exposing a single tube in LUCID to 180 GeV of simulated on-axis pions, it can be concluded that a primary particle should produce a clean Gaussian peak in the pulse-height spectrum at the position of 100 photo-electrons. The contribution of light produced in the tube gas account for 71 photo-electrons while the contributions from the PMT window ac-

counts for the remaining 29 photo-electrons. By letting the pions traverse the LUCID module and thereby interact with the detector material, it can be concluded that even in events with a single particle, a dominating part of the pulse-height spectrum can be ascribed to secondary particles. The position of the signal peaks remains the same, but presence of the secondary particles give rise to a continues background. The same picture emerges when the response of the detector to *pp* collisions are simulated. It can however be concluded, that since the number of secondaries are proportional to the number of primaries, they will not constitute a background source to the luminosity measurement, but rather be a part of the the signal. The detector description is further validated by investigating the different aspects of the particles giving a signal in LUCID. This has been done to track down any inconsistencies and unexpected behavior that might later on lead to a wrong estimation of the luminosity.
The simulation of the readout electronics is addressed in the second half of the chapter. A more realistic simulation of the PMT dynode-chain is motivated and results from the implementation are given. Based on these results it can be concluded that a realistic simulation of the PMT dynode-chain leads to a more realistic simulation of the PMT response as a whole. The last section in this chapter has been devoted to the identification of possible sources of systemic uncertainty in the simulation.

Chapter 7

Performance of LUCID in the early 2010 data-taking period

7.1 Data Samples and Event Selection

7.1.1 Real data

The dataset used in the following performance study corresponds to 11 collision runs at $\sqrt{s} = 7$ TeV taken in the period from March 31 to April 4, 2010. The total number of events recorded in this period is 6.5×10^6 corresponding to an integrated luminosity of 49 mb^{-1}. To clean up the sample and to avoid a too large contamination from beam background a simple pre-selection has been applied:

- Only data with stable beam conditions flagged, are taken into account.
- Only filled and colliding bunches are included.
- Only events triggered by the MBTS double arm trigger has been included in this study.

The preselection requiring stable beam conditions and a minimum bias trigger requirement reduced the original sample by 66 % to 2.2×10^6 events.
The reason why only data from the above-mentioned period have been included is that the number of collisions per bunch crossing (μ) in these runs is very small ($\mu \ll 1$). This means that the probability for having more than one collision per bunch crossing is negligible. Thus it can be assumed that the results presented in this chapter are due to one and only one collisions. Under these conditions the results from data can be compared to results from MC simulation directly without having to correct for pileup since MC simulation is based on bunch crossings with exactly one collision.

7.1.2 Monte Carlo simulation

The inelastic *pp* interactions are simulated using the PYTHIA and PHOJET Monte Carlo generators.

PYTHIA: The simulation of inelastic pp interactions with PYTHIA comprises non-diffractive (ND), single-diffractive (SD) and double-diffractive (DD) processes. The corresponding datasets are identified with the numbers: 105001 (ND), 105003 (SD) and 105004 (DD). The generator-level cross sections at 7 TeV are listed in table 6.2. Tunes that have been used are:

- **PYTHIA MC09 [86]:** A tune which emphasizes the description of underlying event (UE) and minimum bias (MB) distributions for the ATLAS MC production which started in autumn 2009 (hence called MC09).
- **PYTHIA DW [87]:** Rick Field's Tune DW to Tevatron underlying-event and Drell-Yan Data. It has 2 GeV of primordial k_T and uses a very small renormalization scale for initial-state radiation (i.e., more ISR radiation).
- **PYTHIA Perugia [88]:** An updated tune of the p_T-ordered shower and underlying-event model in with respect to the standard PYTHIA tune. The data sets used to constrain the model include hadronic Z^0 decays at LEP, Tevatron minimum-bias data at 630, 1800 and 1960 GeV, Tevatron Drell-Yan data at 1800 and 1960 GeV and SPS min-bias data at 200, 546 and 900 GeV.
- **PYTHIA8 [89]:** This is not an actual tune but a complete rewrite of the PYTHIA program in $C++$ instead of Fortran. The difference of PYTHIA8 compared to default PYTHIA is a more realistic description of diffractive processes.

PHOJET: The simulation of inelastic pp interactions with PHOJET comprises non-diffractive, single-diffractive, double-diffractive and central-diffractive (CD) processes. The corresponding datasets are identified with the numbers: 96096 (ND), 96097 (SD), 96098 (DD) and 96099 (CD). The generator level cross section are likewise listed in table 6.2.

The PYTHIA MC09 tune has been chosen as the default simulation, while the PHOJET sample along with other PYTHIA tunes are used to explore systematic uncertainties in modeling of the inelastic pp interactions[1].

7.2 Data formats

The data from LUCID are recorded in three different ways/streams as mentioned in section 5.3. The distinction between the different streams is crucial in the following study so their properties are briefly summarized here. The first and primary stream is the global ATLAS stream, which contains all events, recorded by the central ATLAS DAQ and which in the case of LUCID contains the hit-pattern from the discriminators as well as the LUCID trigger decisions. The global ATLAS stream contains information from all other sub-detectors in parallel with LUCID, making it possible to correlate hit information in LUCID to any other reconstructed quantity in ATLAS. Having information from the entire ATLAS detector available for each bunch crossing ID (BCID) makes it possible to determine the efficiency of LUCID by a data driven method as will be shown in section 7.5.
The second stream of data for LUCID, is the local data stream. This stream is triggered

[1]The AMI [82] simulation tag was s764 for all used samples.

by local NIM logic that uses the discriminator signals as inputs and requires at least one hit somewhere in the two detector modules. This stream records the QDC and FADC values in addition to the CDF hit-pattern and stores the data with the help of the CERN advanced storage manager (CASTOR). As the name indicates the local stream is indeed decoupled from the global ATLAS stream making it impossible to correlate information from the local stream to any other detector. However, the local stream does record a timestamp and a BCID for each event, making it possible to select events in which two bunches are colliding - so called *paired bunches*. The advantage of this stream is that it contains QDC counts on a tube-by-tube basis for each event, making it possible to do performance studies when the hit threshold is varied.
The third and last data stream is the LUMAT data stream. The data from the LUMAT card is made available online by the so-called information service (IS) and from there picked-up by applications such as the online luminosity calculator (OLC). The LUMAT data is stored using the monitoring data archiving system (MDA) as ROOT [90] histogram files for each individual bunch crossing as well as for entire luminosity blocks. These histograms contain the number of empty events plus the number of hits for the different algorithms that are being used in LUMAT.

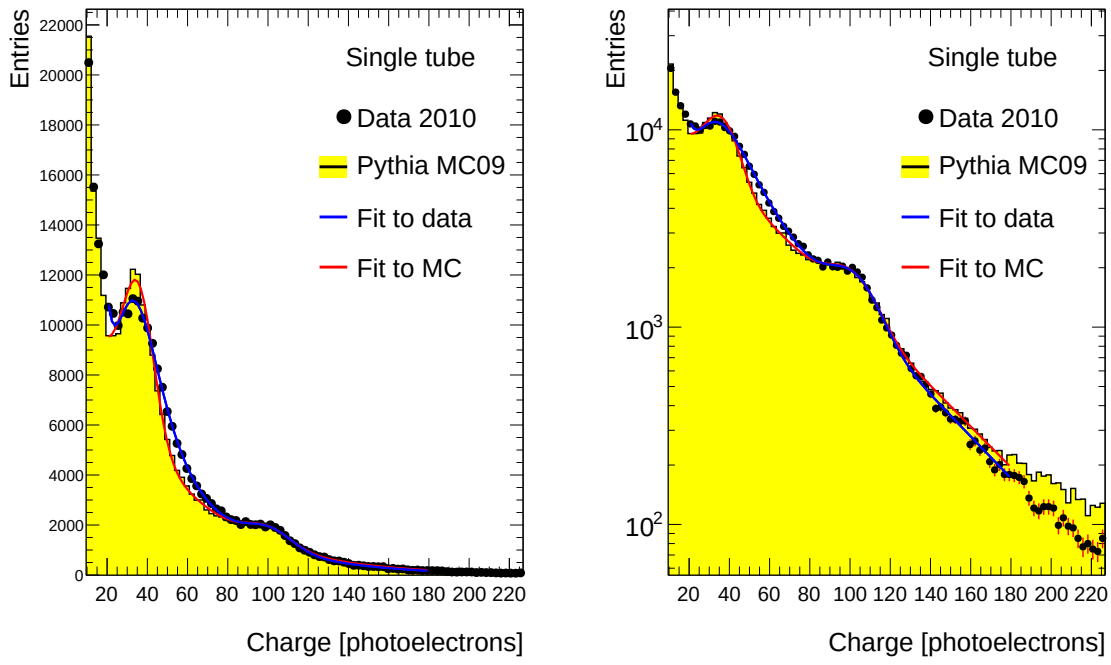
LUCID online trigger selection

The hit pattern for each bunch crossing is fed into a specially designed VME backplane. The signals are then processed by a FPGA in order to provide two trigger bits for the CTP. These triggers requires at least one hit in one of the two detector arms A and C, therefore labeled as LUCID_A and LUCID_C triggers. From these the full set of LUCID LVL1 trigger items can be formed and filled on an event per event basis by the CTP. The list of triggers can be found in table 6.4 and in the following L1_LUCID_X will refer to any of the triggers.
During the early 7 TeV data-taking period, the CTP was providing un-prescaled LUCID triggers whenever LUCID_A or LUCID_C bits were set. In parallel, the LUMAT card can also deliver trigger signals which is independent of the CTP. Analogously to the LVL1 triggers, the LUMAT trigger items are denoted as LUMAT_A and LUMAT_C with LUMAT as the OR of the two (all together referred to as LUMAT_X).

In the 2009 and 2010 data-taking periods, two of the 32 channels in LUCID was unable to record data, leading to slightly reduced detection efficiency. In what follows the corresponding channels have been masked out in MC data to provide a more realistic performance study.

7.3 Charge distributions

Based on the information stored in the local stream, the number of detected photo-electrons can be extracted for each tube on an event per event basis. To do so, the recorded charge, in QDC counts, must be converted into the number of photo-electrons by the calibration procedure described in section 5.3.2. An example of such a photo-electron spectrum is shown in figure 7.1 for a single tube. The corresponding distribution from the MC sample is superim-



(a) (b)

Figure 7.1: *An example of a charge distribution of a single tube recorded by the QDC presented in linear scale (a) and logarithmic scale (b). Fits to both distributions have been superimposed on the plots.*

posed to facilitate a shape comparison between data and MC. The normalization is such that the number of events in the Monte Carlo spectrum corresponds to the measured luminosity. Both distributions have the expected two peaks at approximately the same positions. The first peak around 40 photo-electrons is caused by particles that have only gone through the photomultiplier window and not the gas in the Aluminium tubes. The second peak at around 100 photo-electrons is caused by particles going through the full length of the Cerenkov tube.

Fitting the single tube photo-electron spectra

To obtain a more qualitative comparison between the single tube photo-electron spectra in MC and data, both distributions have been fitted with a sum of two Gaussians to describe the peaks and two exponential functions to describe the rest of the distributions:

$$f(x)_i = C_i \exp\left(-\frac{(x-\lambda_i)^2}{\sigma_\lambda^2}\right) + e^{(K_i - \delta_i x)} \quad \text{where} \quad \text{i=low and high peak} \tag{7.1}$$

$$\mathcal{F}(x) = f(x)_{low} + f(x)_{high} \tag{7.2}$$

where x is the value of the detected charge in units of photo-electrons. The motivation for extracting the exact peak position from data via a fit procedure is to correct the MC spectra in the case they do not agree.

Since the shape of the background level is different for the lower part (< 60 p.e) and higher part of the spectra it has been necessary to introduce a separate background description for the two ranges. Hence the lower and higher part of each spectrum is fitted in turns and when convergence of the individual fits is obtained, the results are combined to fit the full range with function $\mathcal{F}(x)$. The results of the fits are superimposed on the distributions in figure 7.1 and quoted in table 7.1.

Parameter	**single tube (Data)**	**single tube (MC)**
C_{low}	$2.94 \times 10^3 \pm 56.27$	$5.64 \times 10^3 \pm 54.67$
$\lambda_{low}[p.e]$	39.82 ± 0.15	35.55 ± 0.07
$\sigma_{\lambda_{low}}[p.e]$	8.73 ± 0.12	$7.78 \pm 9.74 \times 10^{-3}$
K_{low}	9.03 ± 0.05	8.75 ± 0.03
δ_{low}	$0.02 \pm 3.54 \times 10^{-4}$	$0.02 \pm 1.28 \times 10^{-3}$
C_{high}	730.20 ± 23.44	663.15 ± 15.11
$\lambda_{high}[p.e]$	100.77 ± 0.41	100.30 ± 0.29
$\sigma_{\lambda_{high}}[p.e]$	11.60 ± 0.54	11.30 ± 0.28
K_{high}	12.44 ± 0.24	8.96 ± 0.02
δ_{high}	$0.09 \pm 5.49 \times 10^{-3}$	$0.02 \pm 1.05 \times 10^{-3}$

Parameter	**Side A (Data)**	**Side A (MC)**
C_{low}	$5.13 \times 10^4 \pm 242.17$	$7.59 \times 10^4 \pm 1.12 \times 10^3$
$\lambda_{low}[p.e]$	42.83 ± 0.045	39.84 ± 0.12
$\sigma_{\lambda_{low}}[p.e]$	10.35 ± 0.07	9.05 ± 0.17
K_{low}	183.58 ± 1.37	30.91 ± 8.25
δ_{low}	8.51 ± 0.07	1.03 ± 0.40
C_{high}	782.55 ± 68.34	$8.85 \times 10^3 \pm 293.47$
λ_{high} [p.e]	108.51 ± 0.13	111.99 ± 0.48
$\sigma_{\lambda_{high}}$ [p.e]	12.45 ± 0.16	12.66 ± 0.28
K_{high}	$12.32 \pm 3.83 \times 10^{-3}$	12.16 ± 0.01
δ_{high}	$0.024 \pm 3.37 \times 10^{-5}$	$0.02 \pm 1.76 \times 10^{-4}$

Table 7.1: *Parameter values extracted from a fit of the function in eq 7.2 to the photo-electrons distributions for a single tube (upper table) and a single module (lower table).*

It is clear from the results that the higher part of the distribution in data is fairly well described by MC. Both the position and width of the second peak are compatible within the errors. Given the fact that the two distributions are normalized to the same integrated luminosity, it is possible to compare the constant C_{high} and take it as an expression of the relative contribution of primary particles. Since the values of C_{high}^{data} and C_{high}^{MC} are in agreement within three standard deviations it can be concluded that the contribution of primaries traversing the full length of the Cerenkov tube is well described by the simulation of LUCID.
Compared to the upper part of the distributions, the lower parts of the spectra does not exhibit the same excellent agreement between MC and data. From the results in table 7.1 it can be seen that the MC tends to underestimate the width and positions of the first signal

peak while it overestimates the signal height. Several effects and quite possibly a combination of those can explain such a disagreement. For one, in the simulation of LUCID it is assumed that the PMT window is fully sensitive over the entire surface. If this is not the case in the real detector, then the simulation will overestimate the effective size of the window and thereby overestimate the contributions of secondary particles that only hit the PMT window. A second effect that might lead to the same result is if the forward shielding and the material of the beam pipe is not modeled correctly in the GEANT4 simulation. An excess of material in the simulation will lead to an increased production of secondary particles and thereby an increased contribution of particles which only gives a signal in the PMT window. The two effects mentioned here are troublesome since they are notoriously difficult to check. The first would require setting up a test bench to check the sensitive area of the PMTs installed in LUCID. The other would require a perfect geometric model in the MC of the forward shielding.

Tube number	λ_{low} [p.e]	$\sigma_{\lambda_{low}}$ [p.e]	λ_{high} [p.e]	$\sigma_{\lambda_{high}}$ [p.e]
		MC		
all tubes	35.55 ± 0.07	$7.78 \pm 9.74 \times 10^{-3}$	100.30 ± 0.29	11.30 ± 0.28
		Data 2010 - Side A		
tube 3	40.45 ± 0.17	9.79 ± 0.24	104.61 ± 0.35	10.68 ± 0.41
tube 5	46.27 ± 0.13	9.78 ± 0.18	111.44 ± 0.31	9.82 ± 0.38
tube 6	44.05 ± 0.13	9.63 ± 0.18	111.40 ± 0.34	10.67 ± 0.39
		Data 2010 - Side C		
tube 23	40.65 ± 0.17	9.70 ± 0.25	102.36 ± 0.42	11.64 ± 0.48
tube 24	42.15 ± 0.32	11.38 ± 0.43	135.52 ± 0.68	13.88 ± 1.49
tube 25	30.91 ± 0.41	19.01 ± 0.34	88.26 ± 1.12	31.92 ± 1.14

Table 7.2: *Examples of peak positions and signal width for various tubes.*

Fitting the total photo-electron spectrum

Unfortunately the agreement between data and MC is not as good for all the tubes as the one presented above (see table 7.2 for examples and table A.3 for the full list of fit results). The reason for this is that the stray magnetic field in ATLAS is not the same for LUCID on sides A and C. Since the readout system is based on photomultipliers, which are very sensitive to the field gradient transverse to the longitudinal direction, the stray magnetic field is important for LUCID. To incorporate these features in the simulation of LUCID would require a remodeling of the magnetic field topology in the vicinity of LUCID, and the effect on the photomultipliers, which is beyond the scope of this thesis. Instead, the uncertainty related to the difference in photo-electron spectra between MC and data will be assigned to the systematic uncertainty of the LUCID simulation. To illustrate the difference between the tube response in data and MC, figure 7.2 shows the average charge distribution for all the tubes on side A. The data were recorded using the single side trigger that requires at least one hit in one of the two detectors. The number of photo-electrons produced in the Monte Carlo

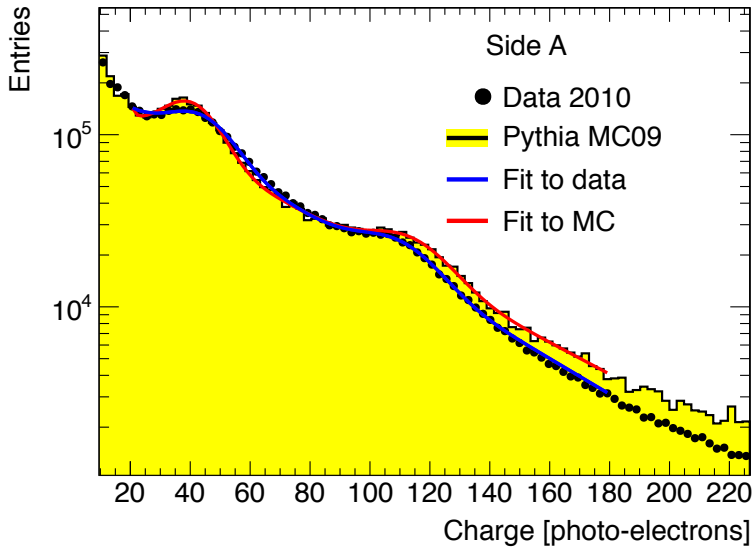


Figure 7.2: *The average charge distribution of all the tubes in one of the two detectors at 7 TeV. The number of events in the Monte Carlo spectrum is normalized to the data using the measured luminosity (29 mb^{-1}).*

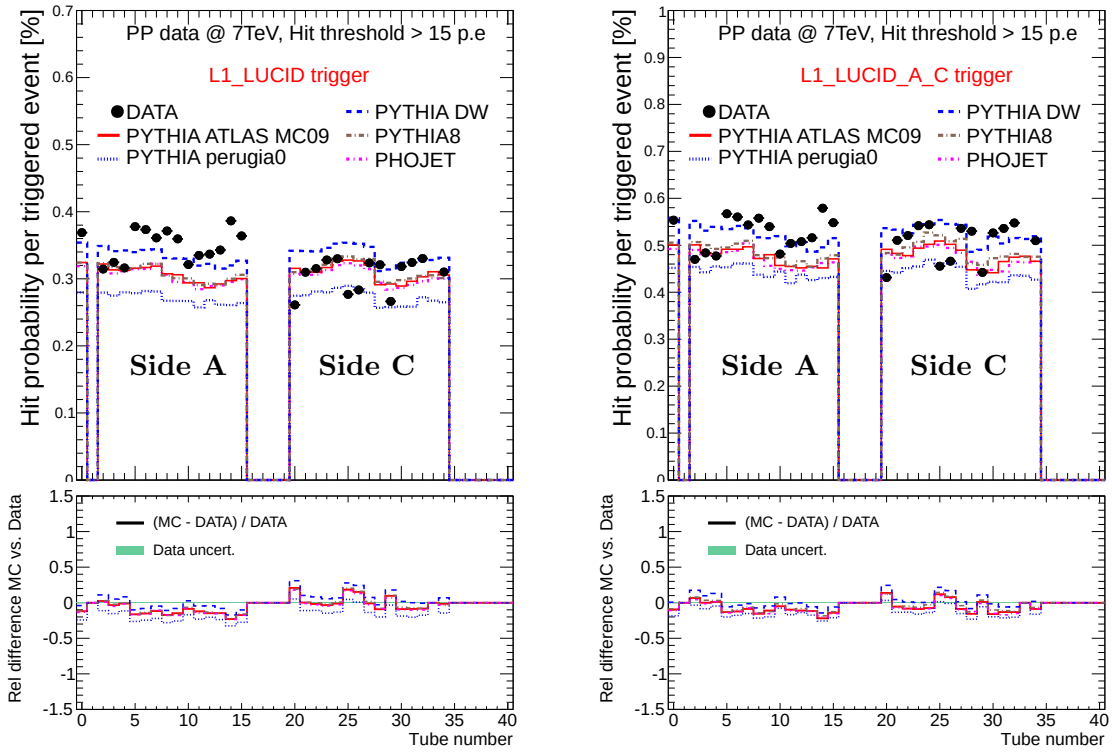
simulation has been recalibrated using data and increased with a factor 1.12 so that the two peaks from the Cerenkov light from only the photomultiplier window and from window+gas agree. Both distributions have been fitted by the same procedure used in the case of the single tube distribution and the results are likewise given in table 7.1. By comparing the results of the fit to the two distributions it is clear that summing up the response from all the tubes in one module worsens the agreement between MC and data. The discrepancy can be ascribed to differences in the shape of the distributions for the individual tubes caused by differences in the magnetic field.

7.4 Hit multiplicity distributions

Charge distributions, as the ones presented in figure 7.1 and 7.2 are very important to understand since they are the fundamental measurements which can be extracted from LUCID. All other information such as hit patterns and multiplicity distributions are derived from the photo-electron distribution. In the following section a number of detectable quantities related to the multiplicity will be presented. The reason for this is to study the performance of LUCID in the early 2010 data-taking period but also to validate the simulation of LUCID.

7.4.1 Hit probability for different tubes

Directly derived from the photo-electron distributions are the hit patterns. The hit patterns are binary maps indicating which tubes for a given event had a recorded charge above the threshold. If the hit patterns are summed over the duration of a run or several runs, the hit probability can be plotted as a function of the tube number, as it is done in figure 7.3 for the

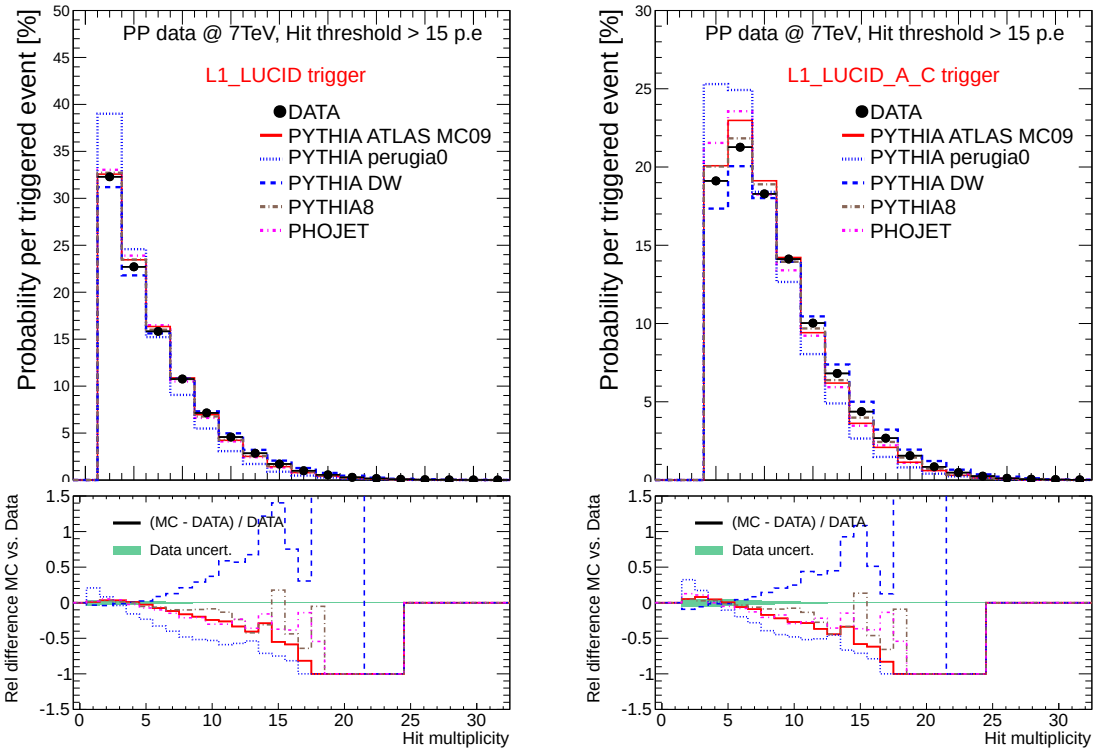


(a) (b)

Figure 7.3: *Hit probability as a function of Cerenkov tube number for events triggered by the single side trigger (a) and the coincidence trigger (b). The dots represent the data and the curves the predictions from different MC models.*

two composite triggers. Similar distributions from the different Monte Carlo generators are superimposed for comparison. From the kinematics of the hard scattering it is expected that the hits are uniformly distributed over all the tubes. Due to the decreasing charged track multiplicity with pseudo-rapidity, it is naively expected that the hit probability will be larger for the tubes in the outer layers[2] than for the inner layers. Figure 7.3 shows that the opposite is the case for the MC distribution. The tubes in the inner layers have a slightly higher hit probability than the outer layers, a tendency that can be explained by the inner layers being more exposed to secondary particles created in the beam pipe. A similar tendency is not seen in the real data sample. Here the variations are simply too large to reveal any underlying structure and as a result the agreement between MC and data is poor. A series of Kolmogorov tests reveals that the probability that each of the MC distributions follows the same original distribution as the data is less than 1%. To get a feeling for the size of the tube to tube variations, the relative difference of the Monte Carlo prediction with the data are shown for each MC generator beneath the hit distributions in figure 7.3. For events which have been triggered by the OR trigger, the MC tends to underestimate the hit probability on the A side. For events triggered by the coincidence trigger, the difference in overall hit probability is less

[2]tube number 8-15 on the A side and tube number 28-35 on the C side.



(a) (b)

Figure 7.4: *The probability to have a certain number hits for events triggered by the single side trigger* L1_LUCID *(a) and coincidence trigger* L1_LUCID_A_C *(b). The dots represent the data and the curves the predictions from different MC models.*

pronounced due to the requirement of hits on both sides. The issue of hit asymmetry between the two LUCID modules will be addressed in greater detail later in this section. However, the level of agreement between MC and data differs as much as 30 % from tube to tube, mostly due to the stray magnetic field.

7.4.2 Hit multiplicity and asymmetry

The hit multiplicity is a measure of activity for a given event. An event with a high track multiplicity will in most cases lead to a high number of hits in LUCID signifying a positive correlation between the track multiplicity and hit multiplicity. In situations where $\mu \geq 1$ multiple interactions will lead to a higher track multiplicity which in turn will lead to a higher hit multiplicity in LUCID - an effect which is essential for using LUCID as a luminosity monitor. In fact the average hit multiplicity along with the detection efficiency are some of the main input to the luminosity algorithms, which will be discussed later in the thesis. Figure 7.4 shows the hit multiplicity[3] for events triggered by L1_LUCID and L1_LUCID_A_C. Because of

[3]The normalization is carried out so that the ordinate gives the probability for a given number of hits and not number of entries.

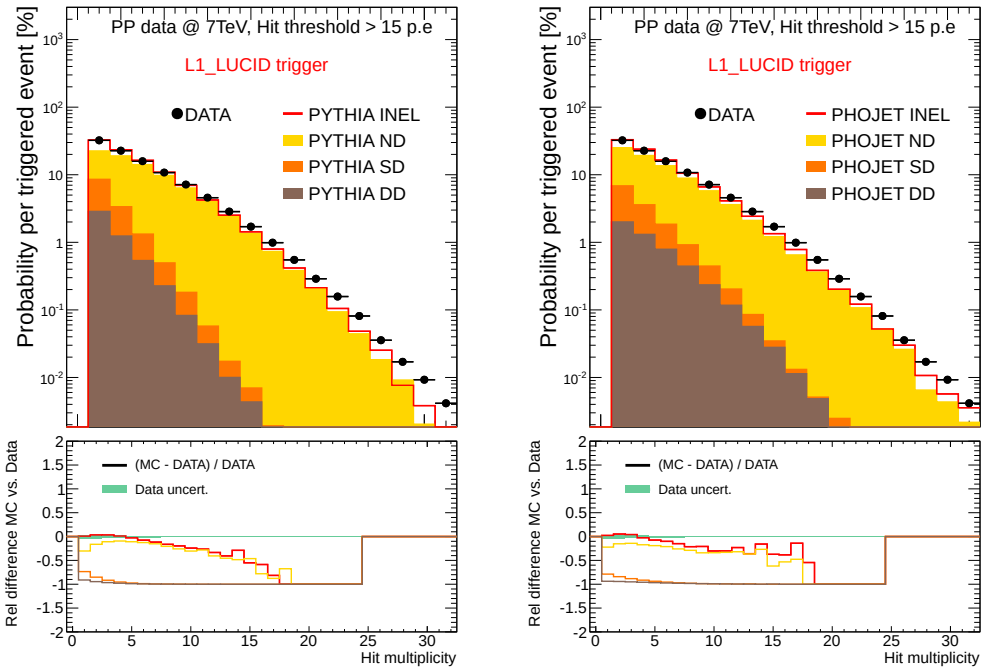
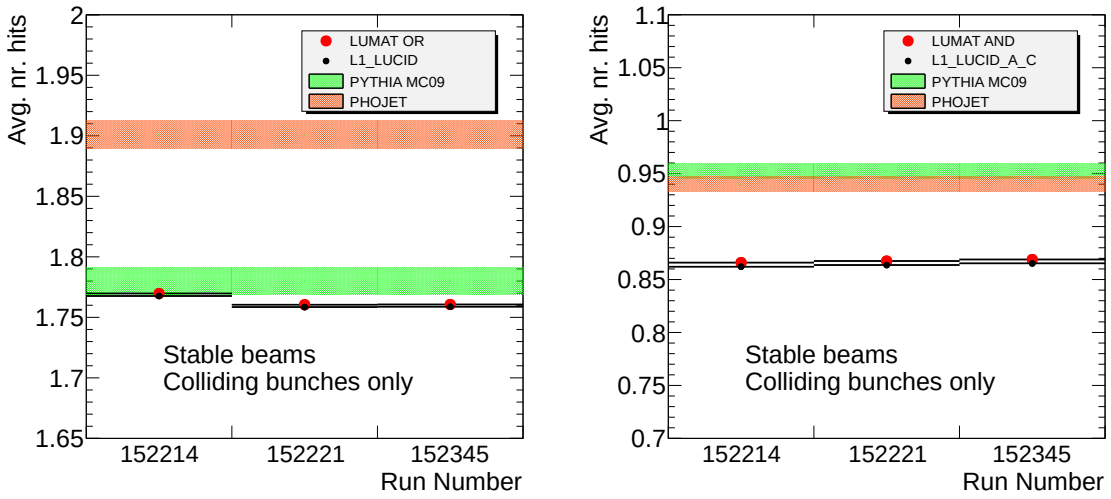


Figure 7.5: *The probability to have a certain number hits for events triggered by the single side trigger* L1_LUCID *(a)(b) and coincidence trigger* L1_LUCID_A_C *(c)(d). Results from real data is compared to the PYTHIA MC09 and PHOJET predictions showing the different components: non-, single- and double-diffractive separately. The different contributions have been scaled according to the cross section given in table 6.2 and presented in logarithmic scale.*

the running condition under which the data was obtained ($\mu \ll 1$), the two distribution are expected to peak at low hit multiplicity. In the case of the single side trigger this indeed seems to be the case since the distributions peak at $N_{hits} = 1$. However, in the case where a coincidence of hits is required, the distributions do not peak at $N_{hits} = 2$ but at $N_{hits} = 3$. A feature, which illustrates that, the coincidence trigger to a larger extent than the single side trigger selects events with a high track multiplicity. A trivial observation perhaps but nevertheless important since beam background events will in general have a low track multiplicity and are thereby more likely to contaminate a data sample collected by using the single side trigger that for the coincidence trigger.
The agreement between MC and data for the two types of triggered events is best in the lower part ($N_{hits} \leq 5$) of the distributions. In this region the predictions from all Monte Carlo models except PYTHIA Perugia are compatible with data within three standard deviations. In the high hit multiplicity region the majority of the MC models tend to underestimate the hit probability with, relative deviation as much as 100%. A possible explanation for part of the poor agreement lies in the relative composition of the total inelastic cross section, more precisely, the ratio of diffractive to non-diffractive events and the mean multiplicity of those events. The diffractive component of the total cross section is different for the different Monte Carlo generators. For PYTHIA the diffractive component constitutes 38% of the cross section whereas for PHOJET the contribution is only 19% (see table 6.2). Because of the inelastic nature of the non-diffractive events, events generated by PHOJET will in principle have a higher hit multiplicity than events generated by PYTHIA and thereby describe data better. Figure 7.5 shows the hit multiplicity for different event types when triggered by the single side trigger. The increased non-diffractive components of PHOJET only leads to a slightly better description at mid multiplicity and an overestimation at high hit multiplicity. It should be noted here that the default version of PYTHIA (MC09) used in this study has been tuned so the non-diffractive component has a higher average track multiplicity than standard PYTHIA. As a result of this, the mean of the hit multiplicity distribution ($\langle N \rangle^{OR}_{hits/pp} = 2.773$) is larger than for PHOJET ($\langle N \rangle^{OR}_{hits/pp} = 2.715$) despite the smaller contribution from non-diffractive events. The distributions show the same tendency for events triggered by the coincidence trigger L1_LUCID_A_C where ($\langle N \rangle^{AND}_{hits/pp} = 4.292$) for PYTHIA MC09 and PHOJET ($\langle N \rangle^{AND}_{hits/pp} = 4.182$).
By extracting the mean values of the hit distribution, one essentially obtains the mean number of hits per detected *pp* collision. A related quantity is the average number of hits per bunch crossing (BX) denoted $N_{hits/BX}$. Since not all bunch crossings contain a *pp* collision which is detected by LUCID, this quantity is expected to be smaller than $N_{hits/pp}$. It is clear however that if LUCID had a trigger efficiency of 100% then the two would coincide. The run by run values of $N_{hits/BX}$ for both LVL1 composite items are compared to the MC prediction in figure 7.6 and table 7.3. For both triggers the run-by-run fluctuations are small and the data points for the two data streams coincide. Some run-by-run fluctuations are expected and can be traced back to a strong variation of beam background in the early 2010 data-taking period. Such variation will affect the single side trigger the most due to the one sided topology of beam gas events. An observation which is supported by the less pronounced fluctuations for the coincidence trigger in figure 7.6(b).



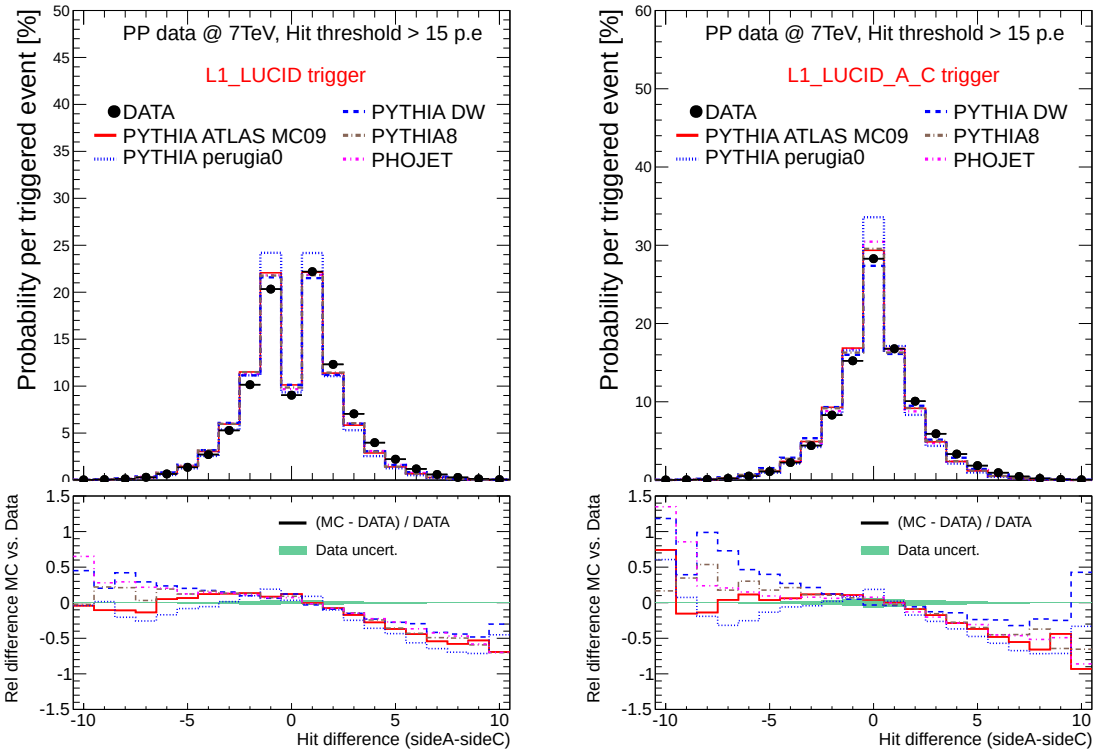
(a) (b)

Figure 7.6: *Average number of hits per bunch crossing for event triggered by the single side trigger (a) and the coincidence trigger (b). The input to the data points is taken from two different data stream, namely from the LUMAT card (red points) and the global ATLAS data stream (black points). Colored bands represent predictions from PYTHIA and PHOJET including statistical errors.*

	$N^{OR}_{hits/BX}$	$N^{AND}_{hits/BX}$
	Data 2010	
LUMAT data stream	1.764 ± 0.001	0.866 ± 0.001
ATLAS data stream	1.763 ± 0.001	0.867 ± 0.003
Model	**Monte Carlo**	
PYTHIA MC09	1.787 ± 0.011	0.953 ± 0.007
PYTHIA DW	1.945 ± 0.012	1.119 ± 0.008
PYTHIA perugia	1.432 ± 0.009	0.653 ± 0.0052
PYTHIA8	1.790 ± 0.011	0.953 ± 0.007
PHOJET	1.901 ± 0.012	0.940 ± 0.007

Table 7.3: *Average number of hits per bunch crossing for events triggered by the single side trigger and the coincidence trigger. The values for the data streams are obtained as a weighted mean of the data points in figure 7.6.*

Hit asymmetry: Since both $N_{hits/pp}$ and $N_{hits/BX}$ are used as inputs when calculating the luminosity with LUCID, stability is a key issue. Any variation in the beam background from a particular beam will lead to an asymmetry in the hit difference distribution. In such a scenario the asymmetry will be higher for events only flagged by the single side trigger, following the same arguments as presented above. Figure 7.7 shows the hit difference for events



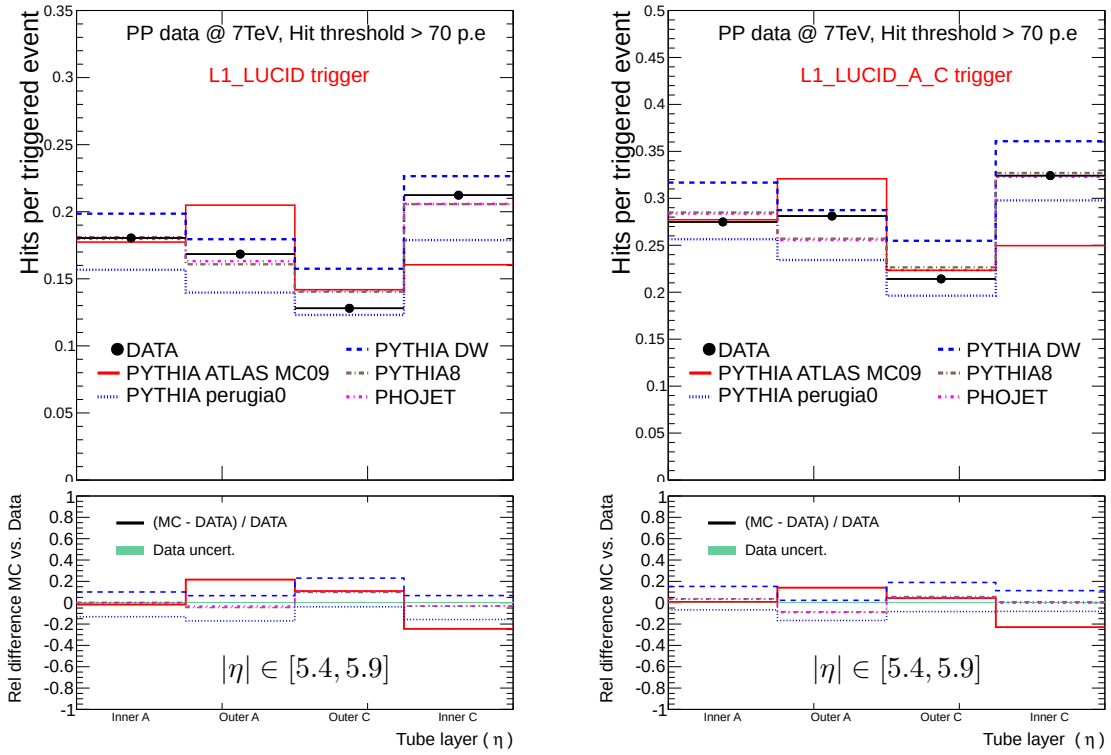
(a) (b)

Figure 7.7: *The probability to have a certain difference in hit multiplicity for events triggered by the single side trigger (a) and the coincidence trigger (b). The dots represent the data and the curves the predictions from different MC models.*

triggered by the two composite LVL1 triggers. A feature of the MC predictions presented in these plots is that they are generated based solely on *pp* collisions and do as such not contain any contribution from beam background. This means that if a background source is present in the data sample then the relative difference between MC and data would show this contribution as negative values and a mean different from 0. By looking at figure 7.7 this does indeed seem to be the case for values of $|\langle N^A - N^C \rangle_{hits/pp}| > 3$. However, this effect is most likely due to the difference in response of the two modules caused by the magnetic field on the two sides as discussed above. In fact it will be shown later in this chapter that the beam background level in the early data-taking period was negligible and thus cannot account for the hit asymmetry seen in figure 7.7.

7.4.3 Hit multiplicity vs. pseudo-rapidity

An extension of the study of hit asymmetry is the investigation of hit frequency for different parts of the detector. Despite the relative low number of channels in LUCID, it is still possible to study how the average number of hits varies as a function of pseudo-rapidity η. Since each module only has two co-cylindrical layers, the acceptance is divided into two bins. The overall $|\eta|$ coverage of the detector is $[5.4, 5.9]$ giving each bin a size of roughly 0.25 units in η. As



(a) (b)

Figure 7.8: *Average number of detected hits per triggered event separated into tube layer.*

demonstrated earlier, the signal in LUCID is heavily dominated by production of secondary particles. In a pseudo-rapidity distribution only the contribution from primary particles should ideally be included. To isolate this contribution, a threshold cut of 70 photo-electrons has been introduced to select particles which have traversed the full length of the Cerenkov tubes. The resulting distribution is shown in figure 7.8 where it is compared to similar Monte Carlo distributions. When the results for the inner layer on side A are compared to the results for the inner layer on the C side, a large discrepancy is observed. This is due to the fact that the inner layer in side A has a dead tube which is not the case for the C side. Similarly, the outer layer on side C has a dead tube which is not the case for the A side. As a consequence the average hit distribution becomes asymmetric around $\eta = 0$.

7.5 Efficiency determination

In this section the efficiency to select events at Level-1 (LVL1) with trigger items based on the LUCID signals is determined. This efficiency is defined as:

$$\varepsilon_{item} = \frac{\text{Events that pass the item conditions}}{\text{Events with one inelastic } pp \text{ collision}} \tag{7.3}$$

The efficiency is per definition calculated for events with one pp interaction. For MC data set, which per construction only contains one interaction per event, one can directly calculate the efficiency. For real data, one can only calculate the efficiency directly if the probability for pile-up is negligible. The data used in the performance study above meets this requirement since $\mu \ll 1$ throughout the data-taking period.

7.5.1 Online trigger selection

The online selection of events is based on the information available to the CTP before any level 1 trigger decision is taken. During the early 2010 running period, LUCID (see section 7.2) in combination with the MBTS and BPTX were the main minimum bias triggers for ATLAS and are therefore the primary input used to calculate the luminosity both online and offline. The relevant MBTS and LUCID trigger items are listed in tables 7.4 and 6.4 respectively.

Trigger Item	**Required Logic**
L1_MBTS_1_Col	(MBTS_A OR MBTS_C) & (BPTX0 & BPTX1)
L1_MBTS_1_1_Col	(MBTS_A & MBTS_C) & (BPTX0 & BPTX1)

Table 7.4: *Level-1 trigger items for MBTS.*

The LVL1 LUCID trigger items used here and in the previous section are identical to the ones used in the simulation with the additional requirement of a BPTX coincidence as for the MBTS triggers. The number of events passing these trigger requirements are counted with scalars and the results stored to the condition database (COOL).

ATLAS BPTX The main task of the ATLAS BPTX detectors [91] is to trigger on filled bunches. To do so, the BPTX signals are discriminated and shaped into 25 ns long pulses, which are fed into the CTP. The filled bunch trigger will enable the trigger system to know at which clock ticks there were particle bunches in the interaction region from either beam. In this study, the BPTX signals have been combined in coincidence with other triggers to form a veto against non-colliding bunches.

MBTS The MBTS provides 32 input signals to the CTP. Each signal pulse is 200 ns long and the total MBTS multiplicity is calculated in the CTP. The MBTS multiplicity is calculated for each side independently, which makes it possible to request a minimum number of hits on each side. From such information two trigger items are formed: L1_MBTS_1 and L1_MBTS_1_1 , both requiring a coincidence with a L1_BPTX signal from at least one side.

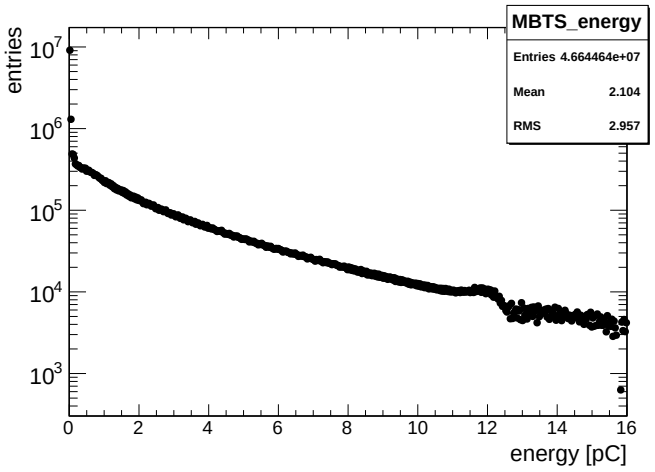


Figure 7.9: *The total energy spectrum of the MBTS.*

The nominal electronic threshold used to define a hit is set to 0.26 pC. Figure 7.9 shows the energy spectrum of the MBTS summed up over all the 32 tiles.
Table 7.4 lists the trigger requirements needed to form the MBTS items. The first item demands at least one MBTS hit, the second at least one MBTS hit on each side. The name extension "_Col" signifies that both BPTX signals are required in coincidence. Note also that due to the pulse length and given the fact that the time of flight from the MBTS station on side A to the station on side C is ~ 20 ns, a MBTS coincidence by itself does not necessarily mean that the hit time is produced by a with collision-like events. Requiring a coincidence with the BPTX system for the same event will remedy this effect.

7.5.2 Efficiency determination from Monte Carlo events

The MC samples used to calculate the efficiency are those described in Section 7.1.2. The samples are divided into groups of events according to the different components of the inelastic cross section: non-, single- and double-diffractive. Since the probability of pile-up events is negligible, the efficiency for a mixture of inelastic events is given by:

$$\varepsilon = \sum_{i=ND,SD,DD} \varepsilon_i \cdot w_i, \quad \text{where} \quad w_i = n_i \cdot \Big(\sum_{i=ND,SD,DD} n_i \Big)^{-1} \tag{7.4}$$

where ε_i and n_i are the efficiency and the number of events for sample i.
The efficiencies have been calculated for the main MBTS and LUCID items using the nominal electronic thresholds and the values are presented in table 7.5.

7.5.3 Data driven efficiency determination

Besides determining the trigger efficiencies using Monte Carlo simulations, it is also possible to determine the efficiencies using input from real data. This is typically done by calculating the relative efficiency from a data sample that has been selected by another detector. The advantage of this approach is that it is possible to move the dependence on the MC simulation

Trigger Item	ε^{ND}	ε^{SD}	ε^{DD}	ε^{INEL}
L1_MBTS_1_Col	1.000	0.704	0.847	0.924
L1_MBTS_1_1_Col	0.986	0.394	0.466	0.801
L1_LUCID_A (Col)	0.547	0.149	0.217	0.432
L1_LUCID_C (Col)	0.548	0.150	0.217	0.434
L1_LUCID (Col)	0.790	0.286	0.391	0.647
L1_LUCID_A_C (Col)	0.306	0.013	0.042	0.220

Table 7.5: *Level-1 MBTS and LUCID item efficiencies as determined with PYTHIA MC09 Monte Carlo simulations at $\sqrt{s} = 7$ TeV. The statistical error on all efficiencies is smaller than 10^{-3}.*

from the detector system in question to another detector system. In the following two methods will be used to extract the LUCID trigger efficiencies using data driven methods.

Method 1 - Using correlations estimated with Monte Carlo

From a data sample selected by a given trigger item, the trigger efficiency of another trigger item can be extracted provided that the two items under consideration have a sizable overlap and that the conditional efficiency between the two items is known. Under these conditions we have:

$$\varepsilon_{\text{item1}} = \frac{n_{\text{item1}}}{N} \tag{7.5}$$

$$\varepsilon_{\text{item2}} = \frac{n_{\text{item2}}}{N} \tag{7.6}$$

$$\varepsilon_{(\text{item1} \mid \text{item2})} = \frac{n_{(\text{item1 \& item2})}}{n_{\text{item2}}} \tag{7.7}$$

$$\varepsilon_{(\text{item2} \mid \text{item1})} = \frac{n_{(\text{item1 \& item2})}}{n_{\text{item1}}} \tag{7.8}$$

$$\varepsilon_{\text{item1}} = \varepsilon_{(\text{item1} \mid \text{item2})} \cdot \frac{\varepsilon_{\text{item2}}}{\varepsilon_{(\text{item2} \mid \text{item1})}} \tag{7.9}$$

where n_{item1}, n_{item1} are the number of events selected by item1 and item2, respectively. The total number of inelastic collisions produced during the data-taking period is denoted N, the conditional efficiency of item1 with respect to item2 is written $\varepsilon_{(\text{item1} \mid \text{item2})}$ and the number of events with both item1 and item2 fireing, is written $n_{(\text{item1 \& item2})}$. In the situation where data sample selected by item1 is fully contained into the one selected by item2, equation 7.9 simplifies to $\varepsilon_{\text{item1}} = \varepsilon_{(\text{item1} \mid \text{item2})} \cdot \varepsilon_{\text{item2}}$. In this case $\varepsilon_{\text{item1}}$ can be estimated from data if $\varepsilon_{\text{item2}}$ is known.
This method is used to estimate the L1_LUCID_X trigger efficiencies from a data sample selected with the L1_MBTS_1_1_Col trigger. An unbiased data sample containing about 6.5 million events have been selected online using only the L1_BPTX trigger. Applying the requirements of the MBTS reduces the data sample to 2.2×10^6 events from which the conditional efficiency of the LUCID trigger items with respect to the L1_MBTS_1_1_Col can be calculated using equation 7.8:

$$\varepsilon_{(\text{L1_LUCID_X} \mid \text{L1_MBTS_1_1_Col})} = \frac{n_{(\text{L1_LUCID_X \& L1_MBTS_1_1_Col})}}{n_{\text{ L1_MBTS_1_1_Col}}} \tag{7.10}$$

In order to extract $\varepsilon_{\text{L1_LUCID_X}}$ from this equation, $\varepsilon_{\text{L1_MBTS_1_1_Col}}$ and the conditional efficiency between L1_MBTS_1_1_Col and L1_LUCID_X must be known. Since the data sample contains events that have been selected by the MBTS trigger it will not be possible to extract these quantities using data. As a consequence the only option is to use MC. Table 7.5 shows the results for $\varepsilon_{\text{L1_MBTS_1_1_Col}}$. To evaluate the systematic uncertainty introduced by relying on MC simulation to estimate the $\varepsilon_{\text{L1_MBTS_1_1_Col}}$ efficiency the trigger has been varied around the nominal threshold of 0.26 pC. The looser configuration requires a cut of 20 pC while the tighter configuration a cut of 30 pC. The variation in the efficiency to inelastic *pp* collisions is within 2%
By using equation 7.9 the expression for $\varepsilon_{\text{L1_LUCID_X}}$ can be found as:

$$\varepsilon_{\text{L1_LUCID_X}} = \frac{\varepsilon_{(\text{L1_LUCID_X} \mid \text{L1_MBTS_1_1_Col})}}{\varepsilon_{(\text{L1_MBTS_1_1_Col} \mid \text{L1_LUCID_X})}} \cdot \varepsilon_{\text{L1_MBTS_1_1_Col}} \tag{7.11}$$

The results for the conditional efficiencies between L1_LUCID_X and L1_MBTS_1_1_Col are shown in table 7.6 along with the results for $\varepsilon_{\text{L1_LUCID_X}}$.

Method 2 - Using uncorrelated triggers

Starting from the same sample as for method 1 the trigger efficiency of a given item (item1) can then be found by comparing the number of events selected by a LUCID trigger and a complementary one (item2). There are no requirements on the complementary trigger other than that is should have a known efficiency. The main assumption in this method is that the two triggers are completely uncorrelated. Under this hypothesis the conditional efficiency of item1 and item2 reduces to $\varepsilon_{(\text{item1} \mid \text{item2})} = \varepsilon_{\text{item1}}$ and the efficiency of item1 can be calculated from the raw trigger counts. Assuming that the efficiency of item2 can be estimated with a Monte Carlo simulation and that the simulation correctly describes the different components of the inelastic cross section, it follows that:

$$\varepsilon_{\text{item1}} = \frac{n_{\text{item1}}}{n_{\text{item2}}} \cdot \varepsilon_{\text{item2}} \tag{7.12}$$

Taking L1_LUCID_X as $item1$ and L1_MBTS_1_1_Col as $item2$ eq. 7.12 becomes

$$\varepsilon_{\text{L1_LUCID_X}} = \frac{n_{\text{L1_LUCID_X}}}{n_{\text{L1_MBTS_1_1_Col}}} \cdot \varepsilon_{\text{L1_MBTS_1_1_Col}} \tag{7.13}$$

By inserting the number of triggers found for L1_LUCID_X and L1_MBTS_1_1 in the BPTX dataset and the L1_MBTS_1_1_Col efficiency from table 7.5 the efficiency of the LUCID items has been calculated and are given in table 7.6.
A further assumption in this method is that both triggers are insensitive to beam background (an assumption which will be tested in the next section).

7.5.4 Efficiency and systematic uncertainty

Identification of sources of systematic uncertainty in the determination of efficiency is essential since the uncertainties propagate directly to the luminosity measurement. Especially at low μ the total systematic error on the luminosity measurement is dominated by the systematic uncertainties from the efficiency determination.

	Method 1			
L1_LUCID_X :	L1_LUCID_A	L1_LUCID_C	L1_LUCID	L1_LUCID_A_C
$\varepsilon_{(\text{L1_LUCID_X} \mid \text{L1_MBTS_1_1_Col})}$	0.487	0.458	0.708	0.237
$\varepsilon_{(\text{L1_MBTS_1_1_Col} \mid \text{L1_LUCID_X})}$	0.961	0.963	0.892	0.995
$\varepsilon_{\text{L1_LUCID_X}}$	0.407	0.382	0.638	0.191
	Method 2			
L1_LUCID_X :	L1_LUCID_A	L1_LUCID_C	L1_LUCID	L1_LUCID_A_C
$\varepsilon_{\text{L1_LUCID_X}}$	0.420	0.394	0.664	0.193

Table 7.6: *LUCID Level 1 trigger efficiencies calculated using the two data driven methods. The statistical error on all efficiencies is smaller than* 10^{-3}.

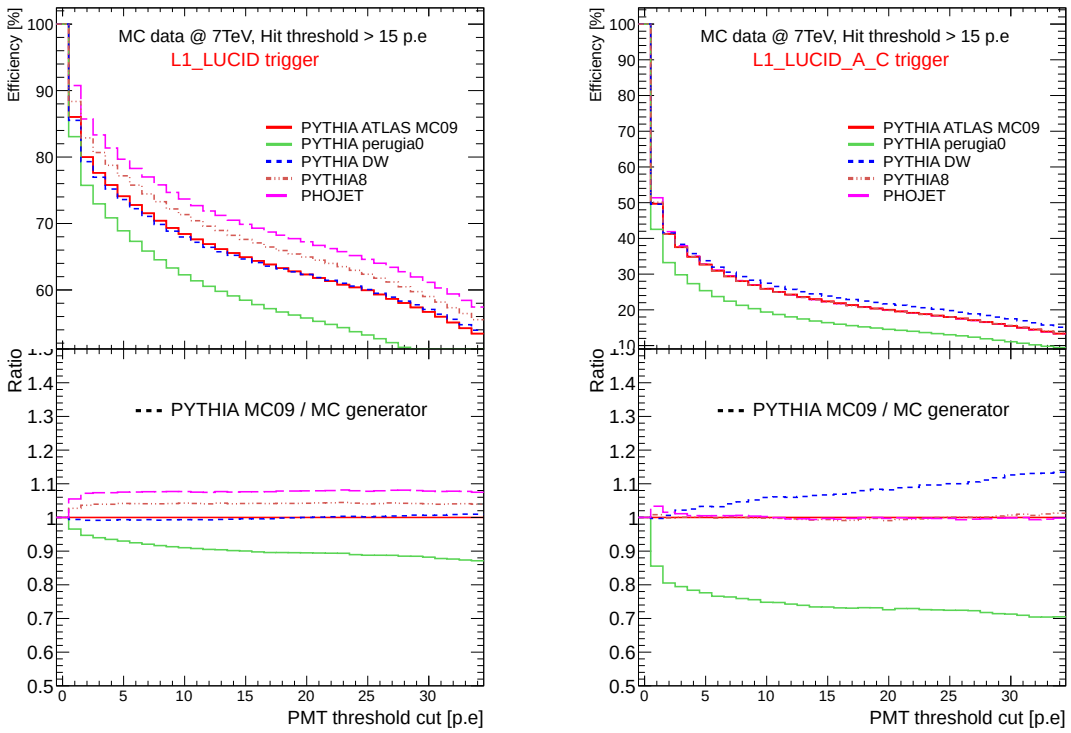
	Monte Carlo			
Generator	$\varepsilon_{\text{L1_LUCID_A}}$	$\varepsilon_{\text{L1_LUCID_A}}$	$\varepsilon_{\text{L1_LUCID}}$	$\varepsilon_{\text{L1_LUCID_A_C}}$
PYTHIA MC09	0.433 ± 0.003	0.434 ± 0.003	0.647 ± 0.002	0.220 ± 0.002
PYTHIA DW	0.441 ± 0.003	0.445 ± 0.003	0.647 ± 0.002	0.237 ± 0.002
PYTHIA perugia	0.373 ± 0.002	0.376 ± 0.002	0.585 ± 0.003	0.164 ± 0.002
PYTHIA8	0.432 ± 0.003	0.441 ± 0.003	0.649 ± 0.002	0.224 ± 0.002
PHOJET	0.462 ± 0.003	0.460 ± 0.003	0.699 ± 0.002	0.223 ± 0.002

Table 7.7: *Level-1 LUCID item efficiencies as determined from different Monte Carlo generators and models at* $\sqrt{s} = 7$ *TeV.*

In the efficiency estimate, three major sources of systematic effects have been explored:

- The modeling of the *pp* inelastic interaction by the MC generators. Several PYTHIA tunes and PHOJET have been employed to study the dependency of the trigger efficiencies on the Monte Carlo models (see table 7.7). Based on the comparison between MC and data conducted earlier in this chapter, no clear conclusion can be drawn regarding which MC model describes data the best. As a consequence, no MC prediction can be ruled out and all models have to be taken in account on an equal footing. However, since the PYTHIA Perugia tunes does not described data well, it has been excluded from the evaluation of systematic uncertainties form the *MC model*. Hence the systematic uncertainty stemming from the uncertainty in the MC model is taken to be the maximum difference between any two models. For the single side trigger and the coincidence trigger this uncertainty is thus evaluated to be 7% and 8% respectively. Likewise for the L1_LUCID_A and L1_LUCID_C items the uncertainty is estimated to be 6%.

- The description of the detector in the simulation. To evaluate to which extent the efficiency estimate is sensitive to the inaccuracy of the detector simulation, the efficiency has been recalculated with a modified simulation (see section 6.5 for details). Only systematic effects that lead to a shift in the signal amplitude are relevant for the effi-

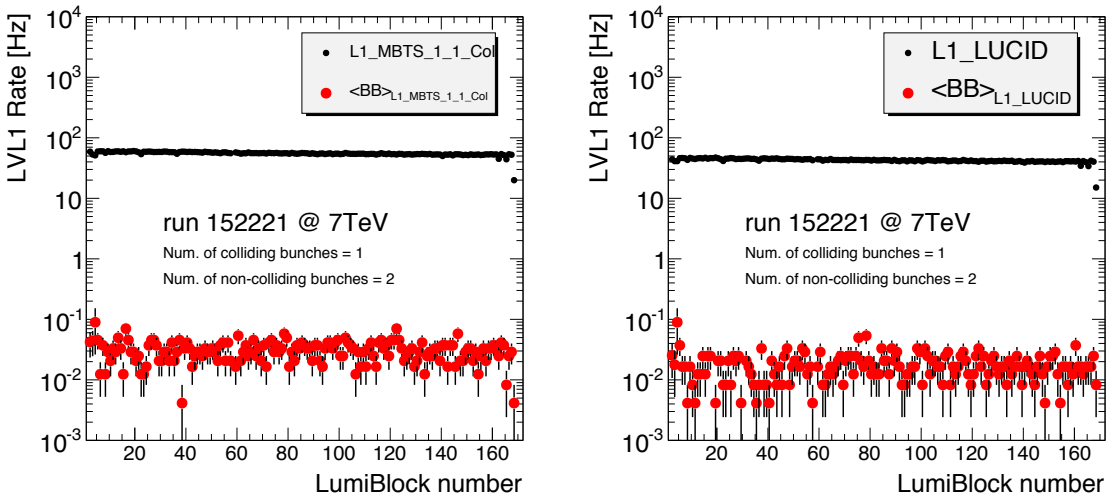


(a) (b)

Figure 7.10: *(top) Variation of the trigger efficiency for the single side trigger (a) and the coincidence trigger (b) as a function of the PMT threshold for different Monte Carlo generators. (bottom) Ratio of the PYTHIA MC09 predictions to the predictions from other MC generators.*

ciency determination. The different contributions from the simulation and digitization are summed up in quadrature and the total error is estimated to be 5% and 6% for L1_LUCID and L1_LUCID_A_C . Likewise for the L1_LUCID_A and L1_LUCID_C items the uncertainty is estimated to be 6%.
An additional source of systematic uncertainty is the precision to which the recorded charge in the PMTs is known. With the current hardware configuration of LUCID, one is expected to know the recorded charge with a precision of 1 photo-electron. It can be seen from figure 7.10 that the trigger efficiencies decrease as a function of the PMTs threshold cut as expected. The systematic uncertainty arising from the precision of the charge measurement is taken to be the variation in trigger efficiency when the PMT threshold is changed by ±2 photo-electrons around the nominal threshold of 15 photo-electrons. From the tables in appendix A these values can be extracted as 1.1% and 0.9% for the single side and coincidence trigger respectively and 1% for L1_LUCID_A and L1_LUCID_C.

- The method used to extract the efficiency. In order to explore possible biases in the efficiency determination introduced by the method used, the efficiency has been estimated with three independent approaches based on MC and data (section 7.5.3).



(a) (b)

Figure 7.11: *The rate of beam background events compared to the trigger rate bunch crossings triggered by the* L1_MBTS_1_1_Col *(a) and* L1_LUCID *trigger items. Both rates are plotted as a function of luminosity block number.*

Of the three sources of systematic error mentioned above the first two are only relevant to the MC estimate of the trigger efficiencies. For the data driven methods the only relevant source of systematic uncertainty are the one which arises from the MBTS simulation. This contribution to the systematic uncertainty was studied above and in [92] and was estimated to be 5% and 1% for the single side and coincidence trigger respectively and 3% for L1_LUCID_A and L1_LUCID_C.

7.6 Background determination and final results

Non-colliding bunches were used in order to evaluate the background from beam-halo and beam-gas interactions. It was assumed that these reproduce well the background in the colliding bunches. For each run, the filling scheme was used to locate the non-colliding BCIDs and the respective beam currents were used to weigh the contribution to the background from these bunches.
The way to extract the beam induced background (BB) from the LVL1 trigger rate in the case of LUCID and MBTS is the same. In both cases the activity in all unpaired bunches (Δ) is summed up and divided by the number of non-colliding bunches to give the average level of beam background in the colliding bunches:

$$\Delta_{\mathsf{L1_X}} = \mathsf{L1_X_UNPAIRED} \tag{7.14}$$

$$\langle BB \rangle_{bunch} = \frac{\Delta_{\mathsf{L1_X}}}{N_{unpaired}} \tag{7.15}$$

$$\langle BB \rangle_{\mathsf{L1_X_Col}} = \langle BB \rangle_{bunch} \cdot N_{paired} \tag{7.16}$$

$\langle BB\rangle_{bunch}$ is here the average BB per bunch, $N_{unpaired}$ (N_{paired}) is the total number of unpaired (paired) bunches and L1_X denotes either the number of L1_LUCID_X or L1_MBTS_1_1 triggers. Figures 7.11(a) and 7.11(b) show the rate of $\langle BB\rangle_{\text{L1_MBTS_1_1}}$ and $\langle BB\rangle_{\text{L1_LUCID}}$ as a function of the luminosity block number for a specific run. Superimposed in the same figures are the trigger rates[4] of the original item for comparison. The total beam background contribution to a specific trigger can be obtained by integrating $\langle BB\rangle$ over the entire run and dividing by the total integrated trigger rate. For L1_MBTS_1_1_Col, the background contribution was at the order of 0.06 % while for the LUCID items the background level was 0.04 % for the single side trigger and 0.03% for L1_LUCID_A and L1_LUCID_C . The coincidence trigger for LUCID was background free. This method can be applied both online using the trigger counters and offline. Offline one can also require the MBTS timing cut $|\Delta t_{AC}| < 10$ ns to further clean up the L1_MBTS_1_1_Col sample. This allows for a further reduction of the beam background to practically zero for the offline luminosity calculation and gives the possibility to estimate the accuracy obtained of the background caculation online. If the offline MBTS timing cut is included along with the background estimates, the formula to calculate the L1_LUCID_X efficiencies using method 2 becomes:

$$\varepsilon_{\text{L1_LUCID_X}} = \frac{n_{\text{L1_LUCID_X}}(1-\alpha^{bck}_{\text{L1_LUCID_X}})\cdot\varepsilon_{MBTS-timing}}{n_{\text{L1_MBTS_1_1_Col}}(1-\alpha^{bck}_{\text{L1_MBTS_1_1_Col}})}\cdot\varepsilon_{\text{L1_MBTS_1_1_Col}} \tag{7.17}$$

where α^{bck} is the fraction of beam background in a given run and $\varepsilon_{MBTS-timing}$ is the efficiency of the MBTS timing cut which is found by MC to be 0.986.

The final background subtracted trigger efficiencies are given in table 7.8 and compared to Monte Carlo predictions in figure 7.13. From figure 7.12 it can be seen that both composite LVL1 items for LUCID remain very stable during the course of a run.

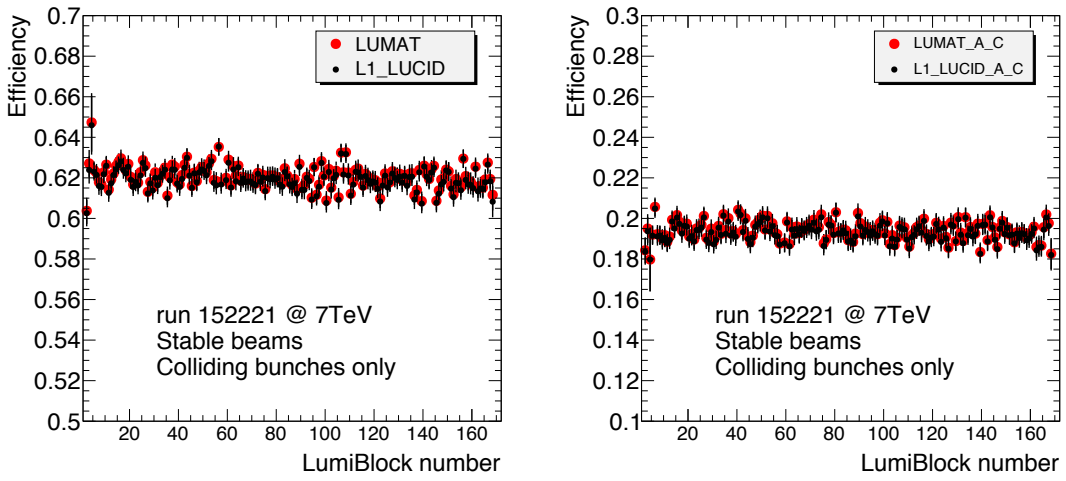
The average value of the results obtained with the MC simulation has been chosen as a

	Data 2010			
Method	$\varepsilon_{\text{L1_LUCID_A}}$	$\varepsilon_{\text{L1_LUCID_C}}$	$\varepsilon_{\text{L1_LUCID}}$	$\varepsilon_{\text{L1_LUCID_A_C}}$
Method 1	0.4071 ± 0.0006	0.3825 ± 0.0006	0.6381 ± 0.0006	0.1912 ± 0.0005
Method 2	0.4203 ± 0.0007	0.3947 ± 0.0007	0.6647 ± 0.0006	0.1938 ± 0.0005

Table 7.8: *Level-1 LUCID item efficiencies as determined by the data driven methods. The number presented here includes corrections for the MBTS timing cut and the beam background.*

reference for the trigger efficiencies. The results obtained with method 1 and method 2 are used as cross checks to assess the systematic uncertainty by extracting the efficiencies with different methods. In summary, the efficiencies for selecting *pp* inelastic collisions with the L1_LUCID_X trigger items are listed in table 7.9.

[4]the rates shown in the figures are corrected for fluctuations in the length of the luminosity block.



(a) (b)

Figure 7.12: *Level 1 trigger efficiencies for items* L1_LUCID *(a) and* L1_LUCID_A_C *(b) as a function of luminosity block number.*

Table 7.9: *Reference efficiencies for the LUCID LVL1 items.*

$\varepsilon_{\text{L1_LUCID_A}} = 0.433 \pm 0.003(stat.) \pm 0.026(MC\ model) \pm 0.025(sim.) \pm 0.014(method)$
$\varepsilon_{\text{L1_LUCID_C}} = 0.434 \pm 0.003(stat.) \pm 0.026(MC\ model) \pm 0.025(sim.) \pm 0.014(method)$
$\varepsilon_{\text{L1_LUCID}} = 0.647 \pm 0.002(stat.) \pm 0.047(MC\ model) \pm 0.030(sim.) \pm 0.029(method)$
$\varepsilon_{\text{L1_LUCID_A_C}} = 0.220 \pm 0.002(stat.) \pm 0.018(MC\ model) \pm 0.014(sim.) \pm 0.003(method)$

7.7 Conclusion

An important step in the validation process of the LUCID Monte Carlo description is the comparison of simulated data to real data. Any discrepancies here will lead to the wrong results when the Monte Carlo program is later used to predict the luminosity in various scenarios. It is therefore crucial that any differences are tracked down and identified, in order to improve the precision of the luminosity determination.
The performance of LUCID is addressed in this chapter by comparing results from the early 2010 data-taking period to predictions from simulations. It can be concluded from these comparisons that the simulation of LUCID in general describes data well. Discrepancies are seen at the level of the collected charge distributions. These discrepancies are not consistent between the two sides of LUCID and can be attributed to the presences of a stray magnetic field which is stronger on C side than on the A side.
By comparing the different types of hit multiplicity distributions in data to the predictions from various Monte Carlo models is can be concluded that the agreement between MC and data for the two types of triggered events is best in the lower part of the distributions. No firm conclusion can be drawn from these results, expect that the Perugia tune of PYTHIA seem to describe the situation in real data less well than the other tunes
The detection efficiency for LUCID is determined in the last part of the chapter. Several

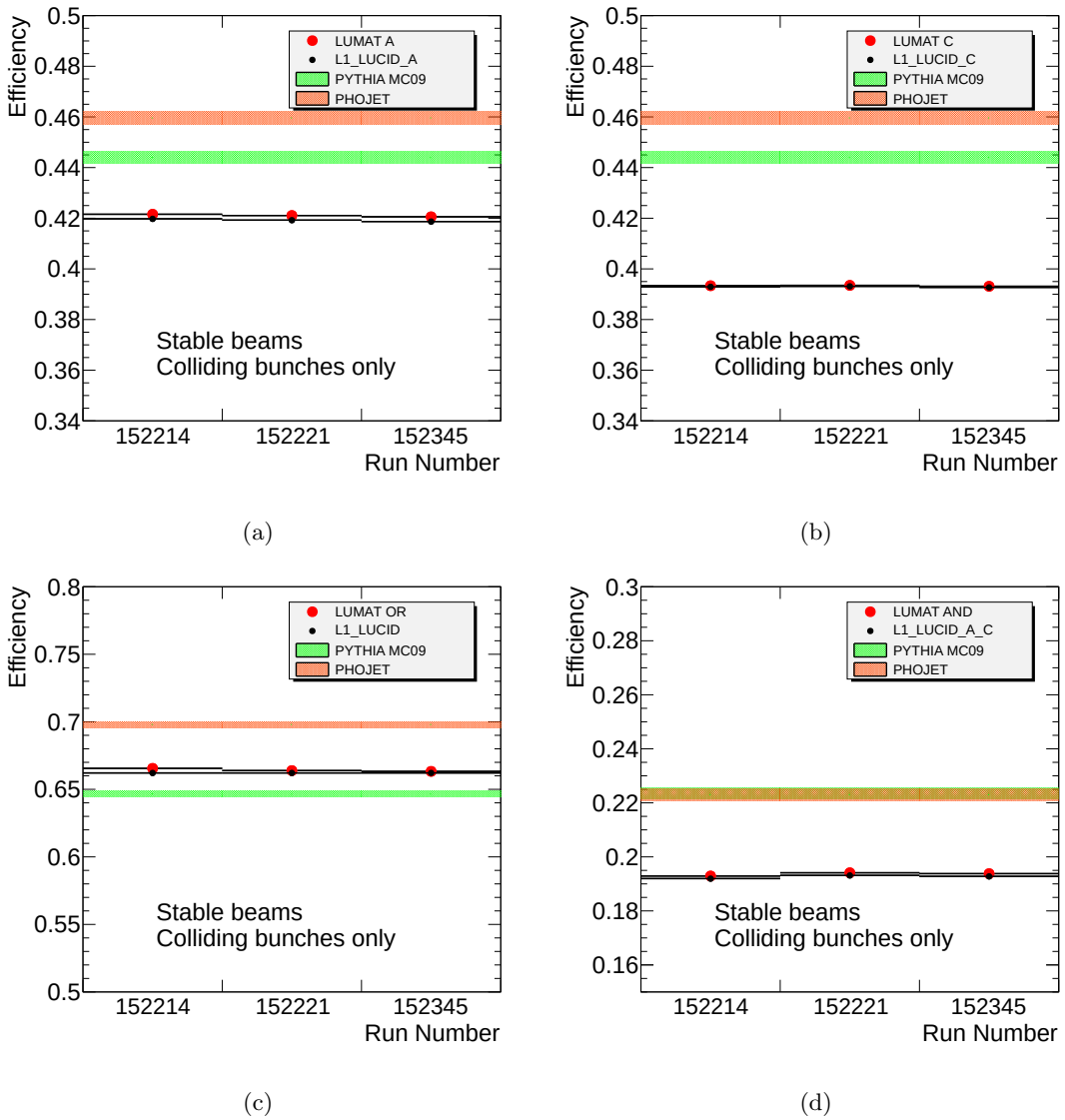


Figure 7.13: *LUCID trigger efficiencies for events triggered by* L1_LUCID_A *(a) and* L1_LUCID_C *(b) and the single side trigger (c) and the coincidence trigger (d). The recorded data used to produce the data points are taken from two different data streams, namely from the LUMAT card (red points) and the global ATLAS data stream (black points). Colored bands represent predictions from PYTHIA and PHOJET including statistical errors.*

methods using different techniques have been described and the results for each method has been presented. In the efficiency estimate, three major sources of systematic effects have been explored. It can be concluded that the two main contributions to the total systematic uncertainty comes from the modeling of the hard scattering in the various Monte Carlo generators and from the simulation of the LUCID detector.

Part IV
Luminosity Determination

Chapter 8

Performance Study of Luminosity Algorithms in ATLAS

8.1 Introduction

As mentioned in section 4.4, the purpose of a relative luminosity monitor, once calibrated, is to extrapolate the absolute measurement during the calibration to any luminosity scenario. The way that this is done is to measure the rate of inelastic interactions at the calibration point and then by means of dedicated algorithms, predict the interaction rate at another luminosity ($R_{inel} = g(\mathcal{L})$). As a result, values of the luminosity are obtained from the rate of inelastic interactions measured by the luminosity monitor. This means that when the luminosity monitor is operated under normal running conditions, where the luminosity is to be determined, one simply measures the rate of inelastic interactions in the luminosity monitor and by inverting g finds $\mathcal{L}$ ($= g^{-1}(R_{inel})$). Although the principles behind the use of luminosity algorithms to extract the luminosity might be simple, the actual implementations introduce a list of issues, which must be dealt with in order to obtain a precise result. Among such issues is the ability of the different luminosity algorithms to precisely predict $\mathcal{L}$ from R_{inel} as measured by the luminosity monitor for a known luminosity. Complications might furthermore arise since the functional relationship between R_{inel} and $\mathcal{L}$ are of such a mathematical nature that an inversion only can be done numerically. Finally, detector related effects can distort the relationship between the measured values of R_{inel} and $\mathcal{L}$. These issues will be addressed in the following section with the example of LUCID as the luminosity monitor. For similar studies of other luminosity monitors see [93].

For most purposes, it is easier to study the average number of inelastic interactions per bunch crossing μ instead of R_{inel}[1]. The relationship between the two quantities are $R_{inel} = \mu \cdot f_{BX}$ where f_{BX} is the bunch crossing rate (which can be calculated as f_{BX}= number of filled bunch crossings/3564 $\cdot$ 40 MHz). The problem of luminosity determination can then be regarded as the attempt to obtain the true value of μ (μ_{true}) by measuring the average number

[1] since μ is independent of the specific bunch filling scheme of the LHC.

of inelastic interactions per bunch crossing (μ_{meas}):

$$\mathcal{L} = \frac{\mu_{true} \cdot f_{BX}}{\sigma_{inel}} = \frac{\mu_{meas} \cdot f_{BX}}{A_{inel} \cdot \varepsilon_{inel} \cdot \sigma_{inel}} = \kappa_{cal}^{-1} \cdot \mu_{meas} = \kappa_{cal}^{'-1} \cdot R_{inel}^{meas} \tag{8.1}$$

where κ_{cal} is a calibration constant.

If there is no pileup, i.e. $\mu \ll 1$, the rate measured by the luminosity monitor is directly proportional to the true rate of inelastic events. Or in other words, the measured number of inelastic interactions is equal to the true number ($\mu_{true} = \mu_{meas}$). It is easy to see that this cannot always be the case if there are several interactions per bunch crossings. For instance if LUCID were only used to count events with at least one tube signal above the PMT threshold (so-called **event counting**). A situation will arise where LUCID detects one such event for each bunch crossing at high values of μ. Increasing μ will therefore not lead to an increase in the event rate, rendering such a method less useful at high luminosity. This type of effects which causes the event rate detected in the luminosity monitor to saturate is called **saturation effects**. The problems with saturation is that it tends to affect the luminosity measurement long before the event rate completely saturates, by distorting the linear relationship between μ_{meas} and μ_{true}. One way to minimize saturation effects is to derive a method in which the number of hits per bunch crossing is used to determine μ (so-called **hit counting**). This method also suffers from saturation effects when the number of hits gets close to the maximal number of channels in the detector. However, this happens at a higher value of μ than for the event counting methods.
Another type of detector related effects which potentially can affect the linear relationship between μ_{meas} and μ_{true} is called the **migration effect**. This problem is caused by the fact that the LUCID pulse-height spectrum is more or less continuous instead of having only a well defined peak for particles from the interaction point, as shown in chapter 6. Migration is combinatorial in nature and arise in LUCID at high μ when many small signals from secondary particles combine to form a signal in one tube above the PMT threshold. When the number of interactions per bunch crossing increases the probability also increases that two or more secondary particles will give a combined signal that is above the threshold value. Low signal particles are in this way said to migrate from the lower part of the pulse-height spectrum to higher values. While saturation effects tend to underestimate the value of μ_{true}, migration tends to overestimate μ_{true}.

To summarize, for LUCID two different classes of methods, each based on separate counting rates, can be used to extract μ_{true}:

Event counting : The fraction of events with a least one hit is used to estimate μ_{true};

Hit counting : The number of hits per event are used to estimate μ_{true}.

A third counting method exists in which the number of detected particles per bunch crossing is used to estimate μ_{true}. This method is called particle counting and it has the advantage that it essentially removes the saturation effect from the luminosity determination. Particle counting relies on the assumption that all particle within the acceptance of LUCID can be successfully detected which is for most cases not true. This method furthermore give rise to new effects which potentially could alter the linearity in equation 8.1 in the same way as

saturation and migration effects does. Due to technical difficulties it has not been possible to implement particle counting in the LUCID electronics and it is therefore only mentioned here for completeness.

In the current version only two classes of luminosity algorithms have been implemented in the LUMAT card firmware. These algorithms are based on the event and hit counting methods and are implemented in such a way that they can be used online as well as offline. The main purpose of the present chapter is to study how saturation and migration effects will affect the measurement of μ when different luminosity algorithms are utilized. It will be shown that the simple assumption of linearity ($\mu_{true} = k'_{LUCID} \cdot R_{LUCID}$) does not hold for all values of μ. New expressions will therefore be developed where μ_{true} is expressed as more complex functions of R_{LUCID} i.e. $\mu_{true} = f(\mu_{LUCID}) = F(R_{LUCID})$. It will also be shown that empirical expressions for these functions can be determined from simulated data.

In section 8.6 a novel method of measuring luminosity will be discussed. This algorithm uses the shape of the hit multiplicity spectrum for $\mu \ll 1$ to extract the luminosity for higher values of μ. Based on data taken by LUCID, under special conditions where $\mu \ll 1$, the hit multiplicity distribution can be constructed for events where only a single interaction took place. This distribution will then be used to construct so called reference distribution for known values of μ and by comparing these to the distribution for an unknown value of μ, the true value of μ can be extracted. The advantage with this type of luminosity algorithm is that it preserves the linearity of equation 8.1 and the need for Monte Carlo input disappears. However, due to the nature of the algorithm, it can only be used offline and only for high values of μ ($\mu \geq 0.5$)

The analysis performed in the following sections is to a certain extent based on the ideas presented in [77].

8.1.1 Data samples

The study performed in the following sections is based on a simulated data sample consisting of 200k inelastic *pp* collisions. Just as in the previous chapters, the event composition in terms of non-, single- and double-diffractive samples are made to match the cross sections at 7 TeV presented in table 6.2. Different Monte Carlo generator have been used to study the effect of model dependence on the luminosity measurement (see section 8.7) but the main study is carried out using a full simulation of the ATLAS detector based on the PYTHIA generator with the ATLAS MC09 tune.
The study presented here makes use of two separate data taking scenarios called the **calibration** and **measurement** scenario:

Calibration scenario : The calibration scenario describes the running conditions when the luminosity is at the order of $\sim 10^{27} cm^{-2} s^{-1}$. Under these conditions it can be assumed that $\mu \ll 1$ which means that the probability for having multiple collisions per bunch crossing is negligible ($\sim \mathcal{O}(10^{-6})$). As a result, the samples taken in the calibration scenario can be assumed to have one and only one *pp* interaction per event. An example of a set of running conditions which matches the calibration scenario is the

early data taking period in 2010 as described in chapter 7. This means that any result needed from the calibration scenario in this study can be taken directly from the result presented in the performance study.

Measurement scenario : The measurement scenario resembles the running conditions, i.e, it can no longer be assumed that $\mu \ll 1$. The measurements scenario is in this sense just another word for normal running of the ATLAS detector at an unknown value of μ. For Monte Carlo studies, data samples from the the measurement scenarios can be built by overlapping single pp interactions events according to Poisson statistics[2]:

$$P_\mu(n) = \sum_{n=0}^{\infty} \frac{\mu^n e^{-\mu}}{n!} \tag{8.2}$$

where $P_\mu(n)$ is the probability to have n interactions in a BX, when the average number of interactions per BX is μ. Using this technique the response of a detector to any interaction rate can be measured. In this situation the way of the luminosity algorithms can be studied by comparing the measured number of pp interactions per event (μ_{meas}) to the true number of pp interactions per event (μ_{true}).

8.2 Simulation of high luminosity events

The measurement samples are built by randomly overlapping single pp interactions according to Poissonian distributions. The overlap is performed by summing up the number of photo-electrons from the different interactions on a tube-by-tube basis. The photo-electron distribution for $\mu = 1$ and $\mu = 10$ are shown in figure 8.1. A noticeable feature of these plots is that while the peaks from primary particles are present in the $\mu = 1$ spectrum they are no longer present in the spectrum for $\mu = 10$. Due to an increased track multiplicity, the combinatorial background from secondaries crossing the tubes at large angles, hides the peaks from primary particles (migration effect).
In this study, a total of 43 data samples have been built in the measurement scenario to cover the range from $\mu = 0.01$ to $\mu = 25$. Depending on the LHC bunch filling scheme, this corresponds to an instantaneous luminosity in the range of $\mathcal{L} = 10^{30} cm^{-2} s^{-1}$ to $10^{34} cm^{-2} s^{-1}$ if the nominal filling scheme is used, or a luminosity range of $\mathcal{L} = 10^{27} cm^{-2} s^{-1}$ to $10^{31} cm^{-2} s^{-1}$ if only a single colliding bunch is filled.

8.3 Counting methods

An integral part of any algorithm used to determine luminosity with LUCID is counting methods as opposed to for example energy measurements by a calorimeter. As hinted in the introduction to this chapter, the counting method determines what detector related quantity is used to extract the average number of pp interactions per event. Common for the two

[2]We recall here that the two hypotheses which define a Poisson distributed process are:

- The rate at which particles occur over the time must be constant throughout;
- The particles must arrive independently of one another.

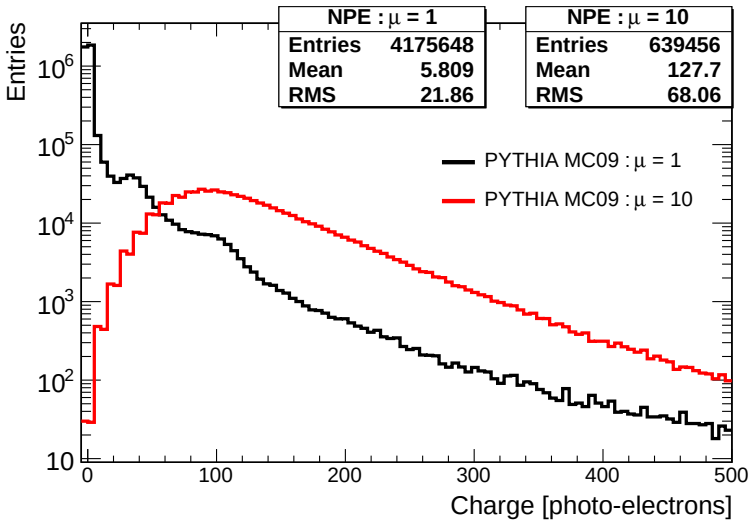


Figure 8.1: *photo-electron yield from different measurement scenarios.*

counting methods presented in this chapter is that they can be operated in two different detection modes - *single side mode* and *coincidence mode* also called "OR" and "AND" mode. In the **event counting** method, the rate of detected events is used to extract μ. In single side mode an event is said to be detected if it has at least one hit in either one of the two LUCID modules. The quantity to be estimated in this case is the probability to detect an event in the single side mode per BX: $P^{OR}_{hits/BX}$. In coincidence mode, events are detected when there is at least one hit in each module. The quantity to be measured in this case is the probability to detect an event in the coincidence mode per BX: $P^{AND}_{hits/BX}$. Both $P^{OR}_{hits/BX}$ and $P^{AND}_{hits/BX}$ can be estimated from the average number of "OR" and "AND" events per bunch crossing ($P^{OR,AND}_{hits/BX} = \frac{N^{OR,AND}_{evt}}{N_{BX}}$).
With the **hit counting** method the total number of hits per event is used to extract μ. In single side mode all hits of the detector are counted in events that have at least one hit somewhere. The quantity to be measured in this method is the total number of hits per BX: $N^{OR}_{hits/BX}$. In coincidence mode all hits of the detector are used in events that have at least one hit in each module. The quantity to be measured in this case is again the total number of hits per BX: $N^{AND}_{hits/BX}$. A method which is statistically equivalent to event counting is called **zero counting** and consists of counting empty events ($P_{0/BX}$) rather than those with hits ($P_{hits/BX}$). Just like event counting which methods saturates at high luminosities, the zero counting method has a similar problem, namely that the rate of empty events essentially is zero at high μ. At design luminosity ($L = 10^{34} cm^{-2} s^{-1}$), the average number of pp interactions per event is 25, which implies a rate of empty events of $e^{-25} \times 40 MHz = 5.6 \times 10^{-4} Hz$(40 MHz is the crossing rate). The different counting methods are summarized in table 8.1[3].
Figure 8.2 shows the full hit distributions for the event counting method at $\mu = 1$ and $\mu = 10$. The fact that the track multiplicity is significantly larger at $\mu = 10$ than at $\mu = 1$ causes the hit distribution at $\mu = 10$ to become almost identical for the two detection modes.
The average number of hits per event in single side mode is reported in table 8.2 for all the

[3]Note that hit counting is equivalent to event counting with a detector with only a single hit.

Measured quantity : $\Delta(\mu)$	Side A	Side C	Name
$P^{OR}_{hits/BX}(\mu)$	$N_{hits} \geq 1$ $N_{hits} = 0$ $N_{hits} \geq 1$	$N_{hits} \geq 1$ $N_{hits} \geq 1$ $N_{hits} = 0$	Event counting "OR"
$P^{AND}_{hits/BX}(\mu)$	$N_{hits} \geq 1$	$N_{hits} \geq 1$	Event counting "AND"
$P^{OR}_{0/BX}(\mu) = 1 - P^{AND}_{hits/BX}(\mu)$	$N_{hits} = 0$ $N_{hits} = 0$ $N_{hits} \geq 1$	$N_{hits} = 0$ $N_{hits} \geq 1$ $N_{hits} = 0$	Zero counting "OR"
$P^{AND}_{0/BX}(\mu) = 1 - P^{OR}_{hits/BX}(\mu)$	$N_{hits} = 0$	$N_{hits} = 0$	Zero counting "AND"
$N^{OR}_{hits/BX}(\mu)$	$N_{hits} \geq 1$ $N_{hits} = 0$ $N_{hits} \geq 1$	$N_{hits} \geq 1$ $N_{hits} \geq 1$ $N_{hits} = 0$	Hits counting "OR"
$N^{AND}_{hits/BX}(\mu)$	$N_{hits} \geq 0$	$N_{hits} \geq 1$	Hits counting "OR"

Table 8.1: *Counting methods. The μ dependence label will be suppressed in what follows to avoid cumbersome notation.*

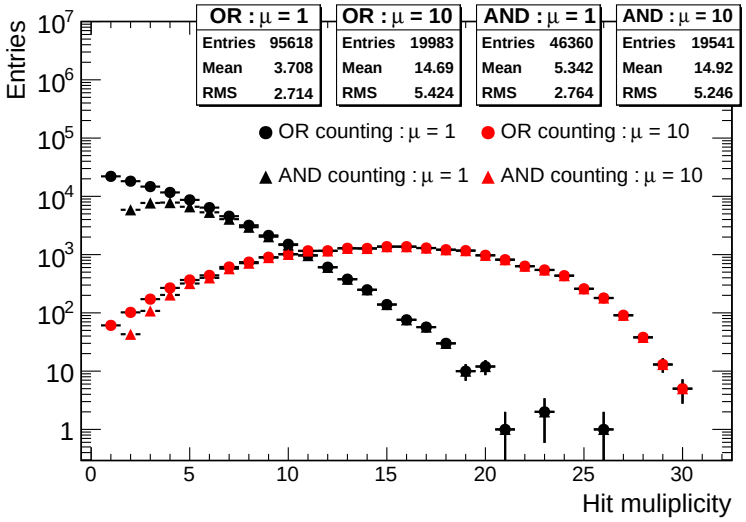


Figure 8.2: *Hit distributions with a 15 p.e. threshold for different measurement scenarios.*

measurement samples.
A set of quantities which will be heavily used in the derivation of the luminosity algorithms in the next sections are detection efficiencies of LUCID and the average number of hits per bunch crossing. These values have already been determined in chapter 7 since the single side mode is operationally equivalent to the L1_LUCID LVL1 trigger item and the coincidence mode is operationally equivalent to the L1_LUCID_A_C LVL1 trigger item. This type of assumption holds only if the pre-scale and dead time of the trigger system are taken into account when calculating the efficiencies and average multiplicities, which was the case for the result

μ	$N^{OR}_{hits/BX}$ **(thr. = 15 p.e)**	μ	$N^{OR}_{hits/BX}$ **(thr. = 15 p.e)**
0.01	0.017 ± 0.001	5.00	8.151 ± 0.043
0.02	0.036 ± 0.001	6.00	9.607 ± 0.055
0.03	0.053 ± 0.001	7.00	11.032 ± 0.068
0.04	0.074 ± 0.001	8.00	12.255 ± 0.080
0.05	0.087 ± 0.001	9.00	13.451 ± 0.094
0.06	0.111 ± 0.001	10.00	14.662 ± 0.107
0.07	0.126 ± 0.001	11.00	15.680 ± 0.120
0.08	0.145 ± 0.001	12.00	16.746 ± 0.134
0.09	0.162 ± 0.001	13.00	17.721 ± 0.147
0.1	0.182 ± 0.001	14.00	18.522 ± 0.159
0.2	0.360 ± 0.002	15.00	19.494 ± 0.173
0.3	0.534 ± 0.002	16.00	20.284 ± 0.186
0.4	0.716 ± 0.002	17.00	21.010 ± 0.198
0.5	0.902 ± 0.003	18.00	21.659 ± 0.210
0.6	1.073 ± 0.003	19.00	22.286 ± 0.222
0.7	1.255 ± 0.004	20.00	22.889 ± 0.234
0.8	1.422 ± 0.004	21.00	23.511 ± 0.246
0.9	1.605 ± 0.005	22.00	23.972 ± 0.257
1.0	1.777 ± 0.005	23.00	24.495 ± 0.268
2.0	3.496 ± 0.013	24.00	24.976 ± 0.279
3.0	5.136 ± 0.022	25.00	25.357 ± 0.289
4.0	6.705 ± 0.032		

Table 8.2: *Average number of hits per event in single side mode for* $0.01 \leq \mu \leq 25$.

presented in chapter 7.

8.4 Online Algorithms : The combinatorial model

With the combinatorial model, the measured quantity (Δ) for each counting method in table 8.1, is computed analytically as a function of μ from probability considerations and is denoted $\Delta_{comb}(\mu)$. Since not all detector related effects, i.e. migration, can be incorporated in the model the actual measured curve for Δ will deviate from the predicted one: $\Delta_{comb}(\mu) \neq \Delta_{meas}(\mu)$ as illustrated in figure 8.3. From the figure its seen that the following should in principle hold:

$$\Delta_{meas}(\mu_{true}) = \Delta_{comb}(\mu_{meas}) \tag{8.3}$$

$$\Delta^{-1}_{comb}(\Delta_{meas}(\mu_{true})) = \mu_{meas} \tag{8.4}$$

However, because of the inherent difference between $\Delta_{comb}(\mu)$ and $\Delta_{meas}(\mu)$, μ_{meas} will deviate from μ_{true} and the level of deviation will depend on how realistic the combinatorial model is. The study of these differences is at the center of the performance study presented in this chapter and is carried out by comparing the measured value of μ to the true value for each measurement sample.

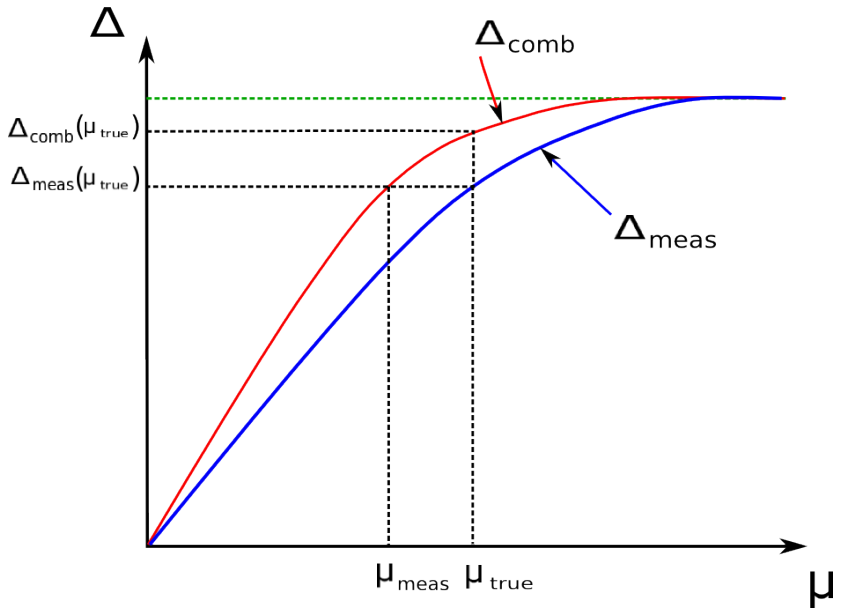


Figure 8.3: *Illustration of the potential difference between Δ_{comb} and Δ_{meas} as a function μ.*

8.4.1 Probability functions

The first step in the derivation of $\Delta_{comb}(\mu)$ for event counting methods, is to derive the probability functions for the different event types. In this process it proves useful to define a set of exclusive probabilities (see table 8.3) which are related to the inclusive efficiencies defined in chapter 7.

Table 8.3: *Definition of exclusive efficiencies and their relation to the inclusive efficiencies.*

P_{00} :	The probability of not detecting an interaction in either A or C $= 1 - \varepsilon_{OR}$
P_{11} :	The probability of detecting an interaction in both modules $= \varepsilon_{AND}$
P_{10} :	The probability of detecting an interaction in A, but not in C $= \varepsilon_A - \varepsilon_{AND}$
P_{01} :	The probability of detecting an interaction in C, but not in A $= \varepsilon_C - \varepsilon_{AND}$

The reason why the word *probability* and not efficiency is used in this connection, is that the latter is reserved for the situation where the number of interactions per bunch crossing is exactly 1.
To generalize the exclusive probabilities to bunch crossings with multiple interactions, one needs to assumed that the single interaction efficiencies do not change when several interactions occur in the same bunch crossing. Under this general assumption one can, for instance, calculate the probability function for *not* detecting a bunch crossing with exactly n interactions:

$$P_{00}(n) = P_{00}^n = (1 - \varepsilon_{OR})^n \tag{8.5}$$

In reality this assumption is not completely true due to migration effects. Since the definition of a hit depends on the fixed PMT discriminator threshold, the probability to detect i interactions in an event with n interactions is smaller than the probability to detect $i + 1$ interactions. The migration effects will not be included in the derivation of the counting

methods, however is will become clear in the following sections, that this is only valid as a first approximation.
If we now assume that n is Poissonian distributed with a mean of μ we get[4]

$$P_{00}(\mu) = \sum_{n=0}^{\infty}(1-\varepsilon_{OR})^n \frac{e^{-\mu}\mu^n}{n!} = e^{-\varepsilon_{OR}\mu} \tag{8.6}$$

8.4.2 Event counting : single side mode ("OR" mode)

The selected events in single side mode have at least one hit in a detector module (side A or side C). The event rate $P^{OR}_{hits/BX}$ for this type of events can be written as

$$P^{OR}_{hits/BX} = 1 - P^{AND}_{0/BX} = 1 - P_{00}(\mu) = 1 - e^{-\varepsilon_{OR}\mu} \tag{8.7}$$

The expression for $P^{OR}_{hits/BX}$ as a function of μ is easy to invert analytically:

$$\mu = -\frac{\ln(1 - P^{OR}_{hits/BX})}{\varepsilon^{OR}} \tag{8.8}$$

thus giving the possibility of extracting μ from a measurement of $P^{OR}_{hits/BX}$.

The measured values of μ as a function of μ_{true} are plotted in figure 8.4. A linear fit to the values of μ_{meas} from the combinatorial model shows that they are statistical compatible with the true value in the range from 0 to 8. This means that event counting in single side mode using the combinatorial model is expected to provide reliable values of the luminosity in this range. In the region above $\mu_{true} > 8$ combinatorial model overestimates the values of μ. Since saturation effects is incorporated in the model, the overestimation can in principle only come from migration effects. However, fluctuations in the values of $P^{OR}_{hits/BX}$ due to limited MC statistics, will close to the logarithmic pole of equation 8.8 lead to large variations in μ_{meas} which is also seen in figure 8.4. Such fluctuations can in principle only be decreased by increasing the size of the MC data sample significantly which has not been possible for this study.

Linear approximation

A Taylor expansion of the logarithm in equation 8.8 gives

$$\ln\left(1 - P^{OR}_{hits/BX}\right) = -\sum_{n=1}^{\infty}\frac{(P^{OR}_{hits/BX})^n}{n} \tag{8.9}$$

To first order in the expansion μ is proportional to the rate of detected events ($P^{OR}_{hits/BX}$):

$$\mu \approx \frac{P^{OR}_{hits/BX}}{\varepsilon^{OR}} \tag{8.10}$$

[4] using the Maclaurin series expansion $e^z = \sum_{n=0}^{\infty}\frac{z^n}{n!}$.

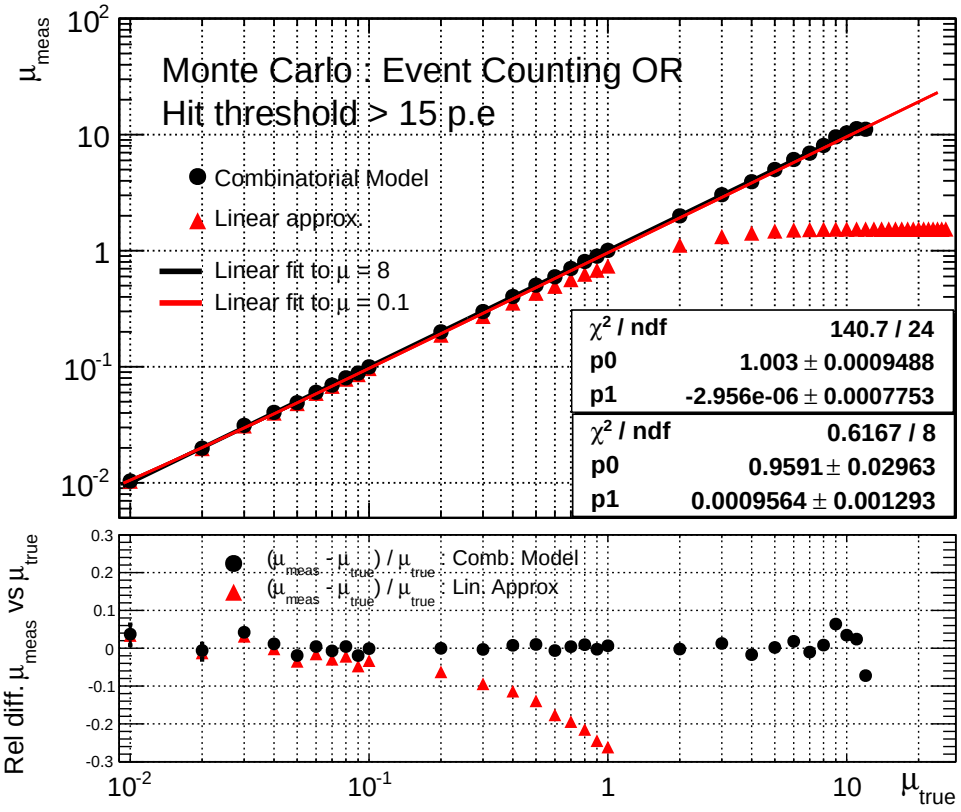


Figure 8.4: *Top: average number of pp interactions per event measured with the single side event counting method as a function of the true value (μ_{true}) for the combinatorial model (black points) and the linear approximation (red points). Bottom: deviation from the true value for both models.*

The values of μ_{meas} obtained from the linear extrapolation of $P^{OR}_{hits/BX}$ are likewise plotted in figure 8.4 as a function of μ_{true}. By fitting the measured values of μ with a straight line it is possible to see for which region of μ the linear approximation is expected to give reliable results. It can be seen from the plot that a linear approximation is only accurate for $\mu \leq 0.1$. For larger value μ is systematically underestimated due to saturation effect when the rate of detected events per BX becomes constant.
An intermediate conclusion from the results above is that the *validity range* of the event counting method is extended from $\mu = 0.1$ up to about $\mu = 8$ when the logarithmic formula is used instead of the linear approximation.

The concept of validity range will be used extensively in the following sections and thus should be defined properly. The validity range of a luminosity algorithm is defined as the range in μ for which a fit of a straight line to the values of μ_{meas} as a function of μ_{true}, i.e figure 8.4, gives results that have a slope of 1 and goes through the origin. It will furthermore be required that the relative difference between μ_{meas} and μ_{true} do not exceed 5 % for any of the points in the validity range.

8.4.3 Event counting : coincidence mode ("AND" mode)

The selected events in coincidence mode have at least one hit in each detector module (side A and side C). The event rate $P^{AND}_{hits/BX}$for this type of events can be written as :

$$P^{AND}_{hits/BX} = 1 - P^{OR}_{0/BX} \tag{8.11}$$

The first step towards finding the probability function $P^{AND}_{hits/BX}$ is to write equation 8.11 for the case of exactly one interaction:

$$P_{11} = 1 - (P_{00} + P_{10} + P_{01}) \tag{8.12}$$

where it has been used that the probabilities P_{ij} adds up to 1. The next step is to generalize the expression to the case of exactly n interactions. In the same way as was done for the generalization of P_{00} above, we also here has to assume that the single interaction probability/efficiency remains constant in the case of multiple interactions:

$$P_{11}(n) = 1 - (P_{00}(n) + P_{10}(n) + P_{01}(n)) \tag{8.13}$$

When generalized to n interactions the probabilities $P_{10}(n)$ and $P_{01}(n)$ have a slightly more elaborate meaning, namely:

$P_{10}(n)$ **:** the total probability to have n interactions out of which k interactions are detected in side A and $n-k$ interactions are not detected in any module.

$P_{01}(n)$ **:** the total probability to have n interactions out of which k interactions are detected in side C and $n-k$ interactions are not detected in any module.

To derive explicit expressions for $P_{10}(n)$ and $P_{01}(n)$ one needs to take the sum of all possible permutations of n and k:

$$P_{10}(n) = \sum_{k=1}^{n} P_{10}^{k}\ P_{00}^{n-k}\binom{n}{k} = (P_{10} + P_{00})^n - P_{00}^n \tag{8.14}$$

$$P_{01}(n) = \sum_{k=1}^{n} P_{01}^{k}\ P_{00}^{n-k}\binom{n}{k} = (P_{01} + P_{00})^n - P_{00}^n \tag{8.15}$$

where the sums have been carried out using the Binomial theorem. Having already calculated the expression for $P_{00}(n)$ in the previous section, the expression for $P_{11}(n)$ can be found as:

$$P_{11}(n) = 1 - (P_{00}(n) + P_{10}(n) + P_{01}(n)) \tag{8.16}$$

$$= 1 - (P_{00}^n + (P_{10} + P_{00})^n - P_{00}^n + (P_{01} + P_{00})^n - P_{00}^n) \tag{8.17}$$

The final step towards calculating the probability function $P^{AND}_{hits/BX}$ is to generalize the number of interactions n from a fixed number to a Poissonian distributed number with a mean μ:

$$P_{11}(\mu) = 1 - \sum_{n=0}^{\infty}((P_{10} + P_{00})^n + (P_{01} + P_{00})^n - P_{00}^n)\frac{e^{-\mu}\mu^n}{n!} \tag{8.18}$$

$$= e^{-\mu(1-P_{10}-P_{00})} + e^{-\mu(1-P_{01}-P_{00})} - e^{-\mu(1-P_{00})} \tag{8.19}$$

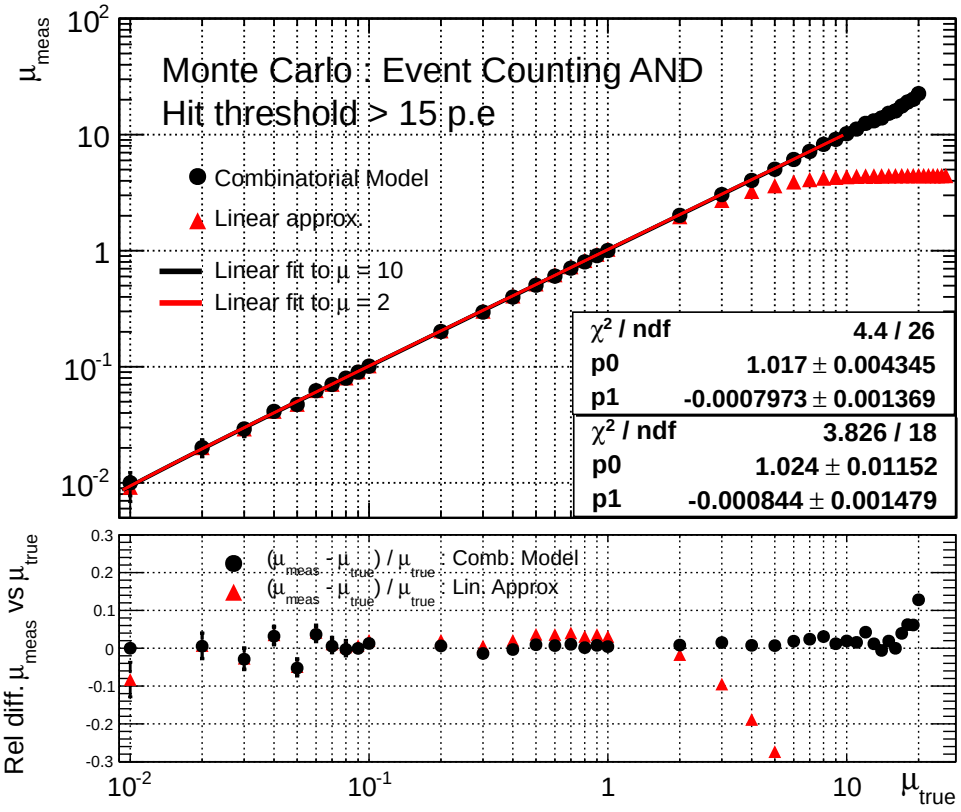


Figure 8.5: *Top: average number of pp interactions per event measured with the coincidence event counting method as a function of the true value (μ_{true}) for the combinatorial model (black points) and the linear approximation (red points). Bottom: deviation from the true value for both models.*

Thus the average number of *pp* interactions per event is related to the rate of detected events and to the detection efficiencies by

$$P^{AND}_{hits/BX} = 1 - e^{-\mu\varepsilon_A} - e^{-\mu\varepsilon_C} + e^{-\mu(\varepsilon_A+\varepsilon_C-\varepsilon_{AND})} \tag{8.20}$$

The functional form of equation 8.20 is such that it can not be inverted analytically and the only option is to invert the expression numerically. For this purpose Brent's method [94] has been applied to extract μ:

$$\mu = f^{-1}(P^{AND}_{hits/BX}) \tag{8.21}$$

When the detection efficiencies (ε_A , ε_C and ε_{AND}) found in table 7.9 are inserted into equation 8.20 and the expression is inverted one obtains a value of μ_{meas}. Figure 8.5 shows the numerically obtained values of μ_{meas} as a function of μ_{true} for the combinatorial model in the different measurement samples. The uncertainty on the measured values of μ is taken to be the maximum variation of μ corresponding to a $\pm\sigma$ variation of $P^{AND}_{hits/BX}$. Brent's method has unfortunately proved to be somewhat unstable in this case, resulting in large fluctuations of the uncertainty estimations, especially at high values of μ. To cross check the uncertainty on μ_{meas}, each measurement sample has been divided into subsamples of 500 events. The value of μ_{meas} has then been extracted for each subsample and plotted in a histograms and fitted with a Poissonian at low μ and a Gaussian at high μ to calculate the standard deviation on μ_{meas}. The uncertainty on μ_{meas} calculated from the standard deviation was then

compared to the uncertainty obtained from the numerical inversion and the two value were not compatible the numerical inversion was redone.

The values of μ_{meas} obtained from the combinatorial models in coincidence mode exhibits some of the same features as in the single side mode. The results from the algorithms are linear and compatible with μ_{true} for small value of μ_{true} until a point is reached where the data points starts deviating from the true value due to migration effects. The position of this point is different for the two detection modes. For single side mode the point was located at about $\mu_{true} = 8$ where as for the coincidence mode the point is located at $\mu_{true} = 10$. The reason why the migration point is higher in coincidence mode is due to the fact that by requiring a hit in both modules simultaneously one lowers the detection efficiency and thereby raises the value of μ where migration effects start to play a role.

Linear approximation

When μ is sufficiently small, combinatorial effects are negligible and the rate of detected events is proportional to the efficiency:

$$\mu \xrightarrow{\mu \ll 1} \frac{P^{AND}_{hits/BX}}{\varepsilon_{AND}} \tag{8.22}$$

The values of μ_{meas} obtained from the linear extrapolation of $P^{AND}_{hits/BX}$ are likewise plotted in figure 8.4 as a function of μ_{true}. In the same fashion as for the single side mode, the validity of the linear assumption can be checked by fitting the measured values of μ with a straight line. A linear fit to the measured data points up to $\mu_{true} = 2$ has a slope consistent with 1 and is consistent with going through the origin. This means that the measurement of μ with the linear approximation is reliable up to $\mu = 2$. For larger μ values, μ is systematically underestimated with as much as 80 % at $\mu_{true} = 20$ (not shown in the figure). This is to be compared with a maximal deviation of 12 % for the combinatorial model. The underestimation in the linear approximation is due to fact that the saturation effect dominates in the region of $\mu_{true} > 2$.

8.4.4 Hit counting : single side mode ("OR" mode)

The basics of every hit counting method is the particle counting method. The hit counting method is nothing more than a particle counting method adapted to the situation where the luminosity detector has a limited acceptance and limited number of channels. Since there is no need to correct for saturation effects with particle counting, the average number of pp collisions per event can be estimated by the ratio between the average number of particles per event ($N^{OR}_{part/BX}$) and the average for one pp collision ($N^{OR}_{part/pp}$):

$$\mu = \frac{N^{OR}_{part/BX}}{N^{OR}_{part/pp}} \tag{8.23}$$

The LUCID detector is not equipped to count particles, only hits and therefore the number of detected particles in equation 8.23 must be turned into the number of detected hits.

From particles to hits In order to turn the number of particles into hits one has to make some assumptions. Firstly, it has to be assumed that the all particles produced in a inelastic interaction are distributed uniformly over the acceptance of LUCID. Figures 7.3 and 7.5 show that this is true, at least to a first approximation for all the different components of the inelastic cross section. Under this assumption the number of detected particles per tube is $N_{part/pp}/N_{tubes}$, where $N_{part/pp}$ is the total number of detected particles per pp interaction and $N_{tubes} = 30$.
Secondly it has to be assumed that the number of particles in a tube is distributed according to a Poissonian which means that the number of hits can be written as the product of N_{tubes} and the probability to have at least one particle in a tube (a hit):

$$N_{hits/pp} = N_{tubes}\left[1 - e^{-\frac{N_{part/pp}}{N_{tubes}}}\right] \tag{8.24}$$

In order to express equation 8.23 in terms of hits and not particles, equation 8.24 must be inverted:

$$N_{part/pp} = -N_{tubes}\ln\left(1 - \frac{N_{hits/pp}}{N_{tubes}}\right) \tag{8.25}$$

An issue with equation 8.25 is that a logarithmic pole at $N_{hits/pp} = N_{tubes}$ leads to infinitely large values of $N_{part/pp}$. If these situations are handled carefully one can obtain μ from a measurement of $N_{hits/BX}$ by using the following relationship:

$$\mu = \frac{N_{part/BX}}{N_{part/pp}} = \frac{\ln\left(1 - \frac{N_{hits/BX}}{N_{tubes}}\right)}{\ln\left(1 - \frac{N_{hits/pp}}{N_{tubes}}\right)} \tag{8.26}$$

where it has been used that equation 8.25 also hold for bunch crossings with several interactions.
Equation 8.26 is only valid at the level of one bunch crossing. To extend the use, for example to a luminosity block, one needs to do the sum over all the individual bunch crossings and then divide by the total number of bunch crossings to obtain the average[5]:

$$\mu = \frac{1}{N_{BX}} \cdot \frac{\sum_{i=1}^{N_{BX}} \ln\left(1 - \frac{N_{hits}(i)}{N_{tubes}}\right)}{\ln\left(1 - \frac{N_{hits/pp}}{N_{tubes}}\right)} \tag{8.27}$$

The values of μ obtained with this expression for the combinatorial model is plotted against μ_{true} in figure 8.6. A linear fit to the values of μ_{meas} shows that they are statistically compatible with the true value in the range from 0 to 2. The overestimation of μ_{true} at higher luminosities is probably due to migration effects and the fact that the hit multiplicity distributions is not Poissonian. With increasing luminosity the migration effect gives an excess of hits compared to the prediction which leads to an overestimation of μ. For the same reason the deviation increases with μ.

[5]It should be noted here that this is arithmetically different from using the value of $N_{hits/BX}$ obtained by averaging over all bunch crossing and then applying the logarithm.

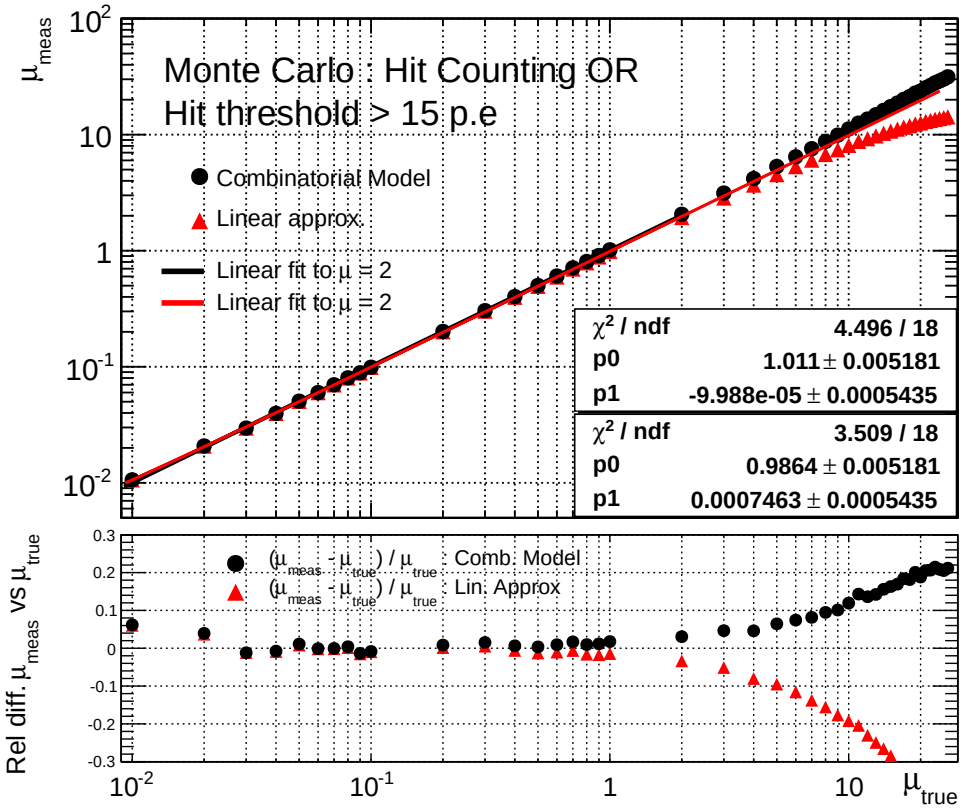


Figure 8.6: *Top: average number of pp interactions per event measured with the single side hit counting method as a function of the true value (μ_{true}) for the combinatorial model (black points) and the linear approximation (red points). Bottom: deviation from the true value for both models.*

Linear approximation

Using the Taylor expansion to first order one can see that μ is proportional to the average number of hits per event ($N^{OR}_{hits/BX}$):

$$\mu = \frac{N^{OR}_{part/BX}}{N^{OR}_{part/pp}} \approx \frac{N^{OR}_{hits/BX}}{N^{OR}_{hits/pp}} \tag{8.28}$$

The measurements of μ as a function of the true values with a linear extrapolation of $N^{OR}_{hits/BX}$ from $\mu = 0.01$ are plotted in figure 8.6. In the same way as for event counting, the validity of the linear assumption can be checked by fitting the values of μ_{meas} with a straight line. A linear fit to the measured points up to $\mu_{true} = 2$ has a slope consistent with 1 and is consistent with going through the origin. This means that the linear approximation is reliable up to $\mu = 2$. For $\mu > 2$, μ the saturation effect starts to play a role and as a consequence μ is underestimated. As opposed to the event counting methods the logarithmic formular do not improve the result of a linear approximation much in the range $\mu \leq 2$.

8.4.5 Hit counting : coincidence mode ("AND" mode)

Hit counting in coincidence mode is perhaps the most technically challenging of the counting methods. Requiring a coincidence to take place between the two modules unavoidably introduces a list of combinatorial effects which have to be taken into account. One such effect stems from the fact that for an event with multiple interactions, a coincidence can be created in two ways, namely as a *true coincidence* ***(TC)*** and a *false coincidence* ***(FC)*** . A true coincidence occurs when at least one interaction is detected simultaneously in both modules. A fake coincidence occurs when no interaction is detected simultaneously in both modules, but at least two interactions are separately detected in different modules. Both types of coincidences have to be incorporated in the derivation in order for the prediction of μ_{true} to be as precise as possible.

Inspired by the two coincidence types one can formulate the requirements that a single bunch crossing with n interactions have to fulfill in order to be detected as a coincidence.

TC : the bunch crossing contains at least one interaction which is detected in both modules, together with any number of interactions which are only detected in module A and not in C, and vice versa;

FC : the bunch crossing contains 0 interactions detected in both modules, together with at least one interaction which is only detected in module A and one which is only detected in module C.

In the same way as in the single side mode, the objective for hit counting in coincidence mode is to find the number of particles per BX: $N^{AND}_{part/BX}$ when the bunch crossing is detected in coincidence mode. This number is found as the sum of the particles produced in bunch crossings of type **TC** and **FC**. For each of the two bunch crossing types, the average number of particles is found as the number of particles produced per detected interaction times the number of detected interactions in the bunch crossing times the probability for either **TC** or **FC** to occur.
Equivalently to the exclusive probabilities defined in table 8.3 one can also define in an exclusive way the average number of particles per interaction (see table 8.4).

Table 8.4: *Exclusive definitions of average number of particles.*

M_{10}	number of particles per detected interaction in A, but not in C
M_{01}	number of particles per detected interaction in C, but not in A
M_{11}	number of particles per detected interaction in both modules
M_{XOR}	number of particles per detected interaction in any module but not in both

The average number of particles as defined in table 8.4 has a one-to-one correspondence with the exclusive efficiencies in the sense that the product $M_{10}P_{10}$ directly yields the number of detected particles when the interaction is detected only on side A. Additionally to the already defined exclusive efficiencies one can also define the efficiency to detect an interaction in any module, but not in both (P_{XOR})[6].

[6] P_{XOR} is nothing more than the sum of P_{10} and P_{01} ($P_{XOR} = P_{10} + P_{01}$ = 1 - P_{11} - P_{00}) introduced to aid with the clarity of the derivation.

Keeping the one-to-one correspondence between P_{ij} and M_{ij} in mind, one can write down the expression for **TC** and **FC** case of a bunch crossing with n interactions.

$$\begin{aligned}
\mathbf{TC} &= \sum_{k=1}^{n} P_{11}^{k} \binom{n}{k} \left[\sum_{l=0}^{n-k} P_{XOR}^{l} P_{00}^{n-k-l} \binom{n-k}{l} \right] [kM_{11} + lM_{XOR}] \\
\mathbf{FC} &= \sum_{k=1}^{n} P_{10}^{k} \binom{n}{k} \left[\sum_{l=1}^{n-k} P_{01}^{l} P_{00}^{n-k-l} \binom{n-k}{l} \right] [kM_{10} + lM_{01}]
\end{aligned}$$

Term TC and FC The logical structure of the expressions follows directly from the contribution of the different detection modes that come into play. The order of the different contributions follows the same order in **TC** and **FC** but the meaning of the contributions are different. For example the first two contributions to **TC** comes from the average number of particles produced in k simultaneous interactions detected in coincidence mode $P_{11}^{k} k M_{11}$ and the average number of particles produced in l simultaneous interactions detected in exclusive single side mode $P_{XOR}^{l} l M_{XOR}$. In the same way, the first two contributions to **FC** comes from the average number of particles produced in k simultaneous interactions detected in side A and not side C, $P_{10}^{k} k M_{10}$ and vice versa for l interactions $P_{01}^{l} l M_{01}$. The final contributions to both **TC** and **FC** come from the probability of not detecting the remaining $n-k-l$ interactions in the bunch crossing $(1 - P_{XOR} - P_{11})^{n-k-l} = P_{00}^{n-k-l}$.

Sum over l and k: Both the l and the k-sums in **TC** and **FC** can be evaluated using the binomial theorem. The l-sums constitutes 4 terms and the k-sums constitutes 7 terms. Each of these sums are in principle straight forwards to carry out but the results are very notation heavy. As a compromise, the general structure of the sums are given here:

$$\begin{aligned}
\sum_{l=0}^{n-k} L_i(l,n,k) \binom{n-k}{l} &= \widetilde{L}_i(n,k) \qquad \text{for } i = 1 \ldots 4 \\
\sum_{k=1}^{n} K_i(n,k) \binom{n}{k} &= \widetilde{K}_i(n) \qquad \text{for } i = 1 \ldots 7
\end{aligned}$$

while the individual coefficients $L_i, \widetilde{L}_i, K_i$ and $\widetilde{K}_i$ are given in table B.1 in Appendix B.

Using definitions of the exclusive probabilities and the average number of particles ($M_{XOR}P_{XOR} = M_{10}P_{10} + M_{01}P_{01}$) the total number of particles produced in **TC** and **FC** can be found to be:

$$\mathbf{TC} + \mathbf{FC} = nM_{11}P_{11} + nM_{10}P_{10}\left[1 - (P_{00} + P_{10})^{n-1}\right] + nM_{01}P_{01}\left[1 - (P_{00} + P_{01})^{n-1}\right] \quad (8.29)$$

From a fixed to a Poissonian distributed number of interactions: The final step towards calculating $P_{part/BX}^{AND}$ is to generalize the number of interactions n from a fixed number to a Poissonian distributed number with a mean μ. This is done by convoluting equation 8.29

with a Poissonian of average μ:

$$N^{AND}_{part/BX} = \sum_{n=0}^{\infty}(\mathbf{TC}+\mathbf{FC})\frac{e^{-\mu}\mu^n}{n!} \tag{8.30}$$

$$= M_{11}\mu + M_{10}P_{10}\mu\Big[1-e^{-\mu(P_{01}+P_{11})}\Big] + M_{01}P_{01}\mu\Big[1-e^{-\mu(P_{10}+P_{11})}\Big] \tag{8.31}$$

where the Maclaurin series expansion and the relation $\sum_{n=0}^{\infty} n\frac{e^{-\mu}\mu^n}{n!} = \mu$ have been used. Using the relationship between the exclusive and inclusive defined quantities:

$$M_{10}P_{10} = N^{A}_{part/pp} - N^{AND}_{part/pp} \tag{8.32}$$

$$M_{01}P_{01} = N^{C}_{part/pp} - N^{AND}_{part/pp} \tag{8.33}$$

$$M_{11} = N^{AND}_{part/pp} \tag{8.34}$$

the expression for $N^{AND}_{part/BX}$can be written as:

$$N^{AND}_{part/BX} = \mu N^{AND}_{part/pp} + \mu\big(N^{A}_{part/pp} - N^{AND}_{part/pp}\big)\big(1-e^{-\mu\varepsilon_C}\big) \tag{8.35}$$

$$+ \mu\big(N^{C}_{part/pp} - N^{AND}_{part/pp}\big)\big(1-e^{-\mu\varepsilon_A}\big) \tag{8.36}$$

The inclusive detection efficiencies (ε_A , ε_C and ε_{AND}) and the average number of particles per pp interaction ($N^{A}_{part/pp}, N^{C}_{part/pp}$ and $N^{AND}_{part/pp}$) are obtained from the calibration sample. The value of $N^{AND}_{part/BX}$ is extracted from each measurement sample by using equation 8.25 on individual brunch crossings. The average number of pp interactions per event can then be obtained by the numerical inversion of equation 8.35:

$$\mu = f^{-1}(N^{AND}_{part/BX}) \tag{8.37}$$

The measurements in Monte Carlo of μ as a function of the true values with the combinatorial model are plotted in figure 8.7. The uncertainty on μ is the maximum variation of μ corresponding to a $\pm\sigma$ variation of $N^{AND}_{part/BX}$ and cross checked by the method described earlier.
The values of μ_{meas} are compatible with the true value for small value of μ. Above $\mu_{true} = 1$ migrations effects and the deviation from Poissonian behavior leads to an overestimation of μ which grows with μ_{true} to a maximum deviation at $\mu_{true} = 20$ of 20%. Above this value the level of the overestimation decreases due to combinatorial effects. An interesting observation of both hit counting methods is that despite the increased level of sophistication when compared to the event counting methods, they still give a worse result. For event counting the algorithms are valid until $\mu = 8$ and $\mu = 10$ for event OR and AND respectively. For hit counting algorithms the corresponding numbers are $\mu = 2$ and $\mu = 1$.

Linear approximation

To first order μ is proportional to the average number of hits per event ($N^{AND}_{hits/BX}$):

$$\mu = \frac{N^{AND}_{part/BX}}{N^{AND}_{part/pp}} \approx \frac{N^{AND}_{hits/BX}}{N^{AND}_{hits/pp}} \tag{8.38}$$

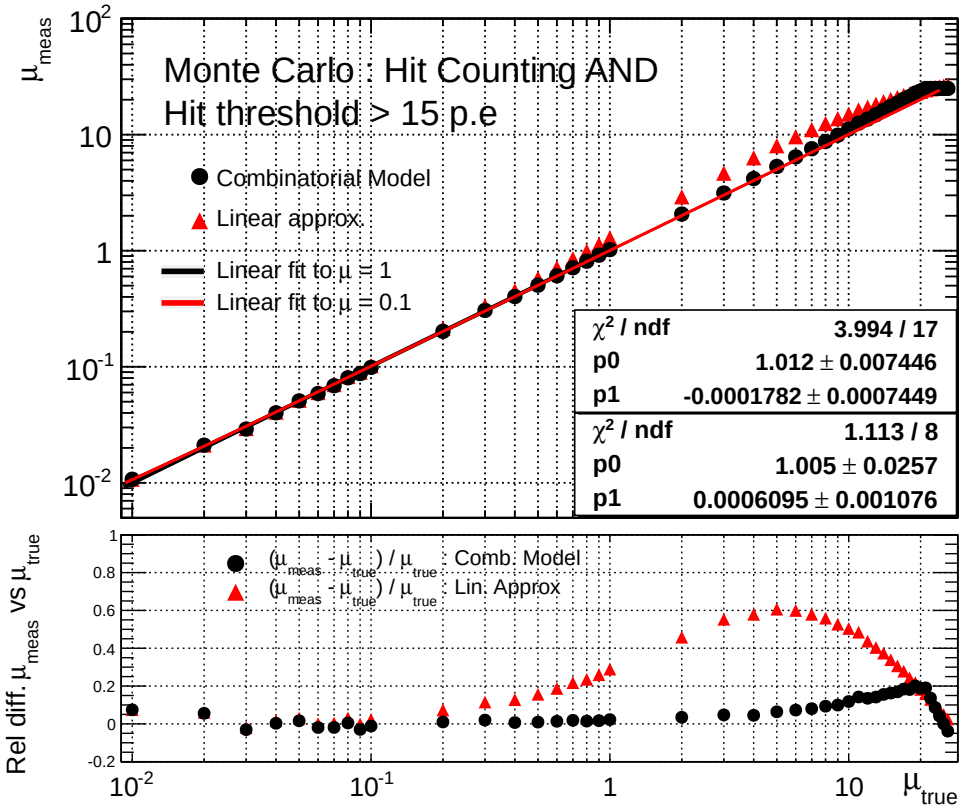


Figure 8.7: *Top: average number of pp interactions per event measured with the coincidence hit counting method as a function of the true value (μ_{true}) for the combinatorial model (black points) and the linear approximation (red points). Bottom: deviation from the true value for both models.*

The measurements of μ as a function of the true values with a linear extrapolation of $N^{AND}_{hits/BX}$ from $\mu = 0.01$ are likewise plotted in figure 8.7. A linear fit to the measured points up to $\mu_{true} = 0.1$ has a slope consistent with 1 and is consistent with going through the origin. This means that the measurement of μ with the linear approximation is reliable up to $\mu = 0.1$. For $\mu > 0.1$, μ is overestimated due to the effects of migration and coincidence. The saturation effect in hit counting arises from counting hits instead of particles. The number of particles increases constantly with μ while the maximum number of hits is limited to 30 (the number of tubes). When μ is sufficiently large ($\mu > 5$), the large number of particles saturates the detector and lead to an underestimate of μ. Since the migration effect leads to an overestimate and the saturation to an underestimate, these two effects cancel to some degree in the linear approximation. In this approximation the maximal deviation due to the migration is reached at $\mu_{true} = 3$ where the relative deviation is 60 %. For $\mu > 3$, saturation effect starts to play a role and the level of overestimation shrinks.

8.5 Online Algorithms : Polynomial parameterization method

It has been shown in the last section, that measurements of μ based on the combinatorial model are not linear over the full range in μ. The main reason for the non-linearity is migration

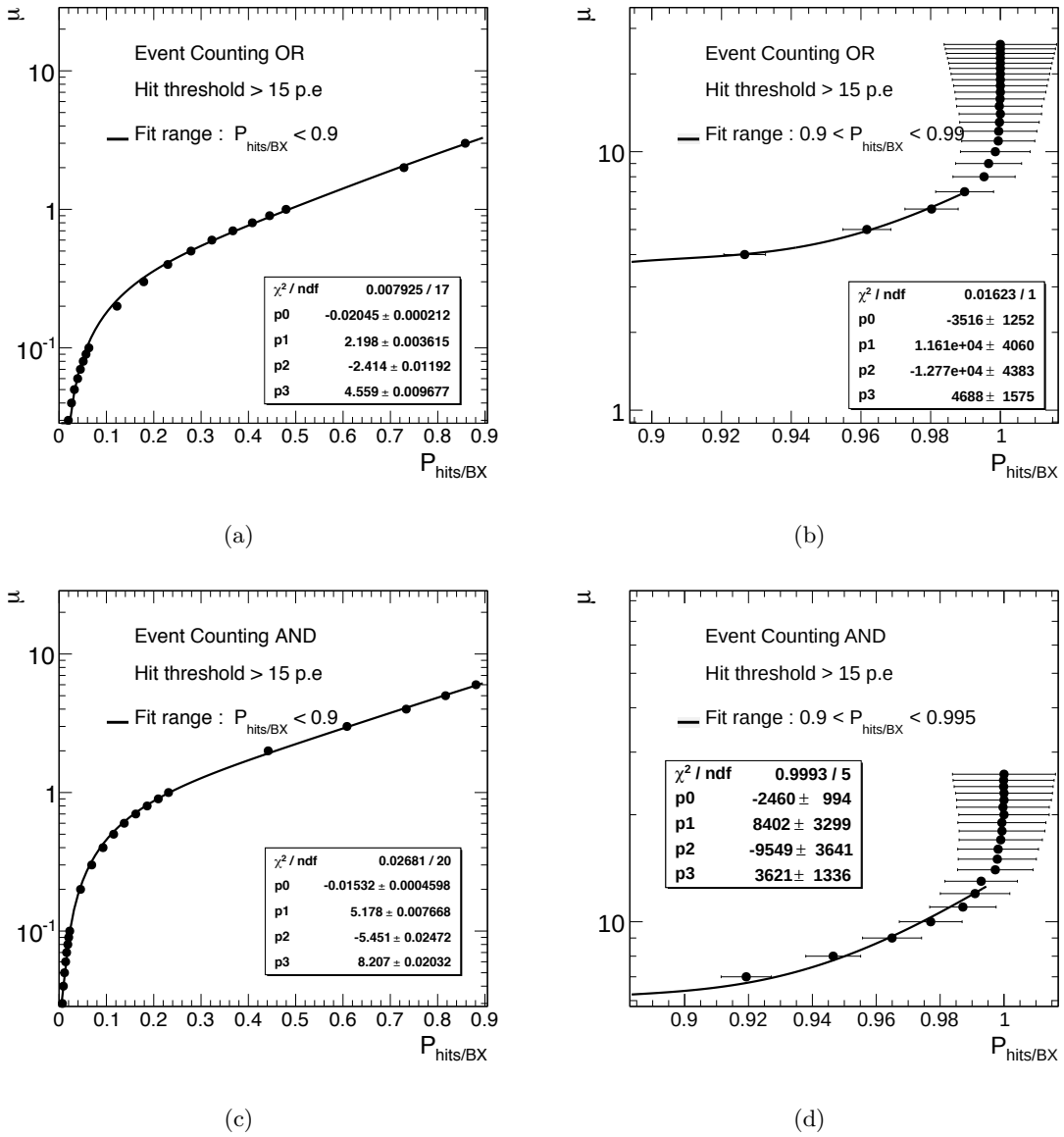


Figure 8.8: *Polynomial fits of the average number of pp interactions per event (μ) as a function of the average number of detected events ($P_{hits/BX}$) with event counting "OR" method for $P_{hits/BX} \leq 0.9$ (a) for $0.9 < P_{hits/BX} \leq 0.99$ (b) and event counting "AND" method for $P_{hits/BX} \leq 0.9$ (a) for $0.9 < P_{hits/BX} \leq 0.995$ (b).*

effects in which signals below the discriminator threshold in one *pp*-interaction are able to pile-up and give a signal above the threshold in multi-interaction events. Saturation effects, despite being included in the combinatorial model, also play a role. The impact is indirect in the sense that small fluctuations in $P_{hits/BX}$ or $N_{hits/BX}$ at high μ, for example due to limited statistics, leads to large changes in μ_{meas}.

An empirical solution to the problem of non-linearities is to parametrize all such effects with polynomial fits to μ as a function of the event rate. In effect, this means that values of μ can

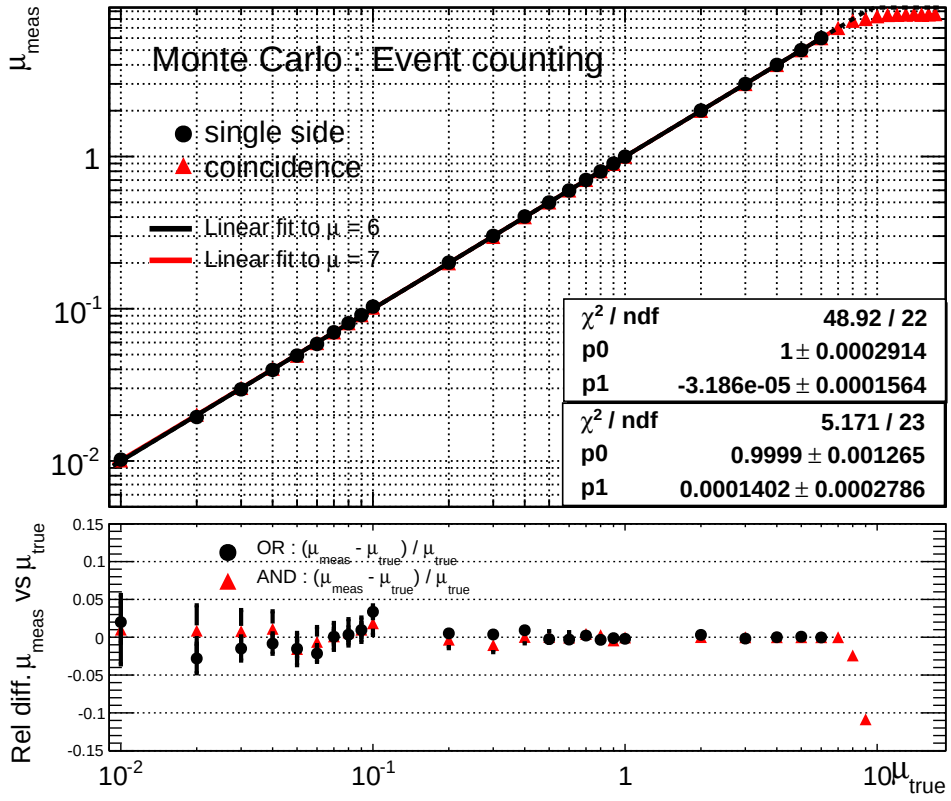


Figure 8.9: *Top: average number of pp interactions per event measured (μ_{meas}) with the polynomial fit model with hit counting "OR" and "AND" methods versus the true value (μ_{true}). A linear fit is superimposed. Bottom: deviation from the true value.*

be extracted directly from fit to $P_{hits/BX}$ for the event counting methods and $N_{hits/BX}$ for the hit counting methods without having to deal with the inversion of equation 8.20 and 8.35. The polynomial fit is in that sense the numerical inversion of the combinatorial formulas. The drawback of this approach is that it lacks physical motivation. There is no physical reason why a polynomial should be used expect that it by construction can give good results for both event and hit counting.

Event counting

If approximated with a polynomial in $P_{hits/BX}$ of degree n, μ can be expressed as:

$$\mu = f(P_{hits/BX}) = \sum_{i=0}^{n} p_i P_{hits/BX}^i \tag{8.39}$$

If n is equal to the number of data point for $P_{hits/BX}$ then the expression is exact, otherwise it is an approximation. The degree of the polynomial fit depends on the counting method and on the range of μ. To keep the order of the polynomial smaller than 4, the polynomial fit is performed in two different ranges of μ. The results of the fits for a threshold of 15 p.e are shown in figure 8.8 for single side and coincidence mode. To study the performance of

the polynomial parametrization approach, the obtained value of μ from the fits are compared to the true value in figure 8.9. The slope of the linear fits are consistent with 1 which means that non-linear effects are taken into account in the range < 6 for event counting in single side mode and in the $\mu < 7$ for event counting in coincidence mode. Any deviation between μ_{meas} and μ_{true} can be tracked back to discrepancies between the fitted polynomial and the data points which could reveal some underlying problem with the fits. An example of such a problem is the inability of the 3 order polynomial to describe the trend of the data points at values of $P_{hits/BX}$ close to 1. As a results the obtained values of μ_{meas} for the coincidence mode exhibits deviations at high μ_{true}.

Hit counting

If approximated with a polynomial in $N_{hits/BX}$ of degree n, μ can be expressed as:

$$\mu = f(N_{hits/BX}) = \sum_{i=0}^{n} p_i N_{hits/BX}^i \tag{8.40}$$

The results of the fits are shown for a 15 p.e. threshold in figure 8.10 for both hit counting methods and the obtained value of μ from the fits are compared to the true value in figure 8.11. The slope of the linear fits in the range of $\mu \leq 25$ are consistent with 1 which means that all non-linear effects are taken into account in the full luminosity range. As opposed to the event counting method, the polynomial parametrization approach in the hit counting method has shown to be a significant improvement over the combinatorial method.

8.6 Offline Algorithms

A shortcoming of the online algorithms presented above, is that they only use a fraction of the information available in the calibration and measurement runs. This is a compromise to keep the online algorithms more suited for automated operation during data taking and to retain stability at all time. For offline algorithms there is a larger degree of freedom to incorporate more detector information in order to minimize the non-linearity effects in the prediction. A new class of algorithms is presented here, in which instead of using the mean value of the multiplicity distributions ($N_{hits/BX}^{OR}$, $N_{hits/BX}^{AND}$), as was the case in the online algorithms presented above, one uses the actual shape of the distributions themselves.
In the following section it will be shown that by basing luminosity algorithms on the shape of the multiplicity distribution, it will be possible to incorporate all non-linear detector effects.

8.6.1 Description of the proposed method

The offline method we propose here is based on the same two type of runs as the online methods, namely the **calibration** and **measurement** runs.

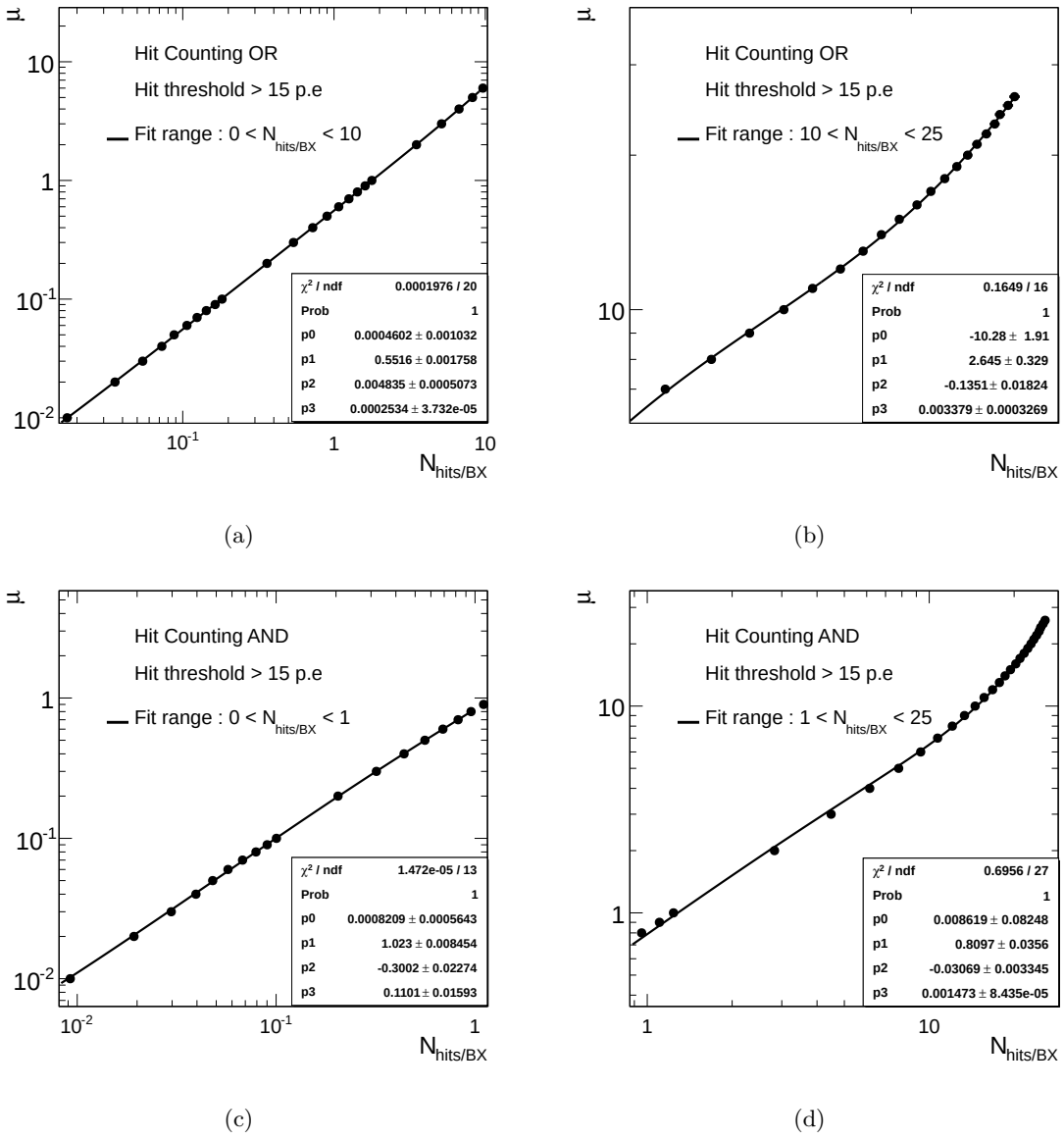


Figure 8.10: *Average number of pp interactions per event (μ) as a function of the average number of hits per event ($N_{hits/BX}$) with hit counting "OR" and "AND" method. The distribution is fitted with a 4th degree polynomial for $\mu \leq 10$ (a) and $10 < \mu \leq 25$ (b) for the "OR" counting and $\mu \leq 1$ (a) and $1 < \mu \leq 25$ (b) for the "AND" counting.*

Calibration runs

The response of a measured generic detector quantity in this type of runs can be considered as the response to a single interaction. If ρ identifies a measurable quantity (for instance hit multiplicity, total energy , etc.) then ρ_1 is that quantity for the calibration sample. The response of the detector to any number n of interactions can be built as a linear superposition starting from ρ_1. In this way one is able to build a set of *reference responses* ρ_n where

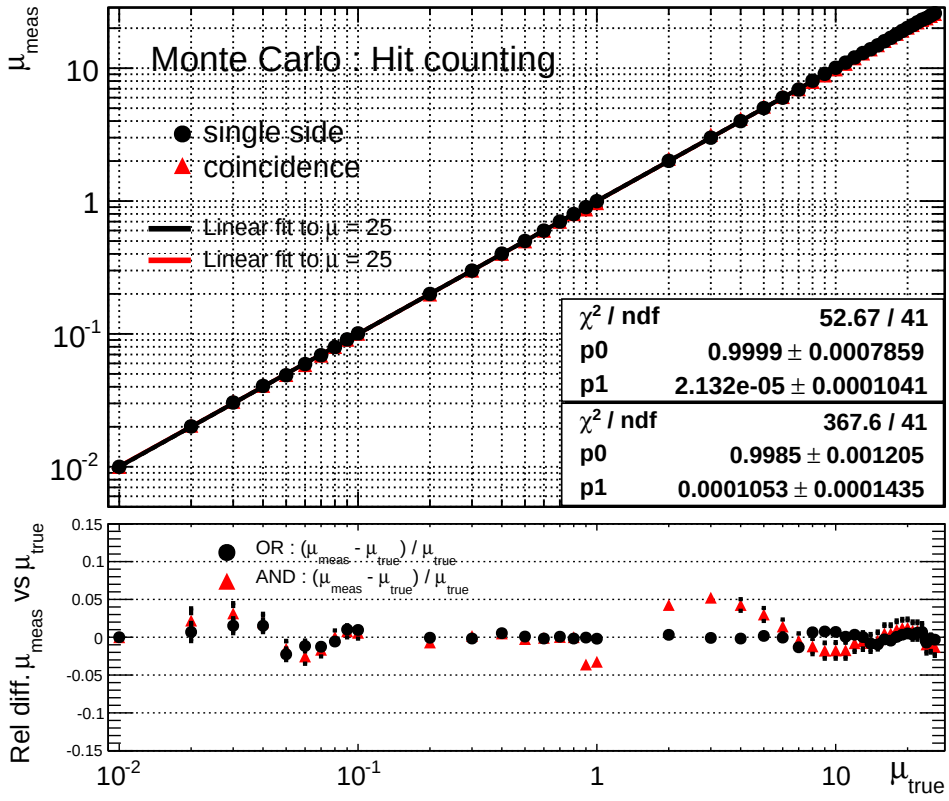


Figure 8.11: *Top: average number of pp interactions per event measured (μ_{meas}) with the polynomial fit model with hit counting "OR" method versus the true value (μ_{true}). A linear fit is superimposed. Bottom: deviation from the true value.*

$n = 1, 2, ...N_{MAX}$ up to a maximum number N_{MAX} of interactions.

Measurement runs

A measurement run is a run performed at an unknown value of μ which has to be measured. If it can be assumed that the BX population follows Poisson statistics (see equation 8.2) then the total response R of the detector (for the quantity described by the *reference responses* ρ_n) when the average number of interactions per BC is μ can be expressed as:

$$R = A \sum_{n=1}^{N_{MAX}} P_\mu(n)\rho_n \tag{8.41}$$

where A is a normalization factor and the upper limit of the summation, N_{MAX}, has to be suitably chosen in order to make the contributions from $n > N_{max}$ negligible.
The theoretical detector response R should then be compared with R_{exp}, the one measured during the measurement run. This can be done on a statistical basis by fitting the R_{exp} response by means of the R function leaving free the two parameters A and μ. In this way, a direct measurement of μ can be obtained. It has to be noted that, by construction, this method will fail for measured values of $\mu \ll 1$. However, it will be shown in the following that

this method can reliably measure any values of $\mu \geq 0.5$, which are the ones to be considered of practical interest for most measurement runs.

8.6.2 Application of the method

When the method is applied to LUCID, one has to define a hit threshold separately for each run type. During the calibration runs, a hit threshold (thr_{cal}) must be imposed to trigger the readout electronics in order to record the event. Without imposing such a threshold, all events (including empty bunches and beam background events) would be recorded and as a consequence the calibration sample would no longer only contain single interaction events. In this study only events with a hit coincidence have been included in the calibration sample. In analysis of real data an equivalent requirement would be to only consider events flagged by the L1_LUCID_A_C trigger. For the measurement runs the hit threshold is denoted by thr_{meas}. It has to be stressed here that the ideas behind the two thresholds are different. In the measurement runs, thr_{meas} is imposed to trigger on a bunch crossing with multiple interactions. In the calibration run however, the hit threshold thr_{cal} is used to trigger the LUCID readout electronics when a single interaction occurs. For this reason thr_{cal} must fixed at a high enough value to filter out beam background events while still low enough to keep the statistics in the calibration runs high.
Figure 8.12(a) shows the effects of applying different values of thr_{cal} on the photo-electron spectrum during the calibration runs. Figure 8.12(b-d) shows the same situation but for different number of collisions per bunch crossing. The discrepancy of the distributions increases with the number of interactions. The reason for this is that a trigger threshold greater than zero *p.e.* tends to suppress the lower part of the distributions. In the current configuration of LUCID the hit threshold is set to 15 p.e. So in order to make the study presented in this thesis as realistic as possible, a similar value has been adapted (the black lines in figure 8.12). The value of thr_{meas} has been set to 50 p.e for the study presented here.

The **reference responses** ρ_n (see Equation 8.41) in the LUCID case are the hit multiplicity distributions for triggered events, which are denoted with $m_n(i)$. The index n refers to the number of interactions and i is the overall multiplicity recorded by $LUCID$. The index i can effectively run from 2 to 30 hits, the lower value being constrained by the coincidence mode. The reference responses $m_n(i)$ are built by mixing n events obtained from the calibration run, piling up the pulse height distribution and then applying the thresholds which is used in the measurement runs.
To extract the value of μ_{meas} from a certain experimental response $R_{exp}(\mu)$, a weighted sum of the reference responses described by 8.41 is fitted to $R_{exp}(\mu)$. Examples of such fits are shown in fig. 8.13 for four different values of μ. Once μ_{meas} has been obtained from the experimental detector responses $R_{exp}(\mu)$ for a suitable range of μ values, the calibration constant κ_{MC} for the data set can be extracted. This is done by plotting the measured values of μ as a function of the true value and fitting the resulting curve with a linear function that goes through the origin. Figure 8.14 shows such a fit to the values of μ_{meas} for the non-, single and double diffractive data sets separately and in figure 8.15 for the total inelastic data set. The dotted black line shows a hypothetical one-to-one correspondence between μ_{meas} and μ_{true}. To illustrate the need for a calibration of the data, the deviation between the measured and true value of μ , $(\mu_{meas} - \mu_{true})/\mu_{true}$ are plotted as a function of μ_{true} for each data set. In

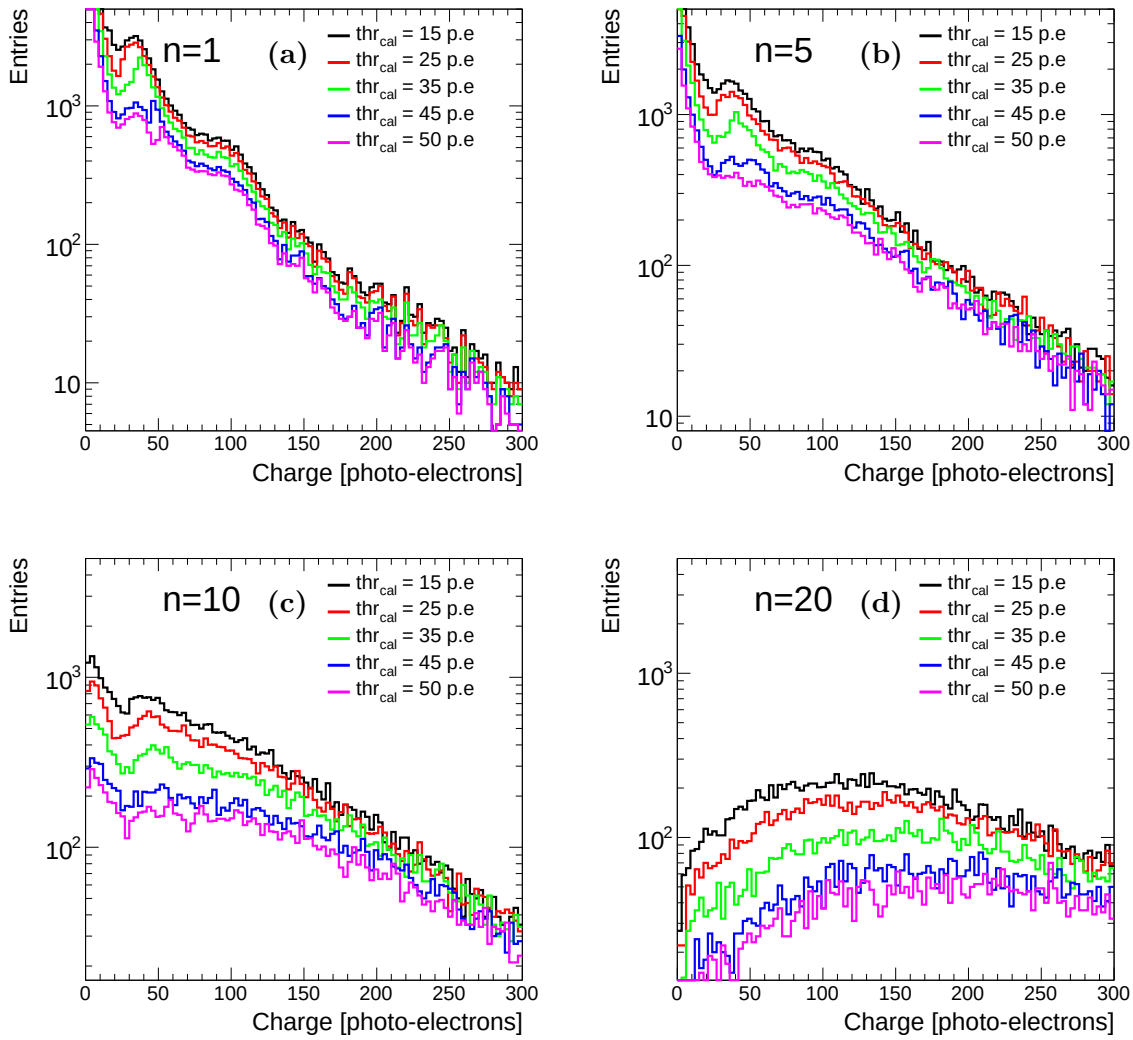


Figure 8.12: *Examples of photo-electrons distributions for triggered events with different values of the trigger threshold thr_{cal} (in number of p.e.) for $n = 1$, $n = 5$, $n = 10$ and $n = 20$ interactions.*

the hypothetical situation where the fitted line is identical to the one-to-one line[7] there would be no need for a calibration constant. In that case the data would be self-calibrated. Table 8.5 gives the calibration constant for the different components of the inelastic data set and for the inelastic data set itself.

The most striking feature of this result is that the prediction of the method is linear over a large range ($0.5 \leq \mu \leq 25$). The predictions for all data sets are compatible with a linear function going through the origin proving that the method yields the correct luminosity at $\mu = 0$. This proves that the range in which the method provides reliable prediction for the luminosity covers a part of the LHC range.

[7] $(\mu_{meas} - \mu_{true})/\mu_{true} = 0$ for all μ_{true}.

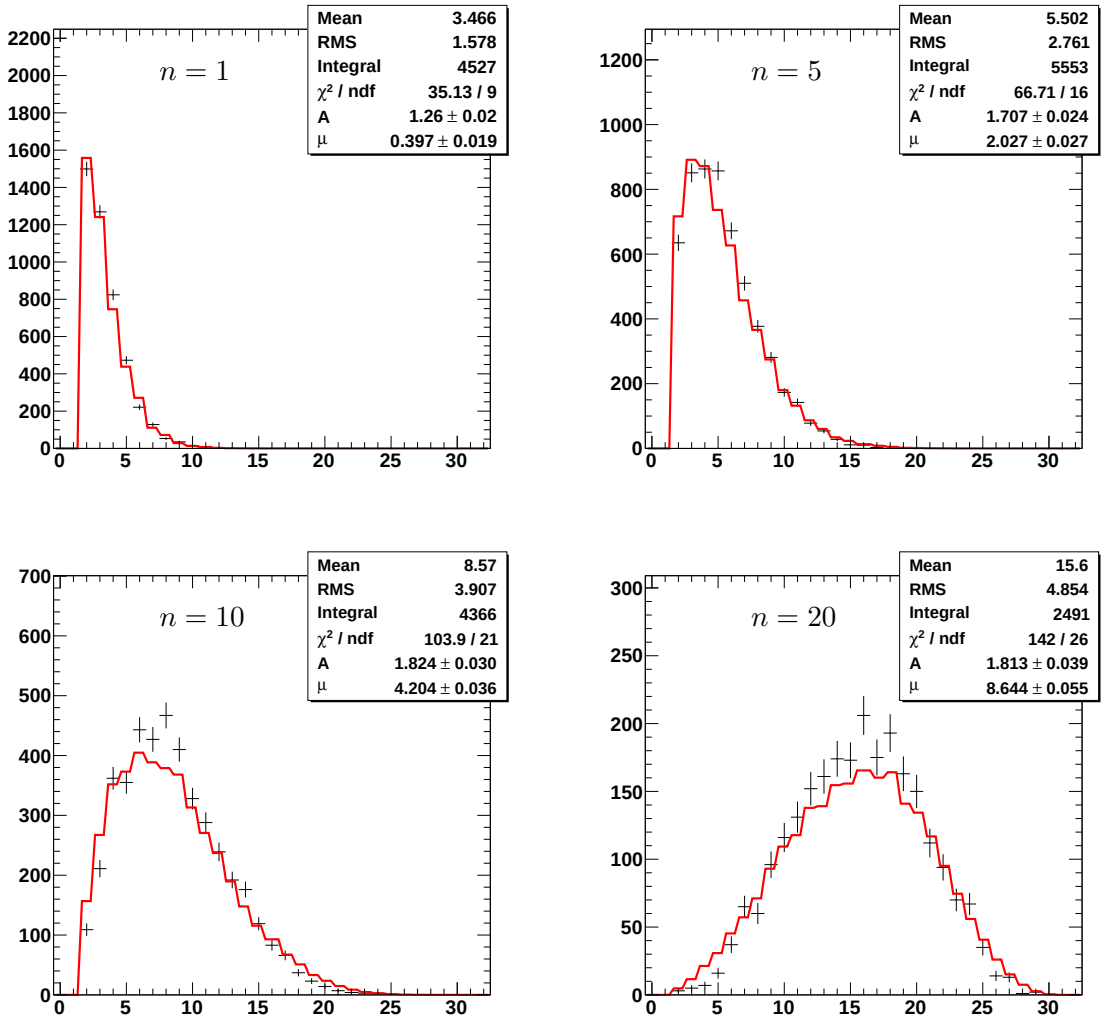
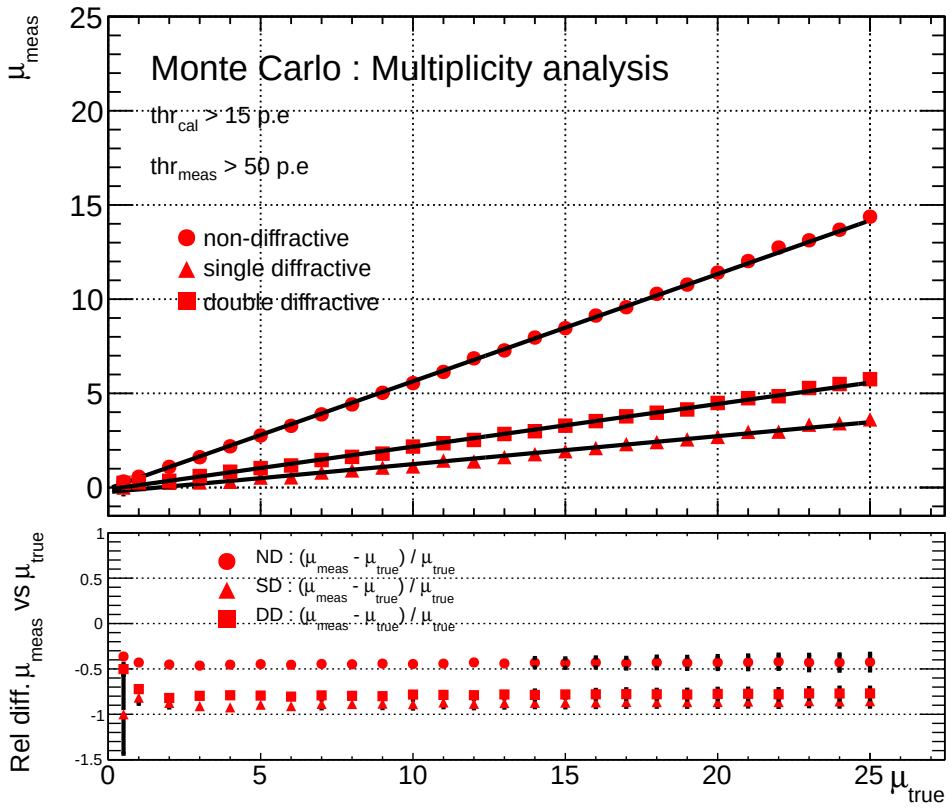


Figure 8.13: *Examples of detector responses $R_{exp}(\mu)$ from the measurement runs at $\mu = 1$, 5, 10 and 20 interactions. The trigger threshold used in the in the measurement runs as $thr_{phys} = 50$ p.e. The red line shows fits of the LUCID response function $R(\mu)$ to the detector responses.*

event type	ND	SD	DD	inelastic
f_i [%]	68 %	19 %	13%	100 %
κ_{MC}	0.569 ± 0.001	0.149 ± 0.002	0.226 ± 0.002	0.434 ± 0.001

Table 8.5: *Calibration constants for the different data sets considered in this analysis.*

Another interesting feature which can be seen from figure 8.14 is that the calibration constant takes on different values for each data set. The reason for this, is that the average track multiplicity is smaller for diffractive events than for non-diffractive events. This means that the hit threshold in the calibration runs (thr_{cal}) will cut harder on diffractive events and



(a)

Figure 8.14: *(Top) The red data points shows the measured values of μ as a function of the true value for non-, single and double diffractive data set. The solid black lines in the plot shows result of linear fit to the data points. The dotted black line shows a one-to-one correspondence between μ_{meas} and μ_{true}.(Bottom) The absolute deviation of μ_{meas} from μ_{true} as a function of μ_{true} for the different data sets. Superimposed in the figure is also the statistical uncertainty on the data points.*

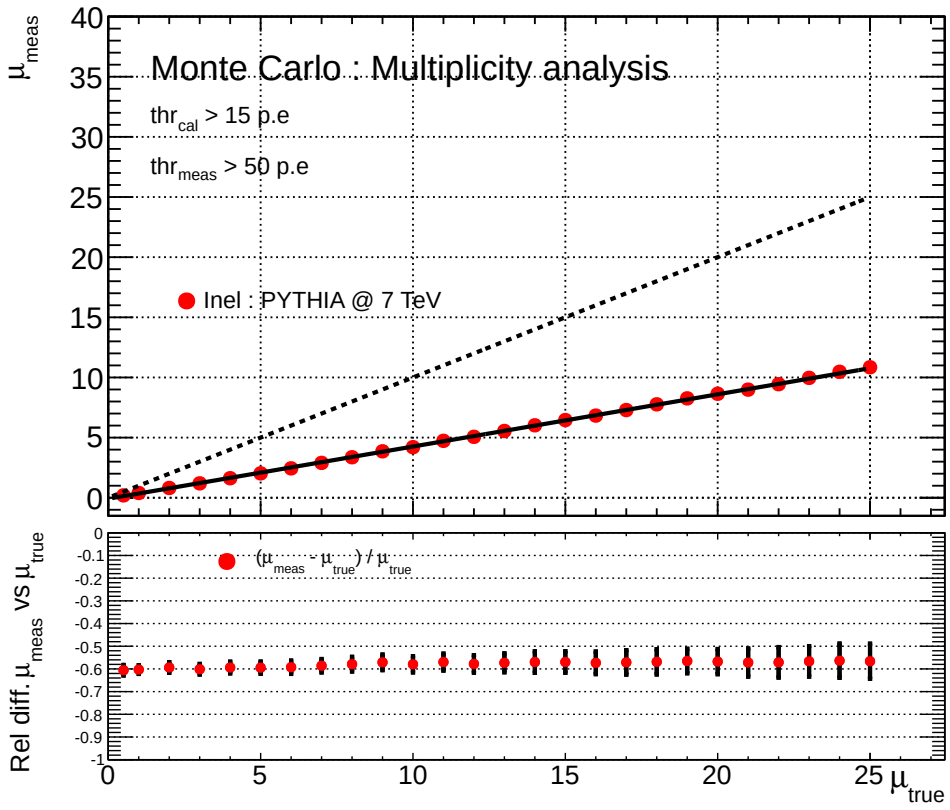
thereby lead to an overestimated mean value of the reference response when compared to the distributions obtained in the measurement runs.

Just as the total luminosity can be calculated from the contributions of the non-diffractive and diffractive parts so can the calibration constant:

$$\kappa_{MC}^{inel} = f_{ND}\kappa_{MC}^{ND} + f_{SD}\kappa_{MC}^{SD} + f_{DD}\kappa_{MC}^{DD} \tag{8.42}$$

where f_i is the fraction of events of type i in the total inelastic data set ($f_{inel} = 1$) and κ_{MC}^{i} is the calibration constant for data set i. Inserting the numbers from table 8.5 one can calculate that the expected value of κ_{MC}^{inel} for the total inelastic data set is 0.444. This value is slightly higher than the measured value, which is 0.434.

One of the main features of the method presented here, is that it yields a linear relationship between μ_{meas} and μ_{true}. This feature is intrinsic to the method and means that one only needs one calibration point apart from the origin to predict the luminosity in most of



(a) μ_{meas} vs μ_{true}

Figure 8.15: *(Top) The red data points shows the measured values of μ as a function of the true value for the total inelastic data set. The solid black line in the plot shows result of linear fit to the data points. The dotted black line shows a one-to-one correspondence between μ_{meas} and μ_{true} .(Bottom) The absolute deviation of μ_{meas} from μ_{true} as a function of μ_{true}. Superimposed in the figure is also the statistical uncertainty on the data points.*

the LHC range. It is assumed that for zero interactions per BX, the measured value of μ will also be zero. Whether or not this is a correct assumption will be discussed in sec. 8.7.6 where the influence of beam background is addressed.

8.7 Systematic Uncertainties

The main experimental systematic uncertainties in the luminosity measurement arise from two sources: the detector itself and the LHC beam. A list of systematics include contributions from: gas pressure and temperature stability, PMT gain stability, trigger conditions, event composition and background. The estimation of these uncertainties is the subject of this subsection.

From the previous sections we know that within the range of validity, each luminosity algorithm yields a linear relationship between μ_{true} and μ_{meas} expressed by equation 8.1. The

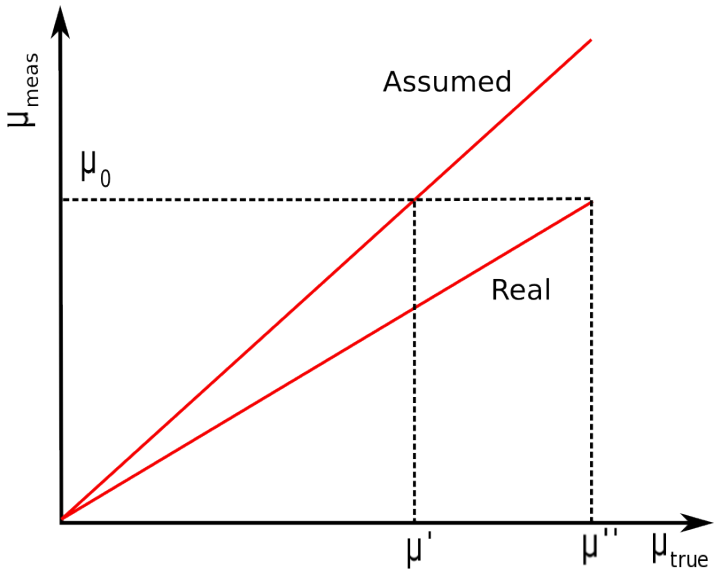


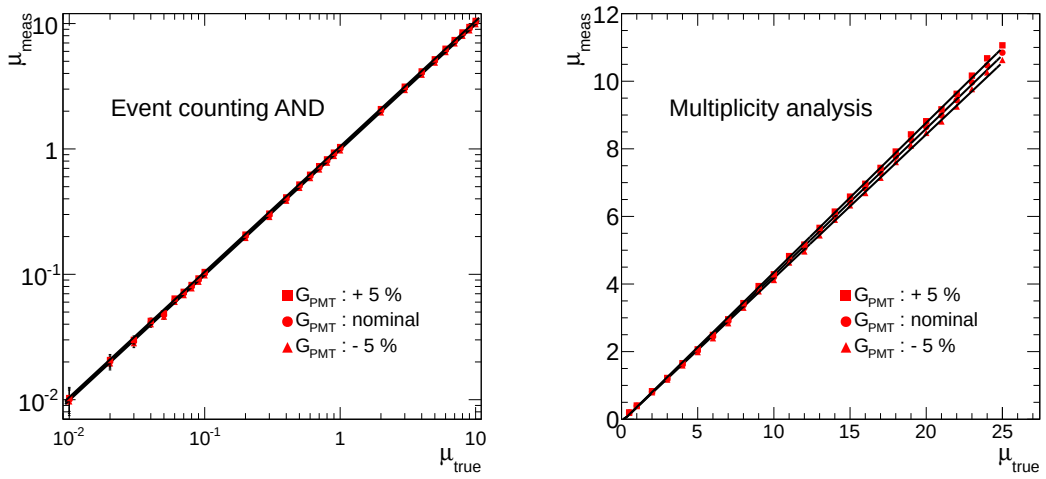
Figure 8.16: *Calculation of luminosity measurement error.*

systematic uncertainties affect the slope of the linear relationship. When the conditions change[8], the calibration constant changes value from the original value of κ_0 to κ_1 giving a new value for μ_{true} : $\mu''_{true} \propto \kappa_1^{-1}\mu_{meas}$, as shown in figure 8.16. The relative error in the luminosity measurement by such a change in the conditions can be estimated by:

$$\frac{\Delta\mathcal{L}}{\mathcal{L}_1} = \frac{\mathcal{L}_0 - \mathcal{L}_1}{\mathcal{L}_1} = \frac{\mu'_{true} - \mu''_{true}}{\mu''_{true}} = \frac{\mu_{meas}/\kappa_0 - \mu_{meas}/\kappa_1}{\mu_{meas}/\kappa_1} = \frac{\kappa_1}{\kappa_0} - 1 \tag{8.43}$$

Due to the different nature of the offline and online algorithms, the different sources of systematic uncertainty do not contribute equally. For the online algorithms which rely on Monte Carlo simulation to provide estimates of the detection efficiency and average hit multiplicity, the details of the simulations are expected to provide the largest sources of systematic uncertainty. For the offline algorithms the largest contributions are foreseen to come from changes in running conditions between the calibration runs and the measurement runs. It is a fundamental assumption of the offline method that any set of calibration and measurement runs can be carried out under the same running conditions. If this is not the case then a bias will be introduced in μ_{meas} by potentially having different shapes of the multiplicity distributions in the two data taking scenarios. Both types of algorithms assume a Poissonian distributed number of collisions per bunch crossings. Any deviation from this behavior may cause loss in accuracy.
In the following sections, Monte Carlo simulations are used to evaluate the impact of the systematic uncertainties on the ability to extract the luminosity. This is done by systematically changing the running conditions and using equation 8.43 to estimate the relative uncertainty. In order to be consistent the full list of systematic errors are taken into account for each luminosity algorithm separately. For the sake of completeness it should be mentioned here that the impact of the systematic uncertainties is only investigated in the region of μ where the given algorithm is linear - the so-called validity range. Outside this range, the estimation of systematics in this way is no longer useful.

[8]assuming the linear relation between μ_{true} and μ_{meas} is maintained



(a) (b)

Figure 8.17: *Impact on the luminosity determination using the event counting (a) and multiplicity analysis (b) from variations in the PMT gain.*

8.7.1 Detector related uncertainties

Online and offline : Possible sources of systematics in the detector description include uncertainties in the gas temperature and pressure and the reflectivity of the tubes internal surface. Another class of detector related uncertainties which could potentially influence the luminosity determination, stems from the readout electronic and includes uncertainties due to the PMT gain and noise level. Both classes of systematic uncertainties were discussed in detail in section 6.5 and will therefore not be discussed further here. As an example, figure 8.17 shows the impact of the uncertainty in the PMT gain on the luminosity measurement for event counting in single side mode and the multiplicity analysis. Table 8.6 summarizes the contributions to the total systematic uncertainty from uncertainties in the detector description.

8.7.2 Event composition

Since the average charged multiplicity is higher for non-diffractive events than for diffractive events (see figure 7.5) it will lead to a shift in μ_{meas} if the composition of the calibration and measurement run is not identical. As the difference in charged multiplicity between single and double diffractive events is not as large as the difference between the non-diffractive and diffractive events, only a difference in the ratio between the two latter in the calibration and measurement data sets will potentially lead to a shift in μ_{meas}.

Offline : Figure 8.18 shows how the value of κ_{MC}^{inel} changes as the fraction of non-diffractive events in the reference sample is changed. From the plot it is clearly seen that as the fraction of diffractive events in the reference samples gets larger, the value of κ_{MC}^{inel} gets smaller. This

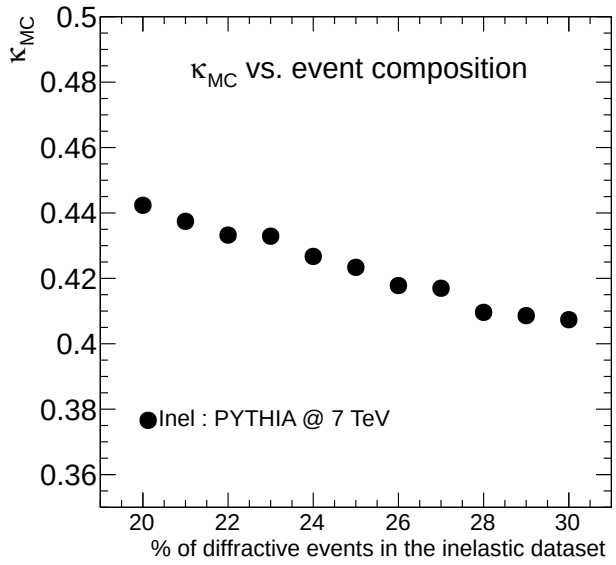


Figure 8.18: *Value of κ_{MC}^{inel} as a function of changes in the fraction of diffractive events in the data set.Only the composition of the reference is modified.*

is expected since as the fraction of diffractive events in the reference samples gets larger, the average multiplicity per event will decrease leading to a smaller value of μ_{meas}.
The inelastic Monte Carlo data sets consist of 68 % non-diffractive events and 19 % and 13 % single and double diffractive events. Since the actual fraction of non-diffractive and diffractive events in inelastic events are not fully known, it has been studied if the value of κ_{MC}^{inel} depends on the overall composition of the data sets. The contribution of this effect to the systematic uncertainty is estimated to be $\approx 3\%$.
Traditionally also central diffractive events (CD) belongs to the category of diffractive events. However since the central diffractive cross section constitutes less than 1 % of the total inelastic *pp* cross section, these events have been ignored in this study.

Online : A similar study have been carried out for the online algorithms. It is estimated that the contribution to the total systematic uncertainty is 2 % for the "OR" algorithms and 3 % for the "AND".

8.7.3 Bunch to bunch variation in μ_{true}

Online and offline : Variations in the average number of collisions between different bunch crossings might have an influence on the calibration constant if the luminosity is not calculated separately for each bunch crossing. In the Monte Carlo simulations it is assumed that the number of collisions per BX is Poissonian distributed around μ. However, in the LHC, bunches might be filled differently leading to different average number of interactions for different bunch crossing. The number of interaction will still follow a Poisson distribution but with a different mean value for each bunch crossing. In the 2010 data-taking period large

variations in the bunch luminosities has been observed so the analysis has to be carried out for individual BCIDs. This will remove the systematics from bunch to bunch variation in μ_{true}.

8.7.4 Applying an external trigger

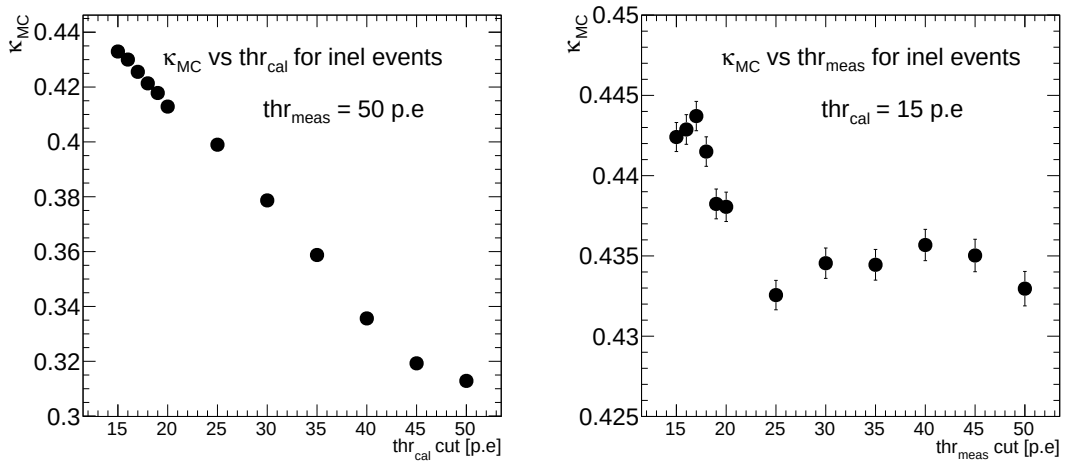
Offline : Because of the need to introduce a calibration threshold (thr_{cal}) when using LUCID as a trigger, some bunch crossings will be detected while others will be left undetected. In order to build a realistic LUCID response to bunch crossings with multiple interactions from the reference samples, it is necessary to know the response of LUCID to undetected bunch crossings. An external trigger could be used in combination with LUCID to provide such a sample of *unbiased single interactions* from the calibration runs. This is possible since an external trigger would be able to select those events, in which LUCID detects some activity but not a large enough signal to separate the signal from general background/noise.
The Minimum Bias Trigger Scintillators (MBTS) is a candidate for an external trigger. Other detector systems could in principle also be used but the MBTS was chosen since it is designed to efficiently detect minimum bias events. Its high efficiency combined with the fact that the min bias events constitutes the bulk part of the total inelastic cross section makes the MBTS a ideal candidate to provide an unbiased trigger for the calibration runs. Another motivation for using an external trigger is due to the influence of systematic uncertainties in the calibration constant. However, with the current setup in the LUCID readout electronics it has not been possible to trigger the data streams with an external trigger and it will therefore not be discussed further in these studies. For future studies, however, the application of an external trigger presents an interesting unbiased alternative to using LUCID itself as a trigger.

8.7.5 Trigger conditions

Offline : The offline method requires stable running conditions. Stable in this case means that the running conditions used in the calibration runs are not considerably different from the ones used in the measurement runs. An important requirement is that the same value of thr_{cal} is used in the two types of runs. Any change to thr_{cal} will lead to a shift in the mean value of the reference responses (ρ_i) which in turn will affect the value of the calibration constant κ_{MC}. Figure 8.19 shows how the value of κ_{MC} changes as a function of thr_{cal} and thr_{meas}. The largest changes to κ_{MC} occur when thr_{cal} is varied. This is expected since the value of thr_{cal} is applied in the calibration runs to collect the data sample from which reference responses are build. As a consequence, thr_{cal} determines the mean values of ρ_i and thereby also the extracted value of κ_{MC}. As will be shown later, the actual value of thr_{cal} is not so important[9] but mostly the precision at which the threshold can be set. Since the value of the recorded signal in the readout electronics is known with a precision of 1-2 p.e it is estimated that the contribution to the systematic uncertainty from a variation of thr_{cal} and thr_{meas} is 2% and 1% respectively.

Online : A similar study has been carried out for the online algorithms. Since the online algorithms only use a hit threshold in the measurement runs, only variations of thr_{meas}

[9] as long as the linearity of the method is preserved.



(a) (b)

Figure 8.19: *Variations in κ_{MC}^{inel} as a function of changes to the trigger conditions. (a) Varations in κ_{MC}^{inel} when thr_{cal} is changed and thr_{meas} fixed. (b) Varations in κ_{MC}^{inel} when thr_{meas} is changed and thr_{cal} fixed.*

are taken into consideration. It is estimated that the contribution to the total systematic uncertainty is 3 % for the "OR" algorithms and 1 % for the "AND".

8.7.6 Background

Online and offline : The main backgrounds in minimum bias events, particularly during early running, will be beam-gas collisions within the beampipe over the length of ATLAS, and beam-halo from interactions in the tertiary collimators in the accelerator. It is important to take these events into considerations since they have the potential of providing spurious triggers. So in order not to pollute the total inelastic data set, beam background events must be filtered out. During early low luminosity running a large fraction of bunch crossings will have no *pp* interactions. Using a trigger based only on bunch-crossings would result in a large number of empty events, which only contain detector noise, being recorded. Therefore, the trigger must be able to reject such events in order to optimize the use of the trigger bandwidth.
Measurements of the beam background level during the early 2010 data taking period (see section 7.6) have shown that for LUCID in single side mode, the level of background is around 0.06 % while the coincidence mode is background free. For this reason the systematics due to background will be ignored in the following.

8.7.7 Evaluation of the total systematics

A summary of the systematic uncertainties is given in table 8.6. The overall uncertainty is 6 % and 7 % for the online "OR" and "AND" respectively and it is dominated by uncertainties

in the PMT gain. For the offline algorithms the dominating contribution (3 %) comes from variations in the event composition. For both types of algorithms the contributions from beam induced background and bunch to bunch variations to the measurement of μ are negligible and have therefore been ignored.

Quantity	$\pm\Delta Q/Q$ [%]	$\pm\Delta\kappa_{MC}/\kappa_{MC}$ [%]				
		Online				**Offline**
Method		**Event count**		**Hit count**		**Mult.**
Mode		"OR"	"AND"	"OR"	"AND"	"AND"
Gas pressure	1	< 1	1	< 1	1	< 1
Gas temperature	5	2	3	1	1	2
Tube polish	5	1	< 1	1	< 1	2
PMT gain (G_{PMT})	5	3	4	4	5	2
amp. factor (G_{AMP})	5	2	3	1	3	1
noise factor (Q_{noise})	5	1	1	< 1	2	1
Event comp.	20	2	3	2	3	3
thr_{cal}	10	–	–	–	–	2
thr_{meas}	10	3	1	3	1	1
Total		6%	7%	6%	7%	5%

Table 8.6: *Summary of systematic uncertainties in the calibration constant κ_{cal}. The total systematic uncertainty is found by adding up the different contributions in quadrature.*

8.8 Summary and conclusion

It was said in the beginning of this chapter that the main difficulty in measuring the luminosity at the LHC, is detector related effects caused by pile-up. The precision of the final luminosity determination therefore depends on the ability to minimize these effects in the luminosity algorithms. This is not a trivial task and the main purpose of the present study was to develop and study the performance of such algorithms.
Two classes of luminosity algorithms have been presented and applied to data from the LUCID detector. The first class is based on Monte Carlo calibrations and designed to be operated online. In this class two different counting methods are used to extract the average number of interactions per bunch crossing. The event counting method is based on the rate of detected events and the hit counting method is based on measuring the average number of hits registered in the detector. Each method is operated using two distinct detection modes: single side mode in which an interaction is detected if a hit is registered in one of the two detector modules, and coincidence mode in which an interaction is detected if a hit is registered in both modules simultaneously. The second class of luminosity algorithms presented in this chapter is designed to be applied offline. Belonging to this category is a method, which uses the hit multiplicity distributions, obtained at low luminosity ($\mu \ll 1$) to extract the luminosity. The performance of all methods is evaluated using Monte Carlo simulations.

It has been shown in this chapter that saturation and migrations effects distort the predictions from both event and hit counting methods. Saturation effects, however, only affect the combinatorial model indirectly. The level of distortion depends on the counting method and the detection mode but is in general expected to grow with μ. This means that the predictions are only expected to be proportional to μ for small μ. The study presented here confirms this expectation by showing that all counting methods can be described by a linear approximation in the region $0 < \mu \leq 0.1$. For event counting in coincidence mode and hit counting in single side mode, however, the linear approximation gives reliable results up to $\mu = 2$. If a model that incorporates combinatorial effects is used instead of the linear approximation, then the range of validity/usability is extended for all the methods. For event counting in single side (coincidence) mode, the range of validity is extended from 0.1 to 8 (2 to 10). The level of improvement is more modest for hit counting where the validity range is extended from 0.1 to 1 for coincidence mode, while the range for single side mode remain unchanged. A somewhat surprising observation in this part of the study is that the full combinatorial model does not improve the result compared to the linear approximation in single side mode. The reason is that migration and saturation are two effects that to some extent cancel out and so if one corrects for saturation but not migration, the result is worse than if no correction is made. For hit counting in coincidence mode the conclusion is different. Here the combinatorial effects are much larger and a linear approximation breaks down already at a μ of 0.1. The full combinatorial model increases in this case the μ range with an order of magnitude but the usable range still remains very limited.

The overall conclusion at this stage is therefore that the best online methods to use are the event counting methods with the full combinatorial model. The systematic uncertainty for these methods is at the order of 6-7 % over a range from $\mu = 0$ to $\mu = 8$. The usable range and total systematic uncertainty for each counting method is summarized in the upper part of table 8.7. It is important to note that the quoted systematic uncertainty for the two counting methods is for different validity ranges. If the validity range of the hit counting would be extended to the same as the event counting then the systematics would increase significantly. A conclusion that can be drawn from the study of the online algorithms is that the deviations are to a large degree caused by the inability to incorporate the migration effects in the combinatorial model. Another approach presented in this chapter is to plot the number of interactions per bunch crossing as a function of the measured number of events or hits (without any corrections). This distribution is then fitted by a polynomial function and this fit function can then be used to estimate the luminosity. With this approach the luminosity can be measured correctly up to a μ value of around 6 with event counting and 25 with hit counting. The limitations of this approach are that the fit procedure in itself introduces an additional source of systematic uncertainty. The contribution to the total systematic uncertainty from the fit procedure is estimated to be 1 % for all the algorithms.

A novel approach to minimizing the non-linear effects is presented in the final part of the chapter. In this approach the hit multiplicity distribution obtained at low luminosity is used to determine the luminosity offline. The results show that the method is linear in the dynamic range ($0.5 \leq \mu \leq 25$), which corresponds to a large fraction of the LHC range. The linearity is a key feature of the method since it allows for a simple extrapolation of the luminosity once a calibration point has been established. Furthermore, the linearity also shows that the method successfully incorporates saturation and migration effects. This proves that using the

	Mode	Calibration	Range	Systematics
		Online		
Event counting	single side	MC	$\mu < 8(0.1)$	6 %
Event counting	coincidence	MC	$\mu < 10(2)$	7 %
Hit counting	single side	MC	$\mu < 2(2)$	6 %
Hit counting	coincidence	MC	$\mu < 1(0.1)$	7 %
		Online : Polynomial parameterization method		
Event counting	single side	data	$\mu < 6$	7 %
Event counting	coincidence	data	$\mu < 7$	8 %
Hit counting	single side	data	$\mu < 25$	7 %
Hit counting	coincidence	data	$\mu < 25$	8 %
		Offline		
Hit multiplicity	coincidence	data	$0.5 < \mu < 25$	5 %

Table 8.7: *Systematic uncertainty of luminosity monitoring with LUCID for different methods and range of validity. The numbers quoted in the parentheses are from the linear approximation.*

shape of the multiplicity distributions instead of just the mean value successfully take the non-linearity effects into account. The total systematic uncertainty quoted for this method is 5 % over the full usable range and this makes the method the most precise luminosity algorithm presented in this chapter. A drawback of the method is that it can only be used offline and only for higher values of μ ($\mu \geq 0.5$). A possible use for this method would be as a precision cross check of the online measurement of the luminosity in ATLAS.
The total validity range for all the luminosity algorithms presented in this study is illustrated in figure 8.20 for comparison.

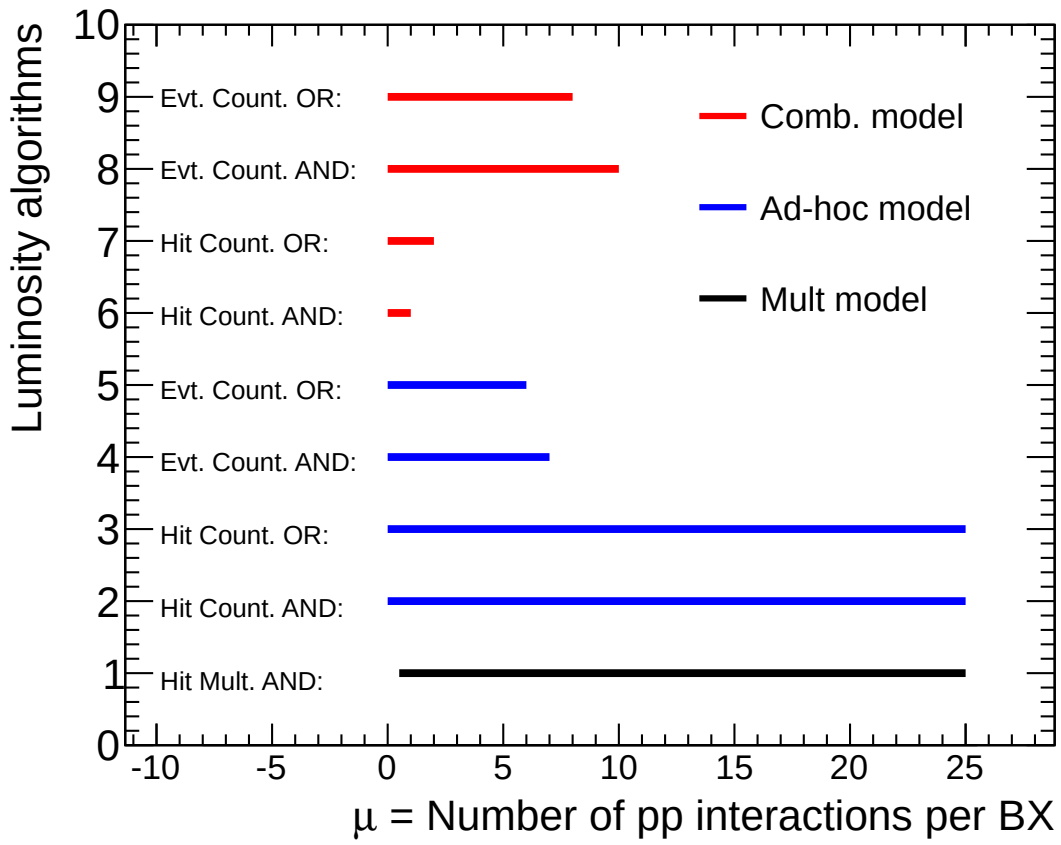


Figure 8.20: *Validity range of the luminosity algorithms.*

Chapter 9

Luminosity determination using the LUCID detector at $\sqrt{s} = 7$ TeV

The results presented in this chapter are a culmination of the methods and results presented in the previous chapters. A selection of the methods discussed in chapter 8 along with the efficiency and average multiplicity determination from chapter 7 will be used to measure the luminosity in a selection of runs taken from the 2010 data-taking period. The analysis carried out in this chapter has been done on the level of a luminosity block but also on the level of the individual bunch crossing. The latter has been done to confirm the claim that LUCID is capable of monitoring the luminosity for individual bunch crossings.
In this chapter it will also be shown how the final result for the measured luminosity depends on the specifics of the calibration scenario. To illustrate this point, the measured values are given using both the Van der Meer calibration method and calibration using Monte Carlo data.

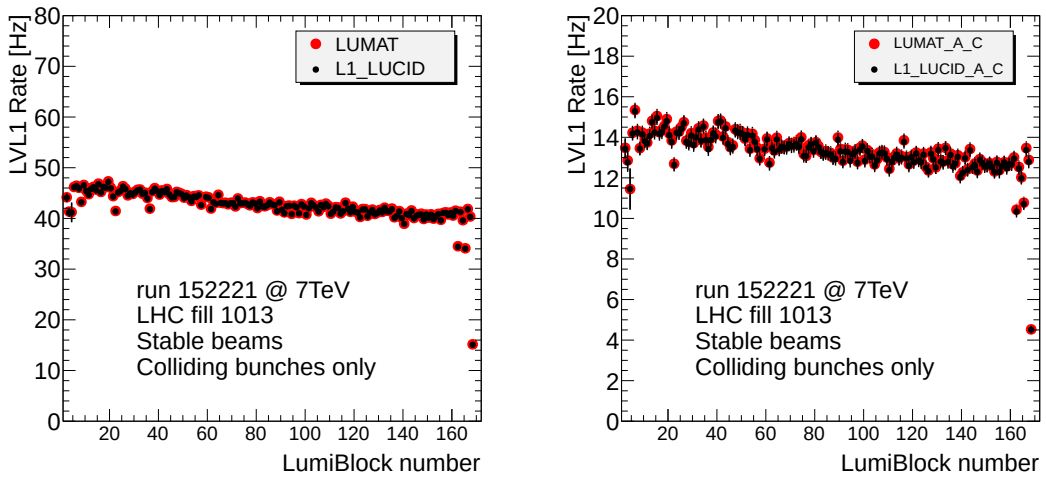
To facilitate an easier comparison between the two calibration scenarios one can introduce a quantity which is referred to as the *visible cross section* defined by $\sigma_{vis} \equiv \varepsilon\sigma_{inel}$ where ε denotes the efficiency of LUCID and σ_{inel} the total inelastic cross section.
Using this definition equation 8.1 can be reformulated as:

$$\mathcal{L} = \frac{\mu n_b f_r}{\sigma_{inel}} = \frac{\mu^{meas} n_b f_r}{\varepsilon\sigma_{inel}} = \frac{\mu^{meas} n_b f_r}{\sigma_{vis}} \tag{9.1}$$

where n_b is the number of colliding bunch pairs and f_r the LHC revolution frequency ($f_{BX} = n_b f_r$).

9.1 The Data sample

The data sample used in the following study consists of 17 runs at $\sqrt{s} = 7$ TeV taken in the period from March 31 to August 25, 2010. The total number of events recorded in this period corresponds to an integrated luminosity of 0.95 pb^{-1}. These runs are chosen since they represent the different stages of the luminosity development from the start of the 2010 data taking period. The run number, number of Luminosity Blocks and number colliding bunches are summarized in table 9.2 for each run.



(a) (b)

Figure 9.1: *Level 1 trigger rate as a function of the luminosity block number for the single side trigger (a) and the coincidence trigger (b). The rate from the CTP (black points) is compared to the rate reported by the LUMAT card (red points) for both triggers.*

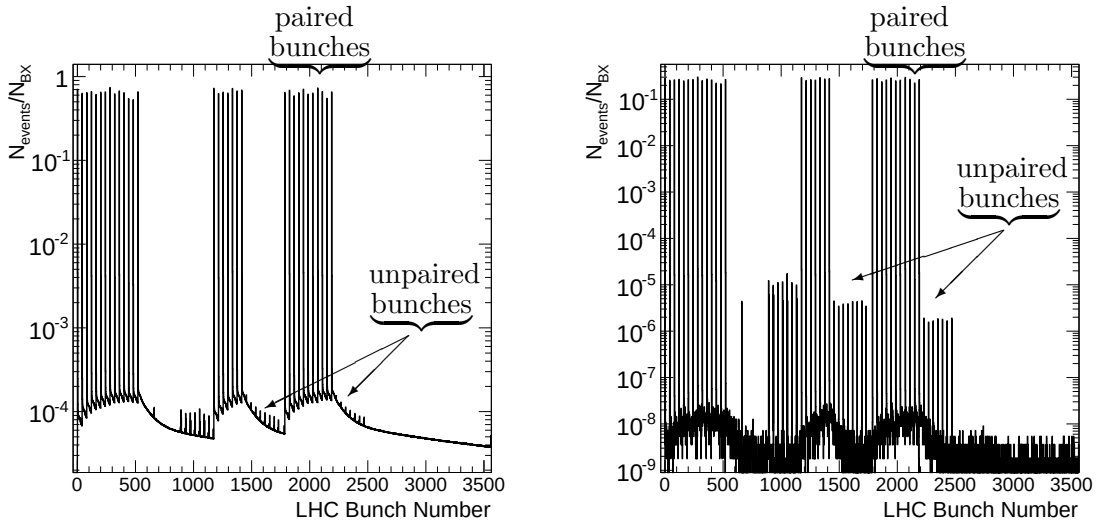
The following sections aims at describing the steps needed to measure the luminosity in real data. Because of the simplicity of the method it has been chosen to illustrate the procedure using only the event counting methods. The corresponding results from the hit counting "OR" method will be given at the end of the chapter. The hit counting "AND" method have not been used in this study due to its relative small validity range.

9.2 Event rates

The first step towards measuring the luminosity using the event counting methods is to extract the event rate. Figure 9.1 shows the level 1 trigger rates as a function of the luminosity block number for one of the early runs in the runs list. It is seen that the trigger rate decays over the course of the run, both for events triggered by the single side trigger and by the coincidence trigger. This tendency is expected and signifies the finite lifetime of the proton beams due to losses.
Since the length of a luminosity block is at the order of 120 seconds, all fluctuations in the trigger rate with a shorter duration will be averaged out when presented in this way. In some situations, however, it proves useful to study the event rate in much smaller time intervals.

9.2.1 Bunch Patterns and Luminosity Backgrounds

Because of its excellent time resolution, LUCID is able to monitor the event rate on a level of the individual bunch crossings. Figure 9.2 shows the event rate per bunch crossing as a function of the LHC bunch number for run 162690. The rates have been time-averaged over the duration of the run that lasted for about 22 hours. The LHC filling scheme used during



(a) (b)

Figure 9.2: *Luminosity block averaged event rates as a function of the LHC bunch number for events triggered by the single side trigger (a) and by the coincidence trigger (b) in run 162690. The paired and unpaired bunches are indicated on the plots.*

the given run consisted in having 32 paired/colliding bunches and 30 unpaired/non-colliding bunches. The structure of the filling scheme is clearly observed in the event rates for both triggers. The paired bunches give rise to distinct peaks that are several orders of magnitude above the background. These peaks are seen for both trigger types but for the single side trigger, the paired bunches are followed by a long tail extending over several BCIDs. This effect is called *afterglow* and is due to activation of the ATLAS components and the cavern material. The radiation from the activation is mainly particles with an energy below the Cerenkov threshold of the gas in LUCID and should in principle not be able to produce a signal in LUCID. However since the Cerenkov threshold in the quartz window of the PMT is significantly lower (see table 6.1), radiation from activation will still have the possibility to create a signal in LUCID. The low Cerenkov threshold and the fact that a charged particle traversing the quartz window produces on the average 40 photo-electrons (see table 7.1), which is above the hit threshold of 15 photo-electrons, makes it possible for low energy radiation to trigger LUCID. The afterglow is not present for the coincidence trigger, which proves that this luminosity background is caused by random signals that are uncorrelated between the two modules of LUCID.

The unpaired bunches do not collide anywhere in ATLAS. This means that unpaired bunches have the possibility to create beam-gas and beam-halo interactions which may fire a LUCID trigger. Figure 9.2 confirms this situation where the event rate in the unparied bunches give rise to spikes which are around four orders of magnitude lower than the paired bunches.

Algorithm	σ_{vis} (mb)	σ_{vis}^{PYTHIA} (mb)	$\frac{\sigma_{vis}^{PYTHIA}}{\sigma_{vis}}$	σ_{vis}^{PHOJET} (mb)	$\frac{\sigma_{vis}^{PHOJET}}{\sigma_{vis}}$
LUCID Event "AND"	12.4 ± 0.1	16.0 ± 0.8	1.29 ± 0.07	17.0 ± 0.9	1.37 ± 0.07
LUCID Event "OR"	40.2 ± 0.1	46.4 ± 2.8	1.15 ± 0.07	53.1 ± 3.2	1.32 ± 0.08

Table 9.1: *Comparison of the visible cross sections determined from beam scans (σ_{vis}) [95] to the predictions of the PYTHIA and PHOJET Monte Carlo generators. The errors affecting the measured visible cross sections are statistical only.*

9.3 Calibration scenario

The aim of all the calibration methods is the same, namely to determine the denominator σ_{vis} in equation 9.1. In the VdM scan scenario σ_{vis} is determined directly by a measurement of the beam profiles as explained in section 4.3. In the Monte Carlo calibration scenario the σ_{vis} is determined from the product of ε and σ_{inel}.

9.3.1 Absolute calibration using Van der Meer scans

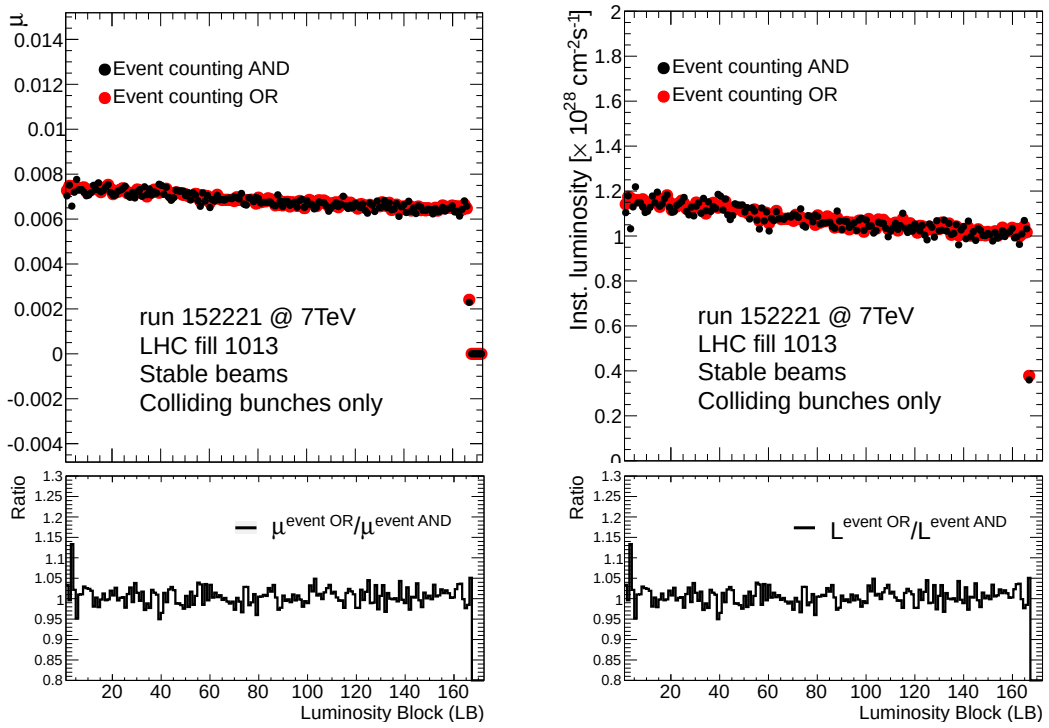
A total of three Van der Meer scans have been performed in ATLAS so far. The procedure to obtain results for σ_{vis} from the beam scans are discussed in details in [65, 95] and the results are given in table 9.1. The main contribution to the systematic uncertainty on σ_{vis} comes from the uncertainty in the measurement of the beam intensities. This contribution accounts for 10 % of the total systematic uncertainty of 11 % which is quoted in [95].

9.3.2 Absolute calibration using Monte Carlo results

A cross check of the results from the VdM scan calibration can be performed by comparing them to the results obtained from the Monte Carlo calibrations. However, using MC simulations to find σ_{vis} presents a list of issues which must be taken into account. Since no actual measurement of σ_{inel} has yet been preformed at 7 TeV, it is not possible to tell which Monte Carlo generator provides the best estimate. The predictions of σ_{inel} by PYTHIA and PHOJET differ by 6.1 % at 7 TeV (see table 6.2) and the relative composition of the cross sections in terms of the diffractive and non-diffractive component, also differ between the two generators. The latter is important since the visible cross section is calculated as follows:

$$\sigma_{vis} = \varepsilon_{ND}\sigma_{ND} + \varepsilon_{SD}\sigma_{SD} + \varepsilon_{SD}\sigma_{SD} \tag{9.2}$$

By inserting the values from PYTHIA and PHOJET one can obtain the Monte Carlo results for σ_{vis} which are given in table 9.1. The uncertainties quoted for the values of σ_{vis}^{PYTHIA} and σ_{vis}^{PHOJET} includes systematic uncertainties. These stems from the calculation of the efficiencies in section 7.5 and can mainly be attributed to the simulation of the LUCID detector.



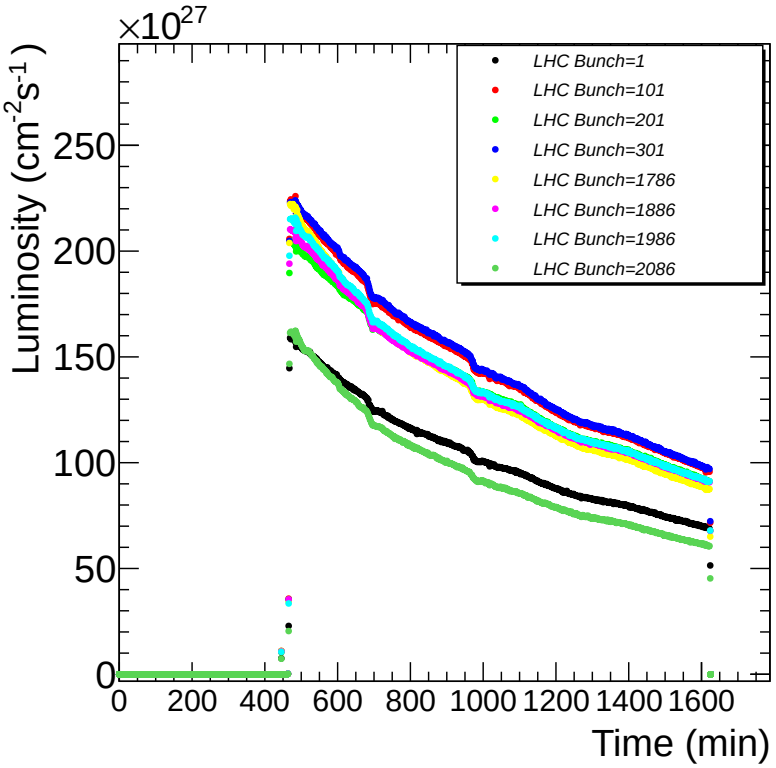
(a) (b)

Figure 9.3: *The value of μ (a) and the instantaneous luminosity (b) as a function of the luminosity block number for the two different event counting methods. The ratio of the "OR" and "AND" methods are given below the plots for the values of μ and $\mathcal{L}$.*

9.4 Results

Once the event rate and the calibration constants have been extracted, the calculation of the luminosity is straightforward. The event rate is used to calculate the values of μ for the different luminosity algorithms as described in great details in chapter 8. Figure 9.3(a) shows the value of μ as a function of the luminosity block number for the two event counting methods. It can be seen that the value of μ is very small ($\mu \sim 0.008$ see tabel 9.2) and agrees well between the two event counting methods throughout the entire run. Figure 9.3(b) shows the instantaneous luminosity for the same run obtained by using equation 9.1 and the VdM calibration.

Just as it was possible to measure the event rate for the individual bunch crossings, as was shown in figure 9.2, so is it possible to do the same for the instantaneous luminosity. Figure 9.4 shows the time evolution of the instantaneous luminosity for each of the paired bunches in run 159224. The luminosity is measured by using the event counting algorithm and VdM calibration. As demonstrated in figure 9.2, the values of the luminosity are different for the individual bunches, but the general time evolutions of all the bunches follow the same trend. This plot proves that LUCID is capable of monitoring the luminosity for individual bunch crossings. This a an important result for the LUCID detector since this was one of the claims that was made to justify the construction of the detector.

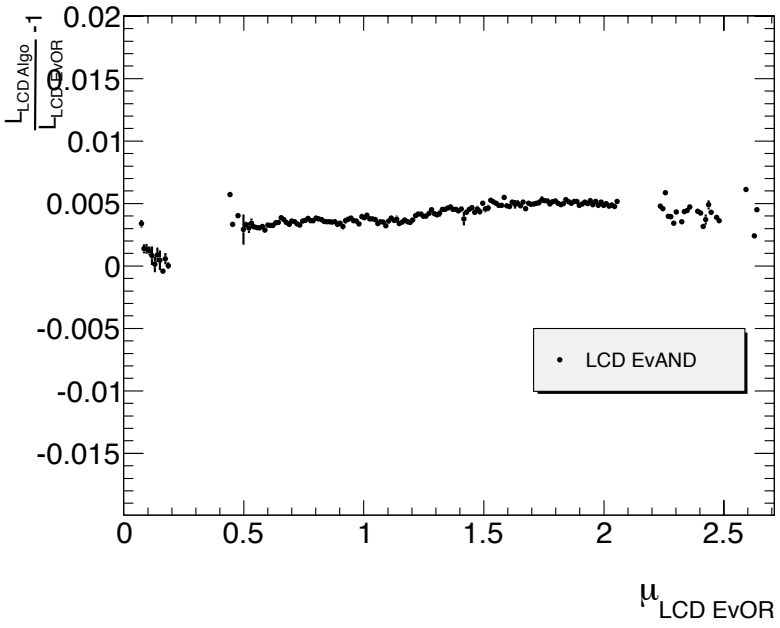


(a)

Figure 9.4: *Time evolution of the instantaneous luminosity for each of the 8 paired bunches in run 159224.*

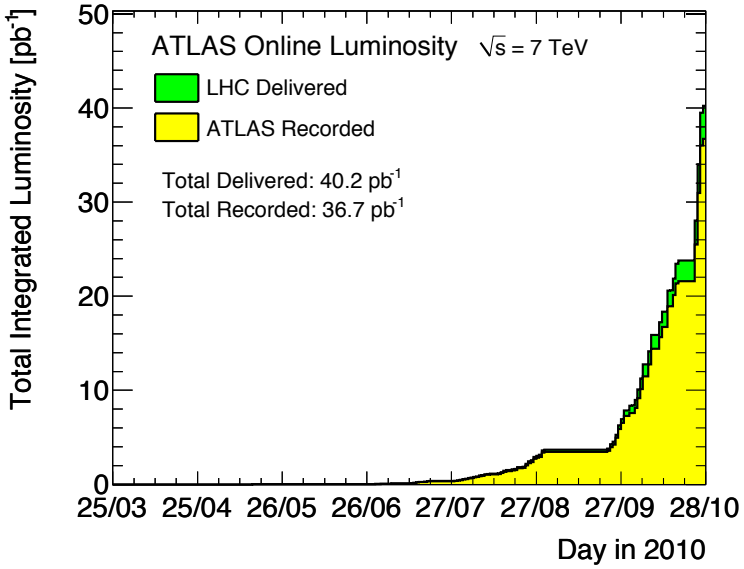
Another requirement one can impose on a luminosity monitor like LUCID is that it provides self-consistent results. What is meant by self-consistent results in this context is that the algorithms used to extract the luminosity provide results which are consistent between each other. To test the consistency of the results one can extract the luminosities from a list of runs with different luminosities using the two different algorithms and compare the results. Figure 9.5 shows the relative difference between the values of the luminosity measured by the "AND" and "OR" algorithm as a function of μ extracted by the "OR" algorithm. It can be seen that the two event counting algorithms agree within 0.5 % over a range of $0.1 < \mu < 2.6$ demonstrating a high degree of self-consistency in the luminosity measurements done by LUCID.

Finally, table 9.2 shows the details of the luminosity determination for the full list of runs used in this study and figure 9.6 shows the evolution of the integrated luminosity from the beginning of the 2010 data-taking period.



(a)

Figure 9.5: *Relative difference of the average value of $\mathcal{L}$ obtained with the event counting "AND" algorithm as a function of μ obtained with the event counting "OR" algorithm.*



(a)

Figure 9.6: *Cumulative luminosity versus day delivered to (green), and recorded by ATLAS (yellow) during stable beams and for 7 TeV centre-of-mass energy [82].*

Run	**Nr of LB**	n_{coll}	**Peak** μ	**Peak** $\mathcal{L}$	$\int \mathcal{L}dt$ (μb^{-1})		
	stable beams			$(10^{27} cm^{-2} s^{-1})$	Event "OR"	Event "AND"	Hit "OR"
152166	105	1	0.006	1.032	9.034 ± 0.015	9.097 ± 0.033	7.401 ± 0.015
152221	172	1	0.008	1.273	21.99 ± 0.025	21.99 ± 0.065	21.52 ± 0.044
152441	371	1	0.014	2.180	70.05 ± 0.041	70.07 ± 0.083	68.57 ± 0.037
154817	300	1	0.113	17.641	555.4 ± 119.4	558.6 ± 0.213	544.5 ± 0.071
155634	205	3	0.133	62.45	$1.118 \times 10^6 \pm 169.7$	$1.123 \times 10^3 \pm 0.309$	$1.094 \times 10^3 \pm 0.103$
155697	270	4	0.187	233.1	$4.280 \times 10^6 \pm 337.8$	$4.308 \times 10^3 \pm 0.5887$	$4.199 \times 10^3 \pm 0.205$
158116	450	2	1.789	557.5	$1.626 \times 10^7 \pm 791.6$	$1.647 \times 10^4 \pm 1.062$	$1.616 \times 10^4 \pm 0.402$
158264	29	2	2.661	828.8	$2.253 \times 10^6 \pm 364.4$	$2.273 \times 10^3 \pm 0.333$	$2.260 \times 10^3 \pm 0.167$
158299	79	2	0.595	184.5	$1.390 \times 10^6 \pm 213.6$	$1.412 \times 10^3 \pm 0.335$	$1.376 \times 10^3 \pm 0.123$
158548	218	4	0.932	580.1	$1.192 \times 10^7 \pm 661.5$	$1.210 \times 10^4 \pm 0.956$	$1.178 \times 10^4 \pm 0.044$
158582	356	4	1.009	627.2	$1.794 \times 10^7 \pm 1355$	$1.821 \times 10^4 \pm 1.162$	$1.774 \times 10^4 \pm 0.625$
159041	300	8	1.154	1.433×10^3	$2.969 \times 10^7 \pm 1102$	$3.013 \times 10^4 \pm 1.505$	$2.935 \times 10^4 \pm 0.627$
159224	576	8	1.291	1.606×10^3	$6.920 \times 10^7 \pm 1654$	$7.019 \times 10^4 \pm 2.283$	$6.850 \times 10^4 \pm 0.993$
161379	394	16	1.322	3.293×10^3	$1.058 \times 10^8 \pm 2357$	$1.073 \times 10^5 \pm 2.827$	$1.049 \times 10^5 \pm 1.442$
161407	109	16	1.532	3.814×10^3	$4.185 \times 10^7 \pm 1534$	$4.233 \times 10^4 \pm 1.692$	$4.164 \times 10^4 \pm 0.875$
162526	395	36	1.626	9.102×10^3	$2.803 \times 10^8 \pm 5628$	$2.844 \times 10^5 \pm 4.517$	$2.791 \times 10^5 \pm 3.116$
162690	397	32	2.075	10.34×10^3	$3.692 \times 10^8 \pm 6922$	$3.736 \times 10^5 \pm 4.813$	$3.693 \times 10^5 \pm 3.478$
total					$9.518 \times 10^5 \pm 6.924$	$9.644 \times 10^5 \pm 4.813$	$9.480 \times 10^5 \pm 3.473$

Table 9.2: *Details of the luminosity determination for the run list used in this study. The numbers given in the table is for stable beam conditions only and the luminosities are extracted using the VdM calibration scenario. The quoted errors in the table is purely statistical. The systematic uncertainty is 6 % , 7 % and 6 % for the Event "OR", Event "AND" and Hit "OR" methods respectively (see table 8.6 for details) plus 11 % from the calibration constants.*

Part V
Luminosity measurements at ATLAS using single gauge boson production

This chapter outlines the feasibility of using the $Z \to \mu^+\mu^-$ channel to measure the absolute luminosity and thereby performing an absolute calibration of LUCID.

Chapter 10

Theoretical context

10.1 Introduction

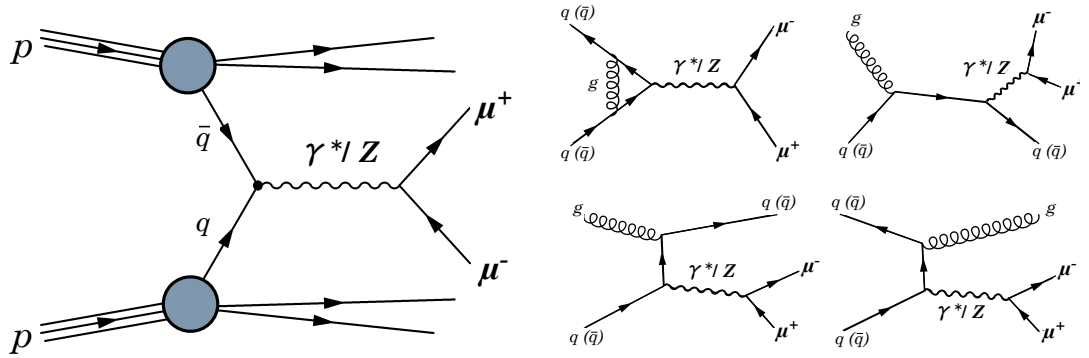
It was seen in chapter 4, that one way to measure the absolute luminosity is to record the event rate of a process with a known cross-section. In the situation where a high precision measurement of the cross-section exits, one still needs to rely on theory to estimate the systematic uncertainties. This means that the accuracy of a luminosity measurement using this method is usually limited by the theoretical uncertainty on the calculated cross-section. Two candidate processes have previously been investigated and deemed feasible for such a measurement at ATLAS, namely $W^{\pm}$ and Z^0 production. It is estimated that with the current knowledge of PDF uncertainties and detector related effects, the absolute luminosity can be determined from leptonic decays of W/Z bosons to about 10% [64, 96].
The analysis presented in the following chapters, builds on ideas presented in [96, 97, 98, 99, 100, 101, 102, 103, 104, 105] and outlines a possible strategy towards making an absolute luminosity measurement at ATLAS using the $Z \to \mu^+\mu^-$ event rate.
Knowing the theoretical cross-section for $Z \to \mu^+\mu^-$ production, σ_Z^{th} [1], the absolute luminosity for a given data-set can be calculated from:

$$\int \mathcal{L}dt = \frac{N_Z^{obs} - N_Z^{bck}}{A_Z \cdot C_Z \cdot \sigma_Z^{th}} \tag{10.1}$$

where

- N_Z^{obs} is the number of observed $Z \to \mu^+\mu^-$ candidates and N_Z^{bck} is the expected number of background events which passes the $Z \to \mu^+\mu^-$ selection.
- A_Z describes the (fiducial/geometrical) acceptance of $Z \to \mu^+\mu^-$ events given by the fraction of decays satisfying the geometrical and kinematical cuts in the event selection. Due to the nature of the acceptance it can only be determined from Monte Carlo simulations.
- C_Z denotes the total efficiency to record a $Z \to \mu^+\mu^-$ event which falls within the acceptance. C_Z is defined as the ratio of signal events passing the full selection chain to the total number of event generated within the acceptance.

[1] in the following σ_Z denotes the product of the cross-section and the $Z \to \mu^+\mu^-$ branching ratio.



(a) (b)

Figure 10.1: *Feyman diagram showing: (a) Drell-Yan pair production at leading order, (b) the main higher order contributions to the Z production cross section [15].*

In an ideal world one could calculate both the theoretical cross section and the acceptance with the same theory. In this case the product $A_Z \cdot \sigma_Z^{th}$ in equation 10.1 becomes:

$$A_Z \cdot \sigma_Z^{th} = \frac{\sigma_Z(\nu)}{\sigma_Z^{th}} \cdot \sigma_Z^{th} = \sigma_Z(\nu) \tag{10.2}$$

where $\sigma_Z(\nu)$ denotes the Z cross-section within some fiducial volume ν defined by a set of selection criteria. This means that the contribution to the systematic uncertainty in the luminosity determination from the product $A_Z \cdot \sigma_Z^{th}$ can be estimated from the systematic uncertainty in $\sigma_Z(\nu)$. It will be shown in the following sections why this is a valid assumption.

The following chapter presents a possible strategy for an absolute luminosity measurement at ATLAS using the $Z \to \mu^+\mu^-$ channel and is organized as follows: section 10.2 briefly reviews the basics of $Z \to \mu^+\mu^-$ production and gives a detailed estimate of the systematic uncertainty on the cross-section. The reason to carry out this study is entirely to get a realistic picture of the total systematic uncertainty of the absolute luminosity when calculated using equation 10.1. Sections 11.1 and 11.2 outline the event characteristics and the procedure used to select $Z \to \mu^+\mu^-$ events. Data driven methods to determine the selection efficiency are also discussed. Section 11.3 describes the various sources of background; section 11.4 presents an optimization of the selection procedure and discusses the effects of this on both background and signal events; finally, section 11.5 gives the result of the proposed method including an evaluation of systematic and statistical uncertainties.

10.2 Accuracy of the predicted cross-section

The dominant production mechanism for Z bosons at hadron colliders is the Drell-Yan process [106]. At leading order (LO) a quark - antiquark pair annihilate to form a vector boson which then decays in to a lepton pair (see figure 10.1(a)). At higher orders (see figure 10.1(b)) the main contribution to the cross sections comes from quark-gluon interactions which presents a

considerable correction to the cross section at leading order. Since the final lepton pair may also be produced via an intermediate photon γ^*, both cases should be considered together.
Z production at the LHC will occur through collisions of two sea quarks or between a valence and a sea quark. In 15 % of the cases this will be $s\bar{s}$ while the remainder of the cases will be split between $u\bar{u}$ and $d\bar{d}$. Summing over all the contribution, the leading order cross section for Z production becomes [15]:

$$\hat{\sigma}_{q\bar{q}\to Z} = \frac{\pi}{3}\sqrt{2}G_F M_Z^2(g_V^2 - g_A^2)\delta(\hat{s} - M_Z^2) \tag{10.3}$$

where g_V and g_A are the vector and axial couplings respectively, G_F is the Fermi constant and M_Z is the Z boson mass. By use of the factorization theorem [14] one can reformulate the hadronic level cross-section as a convolution of the parton density functions of the proton and the partonic cross-section $\hat{\sigma}_{q\bar{q}\to Z}$ from equation 10.3:

$$\sigma_{pp\to Z} = \int dx_1 dx_2 \sum_q \hat{\sigma}_{q\bar{q}\to Z}[f_{q/p_1}(x_1, Q^2) f_{\bar{q}/p_2}(x_2, Q^2) + (q \leftrightarrow \bar{q})] \tag{10.4}$$

where $x_{1,2}$ refers to the fraction of the original proton momentum carried by the colliding partons. The subscript indicates which proton beam the parton belongs to and Q^2 defines the momentum scale at which the two partons collide. In the case of Z production, Q^2 is usually set equal to M_Z^2. In addition to setting the scale at which the Z boson is produced, the momentum fractions $x_{1,2}$ also determine the kinematical distributions of the resulting Z boson, exemplified by the expression for the rapidity $y = \pm \ln(x_{1,2}\sqrt{s}/M_Z)$, where $\sqrt{s}$ =7 TeV.
Perhaps the most phenomenologicaly demanding contribution to equation 10.4 comes from the parton density functions f. The physical interpretation of the parton density functions is that they give the probability to find a certain parton with a given momentum fraction within the proton. In this way $f_{q/p1}(x_1, Q^2)$ gives the probability to find a quark of flavor q with momentum fraction x_1 inside the proton p_1 and vice visa for $f_{\bar{q}/p_2}(x_2, Q^2)$. Compared to the partonic cross-section, the PDFs cannot be fully determined from theory and must therefore be constrained experimentally. The fact that PDFs have to be constrained by experimental input means that predictions of $\sigma_{pp\to Z}$, for unaddressed energy regions, will carry a large systematic uncertainty due to the PDFs. Other sources of theoretical uncertainties stem from the limitations in the order to which $\hat{\sigma}_{q\bar{q}\to Z}$ is calculated, scale dependence and the inclusion of final and initial state radiation. The estimation of the impact of these uncertainties on the Z production cross-section $\sigma_Z(\nu)$ is the subject of the following sections.

10.2.1 Event generation

To study the systematic effects on the Z production cross section from theoretical uncertainties one usually carries out a study using only a Monte Carlo event generator and no detector simulation. This is done mainly to save time but also to separate the systematics related to the hard scattering from those coming from the detector description.
When it comes to generation of $Z \to \mu^+\mu^-$ events there are several programs to choose from but the most widely used in this category includes PYTHIA [52, 89], HERWIG [107], ISAJET [108] or SHERPA [109]. The assumptions behind and the range of effects included vary somewhat from program to program, but the initial conditions are the same. They all start with

	Invariant Mass (GeV/c^2)	Psedorapidity	transverse Momentum (GeV/c)
Cut 1	$M_{\mu\mu} > 60$	$\|\eta_\mu\| < 2.50$	$p_T^\mu > 20$
Cut 2	$M_{\mu\mu} > 60$	$1.37 < \|\eta_\mu\| < 1.52$	$p_T^\mu > 20$
Cut 3	$71.19 < M_{\mu\mu} < 111.19$	$\|\eta_\mu\| < 2.50$	$p_T^\mu > 20$

Table 10.1: *Selection criteria for final state muons.*

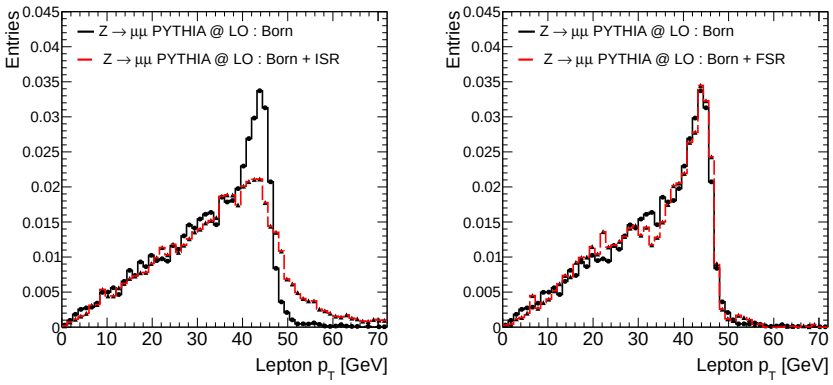
hard parton scattering at a high-energy scale which are then branched into partons at lower scales. A subsequent hadronization of the resulting partons allows for a realistic description of the final states and the full event. Subsequently the final states can be passed though a detector simulation which simulates the response of the detector to the final states. Reponses, which can then be used, to predict the expected value of the kinematics of the Z boson as we shall see in the next chapter.
The Monte Carlo event generator mentioned above, all rely on a leading order calculation of the matrix elements. The ability to describe the production of Z bosons with a large transverse momentum is affected by this since to avoid divergenses at leading order one has to perform a leading-log resummation of the collinear terms in the shower evolution. A partial solution to this problem is to include higher orders in the calculations. The MC generator MC@NLO [110] includes fully exclusive next-to-leading order (NLO) QCD calculations for Z boson production at hadron colliders. MC@NLO on its own does not include a parton shower algorithm and must therefore be used in combination with one of the programs above, to obtain realistic events. Beside the missing shower algorithm, MC@NLO does not include electroweak corrections either. These can be included in the same way as the showering/hadronization was added, namely by employing an external program. PHOTOS [111] is an add-on program which can be combined with MC@NLO to provide realistic electroweak corrections at NLO, which in the current situation means correction under the Z peak due to QED final state radiation.

The study presented in this chapter has been made for dimuon final states at generator level only. The systematic uncertainty from LO effects have been evaluated using PYTHIA6.4 and the NLO effects have been evaluated using MC@NLO in combination with HERWIG and PHOTOS using the CTEQ6.6 PDF set [112]. The sample sizes used to study the individual systematic effects for each generator have been generated large enough so that the statistic uncertainties are smaller than the effects under study. Three sets of experimental cuts have been chosen to reflect the detector capabilities and to demonstrate the impact of physics effects on the cross-section under different selection criteria (see table 10.1). The cut of 60 GeV on the propagator mass channel ($\sqrt{\hat{s}} > 60$ GeV) has been imposed to separate the Drell-Yan continuum at low dimuon mass, from the Z events. The last cut region (cut3) is the one, which resembles the selection that are used in the offline selection presented in the next chapter. Thus, this cut region is used for estimation of systematic uncertainties.

10.2.2 Uncertainties due to Initial and Final State Radiation

In the production of vector bosons, the main source of p_T generation comes from initial state radiation (ISR), where gluons are branched from the colliding partons before the hard

scattering. The inclusion of ISR in the calculations will result in a wider p_T spectrum of the muon from Z decays as seen in figure 10.2(a). Since the acceptance of $Z \to \mu^+\mu^-$ events is calculated by imposing fiducial cuts (including a p_T cut) on the decay products, ISR will change the fiducial cross sections and therefore also the luminosity measurement. It is thus necessary to investigate the level of systematic uncertainty from the ISR.
Figure 10.2(b) illustrates the effects of including final state radiation (FSR) in the description of the $Z \to \mu^+\mu^-$ decay. Naively it is not expected that the p_T spectrum of the muons is altered significantly by the inclusion of FSR. This is due to the fact that the muon, because of its mass and leptonic nature, only produces small amounts of FSR in terms of bremsstrahlung. Figure 10.2(b) confirms the expectation and the systematics from FSR can be ignored.



(a) (b)

Figure 10.2: *Impact of including ISR (a) and FSR (b) on the p_T spectrum of muons from Z-boson decay . The black line gives the PYTHIA prediction at Born level, while the red lines give the Born level prediction including ISR (a) and FSR (b). Both spectra have been normalized to 1.*

	Born	Born + ISR
$\sigma_Z(\nu)$ (Cut 1)	349.06 ± 1.28	353.85 ± 1.30
$\sigma_Z(\nu)$ (Cut 2)	1.14 ± 0.06	0.98 ± 0.06
$\sigma_Z(\nu)$ (Cut 3)	338.30 ± 1.26	341.74 ± 1.27

Table 10.2: *The effects of including ISR on the cross-section $\sigma_Z(\nu)$ for the various cut regions given in table 10.1.*

Table 10.2 shows a comparison between the cross-sections in the naive situation where ISR is neglected and the full generator prediction. Turning on the ISR leads to a larger cross-section because of the fact that a p_T cut at 20 GeV removes less events when the mean p_T of the muon gets larger. However, it is obvious that a naive comparison between fully including ISR and fully excluding ISR, highly overestimates the effect of ISR[2]. Another and more realistic approach suggested by [96], is to vary the parameter λ in PYTHIA which describes the ISR. By varying this parameter between $\lambda_{min} = \lambda/2$ and $\lambda_{max} = 2\lambda$ it can be estimated that the

[2]A full description of ISR requires QCD calculations to high orders, which are not available.

contribution to the total systematic uncertainties is 0.3%. This is to be compared to 1.0%, if ISR is turned off altogether.

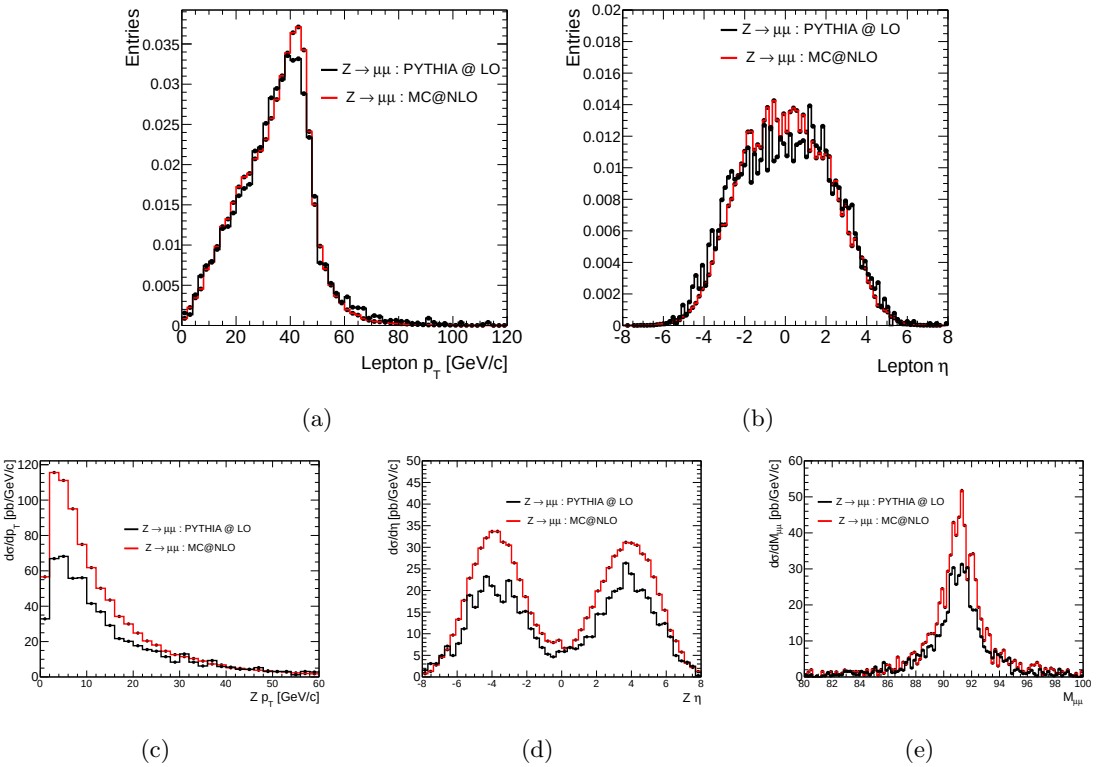


Figure 10.3: *Comparison of the p_T (a) and η (b) spectrum of muons from Z-boson decay as predicted by LO and NLO calculations. (c-e) shows a comparison of the Z boson kinematics from LO and NLO predictions.*

10.2.3 Uncertainties due to Higher Order Corrections

So far, only leading order effects have been taken into account. The next step is to investigate the uncertainties due to effects at NLO and next-to-next-to-leading-order (NNLO). In the following, all calculation of the Z production cross section will be done to NLO using the MC@NLO event generator, so the real issue here it to figure out the level of systematic uncertainty introduced by not including NNLO correction to the cross section. The reason why this is an issue comes from the fact that the only existing NNLO $Z \to \mu^+\mu^-$ event generator FEWZ [113] has some serious limitations when used in standalone mode. As an example, FEWZ cannot be used to determine the cross section and acceptance within a fiducial volume since no higher order approximation to ISR/FSR, nor any treatment of hadronization are included in the program. As a result FEWZ cannot be used to predict the absolute value, but only the effects from including NNLO QCD corrections.
The full inclusive cross sections predicted by FEWZ are shown in table 10.3 for different orders in α_s. From the table it can be seen that by including NLO corrections the value of the cross section increases by 24 %. The corresponding increase when going from NLO to NNLO is

Z boson	$\sigma^{LO}[pb]$	$\sigma^{NLO}[pb]$	$\sigma^{NNLO}[pb]$
inclusive ($\sqrt{\hat{s}} > 60$ GeV)	778 ± 1	962 ± 1	989 ± 10

Table 10.3: *Predicted production cross-section of Z-boson by FEWZ [114].*

only 2.9 %, indicating that the calculations converges as the order of α_s increases. Another interesting feature of table 10.3 is that the NLO and NNLO predictions are in agreement within three standard deviations due to the relatively large error on the NNLO prediction. The author of [96] suggests that by comparing the predicted values at LO and NLO, one can estimate the NNLO effects on the cross-section. Figure 10.3 illustrates the differences in the predictions at LO and NLO. From these predictions it can be calculated that the relative difference in $\sigma_Z(\nu)$ due to corrections at NLO is 10 %. The idea is now to assume that the changes in the fiducially cross section when going from NLO to NNLO are of the same order as the change of the full inclusive cross-section:

$$\Delta\sigma_Z(\nu)^{NNLO} = \delta \cdot \Delta\sigma_Z(\nu)^{NLO} \tag{10.5}$$

Since the changes to the inclusive cross section going from NLO to NNLO was $\delta = 2.9\%$ it can be estimated using the formula above that the contribution to the systematic uncertainty on $\sigma_Z(\nu)$ from NNLO effects is 0.3 %.

10.2.4 Scale dependence

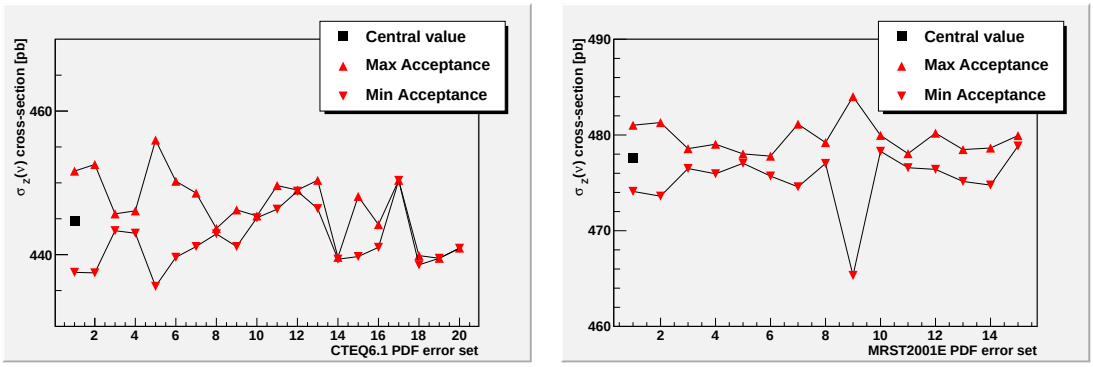
Another source of systematics in the calculations of the cross section is the dependence on the factorization (μ_F) and renormalization scales (μ_R). These scales are introduced in the first place because it is only possible to include a limited number of terms in the pertubative expansion of the cross section. As a consequence, the final result of the cross section calculation will depend on the value which were chosen for μ_F and μ_R. In the case of Z boson production it is customary to fix both scales at M_Z and the dependency of the cross section can be studies by variating the scales around this value. The numbers in table 10.4 gives the value of the cross section when the scale are changed by a factor of two around M_Z. It is estimated that the contribution to the systematic uncertainty on $\sigma_Z(\nu)$ from scale dependence is 0.8%.

	$M_Z/2$	M_Z	$2M_Z$	$\Delta\sigma/\overline{\sigma}[\%]$
σ (Cut 1)	473.33	474.77	477.14	0.5
σ (Cut 2)	1.48	1.49	1.64	1.2
σ (Cut 3)	455.39	458.15	461.80	0.8

Table 10.4: *Scale dependence of the fiducial cross-sections (in pb) for Z boson production with* $M_{ll} > 60\ GeV/c^2$.

10.2.5 Uncertainties due to the parton density function

The parameterizations of the PDFs in equation 10.4 are phenomenological in nature and rely on input from global fits to data. This means that both experimental and theoretical sources



(a) (b)

Figure 10.4: *$Z \to \mu^+\mu^-$ acceptance as a function of the PDF error set for CTEQ6.1 (a) and MRST2001E (b).*

of systematics from the PDFs will propagate into the predictions of the cross sections. A reweighting method [101] has been used to estimate the impact of the PDF uncertainty on the fiducial cross-section.

Reweighting Procedure : As a first step the values of the colliding parton momentum fractions x_1 and x_2, along with the flavors of the partons are extracted from the Monte Carlo truth information[3] of each event. Based on this information, the values of (x_1, x_2, f_1, f_2) and all PDF error set members can be found using the LHAPDF software [115] and subsequently evolved to the Q^2 of the reaction. A vector of weight factors $w^{\pm}$ is then assigned to each event:

$$w_i^{\pm} = \frac{f_1^i(x_1, Q, S_i^{\pm}) f_2^i(x_2, Q, S_i^{\pm})}{f_1^i(x_1, Q, S_0) f_2^i(x_2, Q, S_0)} \tag{10.6}$$

where $f_k^i(x_k, Q, S_i^{\pm})$ is the PDF value for the interacting parton with momentum fraction x_k. S_0 and $S_i\pm$ denotes the central value of the PDF and the error set pair found along the i'th eigenvector by the Hessian method [116]. The length of the vector of weights assigned to each event depends on the number of eigenvectors in the PDF set. For the CTEQ6.1 the number of eigenvector is 41 while for MRST2001 the number is 31. Figure 10.4 shows the comparison between cross-sections calculated for each PDF error set eigenvector, using CTEQ6.1 and MRST2001E. In order to estimate the impact on $\sigma_Z(\nu)$ of the global variation, one can use the asymmetric CTEQ master formula:

$$\Delta\sigma^+ = \sqrt{\sum_{k=1}^{N} [max(\sigma_k^+ - \sigma_0, \sigma_k^- - \sigma_0, 0)]^2} \tag{10.7}$$

$$\Delta\sigma^- = \sqrt{\sum_{k=1}^{N} [max(\sigma_0 - \sigma_k^+, \sigma_0 - \sigma_k^-, 0)]^2} \tag{10.8}$$

[3] the particle level information before any simulation of detector effects.

where σ_0 is the cross section computed with the PDF best fit set and $\sigma_k^{\pm}$ is computed along the k-th eigenvector, in its "+" and "-" direction. Using this prescription, the induced uncertainty on $\sigma_Z(\nu)$ from each PDF set has been calculated and is given in table 10.5. The contribution to the systematic uncertainty is taken to be the largest deviation in cut region 3, which is 4.5%.

				Cut region 1					
PDF Set	$\sigma(pb)$	$\Delta\sigma_+$	$\Delta\sigma_-$	$\sigma(pb)$	$\Delta\sigma_+$	$\Delta\sigma_-$	A	ΔA_+	ΔA_-
CTEQ6.1	943	43.70	42.23	471.50	21.80	21.05	0.5001	0.0231	0.0223
MRST2001	946	21.40	26.93	507.47	10.91	15.27	0.5364	0.0115	0.01613
				Cut region 2					
PDF Set	$\sigma(pb)$	$\Delta\sigma_+$	$\Delta\sigma_-$	$\sigma(pb)$	$\Delta\sigma_+$	$\Delta\sigma_-$	A	ΔA_+	ΔA_-
CTEQ6.1	943	43.70	42.23	1.22	0.08	0.10	0.0013	0.0001	0.0001
MRST2001	946	21.40	26.93	0.32	0.01	0.01	0.0003	0.0001	0.0001
				Cut region 3					
PDF Set	$\sigma(pb)$	$\Delta\sigma_+$	$\Delta\sigma_-$	$\sigma(pb)$	$\Delta\sigma_+$	$\Delta\sigma_-$	A	ΔA_+	ΔA_-
CTEQ6.1	943	43.70	42.23	456.25	20.89	20.09	0.4838	0.0222	0.0213
MRST2001	946	21.40	26.93	491.05	10.66	14.88	0.5191	0.01127	0.0157

Table 10.5: *Cross-sections σ with asymmetric uncertainties as calculated using two PDF sets for the three cut regions defined in table 10.1.*

10.3 Conclusions

The ideas and concepts behind using Z production as a way to determine the absolute luminosity has been presented. It has been argued that the cross-section within a fiducial volume $\sigma_Z(\nu)$ can be used instead of the product of geometrical acceptance and cross-section. Various sources of systematic uncertainty in the determination of $\sigma_Z(\nu)$ have been investigated and listed in table 10.6. From the table it can be seen that the dominant contribution comes from uncertainties in the PDFs.

Uncertainty	Cross section $\Delta\sigma/\sigma$[%]
FSR and ISR	0.3
Higher order QCD corrections	0.3
Scale dependence	0.8
PDF Uncertainty	4.5
Total Uncertainty	4.6

Table 10.6: *Total theoretical uncertainty on the Z production cross-section $\sigma_Z(\nu)$.*

Chapter 11

Single Gauge Boson Production at the LHC

11.1 Data and Monte Carlo samples

The data sample considered for the study presented in this thesis was collected over a five-month period, from April to August 2010. The application of basic beam-, detector- and data-quality requirements resulted in total integrated luminosity of 3.37 pb^{-1}.
The events used in this analysis are all selected by a single muon trigger. In the early data taking period where the luminosity and the event rate was low, it was sufficient to employ only the level 1 trigger. The application of higher level triggers will in this case not change the efficiency. The algorithm behind the trigger selection is designed to search for hit patterns, in a specific rapidity range, consistent with a muon track coming from the interaction point. Such tracks in general deposits a series of hits in coincidence on a path from the IP throughout the detector. The width of the path is fixed by the p_T threshold in the trigger item due to the relationship between the p_T of a particle and the curvature. The $Z \to \mu^+\mu^-$ candidates are then reconstructed from the sample of triggered events.
The results presented in this study are compared to expectations based on Monte Carlo simulations. The signal and background samples used are generated at $\sqrt{s} = 7$ TeV using PYTHIA and the CTEQ6.6 PDF sets. Just as for the generator level study in the previous chapter, photon radiation is handled by PHOTOS [111] and τ decays in the background samples are simulated by TAUOLA [117]. The detector simulation is done using GEANT4 within ATHENA version 15.5.1 and the digitization and reconstruction were done with the same version of ATHENA. The different samples used in the study presented here are summarized in table 11.4 and will be discussed further in section 11.3.

11.2 Event selection

The experimental signature from $Z \to \mu^+\mu^-$ decays is very clean due to the presence of two high-p_T muon tracks in the final state. This means that Z events in the muonic channel should in principle be easy to identify and reconstruct. In the following it will be discussed which kind of cuts have been applied to select the $Z \to \mu^+\mu^-$ candidates. The study of the

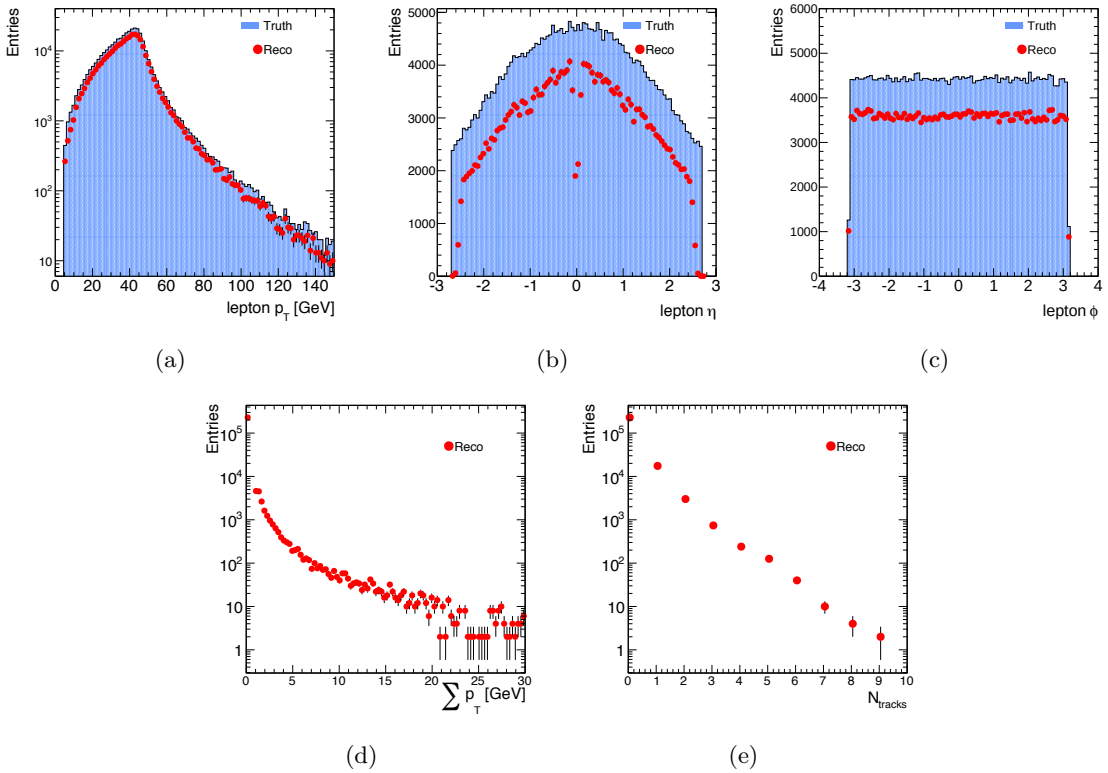


Figure 11.1: *Characteristics of muons from $Z \to \mu\mu$ decays: (a) Transverse momentum distribution (b) pseudo-rapidity distribution (c) azimutal angle ϕ distribution (d)(e) p_T and charged track activity for particles within a 0.3 R-cone around the selected muon. Each plot compares the reconstructed information with the truth information. The offline kinematic cuts described in section 11.2 are highlighted.*

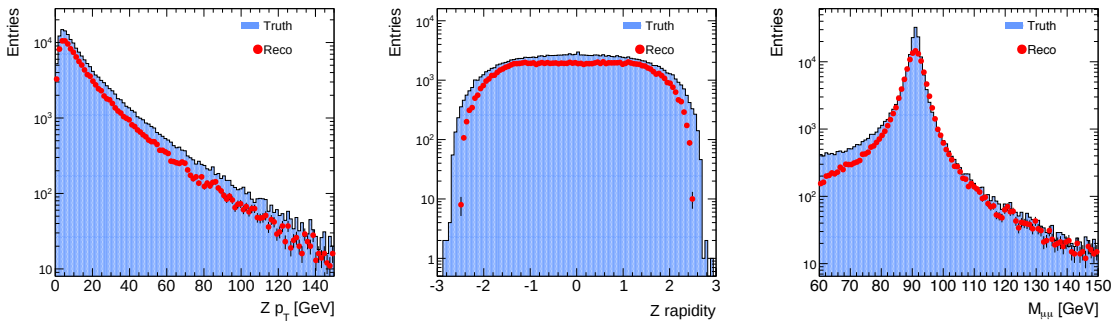


Figure 11.2: *$Z \to \mu\mu$ event characterisics: (a) Transverse momentum distribution (b) pseudo-rapidity distribution (c) azimutal angle ϕ distribution for muon with lower IPS. Each plot compares the reconstructed information with the truth information.*

event selection has been carried out using only signal events from MC but the results from real data will be given in section 11.5 after the various background contributions have been addressed.

Trigger : The first step of the selection procedure is to identify events which could potentially contain a Z candidate. In this study it has been required that all events must pass the `mu10` trigger in the event filter. The trigger selection ensures that all selected events contain at least one muon with transverse momentum larger than 10 GeV. In real data a series of additional requirements has been imposed to single out the collision candidates from background events from cosmic rays or beam-halo. Among these requirements, which are imposed in the level 1 trigger, are a selection which finds at least three tracks coming from a primary vertex with a position consistent with the beam-spot position. Such selection is not required for MC data where each event is from a collision.

Pre-selection : A set of kinematical pre-selection cuts are imposed on the data sample selected by the trigger requirement. In the pre-selection, the existence of two opposite charged tracks is required. Each track must have a transverse momentum larger than 5 GeV and have a pseudo-rapidity smaller than 2.5 ($|\eta| < 2.5$). This is done in order to further clean up the sample by removing events which do not contain two muons. Figure 11.1(a) to 11.1(c) show the kinematics of the muons from $Z \to \mu^+\mu^-$ candidates before the preselection is applied.

p_T check : While muons from $Z \to \mu^+\mu^-$ decays in general have a large p_T (see figure 11.1(a)), muons from background events in general have a low p_T. To filter out backgrounds events it is required that each muon candidate has a p_T larger than 20 GeV.

Isolation cut : A source of background to the $Z \to \mu^+\mu^-$ sample are events which contains a number of high p_T jets. Such jets are likely to contain muons from kaon and pion decays and heavy flavored hadron decays and could therefore be misinterpret as a muon from a Z decay. Because of the hadronic nature of the jets, these types of muons will typically be accompanied by a large number of particles and can therefore be removed by applying a track-based isolation cut. For this study the isolation cut requires that the sum of the track-p_T in a cone of $\Delta R = 0.3$ around the muon candidate is smaller than 5 GeV and that the number of charged tracks within the same cone is less than 6. Figure 11.1(d) and 11.1(e) show the track isolation cuts after preselection.

IP cut : To remove uncorrelated muons it has been required that the two muon candidates have a common vertex no more than 5 mm from the interaction point.

$M_{\mu\mu}$ cut : To remove low mass Drell-Yan products it has been required that the muon pair is in a mass window of 20 GeV around the Z mass.

The cut-flow is summarized in table 11.1.

Cut name	Object	Values
Trigger	EF trigger track	mu10 ($\#\mu > 1, p_T > 10$ GeV)
Pre-selection	2 combined track	$p_T > 5$ GeV and $\|\eta\| < 2.5$
p_T cut	2 combined track	$p_T > 20$ GeV
Isolation cut	p_T activity with a 0.3 cone track activity with a 0.3 cone opposite charge	$\sum p_T^{ID} < 5$ GeV $N_{track} < 6$ $q_1 \cdot q_2 < 0$
IP cut	distance to vertex	$\|vtx - d_0\| < 5mm, \|vtx - z_0\| < 5mm$
Mass cut	mass window	$71.19 \leq M_{\mu\mu}[GeV] \leq 111.19$

Table 11.1: *Event selection in the $Z \to \mu\mu$ analysis.*

11.2.1 Kinematics of selected sample

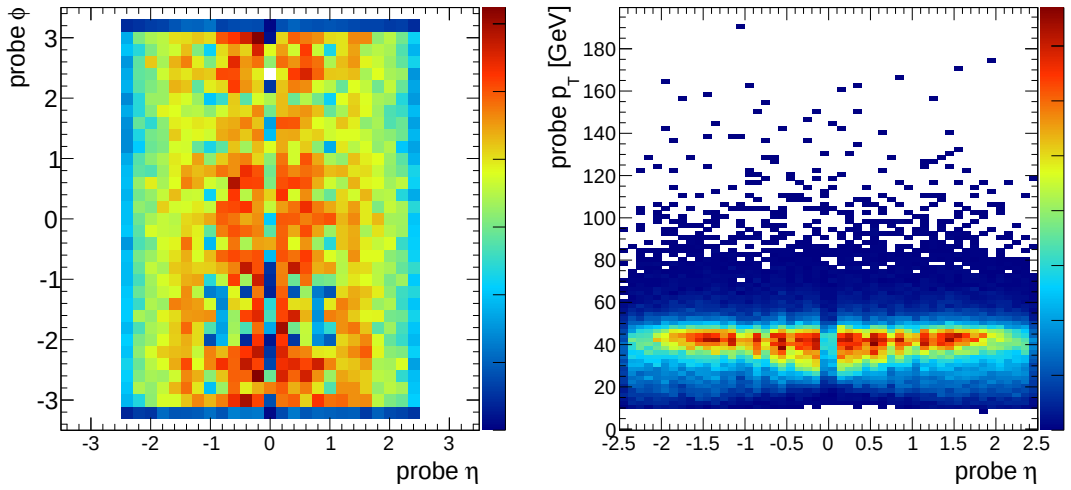
Figure 11.2 shows the kinematic distributions (p_T , rapidity and mass) from MC of the $Z \to \mu^+\mu^-$ candidates which have passed the full set of selection cuts (except for the mass cut). It is seen that the shape of the distributions of the reconstructed quantities is similar to the distributions obtained at generator level (truth information). This means that the $Z \to \mu^+\mu^-$ reconstruction efficiency is more or less uniform throughout the kinematical range. This is also the case for the dimuon mass of Z candidates, as can be seen from figure 11.2(c).

11.2.2 Efficiency determination

The correction factor C_Z is, as mentioned above, the total efficiency to record a $Z \to \mu^+\mu^-$ event which falls within the geometrical acceptance. To determine the value of C_Z it must be broken down into the individual factors which come from detector-related efficiencies such as reconstruction, identification and triggering on leptons. Rewriting C_Z in terms of the individual factors, one gets:

$$C_Z = \varepsilon^Z_{event} \cdot (\varepsilon^Z_{lep})^2 \cdot [1 - (1 - \varepsilon^Z_{trig})^2] \cdot w^Z \tag{11.1}$$

where ε_{event} denotes the efficiency to reconstruct the Z from the sample of muon candidates. This selection includes the primary vertex and mass requirement and the efficiency has been determined to be 0.956 from MC by considering the change in efficiency for the two last steps in table 11.1.
ε_{lep} denotes the single lepton identification/reconstruction efficiency and ε_{trig} denotes the trigger efficiency with respect to selected muon candidates. Both of these efficiencies can be determined by the so-called *Tag&Probe* method which will be discussed in greater details below.
The factor w^Z is introduced ad-hoc to correct for the fact that the Monte Carlo simulation do not describe fully the situation in real data. w^Z is therefore a correction factor which is meant to correct for any sort of effects which can not be modeled by Monte Carlo simulations. The basic idea is to take full advantage of MC simulations of the detector response and kinematics



(a) (b)

Figure 11.3: *Distribution of selected probes in the $\eta - \phi$ plane (a) and $\eta - p_T$ plane (b) for the* `EF_mu10` *trigger item.*

to extract a MC based efficiency determination and then to correct it for experimental effects determined from data-driven methods. This correction factor is derived from the ratio of global event selection efficiencies calculated in data and MC samples:

$$w^Z = \sum_{mc-selected} \frac{\varepsilon^Z_{data}(p_T, \eta)}{\varepsilon^Z_{MC}(p_T, \eta)} \tag{11.2}$$

where the sum runs over all the MC-signal selected events and ε^Z_{data} and ε^Z_{MC} are calculated from single particle efficiencies extracted from data using the Tag&Probe method.

The Tag&Probe method

The fundamental idea behind the Tag&Probe method (TP) is to construct a data-driven method to determine single particle efficiencies by using the known decay channels of certain resonances. As an example, it is possible to determine the reconstruction and trigger efficiencies of a single muon by looking at $Z \to \mu^+\mu^-$ decays. First a muon, *the tag*, is selected from the set of reconstructed muons using all subdetectors and trigger information available. Secondly, another muon candidate is selected based only on the information from the inner detector e.g without using information from the muon spectrometer. If the invariant mass of the tag and probe pair is sufficiently close to the Z mass, then it can be tested if a track in the muon system can be associated to the probe-muon. A direct determination of the overall track reconstruction efficiency of the muon spectrometer is thereby possible by applying this method to a large sample of $Z \to \mu^+\mu^-$ candidates. The selection requirement used to identify the tag and probe tracks can be found in table 11.2.
Figure 11.3 shows distributions of selected probes in the $\eta - \phi$ and the $\eta - p_T$ plane for events

Reco eff.	Selection cuts
Tag	- Associated 10 GeV single muon trigger (`EF_mu10`) - Tight track based isolation requirement within a cone-radius of 0.3 - Combined reconstructed muon track with $p_T > 5$ GeV and $\|\eta\| < 2.5$
Probe	- Inner Detector track with $p_T > 5$ GeV and $\|\eta\| < 2.5$ - Tight track based isolation requirement within a cone-radius of 0.3

Table 11.2: *Tag and probe conditions for efficiency determination.*

selected by the `EF_mu10` trigger item. The muon trigger efficiency can be determined by using a second type of muon probes. By choosing probes which are identified by the muon system only, it is possible to calculated the trigger efficiency with respect to the reconstruction.

Figure 11.4 shows the trigger and reconstruction efficiencies as a function of the probe p_T and η. The efficiencies have been determined from MC data both using the cut-flow method (MC) based on the simulated information and from the Tag&Probe method. With one exception, all the estimates from the TP method are statistically compatible with the MC prediction. The exception is the trigger efficiency as a function of η, where the TP method slightly over-estimates the efficiency. In order to get the overall trigger and reconstruction efficiencies ε_{trig} and ε_{lep}, efficiency maps as a function of p_T and η are created. The overall efficiencies are then found by taking the average over all the (p_T, η) bins weighted by the uncertainty in each bin. The final results, including w^Z, are summarized in table 11.3.

	Central value	uncertainty
ε_{event}	0.956	0.4%
ε_{lep}	0.916	1.7 %
ε_{trig}	0.808	2.8 %
w^Z	1.008	0.1 %
C_Z	0.779	3.3 %

Table 11.3: *Efficiency factors and w^Z as well as their relative uncertainties which enter the calculation of the correction factor C_Z. The uncertainties are determined by taking the difference between the MC prediction and TP values.*

It should be noted here that all efficiencies presented in this chapter have been calculated using MC data only. This has been done since the sample of $Z \to \mu^+\mu^-$ candidates at the time of the analysis was not large enough to determine the efficiencies without a large statistical error. This also means that the plots in figure 11.4 only can be used to illustrate the difference between the cut-flow analysis and the Tag&Probe method in MC and not the difference between the efficiencies found in data and MC. For the same reason, the value of w^Z will by construction be close to unity. However, studies indicate that efficiencies found in real data is in good agreement with the Monte Carlo predictions [105].

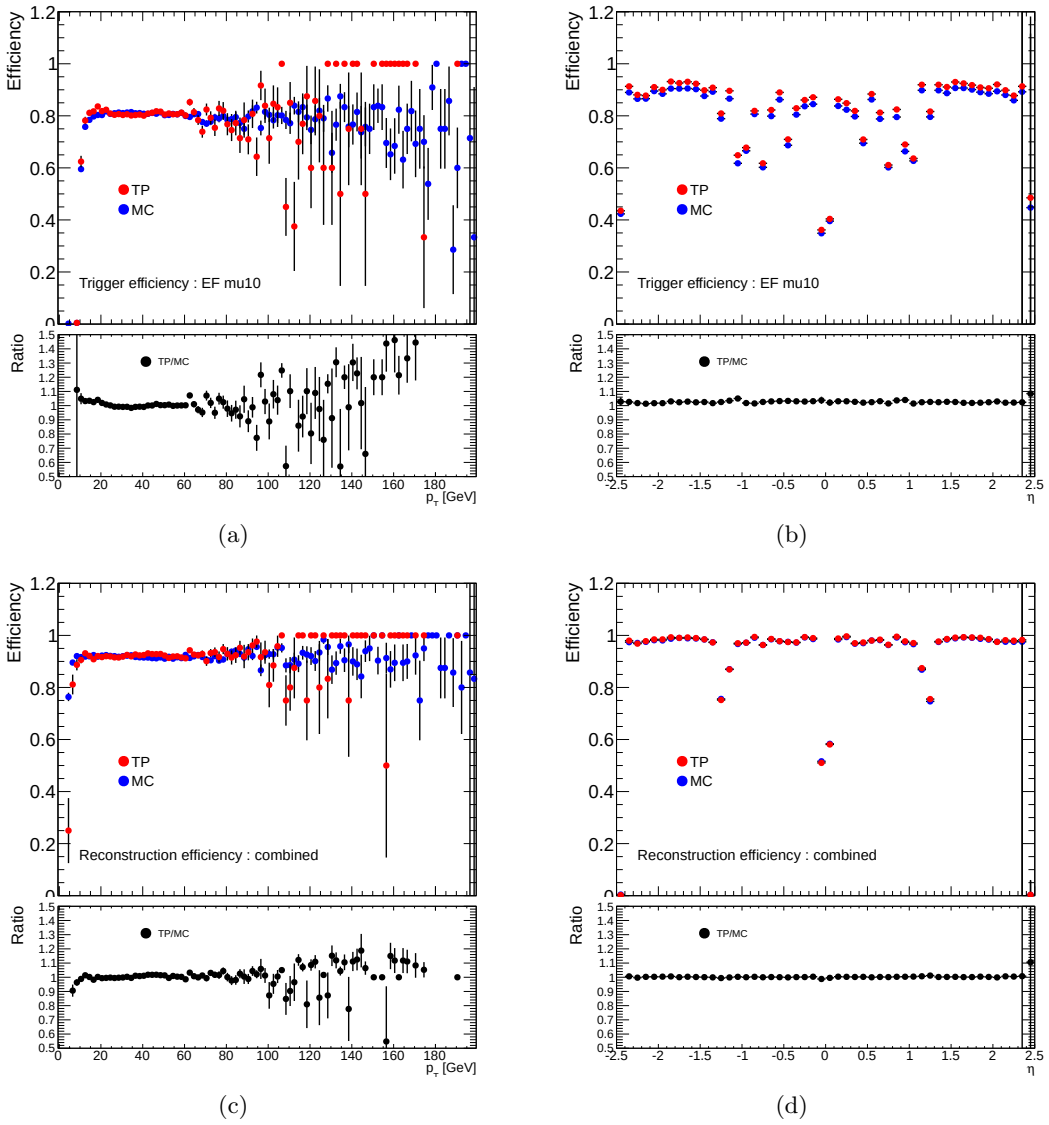


Figure 11.4: *Trigger (top) and reconstruction (bottom) efficiency as function of muon p_T (a)(c) and η (b)(d). Each plot shows the efficiency extracted from MC and by the Tag&Probe method (TP).*

11.3 Background processes

It is not expected that the background will have a large impact on the ability to extract the Z signal from data. The experimental signature of the Z boson in the lepton channel is essentially background-free. This is especially true for the muon channel, since muons can be identified in ATLAS using only the muon spectrometer in stand-alone mode. However, some background will be present and it is important to identify and correct for it in order to obtain a precise measurement of the absolute luminosity. If the background is not taken into account, then the determination of the luminosity from Z counting will overestimate the final result (see equation 10.1).

Sample	Process	Generator level cuts	$\varepsilon_g \times \sigma(pb)$	$\mathcal{L}(pb^{-1})$
$Z \to \mu\mu$	$pp \to Z/\gamma^* \to \mu\mu$ (*)	$\#\mu \geq 1, \lvert\eta\rvert < 2.8$	850	350
$Z \to \tau\tau$	$pp \to Z/\gamma^* \to \tau\tau$ (*)	-	989	600
$W \to \mu\nu$	$pp \to W \to \mu\nu$	$\#\mu \geq 1, \lvert\eta\rvert < 2.8$	8263	120
Dijet	$pp \to jet + jet$	-	1150×10^3	0.3
$t\bar{t}$	$pp \to t\bar{t}X$ (**)	-	80	2500
$b\bar{b} \to \mu\mu X$	$pp \to b\bar{b}X$	$\#\mu \geq 1, \lvert\eta\rvert < 2.5, p_T > 15$ GeV	70.2×10^3	60
$c\bar{c} \to \mu\mu X$	$pp \to c\bar{c}X$	$\#\mu \geq 1, \lvert\eta\rvert < 2.5, p_T > 15$ GeV	27.0×10^3	55

Table 11.4: *List of data samples used in analysis together with their generator-level cuts, cross-sections and the processed integrated luminosity. (*) $\sqrt{\hat{s}} > 60$ GeV (**) $\sqrt{\hat{s}} > 160$ GeV.*

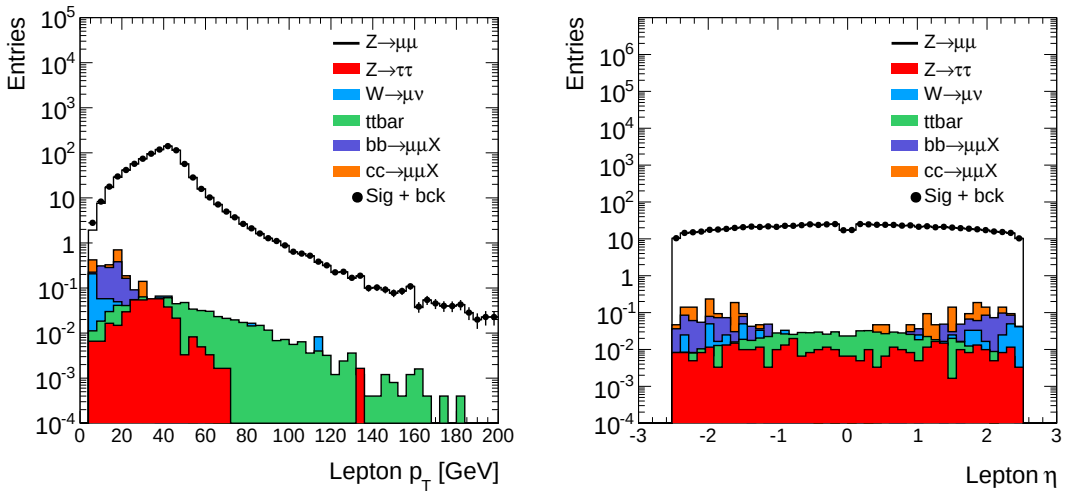
The dominating background to the Z signal comes from events in which two or more high p_T muons are produced by sources other than a $Z \to \mu^+\mu^-$ decay. Candidates for such processes could for instance be decays of Z bosons in other channels and processes which leads to multi-jet production. In the following, the individual background sources will be addressed and their relative importance will be studied using MC simulations.

11.3.1 Electroweak processes

$Z \to \tau\tau$ events, where both taus decay to muons and neutrinos is an example of a process which might be misidentified as $Z \to \mu^+\mu^-$ decays. Z bosons reconstructed in this way will in general have a lower mass since only a fraction of the tau 4-momentum will be carried by the muon. Thus, such a background contribution can be partially removed with the mass cut on the dimuon mass. Other sources of electroweak background include $W \to \mu\nu$ decays combined with a jet that contained a high p_T muon. Also the production of W^+W^- pairs from $t\bar{t}$ decays and their subsequent decay to muons presents a potential source of background events.

11.3.2 QCD processes

The main QCD background contribution is expected to come from heavy-flavor decays. Production of b/c quarks will lead to the formation of B and C hadrons which will lead to the production of muons through the decay of the hadrons. These processes can only present a potential background contribution if the final states contains a muon pair. Since both the B and C hadrons have many decay channels it has been required in the simulation (to save cpu resources) that the hadrons decay semi-leptonically to muons: $b\bar{b} \to \mu\mu + X$. In a similar way the background contribution due to the decay $c\bar{c} \to \mu\mu + X$ has also been investigated. Because of the relative large cross section of these processes compared to the Z production cross section, such events could potentially constitute a significant background contribution. However, one thing sets the muons produced from these sources apart from the muon from $Z \to \mu^+\mu^-$ decays, namely that they in general have a much softer p_T spectrum. Additionally, since these muons are produced in a jet from a secondary vertex it will be possible to remove them by only selecting high-p_T muons associated with the primary vertex.



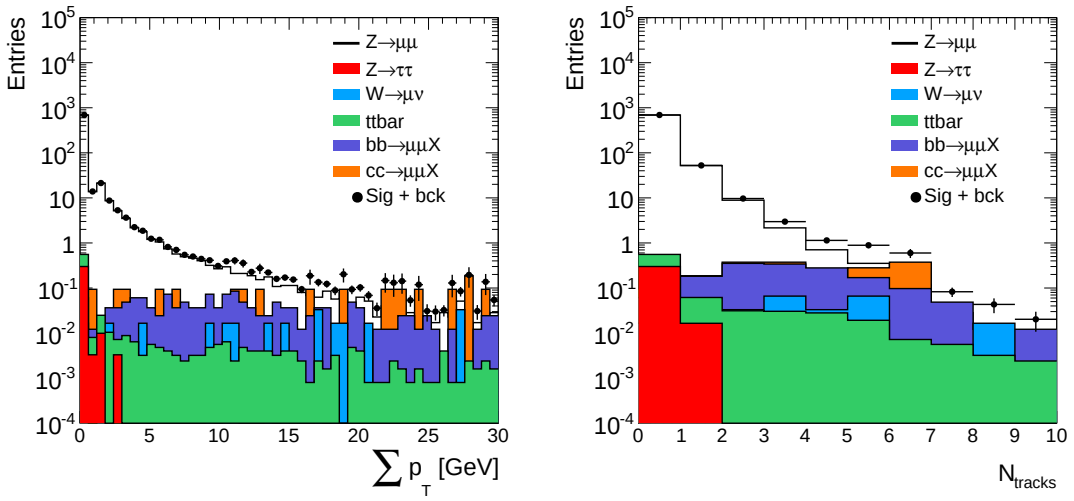
(a) (b)

Figure 11.5: *Relative background contribution: Transverse momentum (a) and pseudo-rapidity of muons (b) after trigger and pre-selection.*

The QCD background contribution can be further reduced (as illustrated in the next section) by imposing the isolation requirement mentioned earlier.

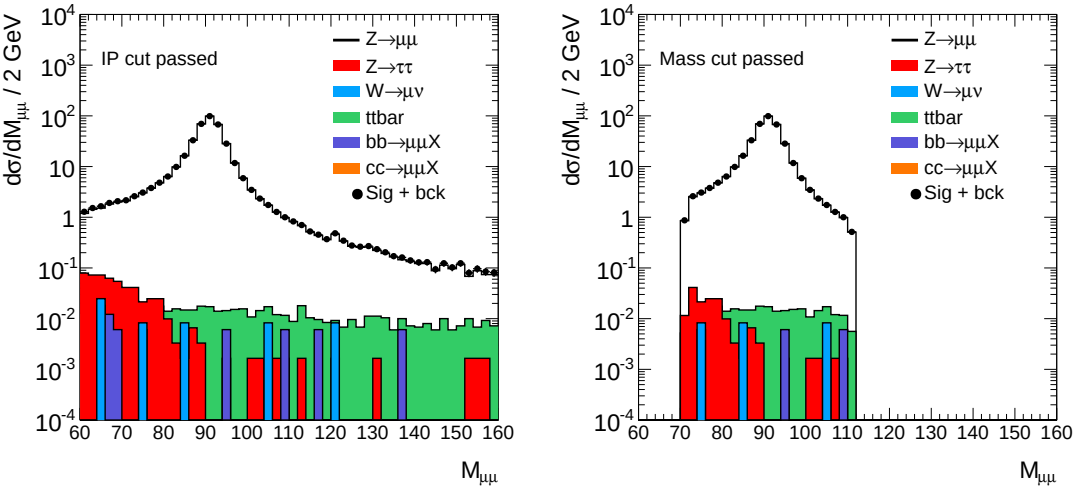
11.3.3 Background estimate

Table 11.4 summarizes the different background and signal samples which have been considered in this study. Figure 11.5 illustrates the relative background contributions to the muon p_T and η spectra after trigger and pre-selection. Each background contribution has been scaled by the respective cross-section, and normalized to the integrated luminosity of the $Z \to \mu^+\mu^-$ sample. The background contributions are, as expected, fairly small compared to the signal events, even at an early stage in the selection procedure. Since the background contributions in general are softer than the signal events, applying a harder p_T cut can further reduce them. The QCD background can be further reduced by imposing the lepton isolation requirements described in table 11.1. Figure 11.6 illustrates how the QCD background can be reduced by applying cuts on the p_T sum and the number of tracks in a cone around the selected muon. Figure 11.7 shows the dimuon invariant mass distributions in the two final steps of the selection procedure. It can be seen that the main background contributions to the final $Z \to \mu^+\mu^-$ sample come from $Z \to \tau\tau$ and $t\bar{t}$ decays. Figure 11.8 shows the selection efficiencies of the signal event and the main background contributions for different steps of the selection procedure. Table 11.5 summarizes the cut-flow for all the samples used in this study and estimates the number of $Z \to \mu^+\mu^-$ candidates produced per pb^{-1} for each sample.



(a) (b)

Figure 11.6: *p_T activity within a 0.3 cone (a) and track activity within a 0.3 cone of muons (b) after p_T cut.*

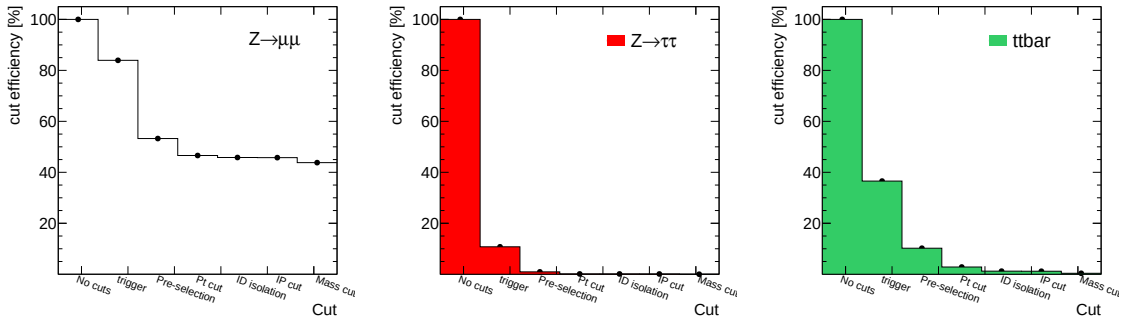


(a) (b)

Figure 11.7: *The dimuon invariant mass distributions for the signal and background processes: (a) after the IP cut has been applied and (b) after the final $M_{\mu\mu}$ cut is applied.*

11.4 Optimization of the selection procedure

With the background samples at hand, an optimization of the selection cuts can be carried out. Usually the specific values of the selection cuts are found by maximizing the signal



(a) (b) (c)

Figure 11.8: *Cut-flow efficiencies for the signal events and the two main background contributions.*

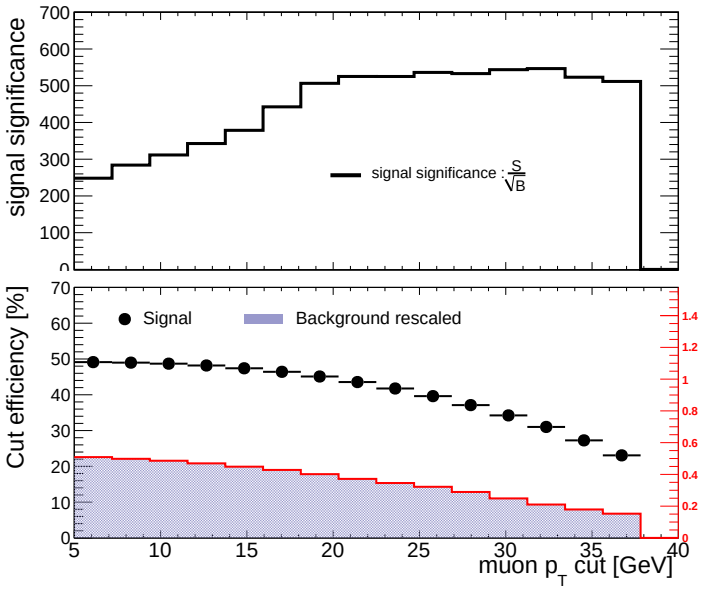


Figure 11.9: *Optimization of the selection procedure: p_T cut.*

significance:

$$Sig(S,B) = \frac{S}{\sqrt{B}} \tag{11.3}$$

where S is the total number of observed Z bosons in the muon channel and B is the amount of background under the signal in a three standard deviation window around the mean value. In this optimization, both S and B are taken from MC. It is also possible to perform an optimization where the S is taken from data and B from MC. This type of optimization often gives the most realistic outcome. Nevertheless, we refrain from this type of optimization here, since the data sample at the time of the analysis was not large enough to facilitate such an analysis. The figure in the top half of figure 11.9 shows how the significance of the $Z \to \mu^+\mu^-$ signal depends on the p_T cut value. The second plot (bottom) shows the cut efficiency as a function of the p_T cut value. The dots represent the effect of the cut on the signal, while the solid histogram represents the background. The remaining optimization plots can be found in

Cut %	$Z \to \mu\mu$	$Z \to \tau\tau$	$W \to \mu\nu$	**di-jet**	$t\bar{t}$	$b\bar{b} \to \mu X$	$c\bar{c} \to \mu X$
Trigger	83.94	10.77	66.54	1.91	36.56	5.10	79.06
Pre-selection	53.25	0.93	0.24	0.24	10.21	0.12	4.52
muon p_T cut	46.59	0.12	0.01	0.02	2.84	0.10	0.13
Isolation cut	45.81	0.12	0.93×10^{-3}	0.0	1.21	0.20×10^{-5}	0.56×10^{-3}
IP cut	45.75	0.11	0.93×10^{-3}	0.0	1.18	0.20×10^{-5}	0.42×10^{-3}
$M_{\mu\mu}$ cut	43.79	0.02	0.35×10^{-3}	0.0	0.376	0.2×10^{-5}	0.00
Events per pb^{-1}	374.01	0.16	0.03	0.00	0.30	0.02	0.00
	374.01	0.51 (0.13 %)					

Table 11.5: *Absolute ($A \times \varepsilon$) cut-flow efficiencies for the $Z \to \mu^+\mu^-$ selection procedure. Efficiencies are calculated using the samples stated in table 11.4.*

appendix C. The optimization has been carried out under the assumption that the selection cuts are uncorrelated and the final results are given in table 11.5.

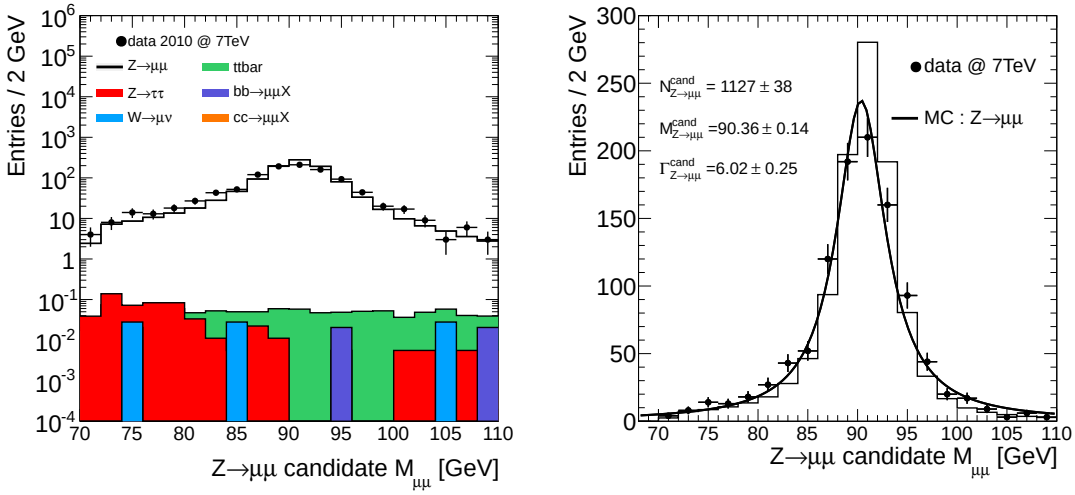
11.5 Signal extraction and absolute luminosity calculation

A set of $Z \to \mu^+\mu^-$ candidates has been obtained by applying the selection procedure to the real data sample[1] described in section 11.1. Figure 11.10 shows the invariant mass distribution of the Z candidates. The number of Z candidates in the data sample is extracted by fitting the invariant mass spectrum with a combination of a Breit-Wigner to describe the signal and an exponential function to describe the background. The motivation for choosing an exponential to describe the background is that the available phase space for dimuon decays dictates this type of behavior. From the fit one gets that a total of 1127 $Z \to \mu^+\mu^-$ candidates pass all requirements within the invariant mass window $M_{\mu\mu}$ = 71.2 -111.2 GeV. A slightly larger width of the Z signal is observed when compared to MC. This is expected [104] and is due to inner-detector alignment modes affecting high-p_T tracks and a misalignments of the muon spectrometer in the forward region. The kinematical distribution of Z candidates and muons from $Z \to \mu^+\mu^-$ decays can be compared to the MC predictions as a further cross check and consistency check. Figure 11.11 shows that agreement between the observed spectra and the predicted ones is quite good and compatible within the statistical uncertainties. However, when Z boson production is used to determine the absolute luminosity, the interesting quantity is the number of $Z \to \mu^+\mu^-$ candidates. This number is found as the number of entries in the invariant mass distribution. In this way a total of 1057 $Z \to \mu^+\mu^-$ candidates were found with ~ 2 expected from background.

11.5.1 Systematic Uncertainties

The correction factor C_Z was determined using Monte Carlo simulations and the results are given in table 11.3. The systematic uncertainties on C_Z according to [105] includes contri-

[1]The data sample was recorded in the period from Apr 11 to Aug 29 corresponding to the LHC fills from 1032 to 1309.



(a) (b)

Figure 11.10: *Invariant mass $M_{\mu\mu}$ of Z candidates in log scale (a) linear scale (b). The breakdown of the various background contributions is also shown in figure (a) where all contributions are normalized to the same luminosity. In figure (b) only the $Z \to \mu^+\mu^-$ MC distribution is superimposed after being normalized to the integral of the distribution in data.*

butions from uncertainties in the momentum scale resolution and isolation/reconstruction efficiencies. The estimation of these uncertainties is time consuming and due to the time constraints imposed on the analysis carried out in this thesis, it has been chosen to use the numbers quoted in [105]. Here a total systematic uncertainty of 5.5 % is quoted for C_Z.
The total systematic uncertainty on $\sigma_Z(\nu)$ was estimated in chapter 10.2 to be 4.6 %, including contributions from such sources as ISR/FSR, higher order corrections and PDF uncertainties. The actual value for $\sigma_Z(\nu)$ is taken from the NNLO estimate by FEWZ which quotes a value of 989 pb [114]. Since the number needed for the calculation of the absolute luminosity is the fiducial cross-section, the fully inclusive value must be multiplied by the acceptance. With the acceptance ($A_Z = 0.476$) calculated from MC the fiducial cross section is found to be $\sigma_Z(\nu) = 470.76\ pb$.
It should be noted here that the reason why the measured cross-section quoted in [105] is not used in this analysis is obviously to avoid a circular argument. The measured cross-section cannot be used to measure a luminosity which was used to determine the cross-section.

11.5.2 Results

The final numbers necessary to determine the absolute luminosity from Z counting are summarized in table 11.6.
If these are inserted in equation 10.1 one finds an integrated luminosity of 2.88 pb^{-1} which is about 14 % lower than the value found by LUCID for the same data taking period using the VdM calibration. If the Monte Carlo calibration of LUCID is used instead, the value is only 1 % lower for PYTHIA and 13 % higher for PHOJET (see table 9.1). A detailed comparison

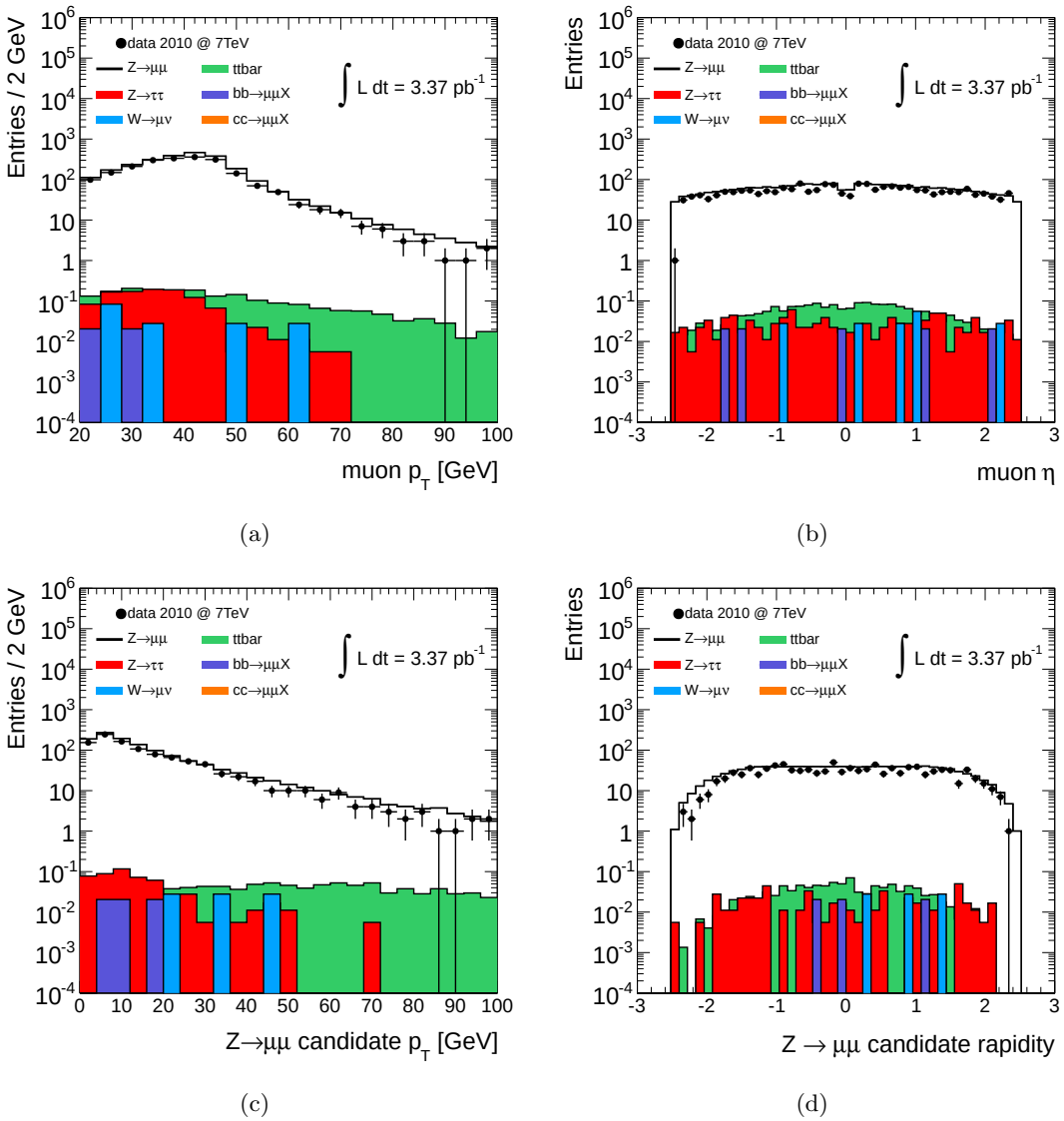


Figure 11.11: *Kinematical distributions: p_T and η distributions of muons from $Z \to \mu^+\mu^-$ decays after final selection (a)(b). p_T and rapidity distributions of $Z \to \mu^+\mu^-$ candidate after final selection (c)(d). The breakdown of the various background contributions are also shown in this figure. All contributions are normalized to the luminosity measured by LUCID and indicated in the plots.*

	$N^{obs}_{Z \to \mu^+\mu^-}$	$N^{back}_{Z \to \mu^+\mu^-}$	$\sigma_Z(\nu)[pb]$	C_Z
central value	1057	1.38	470.76	0.779
stat error	33	0.05	4.76	0.033
sys. uncert.	-	-	19.06	0.055

Table 11.6: *Final numbers used to calculate the integrated luminosity for the data set.*

between the luminosity measured by Z counting and by LUCID is given below.

$$\int \mathcal{L}dt\ (Z \to \mu^+\mu^-) \quad = \quad 2.88 \pm 0.15(stat.) \pm 0.23(sys.)\ pb^{-1}$$

$$\int \mathcal{L}dt\ (LUCID) \quad = \quad \begin{cases} 3.37 \pm (\ll 0.01)(stat.) \pm 0.37(sys.)\ pb^{-1} & \text{(VDM calib.)} \\ 2.92 \pm (\ll 0.01)(stat.) \pm 0.18(sys.)\ pb^{-1} & \text{(MC calib. PYTHIA)} \\ 2.55 \pm (\ll 0.01)(stat.) \pm 0.15(sys.)\ pb^{-1} & \text{(MC calib. PHOJET)} \end{cases}$$

The luminosity determined from the three methods agree within one standard deviation. The dominating contribution to the error in both measurements, comes from the systematic uncertainty. In the case of LUCID, the dominating contribution is the uncertainty on the calibration procedure both when the VdM calibration is used and when the MC calibration is used. For the VdM calibration the systematics is almost entirely due to the measure of the beam intensities as mentioned in chapter 9. For the MC calibration the main systematic uncertainty can be ascribed to the efficiency determination which is necessary to calculate σ_{vis} (see table 7.9). In Z counting, the dominating contribution comes from the uncertainty in C_Z. Figure 11.12 gives a graphical comparison of the integrated luminosities determined by the different methods. The uncertainty on the data points is taken as the quadratic sum of the statistical and systematic uncertainties.

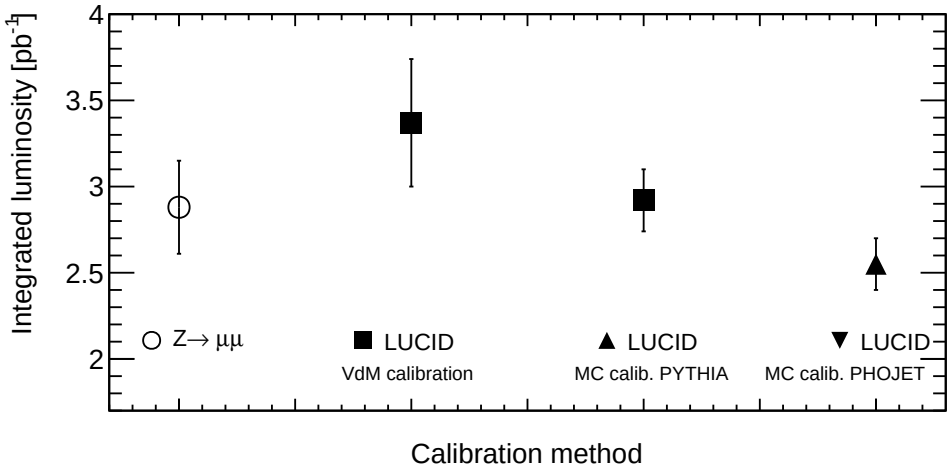


Figure 11.12: *Comparison of the integrated luminosities determined by the different methods.*

11.6 Summary and conclusion

A procedure to select $Z \to \mu^+\mu^-$ events has been presented. The procedure consists in a series of selection cuts which are imposed on the data sample in a specific order. Each selection cut has been described and justified by a Monte Carlo study where the effect of each selection cut on the signal and background samples has been investigated. The value of the selection

cuts has been optimized to give the largest value of signal significance. The total efficiency to select and reconstruct the $Z \to \mu^+\mu^-$ decays has been calculated using both the cut-flow and the Tag&Probe methods and the results were compared.
The selection procedure are used to extract the $Z \to \mu^+\mu^-$ candidates from the data set recorded by the ATLAS detector in the period from April to August 2010. The result is a sample consisting of 1057 $Z \to \mu^+\mu^-$ candidates which corresponds to an integrated luminosity of 2.88 pb^{-1} when the expected background contributions has been subtracted. This value is 14 % lower than the value determined by the LUCID detector when the VdM calibration is used although the two values are compatible within the uncertainties. The corresponding value for the MC calibration of LUCID is 1 % and 13 % derivation for PYTHIA and PHOJET respectively. In the case of the measurement by LUCID the main contributions to systematic uncertainty comes from the uncertainties in the calibration methods. When the luminosity is calculated from Z production then the systematic uncertainty is dominated by the PDF uncertainties. Despite the slight underestimation of the luminosity, Z production might still prove to be useful in the future. If not as a direct measurement of the luminosity then as a cross check of the dedicated luminosity monitors. The method also has the potential to provide a more precise measurement when the rate is higher and the uncertainties on the PDFs have been further constrained at 7 TeV. It has been shown that this method can be used to provide an accurate calibration of luminosity monitors like LUCID.

Chapter 12

Summary and outlook

The aim of this thesis was firstly to describe and validate the detector description of LUCID which has been implemented in the global ATLAS software framework. Secondly, to derive algorithms to determine the luminosity and based on the simulation of LUCID to test the precision of these. Thirdly, to study the feasibility of using Z^0 production as a alternative way to measure the luminosity or to calibrate LUCID.

A detailed description of the LUCID detector has been implemented in the ATLAS software framework. This description incorporates all major effects needed to obtain a realistic description of light production and propagation in a detector based on the detection of Cerenkov light. The detector description has been validated through a series of tests aimed at studying the response in different situations. It was seen that the dominating contribution to the signal in LUCID is from secondary particles. It was however concluded, that since the number of secondaries are proportional to the number of primaries, secondaries will not constitute a background to the luminosity measurement. The simulation of the readout electronics for LUCID was also addressed and it was concluded that a realistic simulation of the PMT dynode-chain leads to a more realistic simulation of the PMT response as a whole.

The performance of LUCID was addressed in chapter 7 by comparing results from the early 2010 data-taking period with predictions from the simulations. It was concluded from these comparisons that the simulation of LUCID in general describes data well. Discrepancies were seen at the level of the collected charge distributions for the individual tubes but the agreement of the overall hit multiplicity distribution is good. Several techniques to calculate the efficiency of LUCID have been described and the results for each method has been presented.

It has been argued in several places in this thesis that the main difficulty in measuring the luminosity at LHC is detector related effects caused by pile-up. The precision of the final luminosity determination therefore depends on the ability to minimize these effects in the luminosity algorithms.
Two classes of luminosity algorithms have been presented and applied to the signals from the LUCID detector in chapter 8. The first class has been designed to be operated online and to extract the luminosity using two different counting methods, namely event and hit counting. The second class of luminosity algorithms are designed to be applied offline. Belonging to

this category is a method, which uses the hit multiplicity distributions, obtained at low luminosity ($\mu \ll 1$) to extract the luminosity. The performance of all methods were evaluated using Monte Carlo simulations.
It was shown that by using a combinatorial model which includes saturation effects, it was possible to obtain reliable predictions of the luminosity up until $\mu \sim$ 8-10 for event counting and $\mu \sim$ 1-2 for hit counting. This is to be compared to a usable range of $\mu < 2$ if a linear approximation to the combinatorial model is used.
The overall conclusion was therefore that the best online methods to use are the event counting methods in the full combinatorial model. The systematic uncertainty for these methods is at the order of 6-7 % over a range from $\mu = 0$ to $\mu =$ 8-10. It can also be concluded that the inability to precisely predict the luminosity at high values of μ is to a large degree caused by the inability to incorporate migration effects in the combinatorial model.
An empirical model was introduced as an attempt to parametrize the non-linear effect by polynomial fits to the event and hit rate. With this approach the luminosity can be measured correctly up to a μ value of around 6 with event counting and 25 with hit counting. The limitations of this approach are that the fit procedure in itself introduces an additional source of systematic uncertainty which in turns leads to a less precise luminosity determination.
A final attempt to minimize the non-linear effects was presented by introducing a new method that uses the full hit multiplicity distribution to determine the luminosity offline. The results show that the method is linear and provides reliable luminosity predictions in the range ($0.5 \leq \mu \leq 25$). With very small fluctuations and a total systematic uncertainty of 5 % this method has proven to be the most precise luminosity algorithm presented in this thesis.

A method to measure the absolute luminosity using the production of Z^0 boson was outlined in the last part of the thesis. Each step of the procedure to select $Z \to \mu^+\mu^-$ events has been studied in detail using Monte Carlo simulations of the various background and signal samples. The total efficiency to select and reconstruct the $Z \to \mu^+\mu^-$ decays has been calculated using both the cut-flow and the Tag&Probe methods and the results are compared.
The selection procedure has been applied to a data sample recorded by the ATLAS detector over a period of 5 month and the resulting integrated luminosity determined from the number of reconstructed $Z \to \mu^+\mu^-$ decays was found to be 2.88 pb^{-1}. This number is about 14% lower than the value obtained by LUCID using the VdM calibration. The corresponding value for the Monte Carlo calibration of LUCID is 1 % and 13 % derivation for PYTHIA and PHOJET respectively. All values are however compatible due to the large systematic uncertainty. Despite the slight underestimation of the luminosity it can still be concluded that Z production proves to be a very promising way to determine the absolute luminosity already at the current stage of data taking.

Outlook

Of the different luminosity algorithms presented in this thesis especially the offline algorithm based on hit multiplicity distributions shows potential. It has been proven to be very stable and linear over almost the full luminosity range of the LHC. Furthermore, the method proves to be the one which is least affected by the systematic uncertainties and it therefore also has the prospect of providing the most precise measurement of the luminosity. This method,

however, remains to be applied to real data offline. An interesting project for the future would be to use this method to cross check results from the online methods. It might even be possible to implement the method to run online averaged over LumiBlocks. However, the real justification of this model is that so far it has proven to be the only luminosity algorithm which is able to provide a precise measurement at luminosities close to the design luminosity. Another method which show great potential for the future, is the resonance counting method. In this thesis only the $Z \to \mu^+\mu^-$ channel has been investigated but also the electron channel could be used. The production of $W^{\pm}$ bosons or J/ψ mesons could furthermore be used in a similar way. A limiting factor on the precision in these measurements is the relative poor knowledge of the PDFs at 7 TeV. It has been shown in this thesis that the PDF uncertainties constitutes the largest contribution to the total systematic uncertainty in this method. At a later stage when the PDFs have been further constraint at 7 TeV, gauge boson production could therefore potentially be a very useful way of measuring the luminosity.

Part VI
Appendix

Appendix A

Simulation of LUCID - Systematic uncertainties

	Signal amplitude A		
Rel. change in %	**Gas temperature**	**Gas pressure**	**Tube polish***
-10%	103.03 ± 0.60	93.92 ± 0.57	84.01 ± 0.44
0%	97.71 ± 0.50	97.72 ± 0.50	$(-5\%)92.72 \pm 0.50$
10%	92.46 ± 0.76	102.75 ± 0.55	97.72 ± 0.50
	Signal width σ_A		
Rel. change in %	**Gas temperature**	**Gas pressure**	**Tube polish***
-10%	11.15 ± 0.54	10.72 ± 0.51	9.65 ± 0.39
0%	11.86 ± 0.42	11.86 ± 0.42	$(-5\%)10.49 \pm 0.44$
10%	10.58 ± 0.54	11.02 ± 0.77	$(0\%)11.86 \pm 0.42$

Table A.1: *Stability of signal amplitude (A) (upper part) and signal width σ_A (lower part) as a function of variation in the simulation parameters. The variation of the tube has been carried out in the range from -10 % to 0% since it is not possible to increase the value beyond already used in the simulation.*

	σ_A/A		
Rel. change in %	G_{PMT}	G_{AMP}	Q_{noise}
−10%	0.129 ± 0.014	0.123 ± 0.013	0.122 ± 0.013
−9%	0.127 ± 0.014	0.124 ± 0.013	0.124 ± 0.013
−8%	0.126 ± 0.012	0.124 ± 0.013	0.122 ± 0.013
−7%	0.126 ± 0.013	0.123 ± 0.013	0.125 ± 0.013
−6%	0.125 ± 0.013	0.125 ± 0.013	0.124 ± 0.013
−5%	0.127 ± 0.013	0.123 ± 0.013	0.120 ± 0.013
−4%	0.127 ± 0.013	0.124 ± 0.013	0.124 ± 0.013
−3%	0.127 ± 0.013	0.127 ± 0.013	0.122 ± 0.013
−2%	0.124 ± 0.012	0.124 ± 0.013	0.123 ± 0.013
−1%	0.125 ± 0.013	0.124 ± 0.014	0.121 ± 0.013
0%	0.123 ± 0.012	0.123 ± 0.014	0.123 ± 0.013
1%	0.123 ± 0.013	0.124 ± 0.012	0.124 ± 0.013
2%	0.123 ± 0.013	0.125 ± 0.013	0.122 ± 0.013
3%	0.121 ± 0.013	0.125 ± 0.013	0.125 ± 0.013
4%	0.121 ± 0.013	0.121 ± 0.013	0.122 ± 0.013
5%	0.123 ± 0.014	0.123 ± 0.013	0.122 ± 0.013
6%	0.121 ± 0.014	0.124 ± 0.013	0.124 ± 0.013
7%	0.120 ± 0.013	0.121 ± 0.013	0.123 ± 0.013
8%	0.118 ± 0.013	0.124 ± 0.013	0.124 ± 0.013
9%	0.120 ± 0.013	0.124 ± 0.013	0.123 ± 0.012
10%	0.119 ± 0.013	0.123 ± 0.012	0.122 ± 0.013
	F		
Rel. change in %	G_{PMT}	G_{AMP}	Q_{noise}
−10%	1.411 ± 0.014	1.383 ± 0.013	1.519 ± 0.013
−9%	1.413 ± 0.013	1.405 ± 0.013	1.550 ± 0.013
−8%	1.446 ± 0.013	1.447 ± 0.014	1.502 ± 0.013
−7%	1.387 ± 0.013	1.433 ± 0.013	1.580 ± 0.013
−6%	1.481 ± 0.013	1.499 ± 0.014	1.544 ± 0.013
−5%	1.514 ± 0.013	1.453 ± 0.014	1.463 ± 0.013
−4%	1.504 ± 0.014	1.503 ± 0.014	1.566 ± 0.013
−3%	1.492 ± 0.013	1.584 ± 0.014	1.508 ± 0.013
−2%	1.501 ± 0.013	1.533 ± 0.013	1.536 ± 0.013
−1%	1.565 ± 0.013	1.539 ± 0.014	1.472 ± 0.013
0%	1.531 ± 0.013	1.529 ± 0.014	1.520 ± 0.013
1%	1.535 ± 0.013	1.559 ± 0.013	1.544 ± 0.013
2%	1.562 ± 0.014	1.608 ± 0.014	1.502 ± 0.013
3%	1.517 ± 0.013	1.633 ± 0.014	1.590 ± 0.013
4%	1.640 ± 0.013	1.522 ± 0.013	1.494 ± 0.014
5%	1.638 ± 0.014	1.594 ± 0.013	1.502 ± 0.013
6%	1.583 ± 0.013	1.666 ± 0.014	1.562 ± 0.013
7%	1.672 ± 0.014	1.590 ± 0.013	1.534 ± 0.013
8%	1.665 ± 0.013	1.678 ± 0.013	1.566 ± 0.014
9%	1.648 ± 0.013	1.693 ± 0.013	1.539 ± 0.013
10%	1.724 ± 0.012	1.692 ± 0.013	1.503 ± 0.013

Table A.2: *Stability of σ_A^2/A (upper part) and F (lower part) as a function of the parameters used in the simulation of the PMT response.*

Tube number	λ_{low} [p.e]	$\sigma_{\lambda_{low}}$ [p.e]	λ_{high} [p.e]	$\sigma_{\lambda_{high}}$ [p.e]
		MC		
all tubes	35.554 ± 0.073	$7.777 \pm 9.736 \times 10^{-3}$	100.301 ± 0.289	11.300 ± 0.283
		Data 2010 - Side A		
tube 0	41.614 ± 0.155	9.448 ± 0.208	110.062 ± 0.270	9.923 ± 0.293
tube 2	41.176 ± 0.149	8.847 ± 0.191	113.571 ± 0.275	9.191 ± 0.280
tube 3	40.448 ± 0.172	9.789 ± 0.240	104.609 ± 0.346	10.677 ± 0.405
tube 5	46.273 ± 0.126	9.784 ± 0.176	111.443 ± 0.306	9.815 ± 0.378
tube 6	44.051 ± 0.129	9.626 ± 0.181	111.403 ± 0.343	10.669 ± 0.391
tube 7	39.816 ± 0.148	8.726 ± 0.118	100.765 ± 0.411	11.603 ± 0.540
tube 8	38.633 ± 0.211	11.540 ± 0.249	105.411 ± 0.451	9.663 ± 0.478
tube 9	42.715 ± 0.184	10.119 ± 0.350	100.707 ± 0.622	11.116 ± 0.820
tube 10	45.269 ± 0.161	7.350 ± 0.128	108.748 ± 2.237	11.122 ± 1.334
tube 11	42.155 ± 0.187	11.711 ± 0.229	123.649 ± 0.442	12.591 ± 0.485
tube 12	43.263 ± 0.212	12.603 ± 0.227	121.206 ± 0.451	16.306 ± 0.625
tube 13	42.108 ± 0.009	10.840 ± 0.051	119.537 ± 0.348	11.629 ± 0.354
tube 14	43.956 ± 0.289	12.963 ± 0.348	106.396 ± 0.284	12.377 ± 0.466
tube 15	40.570 ± 0.195	12.153 ± 0.245	107.478 ± 1.737	11.283 ± 1.674
		Data 2010 - Side C		
tube 20	20.830 ± 1.849	21.266 ± 0.924	83.446 ± 1.494	17.795 ± 0.9748
tube 21	31.817 ± 0.959	20.106 ± 0.600	89.654 ± 2.879	26.548 ± 2.254
tube 22	21.160 ± 1.724	24.906 ± 1.233	99.855 ± 1.120	18.577 ± 1.143
tube 23	40.654 ± 0.172	9.695 ± 0.245	102.361 ± 0.424	11.637 ± 0.475
tube 24	42.148 ± 0.318	11.379 ± 0.431	135.522 ± 0.682	13.879 ± 1.494
tube 25	30.905 ± 0.414	19.014 ± 0.340	88.258 ± 1.123	31.917 ± 1.140
tube 26	30.866 ± 0.507	20.183 ± 0.501	91.148 ± 1.735	29.800 ± 2.182
tube 27	44.244 ± 0.142	10.834 ± 0.205	117.909 ± 0.483	10.191 ± 0.604
tube 28	41.683 ± 0.132	9.290 ± 0.163	110.194 ± 0.486	11.549 ± 0.551
tube 29	$no-fit$	$no-fit$	$no-fit$	$no-fit$
tube 30	35.314 ± 0.686	11.771 ± 0.591	100.621 ± 1.085	14.339 ± 1.079
tube 31	43.080 ± 0.147	9.251 ± 0.206	106.49 ± 0.406	11.014 ± 0.452
tube 32	43.034 ± 0.152	9.591 ± 0.211	110.442 ± 0.305	10.238 ± 0.363
tube 34	41.524 ± 0.137	9.406 ± 0.183	115.347 ± 0.417	9.831 ± 0.420

Table A.3: *Peak positions and signal width for all Cerenkov tubes. "no-fit" signifies that the fit did not converge.*

	PYTHIA MC09 tune			
PMT cut [p.e]	ε^A	ε^C	ε^{OR}	ε^{AND}
0	0.999 ± 0.001	0.999 ± 0.001	1.000 ± 0.001	0.999 ± 0.001
1	0.676 ± 0.002	0.681 ± 0.002	0.860 ± 0.001	0.497 ± 0.002
2	0.603 ± 0.002	0.609 ± 0.002	0.799 ± 0.002	0.412 ± 0.002
3	0.572 ± 0.002	0.579 ± 0.002	0.776 ± 0.002	0.375 ± 0.002
4	0.550 ± 0.002	0.555 ± 0.002	0.757 ± 0.002	0.348 ± 0.002
5	0.530 ± 0.002	0.536 ± 0.002	0.740 ± 0.002	0.326 ± 0.002
6	0.515 ± 0.002	0.522 ± 0.002	0.727 ± 0.002	0.309 ± 0.002
7	0.499 ± 0.002	0.509 ± 0.002	0.715 ± 0.002	0.293 ± 0.002
8	0.487 ± 0.002	0.496 ± 0.002	0.704 ± 0.002	0.280 ± 0.002
9	0.477 ± 0.002	0.485 ± 0.002	0.693 ± 0.002	0.269 ± 0.002
10	0.467 ± 0.002	0.475 ± 0.002	0.684 ± 0.002	0.259 ± 0.002
11	0.458 ± 0.002	0.467 ± 0.002	0.676 ± 0.002	0.250 ± 0.002
12	0.451 ± 0.002	0.460 ± 0.002	0.668 ± 0.002	0.242 ± 0.002
13	0.444 ± 0.002	0.453 ± 0.002	0.661 ± 0.002	0.236 ± 0.002
14	0.438 ± 0.002	0.447 ± 0.002	0.655 ± 0.002	0.229 ± 0.002
15	0.432 ± 0.002477	0.440 ± 0.002	0.649 ± 0.002	0.223 ± 0.002
16	0.426 ± 0.002	0.435 ± 0.002	0.643 ± 0.002	0.218 ± 0.002
17	0.421 ± 0.002	0.429 ± 0.002	0.638 ± 0.002	0.213 ± 0.002
18	0.416 ± 0.002	0.424 ± 0.002	0.632 ± 0.002	0.208 ± 0.002
19	0.412 ± 0.002	0.419 ± 0.002	0.627 ± 0.002	0.203 ± 0.002
20	0.407 ± 0.002	0.416 ± 0.002	0.623 ± 0.002	0.200 ± 0.002
21	0.402 ± 0.002	0.411 ± 0.002	0.618 ± 0.002	0.195 ± 0.001
22	0.398 ± 0.002	0.406 ± 0.002	0.613 ± 0.002	0.191 ± 0.001
23	0.393 ± 0.002	0.402 ± 0.002	0.608 ± 0.002	0.187 ± 0.001
24	0.389 ± 0.002	0.398 ± 0.002	0.603 ± 0.002	0.183 ± 0.001
25	0.385 ± 0.002	0.393 ± 0.002	0.599 ± 0.002	0.179 ± 0.001
26	0.380 ± 0.002	0.388 ± 0.002	0.593 ± 0.002	0.175 ± 0.001
27	0.374 ± 0.002	0.382 ± 0.002	0.586 ± 0.002	0.170 ± 0.001
28	0.368 ± 0.002	0.377 ± 0.002	0.580 ± 0.002	0.165 ± 0.001
29	0.363 ± 0.002	0.371 ± 0.002	0.573 ± 0.002	0.160 ± 0.001
30	0.357 ± 0.002	0.365 ± 0.002	0.567 ± 0.002	0.155 ± 0.001
31	0.351 ± 0.002	0.358 ± 0.002	0.559 ± 0.002	0.150 ± 0.001
32	0.343 ± 0.002	0.351 ± 0.002	0.551 ± 0.002	0.144 ± 0.001
33	0.337 ± 0.002	0.344 ± 0.002	0.542 ± 0.002	0.139 ± 0.001
34	0.329 ± 0.002	0.337 ± 0.002	0.534 ± 0.002	0.133 ± 0.001

Table A.4: *LUCID efficiency when at least one hit is required on side A (ε^A), on side C (ε^C), either of the sides (ε^{OR}), both sides (ε^{AND}) for pp inelastic collisions and a full ATLAS detector simulation collisions at $\sqrt{s} = 7$ TeV.*

Appendix B

Performance Study of Luminosity Algorithms in ATLAS

i	$L_i(l,n,k)$	$\widetilde{L}_i(n,k)$
1	$kM_{11}P_{XOR}^{l}(1-P_{XOR}-P_{11})^{n-k-l}$	$kM_{11}(1-P_{11})^{n-k}$
2	$M_{XOR}lP_{XOR}^{l}(1-P_{XOR}-P_{11})^{n-k-l}$	$P_{XOR}M_{XOR}(n-k)(1-P_{11})^{n-k-1}$
3	$P_{XOR}M_{XOR}(n-k)(1-P_{11})^{n-k-1}$	$kM_{10}\left[(P_{00}+P_{01})^{n-k}-P_{00}^{n-k}\right]$
4	$M_{01}lP_{01}^{l}P_{00}^{n-k-l}$	$P_{01}M_{01}(n-k)(P_{00}+P_{01})^{n-k}$

i	$K_i(n,k)$	$\widetilde{K}_i(n)$
1	$M_{11}kP_{11}^{k}(1-P_{11})^{n-k}$	$nM_{11}P_{11}$
2	$M_{XOR}P_{XOR}nP_{11}^{k}(1-P_{11})^{n-k-1}$	$nM_{XOR}P_{XOR}\left[\left(\frac{1}{1-P_{11}}\right)-(1-P_{11})^{n-1}\right]$
3	$-M_{XOR}P_{XOR}kP_{11}^{k}(1-P_{11})^{n-k-1}$	$-nM_{XOR}P_{XOR}\left(\frac{P_{11}}{1-P_{11}}\right)$
4	$M_{10}kP_{10}^{k}(P_{00}+P_{01})^{n-k}$	$nM_{10}P_{10}(P_{00}+P_{10}+P_{01})^{n-1}$
5	$-M_{10}kP_{10}^{k}P_{00}^{n-k}$	$-nM_{10}P_{10}(P_{00}+P_{10})^{n-1}$
6	$M_{01}P_{01}nP_{10}^{k}(P_{00}+P_{01})^{n-k-1}$	$nM_{01}P_{01}\left[\frac{(1-P_{11})^{n}}{P_{00}+P_{01}}-(P_{00}+P_{01})^{n-1}\right]$
7	$-M_{01}P_{01}kP_{10}^{k}(P_{00}+P_{01})^{n-k-1}$	$-nM_{01}P_{01}P_{10}\left(\frac{(1-P_{11})^{n-1}}{P_{00}+P_{01}}\right)$

Table B.1: *Coefficients used in the derivation of the Hit counting method in coincidence mode.*

Appendix C

$Z \to \mu^+\mu^-$ analysis : Optimization of the selection cuts

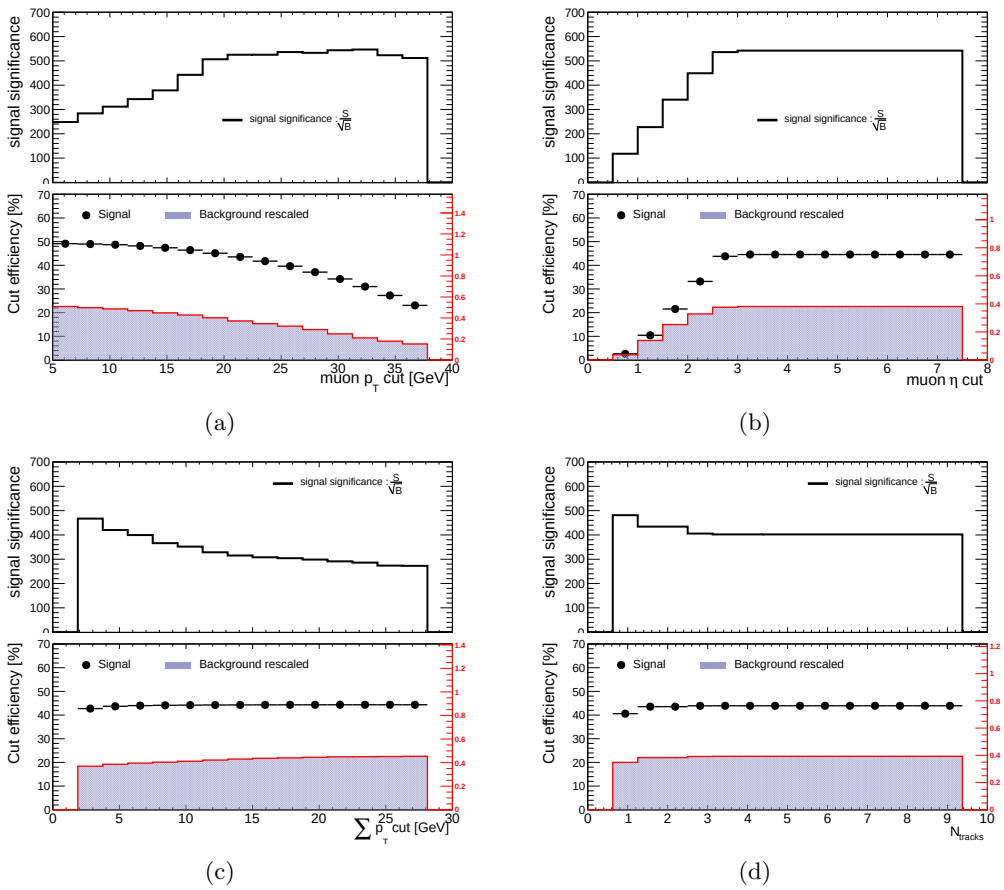


Figure C.1: *The first plot (top) shows how the significance of the $Z \to \mu^+\mu^-$ signal depends on the cut value. The second plot (bottom) shows the cut efficiency as a function of the cut values. The points represent the effect of the cut the signal, while the solid histogram represents the background. The various figures show the optimization of the (a) p_T (b) η (c)(d) isolation plots.*

Bibliography

[1] Jonathan Barnes. *The Presocratic Philosophers.* Routledge Revised Edition, 1982.

[2] Frank Greenaway. *John Dalton and the Atom.* Ithaca, New York: Cornell University Press., 1966.

[3] H. Bethe. Nuclear Dynamics, Theoretical. *Nuclear Physics. B*, 9(69):245, 1937.

[4] Lise Meitner and O. R. Frisch. Disintegration of Uranium by Neutrons: a New Type of Nuclear Reaction. *Nature*, 143(3615):239–240, 1938.

[5] R.P. Feynman and S. Weinberg. *Elementary Particles and the Laws of Physics: The 1986 Dirac Memorial Lectures.* Cambridge Univ. Press, 1987.

[6] W. M. Yao et al. (Particle Data Group Coll.). *Reveiw of Particle Physics, Journal of Physics G*, 33:1 –, 2006.

[7] K.-C. Wang. A suggestion on the Detection of the Neutrino. *Physical Review*, 61(97), 1942.

[8] F.B. Harrison H.W. Kruse A.D McGuire C.L Cowan Jr., F. Reines. Detection of the Free Neutrino: a Confirmation. *Science*, 124(3212):103, 1956.

[9] M. Gell-Mann. A schematic model of baryons and mesons. *Phys. Rev. Lett*, 8:214, 1964.

[10] G. Zweig. An $SU(3)$ model for the strong interaction symmetry and its breaking. *CERN-TH*, 412.

[11] M. A. T. Emmy Noether. Invariant Variation Problems. *Physics/0503066*, 1918.

[12] A. Pich. The standard model of electroweak interactions. *Spires*, hep-ph(0502010v1), 2007.

[13] S. F. Novaes. Standard Model: An Intoduction. *IFT-P*, hep-ph/0001283v1, 2000.

[14] B. R. Holstein J. F. Donoghue, E. Golowhich. *Dynamics of the Standard Model.* Cambridge Monographs. Cambridge Univ. Press, 1992.

[15] B. R. Webber R. K. Ellis, W. J. Stirling. *QCD and Collider Physics.* Cambridge Monographs. Cambridge Univ. Press, 1996.

[16] J. Swinger. *Ann. Phys.*, 2(407), 1957.

[17] S. A. Bludman. *Nuovo Cim*, 9(433), 1958.

[18] M. Gell-Mann R. P. Feynman. *Phys. Rev.*, 109(1611), 1958.

[19] F. J. Hasert et al. *Phys Lett. B.*, 46(121), 1973.

[20] S. L. Glashow. *Nucl. Phys.*, 22(579), 1961.

[21] J. C. Ward A. Salam. *Phys Lett.*, 13:168, 1964.

[22] S. Weinberg. *Phys. Rev. Lett*, 19:1264, 1969.

[23] A. Salam. Elementary Particle Theory. *The Nobel Symposium no. 8*, page 367.

[24] J. Goldstone. *Nuov. Cim.*, 19:154, 1961.

[25] LHC Collaboration. http://lhc.web.cern.ch/LHC/LHC-DesignReport.html. *2010.*

[26] LEP design report. *CERN-LEP*, 1, 1984.

[27] www.cern.ch/. *CERN webpage*, 2010.

[28] ATLAS Collaboration. ATLAS detector and physics performance : Technical Design Report, 1. *(Technical Design Report ATLAS ; 14)*, 1999.

[29] http://www-bdnew.fnal.gov/tevatron/. *TEVATRON webpage*, 2002.

[30] ATLAS Collaboration. http://www.atlas.ch/. *ATLAS webpage.*

[31] LINAC2 Collaboration. http://linac2.home.cern.ch. *2010.*

[32] K. H. Reich. The CERN Proton Synchrotron Booster. *Proceedings of the 3rd IEEE Particle Accelerator Conference.*, 1969.

[33] PS Collaboration. http://ps-div.web.cern.ch/ps-div/welcome.html. *PS webpage.*

[34] SPS Collaboration. http://ab-dep-op-sps.web.cern.ch/. *SPS webpage.*

[35] R Bailey and Paul Collier. Standard Filling Schemes for Various LHC Operation Modes. Technical Report LHC-PROJECT-NOTE-323, CERN, Geneva, Sep 2003.

[36] ALICE Collaboration. Technical Proposal for A Large Ion Collider Experiment at the CERN LHC. *CERN / LHCC / 95–71*, 1995.

[37] CMS Collaboration. CMS physics TDR: Volume i (PTDR1), Detector Performance and Software. *CERN-LHCC-2006-001.*

[38] LHCb Collaboration. LHCb : Technical Proposal. *CERN-LHCC-98-004*, 1998.

[39] LHCf Collaboration. LHCf experiment : Technical Design Report. *CERN-LHCC-2006–004.*

[40] G RUGGIERO et al. The TOTEM Detector at LHC. *CERN-LHCC-2005–002*, 2005.

[41] ATLAS Collaboration. The ATLAS Experiment at the CERN Large Hadron Collider. *JINST*, 3, 2008.

[42] ATLAS Collaboration. Atlas detector and physics performance : Technical Design Report, 2. *(Technical Design Report ATLAS ; 15)*, 1999.

[43] A. Yamamoto et al. The ATLAS central solenoid. *Nucl. Instrum. Meth. A*, 584(53), 2008.

[44] *ATLAS magnet system: Technical Design Report, 1.* Technical Design Report ATLAS. CERN, Geneva, 1997.

[45] *ATLAS inner detector: Technical Design Report, 1.* Technical Design Report ATLAS. CERN, Geneva, 1997.

[46] S Haywood, L Rossi, R Nickerson, and A Romaniouk. *ATLAS inner detector: Technical Design Report, 2.* Technical Design Report ATLAS. CERN, Geneva, 1997.

[47] W.R Leo. *Techniques for Nuclear and Particle Physics Experiments.* Springer-Verlag, 1994.

[48] Dan Green. *The Physics of Particle Detectors.* Cambridge Monographs. Cambridge Univ. Press, 2000.

[49] G. Aad et al. ATLAS pixel detector electronics and sensors. *JINST*, 3, 2008.

[50] A Abdesselam et al. The barrel modules of the ATLAS semiconductor tracker. *Nuclear Instruments and Methods in Physics Research Section A*, 568(2):642–671, 2006.

[51] E. Abat et al. The ATLAS Transition Radiation Tracker (TRT) proportional drift tube: design and performance. *JINST*, 3, 2008.

[52] Torbjorn Sjostrand et al. PYTHIA 6.4 Physics and Manual. *arXiv*, hep-ph/0603175v2, 2006.

[53] ATLAS Collaboration. Liquid argon calorimeter technical design report. *CERN/LHCC/96-041*, 1996.

[54] *ATLAS Tile calorimeter: Technical Design Report.* Technical Design Report ATLAS. CERN, Geneva, 1996.

[55] ATLAS Collaboration. *ATLAS Muon Spectrometer : Technical Design Report*, volume CERN/LHCC97–22. CERN, Geneva, 1997.

[56] F. Bauer et al. Construction and test of MDT chambers for the ATLAS muon spectrometer. *Nucl. Instrum. Meth. A*, 461(17), 2001.

[57] I. Dolenc et al. The ATLAS Beam Conditions Monitor. *JINST*, 2008.

[58] E. J. Feng and J. Pilcher. Triggering ATLAS with Minimum Bias Trigger Scintillators. *ATL-TILECAL-INT-2007-004*, 2007.

[59] The LUCID collaboration. ATLAS forward detectors for luminosity measurement and monitoring. *CERN-LHCC-2004-10, LHCC I-014, http://cdsweb.cern.ch/record/721908*, 2004.

[60] Peter Jenni, Marzio Nessi, and Markus Nordberg. Zero Degree Calorimeters for ATLAS. Technical Report LHCC-I-016. CERN-LHCC-2007-001, CERN, Geneva, Jan 2007.

[61] Peter Jenni, Markus Nordberg, Marzio Nessi, and Kerstin Jon-And. *ATLAS Forward Detectors for Measurement of Elastic Scattering and Luminosity.* Technical Design Report. CERN, Geneva, 2008.

[62] M. Month. Collider Performance with ideal Collisions. *Accel. Div. Report 85-1, , D0 Note 201*, 1985.

[63] B. Muratori W. Herr. Concept of luminosity. *CERN 2006-002*, 2006.

[64] Thilo Pauly Marjorie Shapiro Stefan Ask, David Malon. Report from the Luminosity Task Force. *ATL-GEN-PUB-2006-002.*

[65] The ATLAS Collaboration. Luminosity Determination Using the ATLAS Detector. *ATL-ATLAS-CONF-2010-060*, 2010.

[66] A. Bertin et al. Calibrating the ATLAS luminosity detectors using beam separation scans. *ATL-COM-LUM-2010-021*, 2010.

[67] S. Van der Meer. Calibration of the effective beam height in the ISR. *CERN-ISR-PO-68-31.*

[68] F. Pauss M. Dittmar and D. Zurcher. Towards a precise parton luminosity determination at the CERN LHC. *Phys. Rev. D*, D56(7284), 1997.

[69] D. Acosta et al. The CDF Cherenkov luminosity monitor. *Nucl. Instrum. Meth. A*, 461(540), 2001.

[70] T.L. Cheng and P. Teixeira-Dias. Sensitivity of ATLAS to FCNC single top quark production. *ATLAS Note ATL-PHYS-PUB-2006-029.*

[71] S. Baranov et al. Estimation of Radiation Background, Impact on Detectors, Activation and Shielding Optimization in ATLAS. *ATL-GEN- 2005-001*, 2005.

[72] J. D. Jackson. *Classical Electrodynamics.* Wiley and Sons, 1975.

[73] Anders Floderus. Monitoring of the LUCID detector in the ATLAS experiment. Master's thesis, Lund University, 2009.

[74] A. Menzione I. Sykora S. Tokar I. Chirikov-Zorin, I. Fedorko. Precise analysis of the metal package photomultiplier spectra. *Nucl. Instr. and Meth. A*, 461:587–590, 2001.

[75] *The GeoModel Toolkit for Detector Description, in Proceedings of the Conference on Computing in High Energy and Nuclear Physics*, 2004.

[76] S. Agostinelli et al. (GEANT4 Collaboration). GEANT4: A simulation toolkit,. *Nucl. Instrum. Meth. A*, 506:250–303, 2003.

[77] J.Groth-Jensen et al. Simulation of ATLAS Luminosity Monitoring with LUCID. *ATLAS NOTE*, ATL-COM-LUM-2010-003, 2010.

[78] R. Arnold et al. *NIM A*, 270:289, 1988.

[79] T. Kittelmann et al. Virtual Point One (VP1). *http://atlas-vp1.web.cern.ch/atlas-vp1/*, 2008.

[80] R. Engel. PHOJET manual (program version 1.05c, June 96). *http://www-ik.fzk.de/engel/phojet.html*, 1996.

[81] ATLAS Collaboration. Charged-particle multiplicities in pp interactions at $\sqrt{s} = 900$ gev measured with the ATLAS detector at the LHC. *Phys Lett B 688, 1, 21*, 2010.

[82] ATLAS Collaboration. Public results, 2010.

[83] J Groth-Jensen. LUCID in ATLAS. *ATL-COM-LUM-2009-022*, Dec 2009.

[84] S. Tokar et al. Single Photoelectron Spectra Analysis for the Metal Dynode Photomultiplier. *ATL-TILECAL-99-005*, 1999.

[85] N.Bouhemaidetal. Characterization of the Hamamatsu 10–stages R5900 photomultipliers at Clermont for the TILE calorimeter. *ATL–TILECAL–97–108*.

[86] ATLAS Collaboration. ATLAS monte carlo tunes for MC09. *ATLAS-PHYS-PUB-2010-002*, 2010.

[87] S. Jindariani. Soft QCD and the underlying event at CDF. *Nuclear Physics B - Proceedings Supplements*, Volumes 177-178, 2008.

[88] Peter Zeiler Skands. The Perugia Tunes. *arXiv*, 1005.3457, 2010.

[89] Torbjorn Sjostrand et al. A Brief introduction to PYTHIA 8.1. *arXiv:0710.3820*, 2007.

[90] Rene Brun. ROOT software framework. *http://root.cern.ch/drupal/*.

[91] C. Ohm and T. Pauly. The ATLAS beam pick-up based timing system. *ATL-DAQ-PROC-2009-005*, 2009.

[92] David Berge et el. Luminosity measurement using the ATLAS Minimum Bias Trigger Scintillator System. *ATL-LUM-INT-2010-004*, 2010.

[93] S. Ask. Simulation of Luminosity Monitoring in ATLAS. *ATL-LUM-PUB-2006-001*, 2006.

[94] R.P Brent. *Algorithms for Minimization without Derivatives*. Number ISBN 0-486-41998-3. Prentice-Hall, Englewood Cliffs, 1973.

[95] The ATLAS Collaboration. Luminosity determination in pp collisions at $\sqrt{s} = 7$ tev using the ATLAS Detector at the LHC. *ATL-ATLAS-COM-LUM-029*, 2010.

[96] M. Schott. Theoretical uncertainties on the W- and Z-boson acceptance in the first phase of lhc. *ATL-COM-PHYS-2009-133*.

[97] Nadia E. Adam et al. Evaluation of the theoretical uncertainties in the $Z \to l^+l^-$ cross sections at the LHC. *JHEP05*, 2008.

[98] E.Dobson M.Schott and T.Petersen. Feasibility study on the measurement of the W to Z leptonic cross section ratio in the muon decay channel with early data. *ATL-PHYS-INT-2009-084*.

[99] M. Goulette. Comparison of acceptances and radiative effects for W or Z into leptons for the event generators Pythia, Herwig and MC@NLO. *ATL-PHYS-INT-2008-044-1*, 2008.

[100] M. Simonyan. The standard model W and Z boson production cross-sections and their uncertainties. *ATL-PHYS-INT-2009-076*, 2009.

[101] Bryan Lawrence Caron. *Luminosity Measurement at the Large Hadron Collider*. PhD thesis, University of Alberta, 2006.

[102] M. Schott. Common Approach to ATLAS Performance Determination in Data. *ATL-SOFT-PUB-2009-003*, 2009.

[103] Jonathan Steven Anderson. *Testing the electroweak sector and determining the absolute luminosity at LHCb using dimuon final states*. PhD thesis, UCD School of Physics, 2008.

[104] The ATLAS Collaboration. Measurement of the $Z \to ll$ production cross section in proton-proton collisions at $\sqrt{s} = 7$ tev with the ATLAS detector. *ATLAS-CONF-2010-076*, 2010.

[105] ATLAS Collaboration. Measurement of the $W \to l\nu$ and $Z \to ll$ production cross sections in proton-proton collisions at $\sqrt{s} = 7$ tev with the ATLAS detector. *JHEP (to be submitted)*, 2010.

[106] S.D. Drell and T.-M. Yan. Massive lepton pair production in hadron-hadron collisions at high-energies. *Phys. Rev. Lett. 25 (1970) 316*, 1970.

[107] G. Corcella et al. HERWIG 6.5. *JHEP 0101 (2001) 010*, 2001.

[108] H. Baer et al. ISAJET 7.80. *Manual*, 2010.

[109] T. Gleisberg et al. Event generation with Sherpa 1.1. *JHEP 02 (2009) 007*, 2009.

[110] S. Frixione and B.R. Webber. Matching NLO QCD computations and parton shower simulations. *JHEP 0206 (2002) 029*, 2002.

[111] E. Barberio et al. PHOTOS: a universal Monte Carlo for QED radiative corrections in decays. *Comput. Phys. Commun. 66 (1991) 115;*, 1991.

[112] Edmond L. Berger. The handbook of perturbative qcd. *Reviews of Modern Physics, Volume 67, Number 1, January 1995, (pp. 157-248)*, 1995.

[113] K. Melnikov and F. Petriello. Electroweak gauge boson production at hadron colliders through $O(\alpha(s)^2)$. *Phys. Rev. D74, 2006*, 2006.

[114] J.M. Butterworth et al. Single boson and diboson production cross sections in pp collisions at $\sqrt{s} = 7$ tev. *ATL-COM-PHYS-2010-695*, 2010.

[115] M. R. Whalley, D. Bourilkov, and R. C. Group. The Les Houches Accord PDFs (LHAPDF) and Lhaglue. *hep-ph/0508110*, 2005.

[116] J. Pumplin et al. New generation of parton distributions with uncertainties from global QCD analysis. *JHEP, 07:012*, 2002.

[117] Z. Was. TAUOLA the library for tau lepton decay. *arXiv:hep-ph/0011305v1*, 2000.